

HEAVY VEHICLE SYSTEMS OPTIMIZATION PROGRAM

VEHICLE TECHNOLOGIES PROGRAM

**Less dependence on foreign oil today,
and transition to a petroleum-free,
emissions-free vehicle tomorrow.**

2 0 0 7
annual progress report



U.S. Department of Energy
**Energy Efficiency
and Renewable Energy**
Bringing you a prosperous future where energy
is clean, abundant, reliable, and affordable

**U.S. Department of Energy
Vehicle Technologies Program
1000 Independence Avenue, S.W.
Washington, DC 20585-0121**

FY 2007

**Annual Progress Report for
Heavy Vehicle Systems Optimization Program**

**Submitted to:
U.S. Department of Energy
Energy Efficiency and Renewable Energy
Vehicle Technologies Program
Advanced Vehicle Technology Analysis and Evaluation**

Lee Slezak, Technology Manager

CONTENTS

I. AERODYNAMIC DRAG REDUCTION 1

A. DOE Project on Heavy Vehicle Aerodynamic Drag..... 1

B. Investigation of Tractor Base Bleeding for Heavy Vehicle Aerodynamic Drag Reduction..... 5

C. Experimental Investigation of Tractor Base Bleeding on a Full-Scale Heavy Vehicle..... 9

D. Experiments on Spray from a Rolling Tire..... 15

E. Commercial CFD Code Validation for External Aerodynamics Simulations of Realistic Heavy-Vehicle Configurations..... 16

F. Test, Evaluation, and Demonstration of Practical Devices/Systems to Reduce Aerodynamic Drag of Tractor/Semitrailer Combination-Unit Trucks..... 25

II. THERMAL MANAGEMENT 29

A. Efficient Cooling in Engines with Nucleate Boiling..... 29

B. Nanofluids for Thermal Control Applications 38

C. Erosion of Materials in Nanofluids 45

D. Diesel Engine Underhood Thermal Analysis..... 51

III. FRICTION AND WEAR..... 55

A. Boundary Lubrication Mechanisms 55

B. Parasitic Energy Loss Mechanisms..... 66

C. Efficiency Improvement Through Reduction of Friction and Wear in Powertrain Systems..... 76

D. Superhard Coatings 85

E. Residual Stresses in Thin Films 91

IV. ANALYSIS..... 99

A. PSAT Heavy-Duty Vehicle Modeling and Simulation..... 99

B. Development of Medium and Heavy Truck Systems Models 102

C. Heavy Truck Duty Cycle (HTDC) Project..... 107

V. OFF-HIGHWAY 113

A. Hybrid energy storage and fuel optimization..... 113

B. Advanced Hybrid Propulsion and Energy Management System for High Efficiency, Off Highway, 240 Ton Class, Diesel Electric Haul Trucks 117

VI. EFFICIENCY IMPROVEMENTS FOR HEAVY VEHICLES..... 125

A. Truck Essential Power Systems Efficiency Improvements for Medium-Duty Trucks..... 125

B. Advanced Electric Systems and Aerodynamics for Efficiency Improvements in Heavy Duty Trucks 131

CONTENTS (CONT.)

VII. ULTRALIGHT TRANSIT BUS SYSTEM 147
 A. The Vehicle System Optimization Of A Lightweight Stainless Steel Bus..... 147

VIII. APPENDIX A..... 150

IX. APPENDIX B..... 167

I. AERODYNAMIC DRAG REDUCTION

A. DOE Project on Heavy Vehicle Aerodynamic Drag

Project Principal Investigator: R. C. McCallen

Lawrence Livermore National Laboratory

P.O. Box 808, Livermore, CA 94551-0808

(925) 423-0958, e-mail: mccallen1@llnl.gov

Principal Investigator: K. Salari

Co-Investigators: J. Ortega

Lawrence Livermore National Laboratory

P.O. Box 808, Livermore, CA 94551-0808

(925) 424-4635, e-mail: salari1@llnl.gov

Principal Investigator: F. Browand

Co-Investigators: Charles Radovich and Dennis Plocher

Aerospace & Mechanical Engineering, University of Southern California

RRB 203, Los Angeles CA 90089-1191

(213) 740-5359, e-mail: browand@spock.usc.edu

Principal Investigator: J. Ross

Co-Investigators: B. Storms

NASA Ames Research Center

MS 260-1, Moffett Field, CA 94035

(650) 604-6722, e-mail: jcross@mail.arc.nasa.gov

Technology Development Manager: Lee Slezak

(202) 586-2335, e-mail: Lee.Slezak@ee.doe.gov

Technical Program Manager: Jules Routbort

(630) 252-5065, e-mail: routbort@anl.gov

Contractor: Lawrence Livermore National Laboratory

Contract No.: DE-AC52-07NA27344

Objective

Class 8 tractor-trailers consume 11-12% of the total US petroleum use. At highway speeds, 65% of the energy expenditure for a Class 8 truck is in overcoming aerodynamic drag. The project objective is to improve fuel economy of Class 8 tractor-trailers by providing guidance on methods for reducing drag by at least 25%. This 25% reduction in drag would present a 12% improvement in fuel economy at highway speeds, equivalent to about 130 midsize tanker ships per year. The specific goals of this project include:

- Providing guidance to industry in the reduction of aerodynamic drag of heavy truck vehicles
- Developing innovative drag reducing concepts that are operationally and economically sound
- Establishing a database of experimental, computational, and conceptual design information
- Demonstrating the potential of new drag-reduction devices

Approach

- Simulate and analyze the aerodynamic flow around heavy vehicles using advanced computational fluid dynamics (CFD) tools
- Generate an experimental database for code validation and for understanding the drag producing flow phenomena
- Provide industry with design guidance and insight into the flow physics about a heavy vehicle from experiments and computations
- Investigate aerodynamic drag reduction devices (e.g., base flaps, tractor-trailer gap stabilizer, underbody skirts and wedges, and blowing and acoustic devices, etc.)
- Provide industry with conceptual designs of drag reducing devices
- Demonstrate the full-scale fuel economy potential of these devices

Accomplishments

- Conducted a 1:20 scale wind-tunnel test at NASA Ames on the drag reduction capability of tractor base bleeding
- Performed supporting CFD simulations of the tractor base bleeding concept on a full-scale heavy vehicle in order to provide additional insight into the influence of the bleeding flow on the tractor-trailer gap flow physics
- Presented the 1:20 scale wind-tunnel data and full-scale CFD simulations at *The Aerodynamics of Heavy Vehicles II* conference; documentation of this research effort will appear as an article in the conference proceedings
- Partnered with Freightliner LLC in conducting a full-scale wind-tunnel test on the drag reduction capability of tractor base bleeding
- In collaboration with Michelin Americas Research & Development Corporation, performed an experimental study of spray from rolling tires.
- Organized an international conference, *The Aerodynamics of Heavy Vehicles II: Trucks, Buses, and Trains*, that was attended by over 80 people from academia, fleet companies, aerodynamic testing centers, automobile, tractor, trailer, engine, and tire manufacturing companies, CFD software companies, high-speed train manufacturing companies, and national laboratories. The objective of this conference was to provide a forum for discussing the development and application of advanced computational and experimental methods for the aerodynamic design of trucks, buses, and trains. In addition, the conference gave the opportunity for fleet operators and tractor and trailer manufacturers to share an industry perspective on the shortcomings of current drag reduction devices and to make suggestions for operationally-minded improvements for these devices. A follow-on conference to take place in two to three years in Europe is currently in the planning stages.



Attendees to *The Aerodynamics of Heavy Vehicles II: Trucks, Buses, and Trains* conference, August 26-31, 2007, Granlibakken Conference Center, Tahoe City, California.

Future Direction

- Getting devices on road
 - From an understanding of key flow mechanisms, develop operationally-minded drag reduction concepts; current computational efforts are investigating a trailer underbody device that could potentially overcome the shortcomings of trailer side skirts, while providing comparable reductions in drag
 - Conduct a full-scale wind-tunnel test at the NASA Ames 80'x120' wind-tunnel by leveraging support from TMA/DOE, California Air Resources Board (CARB), EPA, and International Trucks
 - Seek collaborative feedback and demonstrations of drag reduction devices from fleet owners and operators
 - Economic/duty cycle evaluation with PSAT (ANL's system model)
 - Provide mechanistic data: strong variation in the drag coefficient with yaw, air speed, geometry/devices, environmental turbulence, etc.
 - Develop and transfer technology and information to industry
 - Contouring the tractor hood provides a reduction in drag, but also reduces the grille area and coolant air flow. Since the underhood exhaust gas recirculation to meet EPA regulations requires more underhood cooling, we are including underhood flow in the aerodynamic drag simulations and in the planning for the 80'x120' wind-tunnel tests. This will allow us to provide additional insight into this coupled (thermal, fluid) flow phenomena.
 - Identified the need for experimental and computational methods for evaluation of design options for improved efficiency, e.g., optimization methods and tools.
 - Leverage Program work and seek funding from other agencies.
-

In the following pages are detailed reports from each of the participating organizations on the findings and accomplishments for fiscal year 2007. There are three areas identified for aerodynamic drag reduction and several devices have been investigated. The areas in which drag reduction can be achieved include the tractor-trailer gap, wheels and underbody, and trailer base. Currently, over 12% increase in fuel economy is possible by employing several devices simultaneously, e.g.,

- > 4% trailer base-flaps
- > 6% trailer skirts
- > 2% gap splitter plate
- > 12% Total

Unfortunately, these devices have a number of operational and maintenance issues and are not used by the shipping fleets. With our understanding of the aerodynamics of heavy

vehicles, we are developing operationally-minded and innovative drag reduction concepts using CFD and experiments. In addition to obtaining feedback from the fleets on these devices, we are collaborating with other government agencies (e.g., DOT, EPA, CARB) and industry (i.e., Michelin is providing partial support for experiments at USC) to further investigate device performance at full-scale operating conditions. Lastly, the rolling resistance and splash and spray effort will continue to receive complimentary support from industry and we will actively seek joint government funding.

Acknowledgments

This work was performed under the auspices of the U.S. Department of Energy by Lawrence Livermore National Laboratory under Contract DE-AC52-07NA27344

B. Investigation of Tractor Base Bleeding for Heavy Vehicle Aerodynamic Drag Reduction

Kambiz Salari and Jason Ortega

Lawrence Livermore National Laboratory

7000 East Ave, L-098, Livermore, CA 94551

(925) 423-0958, fax: (925) 422-3389, e-mail: salari1@llnl.gov

Technology Development Manager: Lee Slezak

(202) 586-2335, e-mail: Lee.Slezak@ee.doe.gov

Technical Program Manager: Jules Routbort

(630) 252-5065, e-mail: routbort@anl.gov

Contractor: Lawrence Livermore National Laboratory

Contract No.: DE-AC52-07NA27344

Objective

One of the main contributors to the aerodynamic drag of a heavy vehicle is tractor-trailer gap drag, which arises when the vehicle operates within a crosswind. Under this operating condition, freestream flow is entrained into the tractor-trailer gap, imparting a momentum exchange to the vehicle and subsequently increasing the aerodynamic drag. While a number of add-on devices, including side extenders, splitter plates, vortex stabilizers, and gap sealers, have been previously tested to alleviate this source of drag, side extenders remain the primary add-on device of choice for reducing tractor-trailer gap drag. However, side extenders are not without maintenance and operational issues. When a heavy vehicle pivots sharply with respect to the trailer, as can occur during loading or unloading operations, the side extenders can become crushed against the trailer. Consequently, fleet operators are forced to incur additional costs to cover the repair or replacement of the damaged side extenders. This issue can be overcome by either shortening the side extenders or by devising an alternative drag reduction concept that can perform just as effectively as side extenders. To explore such a concept, we investigate tractor base bleeding as a means of reducing gap drag.

Approach

Wind tunnel measurements are made on a 1:20 scale heavy vehicle model (Figure 1) at a vehicle width-based Reynolds number of 420,000. The tractor bleeding flow, which is delivered through a porous material embedded within the tractor base, is introduced into the tractor-trailer gap at bleeding coefficients, C_{μ} , ranging from 0-0.018, where the bleeding coefficient is defined to be equal to $C_{\mu} = U_b A_b / U_o A_o$ and U_b is the bleeding velocity, A_b the bleeding area, U_o the freestream velocity, and A_o the characteristic area of the vehicle. To determine the performance of tractor base bleeding under more realistic operating conditions, computational fluid dynamics simulations are performed on a full-scale heavy vehicle within a crosswind for bleeding coefficients ranging from 0-0.13.

Accomplishments

- *Wind-tunnel measurements of tractor base bleeding at 1:20 scale*

The wind tunnel measurements demonstrate that the drag coefficient decreases as the bleeding coefficient is increased for the two gap distances in this study. Though, a greater reduction in drag is observed for the larger gap distance both with and without side extenders. When $C_{\mu} > 0.006$, tractor base bleeding with no side extenders for the larger gap distance yields a greater reduction in drag greater than that of side extenders alone with no bleeding flow (Figure 2). It should also be noted that the wind-averaged drag coefficients for the larger gap are greater than those of the smaller gap, indicating the presence of a larger amount of entrained flow into the tractor-trailer gap.

- *CFD simulations of tractor base bleeding at full-scale*

While the wind tunnel measurements demonstrate that tractor base bleeding can indeed reduce the drag of the 1:20 scale heavy vehicle model, further investigation is needed both to demonstrate the effectiveness of this concept at a full-scale Reynolds number and to understand the changes in the gap flow physics arising from the base bleeding. For these reasons, we perform computational fluid dynamics (CFD) simulations on a full-scale Freightliner Columbia (Figure 3) operating at highway conditions within a crosswind (6.1° vehicle yaw angle). The tractor-trailer gap distance is set to 1.02m and a 13.6m long freight van is attached to the tractor.

A plot of the drag coefficient as function of the bleeding coefficient (Figure 4) reveals that, in much the same manner as that of the wind tunnel measurements, increases in bleeding flow decrease the drag coefficient. In addition, the drag reduction of $\Delta C_d \approx 0.025$ observed for $C_{\mu} \approx 0.018$ is about equal to that seen experimentally ($\Delta C_d \approx 0.02$) at 6° yaw for the larger gap distance despite the relatively large difference in vehicle Reynolds number. For the computational results, the drag coefficient decreases in a nearly linear fashion for the largest bleeding coefficients, values of which were not attainable in the wind tunnel measurements. The largest reduction in drag ($\Delta C_d = 0.146$) occurs at the maximum bleeding coefficient of 0.13. It is also evident bleeding coefficients greater than 0.04 provide a larger reduction in drag than that of the side extenders ($\Delta C_d = 0.049$). Obviously, a portion of the drag reduction produced by base bleeding is due to the thrust of the bleeding flow and not to modifications of the tractor-trailer gap flow physics. Removing this thrust contribution from the drag coefficient data in Figure 4 demonstrates that, for all bleeding coefficients, a significant drag reduction occurs solely due to changes in the gap flow physics.

- For a complete discussion of both the 1:20 wind-tunnel measurements and the full-scale CFD simulations, the reader is referred to the conference paper, Investigation of Tractor Base Bleeding for Heavy Vehicle Aerodynamic Drag Reduction, in Appendix A.

Near Term Direction

- Publish the 1:20 scale wind tunnel measurements and full-scale CFD simulations in the proceedings for *The Aerodynamics of Heavy Vehicles II: Trucks, Buses, and Trains* conference

Far Term Direction

- Collaborate with industry and NASA and determine if tractor base bleeding should be investigated in the full-scale aerodynamic tests in the 80' x 120' wind tunnel

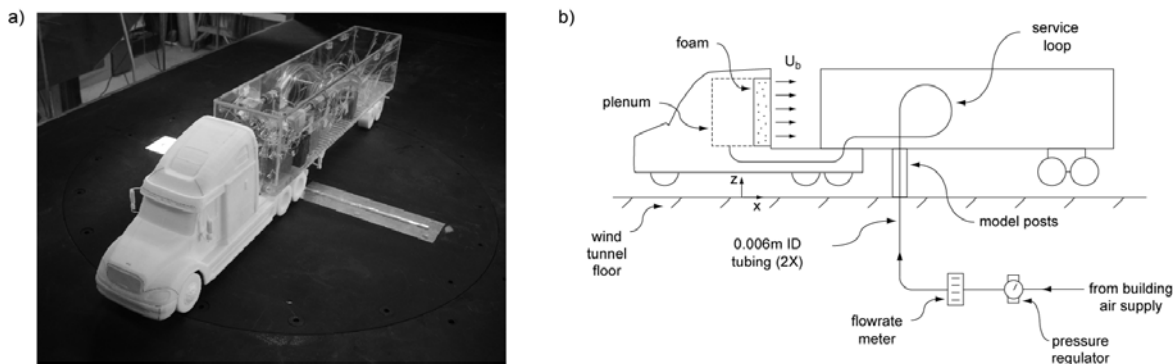


Figure 1. a) 1:20 scale wind-tunnel model. b) Schematic of the tractor base bleeding system

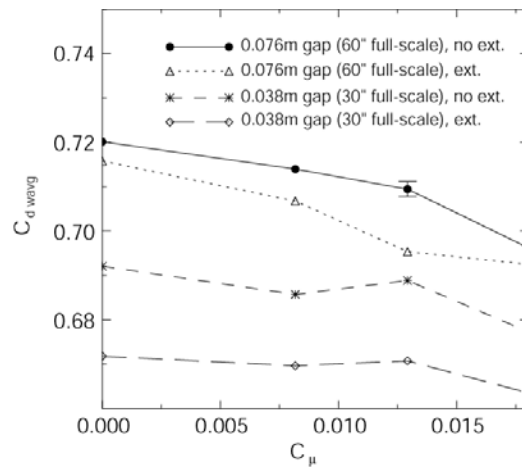


Figure 2. Wind-averaged drag coefficient, $C_{d,wavg}$, as a function of the bleeding coefficient, C_{μ} , for the 1:20 scale wind-tunnel model.



Figure 3. Freightliner Columbia model used in the full-scale CFD simulations.

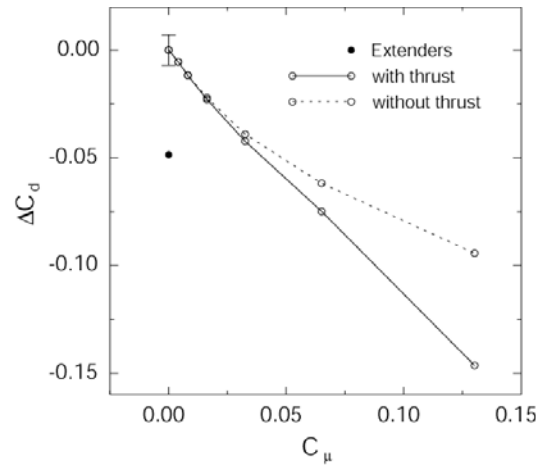


Figure 4. Change in the drag coefficient as a function of the bleeding coefficient for the full-scale CFD simulations.

C. Experimental Investigation of Tractor Base Bleeding on a Full-Scale Heavy Vehicle

Kambiz Salari, Jason Ortega
Lawrence Livermore National Laboratory
7000 East Ave, L-098, Livermore, CA 94551
(925) 423-0958, fax: (925) 422-3389, e-mail: salari1@llnl.gov

Technology Development Manager: Lee Slezak
(202) 586-2335, e-mail: Lee.Slezak@ee.doe.gov

Technical Program Manager: Jules Routbort
(630) 252-5065, e-mail: routbort@anl.gov

Contractor: Lawrence Livermore National Laboratory
Contract No.: DE-AC52-07NA27344

Objective

- The purpose of this study is to measure the drag reduction capability of tractor base bleeding on a full-scale heavy vehicle.

Approach

- Wind tunnel measurements are made on a Freightliner Century Class heavy vehicle at the Freightliner Test Engineering wind-tunnel in Portland, Oregon.

Accomplishments

- For several of the configurations tested, tractor base bleeding reduced the drag coefficient by as much as 0.016 and modified the gap flow in a measurable manner. However, the net power saved by reducing aerodynamic losses was not greater than the amount of power consumed by the bleeding system.

Near Term Direction

- Determine if a more efficient tractor base bleeding system can be designed

Far Term Direction

- Collaborate with industry and NASA and determine if tractor base bleeding should be investigated in the full-scale aerodynamic tests in the 80' x 120' wind tunnel.
-

Motivation and Background

Following the 1:20 scale wind-tunnel measurements and the full-scale CFD simulations of tractor base bleeding, a number of questions remained unanswered regarding the feasibility of the base bleeding concept. Some of these questions were: Will tractor base bleeding reduce the aerodynamic drag of an actual full-scale heavy vehicle? What is the order of magnitude of the power required to produce the necessary bleeding flow? How effective is such a drag reduction concept? To answer these questions, a collaborative effort was formed between LLNL and Freightliner LLC to perform full-scale wind-tunnel measurements on the tractor base bleeding concept.

Experimental Setup

Aerodynamic measurements are made at the Freightliner Test Engineering wind-tunnel in Portland, Oregon, on a Freightliner Century Class tractor that has a characteristic area of $A_o = 10.2\text{m}^2$ (Figure 1). The wind tunnel has a contraction ratio of 4:1 and a nominal cross-sectional area of $7.6\text{m} \times 6.1\text{m}$ with contoured side and top walls. Freestream wind speeds, U_o , ranging from 13-26m/s are produced by altering the blade pitch of ten fans located at the downstream outlet of the tunnel. For this test, the tractor is positioned at a yaw angle of 6° on a force balance that measures the drag coefficient, C_d , to within ± 0.002 . In order to increase the signal-to-noise ratio of the changes in drag due to the bleeding flow, the mirrors and visor are removed from the tractor and a belly pan is placed on the engine underbody. The bleeding flow, which is produced by five industrial carpet blowers (3600W of total power consumption) located within the tractor cabin, is passed through two large holes on the tractor base (Figure 2a). These holes, which span an area of $A_b = 3.6\text{m}^2$ ($0.35A_o$), are covered with chicken wire and window screen material. A handheld wind anemometer is used to measure the bleeding velocity profile (Figure 2b) across the tractor base.

Integrating this velocity data over the entire bleeding area indicates that the bleeding flowrate, Q_b , is $3.97\text{m}^3/\text{s}$ (8420cfm).

Pressure measurements are made on the front face of the trailer using 13 pressure taps (Figure 3) located at the mid-height of the trailer. A total of 16 hours of wind-tunnel testing is conducted on the tractor base bleeding concept, thus providing data for 94 different run configurations (Figure 4) in which the following parameters are varied:

- $U_o = 13.1\text{m/s}$ (29.3mph), 19.5m/s (43.6mph), and 25.7m/s (57.5mph)
- Base bleeding coefficients, $C_\mu = Q_b/U_o A_o$, of 0.0, 0.015, 0.020, 0.029
- Variable gap width: 0.9, 1.2, 1.6, 1.9m
- Gap deck plate on and off
- Side extenders on and off
- Engine grill open and closed

Results

Of the 94 run configurations, a reduction in drag due to the bleeding flow is observed in 8 run configurations (Table 1). The greatest reduction in drag ($\Delta C_d = -0.016$, Runs 90, 93) is seen for the case with $U_o = 19.5\text{m/s}$, an open engine grill, no side extenders, and 0.9m tractor-trailer gap. However, in these 8 configurations, the net power saved by reducing aerodynamic losses is not greater than the amount of power consumed by the bleeding system.

The pressure measurements (Figure 5) on the front of the trailer indicate that the tractor base bleeding modifies the flow within the tractor trailer gap. For the configurations with $U_o = 13.1\text{m/s}$, $C_\mu = 0.029$, the engine grill closed, no gap deck plate, and the side extenders installed, the bleeding flow reduces the pressure on the windward side of the trailer frontal face for the three tractor-trailer gap distances, suggesting that the bleeding flow is laterally shifting the windward shear layer in the manner shown in Figure 6.



Figure 1. Freightliner Century Class tractor in the Freightliner 7.6m × 6.1m wind tunnel.

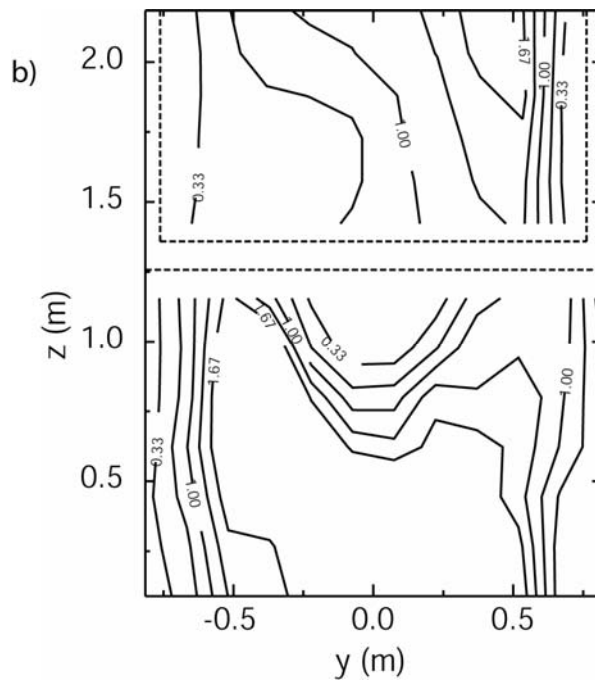
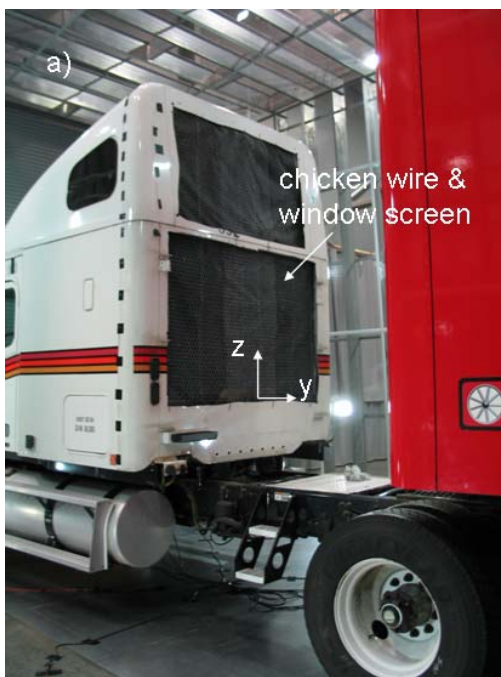


Figure 2. a) Tractor base bleeding area. b) Bleeding velocity contours (in m/s).

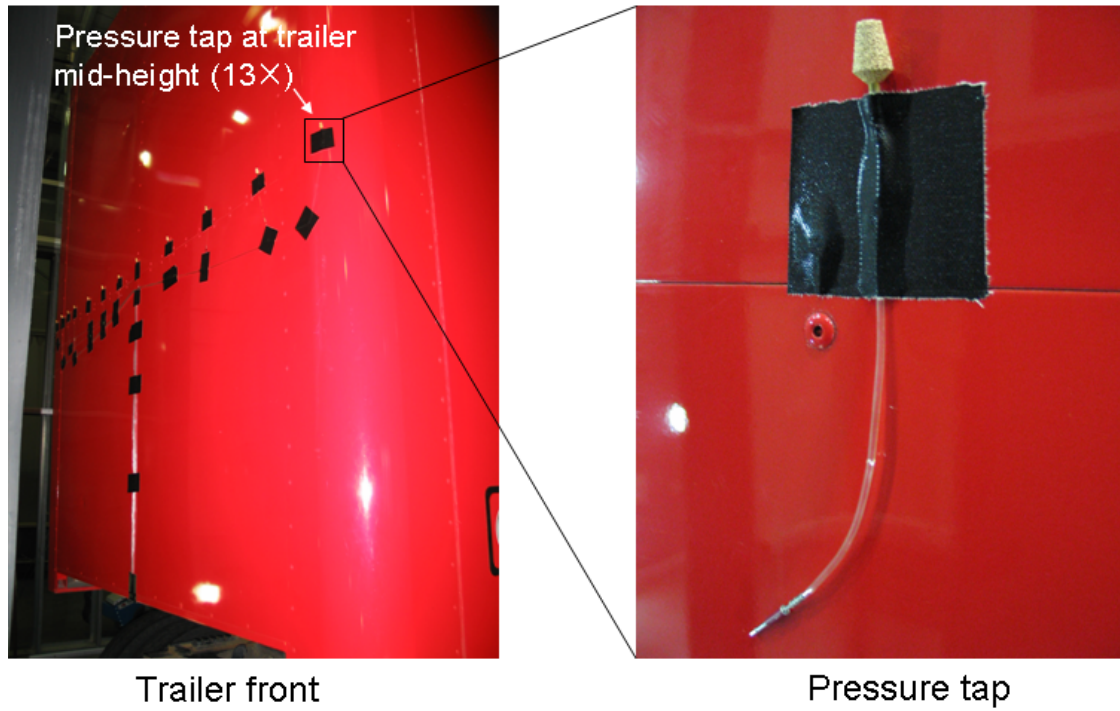


Figure 3. Pressure taps positioned on the trailer frontal face.

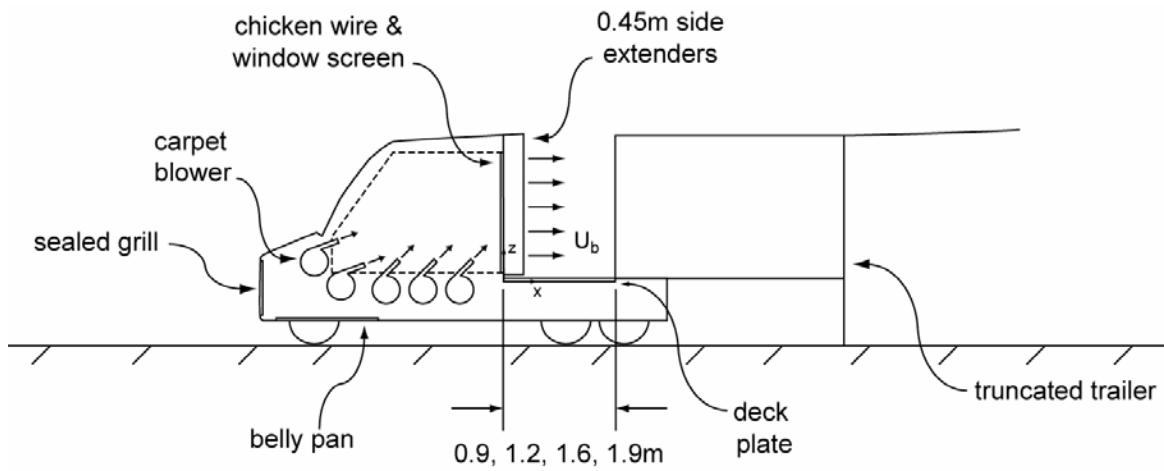


Figure 4. Experimental setup for the 94 run configurations.

Table 1. Run configurations in which a reduction in drag is measured.

Runs	Description	Gap (m)	U_o (m/s)	C_{μ}	ΔC_d	$(P_{\text{saved}} - P_{\text{blower}}) / P_{\text{blower}}$ (%)
91,92	No side ext., grill open	0.9	13.1	0.029	-0.010	-95.93
90,93	No side ext., grill open	0.9	19.5	0.020	-0.016	-79.35
89,94	No side ext., grill open	0.9	25.7	0.015	-0.011	-67.29
83,87	No side ext., grill closed	0.9	19.5	0.020	-0.004	-94.84
82,88	No side ext., grill closed	0.9	25.7	0.015	-0.006	-82.25
75,79	No side ext., grill closed	1.2	19.5	0.020	-0.007	-91.02
74,81	No side ext., grill closed	1.2	25.7	0.015	-0.003	-91.14

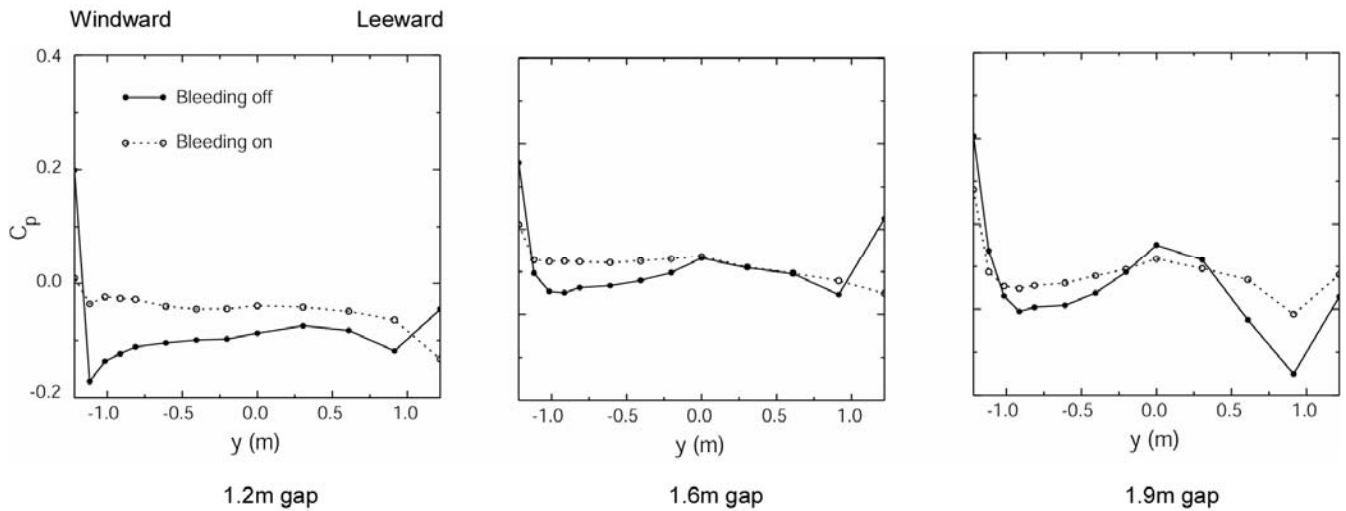


Figure 5. Pressure distribution across the trailer frontal face for the configurations with $U_o = 13.1\text{m/s}$, $C_{\mu} = 0.029$, the engine grill closed, no gap deck plate, and the side extenders installed.

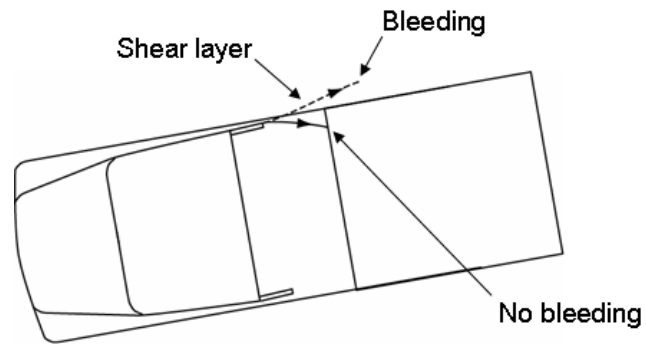


Figure 6. Schematic of how the bleeding flow may be modifying the windward shear layer in the tractor trailer gap.

D. Experiments on Spray from a Rolling Tire

Principal Investigator: F. Browand

Co-Investigators: Charles Radovich and Dennis Plocher

Aerospace & Mechanical Engineering, University of Southern California

RRB 203, Los Angeles CA 90089-1191

(213) 740-5359, e-mail: browand@spock.usc.edu

Technology Development Manager: Lee Slezak

(202) 586-2335, e-mail: Lee.Slezak@ee.doe.gov

Technical Program Manager: Jules Routbort

(630) 252-5065, e-mail: routbort@anl.gov

Contractor: Lawrence Livermore National Laboratory

Contract No.: W-7405-ENG-48

Objective

- The purpose of this study is to understand the key mechanisms behind spray emerging from a rolling tire.

Approach

- A novel laboratory apparatus has been built to study water leaving the tire from a single circumferential groove. Data collection is achieved using high-speed imaging.

Accomplishments

- Visualizations reveal the formation of thin sheets of water connecting the roadway and the tire that eventually break into a droplet field. It is proposed that sheet breakup is the result of hydrodynamic instability.
-

For a complete discussion, the reader is referred to the paper, Experiments on Spray from a Rolling Tire, in Appendix B.

E. Commercial CFD Code Validation for External Aerodynamics Simulations of Realistic Heavy-Vehicle Configurations

Principal Investigator: W. D. Pointer

Argonne National Laboratory

9700 S Cass Avenue, NE-208, Argonne, IL 60439

(630) 252-1052, fax: (630) 252-4500, e-mail: dpointer@anl.gov

Technology Development Area Specialist: Lee Slezak

(202) 586-2335, e-mail: Lee.Slezak@ee.doe.gov

Technical Program Manager: Jules Routbort

(630) 252-5065, e-mail: routbort@anl.gov

Contractor: Argonne National Laboratory

Contract No.: W-31-109-ENG-38

Objective

- Evaluate capabilities in standard commercial computational fluid dynamics (CFD) software for the prediction of aerodynamic characteristics of a conventional U.S. Class 8 tractor-trailer truck.
- Develop practices and procedures for the application of commercial CFD software in the design process of Class 8 vehicles.
- Apply practices and procedures to evaluation of geometric modifications and drag-reducing devices to assess potential energy savings

Approach

- Develop computational models of simplified vehicles based on the Generic Convention Model geometry used in experiments completed in the NASA Ames Laboratory's 7 ft. by 10 ft. wind tunnel.
- Compare the predictions of the computational models with experimental measurements of vehicle aerodynamic drag force and pressure field distributions.
- Assess variation in aerodynamic performance for changes in radiator configuration

Accomplishments

- Experimental measurements and computational predictions of the vehicle drag coefficient agree within less than 1 percent in the best case simulations at zero yaw and within less than 5% at higher yaw angles. Experimental measurements and computational predictions of the pressure distribution along the surface of the vehicle agree well everywhere except the rear faces of the cab and the trailer.
- Established that small changes in radiator width, height, or surface area do not significantly impact the drag coefficient if all other dimensions are held constant.
- Established that the flow into the underhood through the radiator does not significantly impact the drag losses.

Future Direction

- Work with team members in the development of an integrated approach to development of the next generation heavy vehicle transportation
-

Abstract

Work began in late 2004 to quantify the aerodynamics-related fuel economy impacts of potential changes in tractor-trailer designs in response to EPA emissions regulations to take effect in 2007 and in 2010. Although the new standards are expected to increase engine heat rejection requirements and, consequently, radiator sizes, new technologies being developed under a U.S. Department of Energy sponsored effort led by Caterpillar, Inc. may provide opportunities to even reduce the size of radiators while meeting the new emissions requirements. Computational fluid dynamics simulations have been used to numerically evaluate the potential impacts of small changes in radiator size and configuration on the aerodynamic characteristics of a conventional tractor-trailer vehicle. For a reasonably aerodynamic vehicle, these studies show that neither small increases nor small decreases in radiator dimensions have a significant impact on the drag-related energy losses of a tractor trailer.

Introduction

In December 2004, Argonne National Laboratory and Caterpillar Inc. established a Cooperative Research and Development Agreement (CRADA) with support from the U.S. Department of Energy Office of Energy Efficiency and Renewable Energy's Vehicle Technologies Program as a component of a larger consortium effort led by Caterpillar Inc. to investigate and implement reductions in parasitic energy losses in heavy-duty Class 3-8 trucks through electrification and optimization of thermal management. The purpose of this collaboration is to quantify the impact of changes in the frontal area of the radiator of a conventional U.S. Class 8 tractor-trailer vehicle on the aerodynamic characteristics of the vehicle.

Background

The October 2002 EPA emissions regulations resulted in increased engine heat rejection, and the 2007 regulations have resulted further increases as a consequence of exhaust gas recycle. Caterpillar Inc.'s More Electric Truck concept offers technology solutions to mitigate or even neutralize the effects of this trend. The concept also presents opportunities to reduce cooling system frontal area and possibly

benefit from reduced aerodynamic drag losses. If better fuel economy can accompany emissions reductions, customers may be encouraged to purchase the vehicles as an improved capital investment.

A major goal of the program as a whole is to analyze, design, build, and test a cooling system that provides a minimum of 10% greater heat rejection in the same frontal area, with no increase in parasitic fan load. The cooling system will use a combination of key new and in-depth analyses will be performed to determine maximum system airflow required, and resultant fan power and configuration requirements. In support of this program, Argonne National Laboratory has applied validated commercial Computational Fluid Dynamics tools to the quantification of potential fuel savings or costs that result from changes in the tractor aerodynamic characteristics due to changes in the heat exchanger package geometry.

Modeling Strategy

Prior efforts [1, 2, 3] as part of the U.S. Department of Energy's Heavy Vehicle Aerodynamics Working Group [4] have evaluated the applicability of commercial CFD software in heavy vehicle design, including assessments of the expected impact of grid resolution and structure on prediction accuracy, the impact of the RANS turbulence model formulation selected, the impact of considering only half of a vehicle to speed up initial simulations. The experience developed by this program provides generic advice for the application of a commercial finite-volume based CFD software package to the prediction of heavy vehicle aerodynamic drag coefficients. In this effort, the experience accumulated in the application of commercial CFD tools to heavy vehicles is applied to enable the quantification of the effects of changing the design of the heat exchanger package.

Selection of Commercial CFD Software

All computational simulations presented herein have used version 3.26 of the commercial CFD code Star-CD. [5] The Star-CD software was selected for this purpose largely because the code offers a great deal of the flexibility in computational mesh development with the ability to utilize polyhedral "cut" cells and recognize both integral and arbitrary interfaces

between regions of the computational domain. Furthermore, user subroutines allow the user to implement significant modifications to most features of the code if such modifications are needed. It is anticipated that the applicability of the general observations on modeling strategy extends to other commercial CFD codes using the finite volume methodology and that those codes will provide similar results to those presented herein.

Selection of Tractor Trailer Geometry

The broader program objectives have been implemented on a Kenworth T-2000 tractor, which was the vehicle platform of the program’s predecessor, the More Electric Truck. Since business proprietary data issues prevented the use of the Kenworth T-2000 tractor geometry directly in the assessment of potential fuel savings, the U.S. Department of Energy’s Generic Conventional Model geometry has been used as a surrogate, representative aerodynamic tractor.

The Generic Conventional Model (GCM), developed by NASA Ames Research Center for scaled wind tunnel testing, is a generalized representation of a conventional aerodynamic U.S. tractor-trailer truck, as shown in Figure 1. The 1/8th scale model is approximately 2.5 m long by 0.3 m wide by 0.5 m high. The studies contained herein consider experiments that were completed in the NASA Ames 7ft. by 10 ft. wind tunnel. Instrumentation included a force balance, 476 steady pressure transducers, 14 dynamic pressure transducers, and three-dimensional Particle Image Velocimetry (PIV). Data was collected at various Reynolds number values and yaw angles. [6]

Computational Model

The computational model employed in these studies was developed using the ES-Aero tool for aerodynamic drag simulation that is available as part of the Star-CD software package. The surface of the standard configuration GCM is defined using approximately 500,000 triangular surface elements based upon CAD data representations taken from optical scans of the actual model. A computational domain, which as external dimensions that are based on the cross-sectional dimensions of the wind tunnel, is developed based upon this surface definition using a semi-automated process that begins by creating a hexahedral mesh that is successively refined in

smaller zones around vehicle, with integral cell coupling employed at the interfaces between zones. The dimensions of hexahedral elements that make up the zone immediately surrounding the vehicle are specified by user as the near vehicle cell size. The mesh elements near the vehicle surface are then further refined based upon local surface features identified by the user or selected automatically based on curvature or gap width. The user specifies a minimum allowable cell size that limits the refinement of the mesh in this step.

Using this locally refined hexahedral mesh, the original surface is “wrapped” by projecting the hexahedral mesh onto the original surface. The “wrapped” surface definition is then volumetrically expanded to create a subsurface which is used to cut away the portions of the locally-refined hexahedral mesh that fall inside the vehicle. A brick and prism cell extrusion layer is then created to fill the gap between the sub-surface and the “wrapped” surface. In this way, the polyhedral cut cells are removed some distance from the surface, and a consistent y+ value between approximately 20 and 200, can be maintained regardless of grid resolution, insuring that the computational meshes are suitable for the turbulence models used in these studies. A final step further refines the wake region and the underbody region in order to better capture a steady state representation of important flow features. An example of the mesh construction of the computational domain used in the GCM simulations is shown in Figure 2.



Figure 1. Generic Conventional Model (GCM)



Figure 2. Example of computational mesh structure used in the simulation of the aerodynamic characteristics of the Generic Conventional Model (GCM)

Using locally-refined, face-coupled computational domains with substantial numbers of non-hexahedral cells makes the standard practice of evaluating grid convergence by uniformly refining the entire mesh in all directions intractable. In the computational meshes used in these studies, two separate parameters determine the size of the mesh. Mesh sensitivity analyses included in these studies examine the effects of changes in the near-vehicle cell size and minimum cell size parameters on the prediction of the drag coefficient. However, this is not equivalent to the traditional grid convergence study because the grid is not uniformly refined in all directions throughout the domain and the vehicle surface definition cannot be exactly maintained for all models since the final surface definition is dependent upon the local refinement of the computational mesh.

Brief Summary of Prior Results

Brief Summary of Prior Validation and Sensitivity Results

Prior studies focused on establishing the validity of commercial CFD software for the prediction of the aerodynamic characteristics of a tractor-trailer vehicle. This previous effort included a mesh sensitivity study considering the effect of near vehicle cell size and minimum cell size on the accuracy of aerodynamic characteristics as well as the impact of turbulence model selection and the use of half vehicle versus full vehicle models. Additional studies have examined the ability to predict the impact of cross-winds on aerodynamic performance.

Computational Mesh Sensitivity

A series of studies have been completed to evaluate sensitivity of the predictive accuracy to selection of the two primary characteristic dimensions of the generated computational mesh: the near vehicle cell size and the minimum cell size. The near-vehicle cell size defines the dimensions of the cells in the region of tunnel-aligned hexahedral brick cells closest to the model surface. The minimum cell size is the limit applied to the automatic refinement of the region immediately adjacent to the vehicle surface and defines the smallest cell that can be used to capture local surface characteristics.

To assess the impact of the near-vehicle cell size, a series of parametric simulations was completed

specifying near-vehicle cell sizes between 6mm and 10 mm for the 1/8th scale GCM. Results, summarized in Table 1, indicate that the drag coefficient can be predicted with acceptable accuracy using a near vehicle cell size of 6 mm. Furthermore, coarser meshes using near vehicle cell sizes as large as 12 mm can likely be used for initial coarse evaluations and trending.

Table 1. Effects of Near-Vehicle Cell Size Parameter on Accuracy of Drag Coefficient Prediction.

Near-Vehicle Cell Size (mm)	Predicted Drag Coefficient	Error in Drag Coefficient
experiment	0.398	
16	0.449	12.0
12	0.441	10.3
10	0.418	4.9
8	0.415	4.2
6	0.405	1.7

Based on these results, an additional study was completed to evaluate the impact of the minimum cell size. The default minimum cell size in the previous study was 1/8 the near-vehicle cell size. In this study the minimum cell size was reduced to determine whether the same computational accuracy observed in the 6mm case could be achieved using a smaller number of computational cells. When the minimum cell size in the 8 mm case was reduced from 1 mm to 0.5 mm, the accuracy of the drag coefficient prediction improved from 4.2 percent error to 1.0 percent error. This level accuracy was achieved using 30% fewer computational cells than in the most refined model in the near-vehicle cell size study. Further studies have shown that the further refinement of the near wall cells does not improve the accuracy of the drag coefficient predictions.

Turbulence Model Effects

In all simulations completed for the computational mesh sensitivity studies, the high Reynolds number k-ε turbulence model was used in conjunction with a standard logarithmic wall function for the prediction of turbulent kinetic energy and eddy diffusivity. While the high Reynolds number k- ε turbulence

model is a robust general purpose turbulence model, the strong adverse pressure gradients and large flow recirculation regions associated with the GCM geometry may limit the applicability of steady state RANS modeling strategies. Using the computational mesh with a near vehicle cell size of 8 mm and a near wall cell size limit of 0.5 mm, simulations of the aerodynamic characteristics of the GCM model were repeated using five steady RANS turbulence models and their associated wall functions: 1) the standard high-Reynolds number $k-\epsilon$ model with logarithmic wall function, 2) the Menter $k-\omega$ SST model, 3) the renormalization group (RNG) formulation of the $k-\epsilon$ model, 4) the Chen formulation of the $k-\epsilon$ model, and 5) the quadratic formulation of the $k-\epsilon$ model. Drag coefficients predicted using each of the selected steady-RANS turbulence models are shown in Table 2. Comparisons of the predicted pressure coefficient distributions when using the selected turbulence models are shown in Figure 3. The differences in the predicted drag coefficient are largely a result of localized discrepancies in the surface pressure coefficient predictions in the regions of separated flow, with the largest discrepancies appearing in the underbody region just behind the tractor.

Yaw Angle Effects

The effects of cross-winds on the vehicle performance are evaluated by rotating the model in the wind tunnel to introduce an effective yaw angle between the wind direction and the vehicle direction. In the wind tunnel experiments, yaw angles between 14 degrees and -14 degrees were considered. In the experiments, a low drag state is observed at low yaw angles. For yaw angles greater than 3 degrees a higher drag state was observed, where large flow separation zones begin to form along the leeward side of both the tractor and trailer, introducing significant turbulent instability into the flow field. The instability is further exacerbated by the formation of a highly turbulent jet through the gap between the tractor and trailer which washes over the logical separation points on the leeward side of the trailer, extending the separation zone.

Using this data for comparison, a series of simulations were completed to evaluate the effects of the computational mesh parameters on predictive accuracy at yaw angles greater than zero. Results of the mesh sensitivity study are summarized in

Table 2. Results of evaluation of two-equation turbulence models for prediction of drag coefficients for the GCM geometry.

Turbulence Model	Predicted Drag Coefficient	Percent Error in Prediction
Experiment	0.398	--
High-Reynolds Number $k-\epsilon$ Model	0.402	1.0
Menter $k-\omega$ SST model	0.401	0.8
RNG model	0.389	2.3
Chen's model	0.3919	1.61
Quadratic model	0.3815	4.32

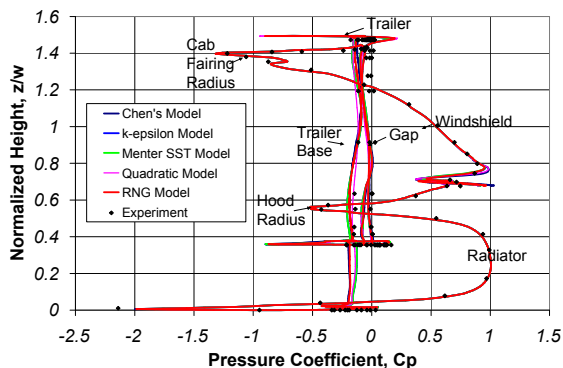


Figure 3. Comparison of predicted pressure coefficient distributions on the vehicle surface with experimental data for selected turbulence models.

Figure 4. These studies show that the transition between the high and low drag state can be accurately captured using the methodology developed for the GCM at zero yaw angle. Furthermore, the studies demonstrate that the aerodynamic coefficients of the vehicle can be predicted within a few percent error when sufficient resolution is used near the vehicle surface. Additional simulations included in this study indicate that little difference in drag coefficient predictions is observed for cases using the 8mm near vehicle cell size when the minimum cell size is further reduced from 0.5 mm to 0.25 mm.

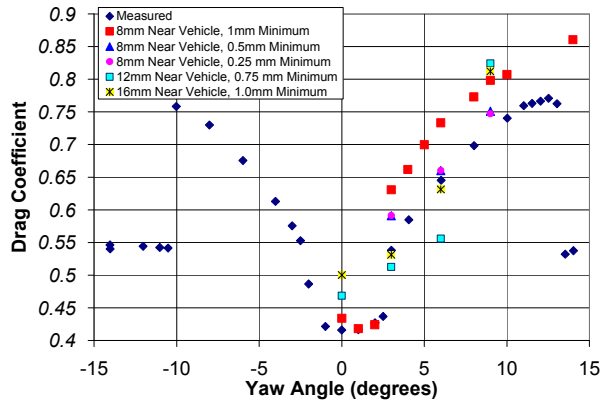


Figure 4. Comparison of Drag Coefficient Predictions as a Function of Yaw Angle and Mesh Size Parameters.

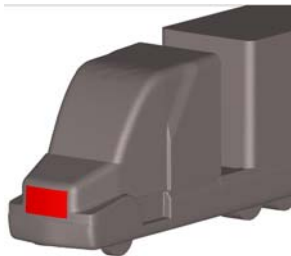


Figure 5. Location of Outlet Boundary Surface in Evaluation of Radiator Flow Effects.

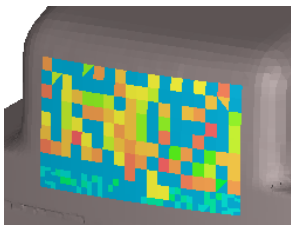


Figure 6. Drag Force Distribution on Surfaces where Outlet Boundary Condition is Placed.

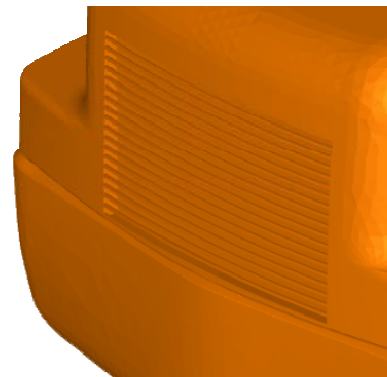


Figure 7. Grill Geometry of the Modified Generic Conventional Model used for Evaluations of the Effects of Radiator Flow on Aerodynamic Characteristics.

Radiator Flow Effect Studies

To determine whether the flow of external air through the radiator and into the engine compartment must be modeled when considering tractor design changes, a series of simulations was completed in which an outlet condition is placed at or near the grill location. In these cases, air entering the engine compartment does not exit to rejoin the bulk flow, as if the vehicle contained a tank of infinite volume into which it was transferred. While not physically representative, this approach allows the effects of flow entering the radiator to be isolated from the effects of flow exiting the underhood region into the bulk flow around the vehicle.

In the simplest case, the flow into the radiator is modeled by applying a zero-gradient outlet boundary condition directly on the surface of the tractor in the position of the grill, as shown in Figure 5. For zero yaw, this change resulted in a 7 percent increase in drag coefficient above the nominal geometry result using similar computational mesh and the same high-Reynolds number k-epsilon turbulence model. However, the calculation of forces acting on a zero-gradient outlet boundary tends to result in irregular surface force distribution on that boundary, as shown in Figure 6, and is not recommended by the code developer.

To reduce the inaccuracy resulting from this approximation, the CAD data was modified to include an open grill region as shown in Figure 7. Flow then passes through this grill before exiting the model through an outlet condition placed roughly at the position of the radiator surface. With the majority of the stagnation pressure acting on the surface of the grill rather than the outlet boundary, smoother pressure contours are observed on the grill region, as shown in Figure 8. Since flow velocities within the gap between the grill and radiator are very small and the pressure within the gap is much lower than the stagnation pressure, the impact of the inaccuracy of the force calculation on the outlet boundary on the total drag force calculation is minimized. With the modified geometry, consideration of flow into the radiator results in an increase in the vehicle drag coefficient of approximately 1 percent. Based on these results, it is assumed that the flow into the radiator can be neglected.

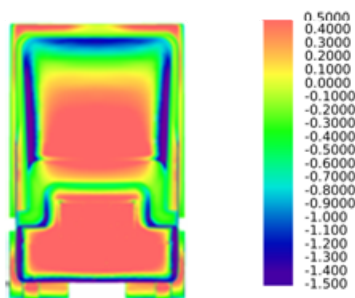


Figure 8. Predicted Pressure Distribution using the Modified GCM Geometry, shown in Figure 7.

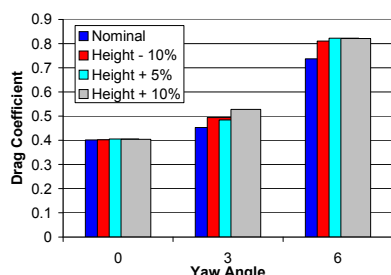


Figure 9. Comparison of Predicted Drag Coefficients as a Function of Radiator Height and Vehicle Yaw Angle.

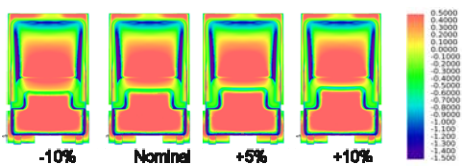


Figure 10. Comparison of Predicted Surface Pressure Coefficient Distributions for Changes in Radiator Height at Zero Yaw Angle.

Radiator Configuration Effect Studies

Radiator configuration effect studies have considered:

- Changes in grill/radiator height
- Changes in grill/radiator width
- Changes in grill/radiator surface area (aspect ratio maintained)
- Changes in grill/radiator tilt with respect to the vertical axis of the vehicle

In all cases, the GCM geometry is modified such that only the dimensions of the radiator and the angle of the top and side hood panels are changed. Although the curved segments of the hood region have a complex geometry, the primary radius of curvature between the hood panels and between the top of the hood and the grill is maintained in all cases. A

significant number of trial and error iterations between the CAD model and the CFD model were required for each geometric change to ensure that no defects were introduced by the modification of the CAD model which negatively impacted the ability to properly mesh the model or artificially introduced large changes in drag forces. All results presented herein are based on CAD surfaces which have been corrected through this procedure. These issues would almost certainly be avoided had a standard CAD model that was not based on an optical scan been used, since more of the surface construction information would have been recoverable in a standard CAD model.

Changes in Grill/Radiator Height

The effects of changes in grill height on the aerodynamic characteristics of the GCM geometry were evaluated for a 10% reduction in grill height as well as 5% and 10% increases in grill height. To account for the effects of cross-winds on real highway vehicles, yaw angles of 0, 3 and 6 degrees were considered for each case. Predicted drag coefficients are compared with those for the nominal configuration, as shown in Figure 9. All changes in drag coefficient observed fall within the expected accuracy of the simulation, which is +/- 1% for zero yaw and +/- 5% for higher yaw angles, and no significant impacts on drag-related parasitic losses can be expected to result from these design changes. The conclusion is supported by the surface pressure coefficient contours compared for the three variations and the nominal case in Figure 10, which show that only the spatial distribution, not the integral sum, of the pressure force acting on the tractor is altered by this change in geometry.

Changes in Grill/Radiator Width

The effects of changes in the width of the radiator and grill region on the aerodynamic characteristics of the GCM geometry were evaluated for both a 10% reduction and a 10% increase in the grill width. Yaw angles of 0, 3 and 6 degrees were again considered for each case. Predicted drag coefficients, shown in Figure 11, exhibit even less variation than are observed for changes in height and are again within the expected error of the simulations. No significant change in drag force acting on the vehicle is expected as a consequence of small changes in the radiator width. Predicted surface pressure coefficient data, as shown in Figure 12, supports this conclusion

since only the spatial distribution, not the integral sum, of the pressure force acting on the tractor is altered by this change in geometry.

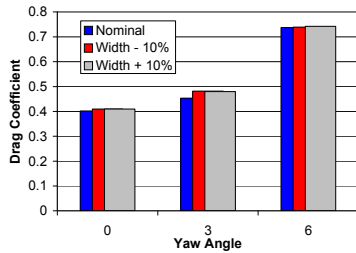


Figure 11. Comparison of Predicted Drag Coefficients as a Function of Radiator Width and Vehicle Yaw Angle.

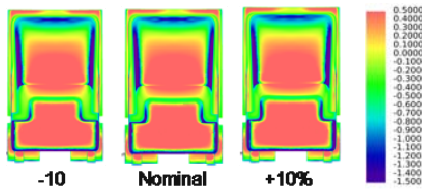


Figure 12. Comparison of Predicted Surface Pressure Coefficient Distributions for Changes in Radiator Width at Zero Yaw Angle.

Changes in Grill/Radiator Surface Area

Since the effects of changes in both height and width of the grill and radiator region where minimal, the effects of changing the total surface area of the radiator and grill region without changing the ratio of the height to the width was evaluated for only a 10% reduction in surface area. Yaw angles of 0, 3, and 6 degrees were considered to account for cross wind effects. Predicted drag coefficients are shown alongside results for the nominal geometry in Figure 13. Again, no significant variation in the predicted drag coefficient is observed, and predicted surface pressure coefficient data, shown in Figure 14, appears to confirm that only the spatial distribution, and not the integral sum, of the drag force is altered by the change in geometry.

Changes in Grill/Radiator Tilt

In the final study, the effects of the tilt of the grill and radiator is investigated. The bottom of the grill/radiator region is held fixed and the top is tilted backward toward the rear of the vehicle until it is 10° from the vertical axis. Since the drag coefficient of this configuration at zero degrees is within 0.25 percent of the prediction for the nominal geometry, only this case was considered for this configuration.

The surface pressure coefficient distribution, shown in Figure 15, again confirms that the integral sum of the drag force is unchanged although the spatial distribution changes slightly.

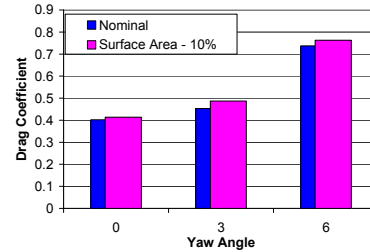


Figure 13. Comparison of Predicted Drag Coefficients as a Function of Radiator Surface Area (Constant Aspect Ratio) and Vehicle Yaw Angle.

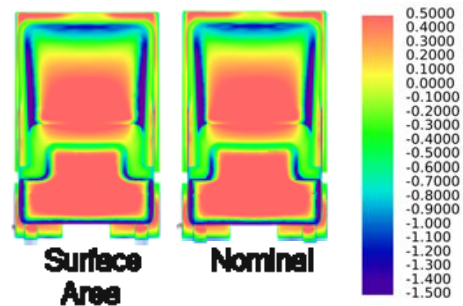


Figure 14. Predicted Surface Pressure Coefficient for a Change in Radiator Surface Area (Constant Aspect Ratio) at Zero Yaw Angle.

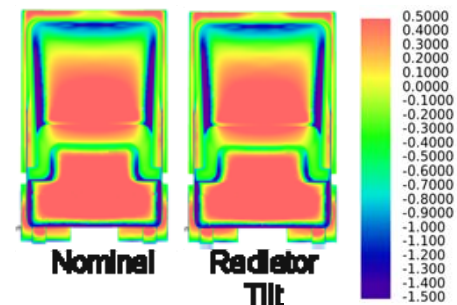


Figure 15. Comparison of Predicted Surface Pressure Coefficient Distributions for a Change in Radiator Tilt at Zero Yaw Angle.

Summary and Conclusions

The purpose of this work was to quantify the effects of small changes in radiator configuration on the aerodynamic performance of an aerodynamic tractor trailer truck. These effects were quantified through a series of parametric engineering design studies using Computational Fluid Dynamics simulations. A nominal geometry based on the Generic Conventional Model was developed and the modified geometries were defined by altering the dimensions of the GCM using commercial CAD software. CFD models were developed using the commercial code Star-CD and the approach developed as part of Argonne's contributions to the U.S. Department of Energy's Heavy Vehicle Aerodynamic Working Group.

Based on these results, small changes in radiator configuration offer neither a significant improvement in fuel economy when reducing the radiator size nor a significant penalty when increasing the radiator size – at least for reasonably aerodynamic vehicles. Small changes in radiator tilt also have a limited effect. These results do not, however, indicate that reductions in radiator size provide no benefit to all tractor trailer vehicles. For less aerodynamic tractors that do not already take advantage of the very significant benefits of corner rounding with relatively large radii of curvature, reductions in radiator size likely enable the development of new designs which do capitalize those benefits. Perhaps counter intuitively, these results also show that a well designed tractor can allow for slight increases in radiator size to meet emissions restriction requirements without a significant penalty to aerodynamic performance and fuel economy.

References

1. W. David Pointer, Tanju Sofu, and David Weber, "Development of Guidelines for the Use of Commercial CFD in Tractor-Trailer Aerodynamic Design," 2005 SAE Commercial Vehicle Engineering Conference, Chicago, IL, November 2005. (SAE Paper No. 05CV-120).
2. W. David Pointer, "Evaluation of Commercial CFD Code Capabilities for Prediction of Heavy Vehicle Drag Coefficients," Proceedings of the 2004 AIAA Fluid Dynamics Conference and Exhibition, Portland, Oregon, June 2004. (AIAA-2004-2254)
3. W. David Pointer, Tanju Sofu, and David Weber, "Commercial CFD Code Validation for Heavy-Vehicle External Aerodynamics Simulation", in R. McCallen, F. Browand, and J. Ross, eds., *The Aerodynamics of Heavy Vehicles: Trucks, Buses and Trains*, Berlin: Springer Verlag, 2004, pp 473-484.
4. Rose McCallen, et al., "DOE's Effort to Reduce Truck Aerodynamic Drag - Joint Experiments and Computations Lead to Smart Design", Proceedings of the 2004 AIAA Fluid Dynamics Conference and Exhibition, Portland, Oregon, June 2004.
5. Star-CD, CD-adapco group, Melville, NY.
6. Satran, D., "An Experimental Study of the Generic Conventional Model (GCM) in the NASA Ames 7-by-10-Foot Wind Tunnel," United Engineering Foundation Conference on the Aerodynamics of Heavy Vehicles: Trucks, Buses, and Trains, United Engineering Foundation, New York, 2002.

F. Test, Evaluation, and Demonstration of Practical Devices/Systems to Reduce Aerodynamic Drag of Tractor/Semitrailer Combination-Unit Trucks

Principal Investigator: Robert M. Clarke

Truck Manufacturers Association

1225 New York Avenue, NW, Suite 300

Washington, DC 20005

(202) 638-7825, fax : (202) 737-3742, e-mail: robertmclarke@truckmfgs.org

DOE Project Officer: Keith Carrington

National Energy Technology Laboratory

Morgantown, WV 26505

(304) 285-4456, e-mail: keith.carrington@netl.doe.gov

DOE Technology Development Area Specialist: Lee A. Slezak

Office of Vehicle Technologies

U.S. Department of Energy

1000 Independence Ave., S.W.

Washington, D.C.

(202) 586-2335, fax: (202) 586-2476, email: lee.slezak@ee.doe.gov

Field Technical Manager: Jules L. Routbort

(630) 252-5065, fax: (630) 252-4289, e-mail: jules.routbort@anl.gov

Participants

Scott Smith, Karla Younessi, Freightliner LLC

Ronald Schoon, International Truck and Engine Corporation

Justin Clark, Conal Deedy, Volvo Technology of America (Volvo Trucks, Mack Trucks)

*Contractor: Truck Manufacturers Association, 1225 New York Avenue, NW, Suite 300,
Washington, DC 20005*

Contract No.: DE-FC26-04NT42117

Objective

- To reduce aerodynamic drag of tractor/semi trailer combination trucks through development, test, and demonstration of aerodynamic aids and systems of aerodynamic aids from the viewpoint of manufacturability and practicality for over-the-road use.

Approach

- Pursue complimentary research paths for aerodynamic devices and systems.
 - Research areas include the effect of mirror design on truck aerodynamics; the effect of aerodynamic treatments of tractor trailer gap, trailer side, and trailer wake on truck aerodynamics; the effect of trailer aerodynamics, trailer gap enclosure, and trailer gap flow control on truck aerodynamics; and the effect of vehicle underside design and management of tractor-trailer air flows on truck aerodynamics.

- Phase I: Conduct preliminary testing and analysis on a wide range of candidate devices and systems to determine effectiveness of such devices and establish promising sets of devices for further research. This testing will involve both full-size vehicles and scale models in wind tunnels and real-world driving tests. Computational fluid dynamics will also be used to establish effects of aerodynamic devices on truck aerodynamics.
- Phase II: Construct prototype devices for installation on full-size Class 8 trucks for testing in wind tunnels or in real-world environments (potentially in fleet applications). This testing will quantify the optimal fuel economy benefits achievable through the use of these devices and systems in terms of a percentage improvement relative to a similar baseline truck and trailer.

Accomplishments

- Completed Phase II technical report and combined Phase I and II technical report for publication.

Future Direction

- Current project (Phase I and Phase II work) has been completed.

Introduction

Class 8 heavy-duty trucks represent over three-quarters of the total diesel fuel use for trucks in the United States each year, transporting vital goods to destinations across the country. At highway speeds for these trucks, aerodynamic drag is a major part of total horsepower needs for driving the truck down the highway, and reductions in aerodynamic drag can yield measurable benefits in fuel economy with relatively inexpensive and simple devices. The goal of this project is to examine a number of aerodynamic drag devices and systems and determine their effectiveness in reducing aerodynamic drag of Class 8 tractor/semitrailer vehicles, thus contributing to DOE's goal of reducing petroleum use for transportation.

Project Team

The project team represents virtually all of the key heavy truck manufacturers in the United States, along with the management and industry expertise of the Truck Manufacturers Association as the lead investigative organization. The Truck Manufacturers Association (TMA) is the national trade association representing the major North American manufacturers of Class 6-8 trucks (GVWRs over 19,500 lbs). Four major truck manufacturers are participating in this project with TMA: Freightliner, LLC; International Truck and Engine Corporation; Mack Trucks Inc.; and Volvo Trucks North America, Inc. Together, these manufacturers represent over three-quarters of total Class 8 truck sales in the

United States. These four manufacturers pursued complementary research efforts in order to provide a wide range of potential aerodynamic improvements to on-highway trucks.

Project Structure and Roles

The project work was separated into two phases conducted over a period of two years. In Phase I, initial screening of aerodynamic devices and systems was conducted to focus research and development attention on devices that offer the most potential. This screening was done through full-size vehicle testing, scale model testing, and computational fluid dynamics analysis. In Phase II, the most promising devices were installed on full-size trucks and their effect on fuel economy will be determined, either through on-road testing or full-size wind tunnel testing.

As noted above, the participating manufacturers conducted complementary research and development of aerodynamic aids. In particular, Freightliner is working on outside mirrors; International is looking at tractor trailer gap, trailer side, and trailer wake effects on truck aerodynamics; Mack is examining trailer aerodynamics, trailer gap enclosure, and trailer gap flow control; and Volvo is working on vehicle underside design and management of tractor-trailer air flows. All of the manufacturers are working with devices and systems that offer practical solutions to reduce aerodynamic drag, accounting for functionality, durability, cost effectiveness, reliability, and maintainability.

Project Activities

In FY 2007, the four participating truck manufacturers completed the final Phase II and full project reporting for submission to the Department of Energy. These reports were submitted and approved for publication and the project closed.

Summary

Through the two phases of this project, the four truck manufacturers performed testing and analysis on a number of areas of the tractor-semitrailer combination with an eye toward aerodynamic improvements. Technologies were identified for the tractor and trailer that could provide combined real-world fuel economy benefits of 1 percent to 8 percent, as described in detail in past annual reports.

Publications

A combined Phase II technical report was provided to the Department of Energy detailing the work done in the second year of the project. A full report detailing both Phase I and Phase II was submitted for public dissemination, and was also published by the Truck Manufacturers Association on their website. The Truck Manufacturers Association presented an overview of the project at the 21st Century Truck Partnership session at the 2007 SAE Commercial Vehicle Engineering Congress and Exhibition in Chicago, Illinois. Additionally, International published a technical paper on their Phase II work at the 2007 SAE Commercial Vehicle Congress (*On-Road Evaluation of Devices to Reduce Heavy Truck Aerodynamic Drag*, 2007-01-4294).

II. THERMAL MANAGEMENT

A. Efficient Cooling in Engines with Nucleate Boiling

Principal Investigator: W. Yu (coworkers: David M. France and Roger K. Smith)

Argonne National Laboratory

9700 South Cass Avenue, Building 212, Argonne, IL 60439

(630) 252-7361, fax: (630) 252-5568, e-mail: wyu@anl.gov

Technology Development Manager: Lee Slezak

(202) 586-2335, e-mail: Lee.Slezak@ee.doe.gov

Technical Program Manager: Jules Routbort

(630) 252-5065, e-mail: routbort@anl.gov

Contractor: UChicago Argonne, LLC

Contract No.: DE-AC02-06CH11357

Objective

- Investigate the potential of two-phase flow in engine cooling applications.
- Determine limits on two-phase heat transfer (occurrence of critical heat flux or flow instability).

Approach

- Experimentally determine heat transfer rates and critical heat fluxes in small channels with water and a mixture of 50% ethylene glycol in water.
- Perform experiments over a large concentration range of ethylene glycol in water.
- Experimentally determine heat transfer characteristics for subcool flow boiling of water and ethylene glycol/water mixtures.
- Perform experiments with alternative fluids to conventional coolants.

Accomplishments

- Completed experimental tests and data analysis for the two-phase pressure gradients and boiling heat transfer coefficients of horizontal flows to water and ethylene glycol/water mixtures.
- Developed a new procedure to analytically calculate the boiling temperature along the test section and, subsequently, the local heat transfer coefficients. This procedure is based on ideal-mixture and equilibrium assumptions along with Raoult's law.
- Developed a pressure drop correlation modified from Chisholm's correlation with a concentration factor to better predict pressure drops for ethylene glycol/water mixtures.
- Developed a general correlation of boiling heat transfer coefficients, modified from Argonne's boiling heat transfer correlation, with a concentration factor for the prediction of heat transfer rates of flow boiling in small channels, including refrigerants, water, and ethylene glycol/water mixtures.
- Fabricated a new vertical experimental test section, calibrated the instruments attached to the test section, and modified the test facility and test monitoring program for vertical-flow boiling tests. Rewired the interfacial

connection device between the instruments attached to the horizontal and vertical test sections and the data acquisition computer system for easy switching between the horizontal- and vertical-flow test sections.

- Completed single-phase calibration tests for vertical flow on the nucleate boiling test facility. Performed preliminary experimental tests and data analysis for two-phase vertical-flow boiling to pure water.

Future Directions

- Continue systematic two-phase heat transfer experiments of water and ethylene glycol/water mixtures with vertical flows to provide essential information for design of a nucleate-boiling cooling system.
- Study the effect of vertical versus horizontal flows on two-phase heat transfer.
- Experimentally determine heat transfer characteristics for subcool flow boiling of water and ethylene glycol/water mixtures.
- Perform systematic experiments with alternative fluids.

Introduction

Analyses of trends in the transportation sector indicate that future engine cooling systems will have to cope with greater heat loads because of more powerful engines, more air conditioning, more stringent emissions requirements, and additional auxiliary equipment. Moreover, there is considerable interest in reducing the size of the cooling systems to obtain a better aerodynamic profile for vehicles. To meet these conditions, researchers need to design cooling systems that occupy less space, are lightweight, have reduced fluid inventory, and exhibit improved performance. Among various new cooling systems proposed, nucleate boiling has great potential to meet these challenges. Order-of-magnitude higher heat transfer rates can be achieved in nucleate-boiling cooling systems when compared with conventional, single-phase, forced-convective cooling systems. However, successful design and application of nucleate-boiling cooling systems for engine applications require that the critical heat flux and flow instabilities not be reached. Therefore, a fundamental understanding of flow boiling mechanisms under engine application conditions is required to develop reliable and effective nucleate boiling cooling systems.

Cooling engine areas such as the head region often contain small metal masses that lead to small coolant channels. This geometry, in turn, leads to low mass flow rates that minimize pressure drop. Although significant research has been performed on boiling heat transfer and the critical heat flux phenomenon,

results applicable for engine cooling systems are limited. The purpose of the present study is to investigate the characteristics of coolant boiling, critical heat flux, and flow instability under conditions of small channel and low mass fluxes.

The test apparatus used in this investigation was designed and fabricated to study boiling heat transfer, two-phase pressure drop, critical heat flux, and flow instability of flowing water, ethylene glycol, and aqueous mixtures of ethylene glycol at high temperature (up to 250°C) and low pressure (<345 kPa). Figure 1 shows a schematic of the apparatus.

The apparatus is a closed loop that includes two serially arranged pumps with variable speed drives, a set of flowmeters, an accumulator, a preheater, a horizontal test section, a vertical test section, and a condenser. The flowmeter set, including various types and sizes, was chosen to cover a large range of flow rates and was calibrated with a weighing-with-stop-watch technique. The estimated uncertainty in the measurements of flow rates was $\pm 3\%$. The bladder-type accumulator allows for stable control of the system pressure. The preheater provides a means to set the inlet temperature of the test sections at various desired levels. Both the preheater and test sections were resistance-heated with controllable direct current (DC) power supplies. Provisions were made to measure temperatures along the test section for calculating heat transfer coefficients. The pressures and temperatures at the inlet and outlet of the test section were also measured. Pressure

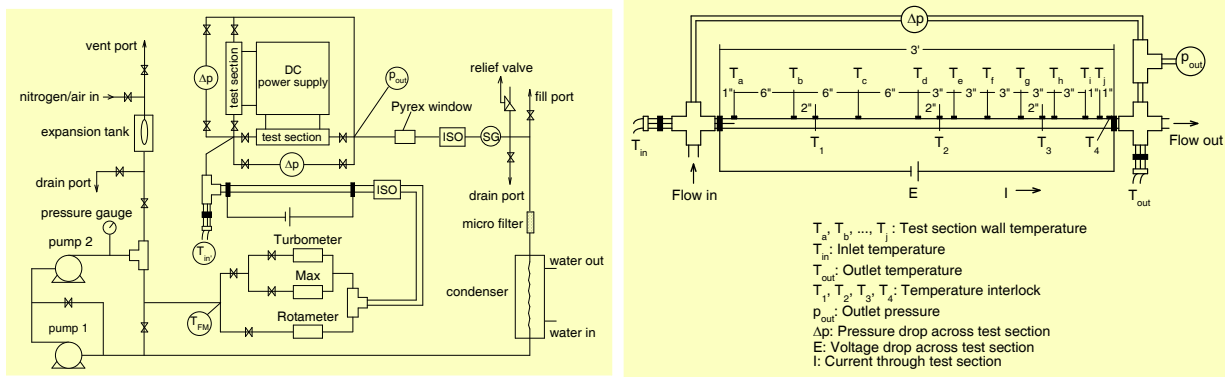


Figure 1. Schematic diagram of nucleate-boiling cooling test apparatus (top) and test section (bottom)

transducers and thermocouples were calibrated against known standards. The estimated uncertainty in the measurements of pressures and temperatures were $\pm 3\%$ and $\pm 0.2^\circ\text{C}$, respectively. As a safety precaution, both the preheater and test sections were provided with high-temperature limit interlocks to prevent them from overheating. After leaving the test section, the two-phase flow was condensed into a single-phase flow, which returned to the pumps to close the system.

To switch between the horizontal- and vertical-flow test sections, an interfacial connection was fabricated, shown in Figure 2. This device establishes a connection between the test-section sensor instruments and the data-acquisition computer system, and allows for a quick and easy switch between the horizontal and vertical test sections, which share the rest of the test loop.



Figure 2. Interfacial connection

A data acquisition system consisting of a computer and a Hewlett-Packard multiplexer was assembled to

record outputs from all sensors. A data acquisition program, which includes all calibration equations and conversions to desired engineering units, was written. The data acquisition system provides not only an on-screen display of analog signals from all sensors and graphs of representative in-stream and wall-temperature measurements, but also a means of recording temperature and pertinent information such as input power (voltage across the test section and current through the test section), mass flux, outlet pressure, pressure drop across the test section, and outlet quality for further data reduction.

Results and Discussion

To calculate local boiling heat transfer coefficients of an ethylene glycol/water mixture, the water-vapor mass fractions, mixture vapor mass qualities, and mixture temperatures along the experimental test section must be determined. Researchers have used various approaches in making these determinations. Perhaps the simplest approach is to assume that the mixture boiling temperature is constant along the test section and equal to the mean of the zero quality temperature and the temperature at the test section outlet. This approach is not conducive to the determination of local heat transfer coefficients along the length of the test section, as in the present study. Accuracy can be increased by assuming a linear mixture temperature distribution along the test section. Another approach is to utilize a mixture equation of state, such as the hard-sphere equations. However, ideal mixture and equilibrium assumptions along with Raoult's law are sufficient to calculate the boiling temperature along the test section and, subsequently, the local heat transfer coefficients.

This approach was developed and adopted in this study. Assuming an ideal mixture and applying Raoult's and Dalton's laws to the ideal mixture, one can derive the following equations for determining the water vapor mass fraction F_v , mixture vapor mass quality x , and mixture temperature T_m

$$F_v = \frac{9p_w(p_m - p_{EG})}{31p_m(p_w - p_{EG}) - 22p_w(p_m - p_{EG})}$$

$$x = \frac{31F_m(p_w - p_{EG}) - (9 + 22F_m)(p_m - p_{EG})}{31F_v(p_w - p_{EG}) - (9 + 22F_v)(p_m - p_{EG})}$$

$$T_m = T_{m0} - \frac{\dot{q}/\dot{m} + [F_{vi}i_{fgwi} + (1 - F_{vi})i_{fgGi}]x_i - [F_{vo}i_{fgwo} + (1 - F_{vo})i_{fgGo}]x_o}{[F_m C_{pwi} + (1 - F_m)C_{pEGi}]}$$

where p is the pressure, T is the temperature, F is the mass fraction, x is the mass quality, C_p is the specific heat, i_{fg} is the latent heat of vaporization, \dot{q} is the heat transfer rate, and \dot{m} is the mass flow rate.

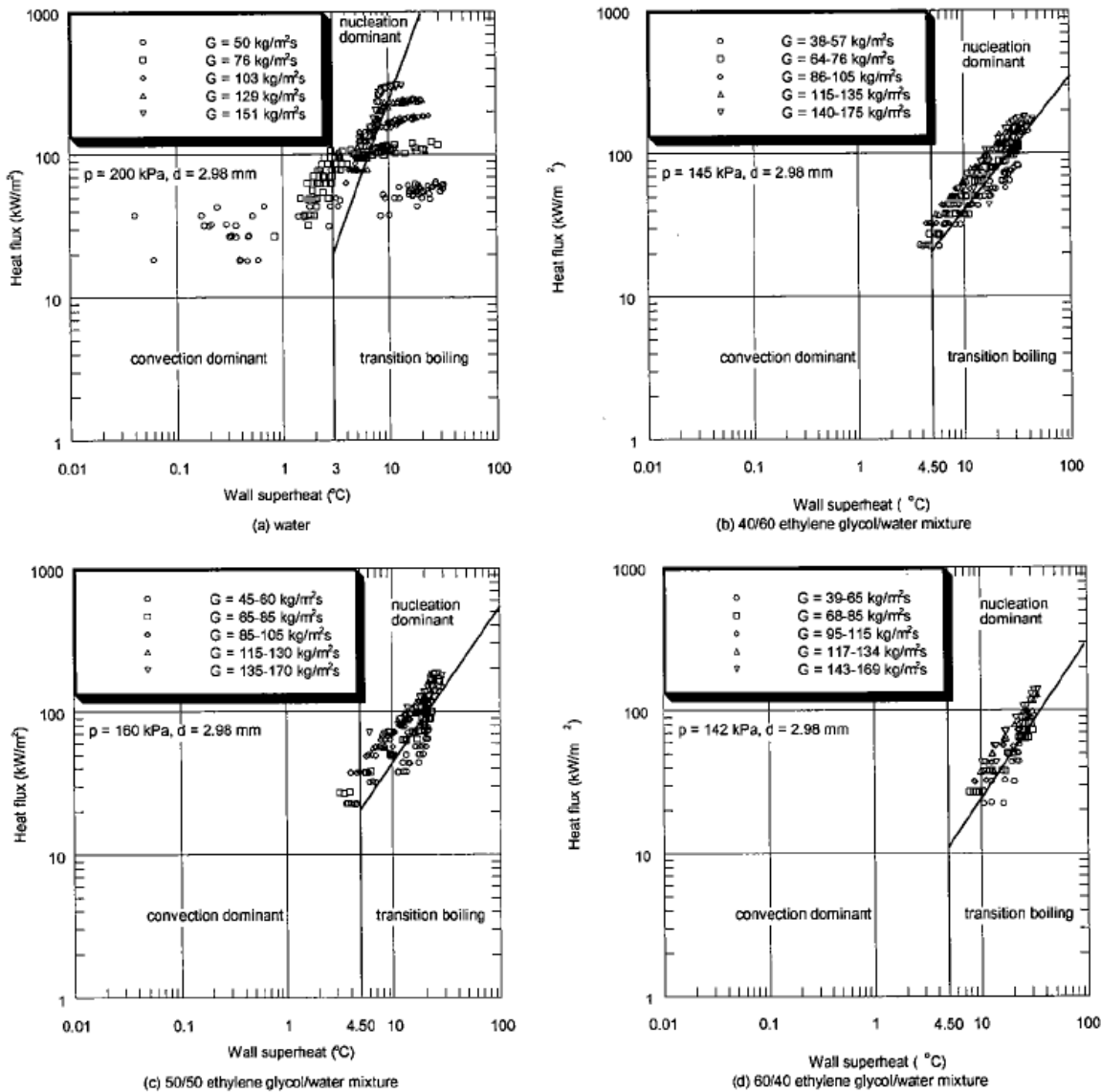


Figure 3. Heat flux as a function of wall superheat

Horizontal Flow Boiling

Both experimental tests and data analysis for two-phase boiling heat transfer of horizontal flows to water and ethylene glycol/water mixtures have been completed. The main results are reported below.

Boiling Curve. Figure 3 shows the heat flux as a function of wall superheat for boiling of water and ethylene glycol/water mixtures in small channels. As can be seen from Figure 3, generally, the saturation boiling in small channels can be divided into three boiling regions, namely, convection dominant, nucleation dominant, and the transition between the two.

Both convective heat transfer and boiling heat transfer exist in all three regions, but their proportions are different in these regions. In the convection-dominant-boiling region, the wall superheat is low, usually less than a few degrees centigrade. Although there is boiling heat transfer, the dominant mechanism is convective heat transfer. As a result, the mass quality and heat transfer rate are quite low compared with those in the other two regions. In the nucleation-dominant-boiling region, the wall superheat is higher than that in the convection-dominant-boiling region but lower than certain upper limits that depend on mass flux. Opposite to the convection-dominant boiling, the boiling heat transfer in the nucleation-dominant boiling is so developed that it becomes dominant, and the heat transfer rate is much higher than that in convection-dominant boiling. As can be seen from Figure 3, the heat flux in this region is independent of mass flux and can be predicted with a power-law function of wall superheat. This characteristic was used in correlating the heat transfer data. In the transition-boiling region, the wall superheat is relatively high. The heat flux in this region is also high and close to the critical heat flux. The boiling in this region is unstable, and a small change in the heat flux will result in a big change in wall superheat. If the heat flux increases further, it is possible for the system to reach a critical point, producing an undesirably large jump in the wall superheat.

The above discussion shows that nucleation-dominant boiling is desired in engineering

applications for both high heat transfer rate and stable flow boiling without reaching the critical point.

Two-Phase Pressure Drop. The concept of two-phase multipliers proposed by Lockhart and Martinelli and the correlation of those multipliers by Chisholm were used to compare predictions with the present experimental data. As can be seen from Figure 4, the experimental data are in reasonable agreement with the Chisholm predictions both in values and trends, although the Chisholm correlation slightly overpredicts the experimental data.

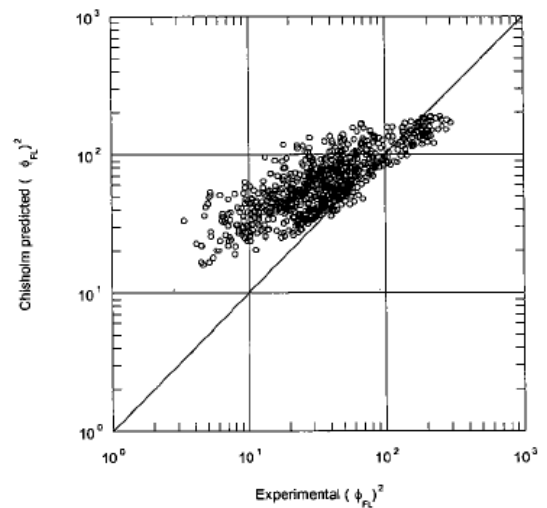


Figure 4. Two-phase frictional pressure gradient

To better predict the experimental data and to take the concentration factor into account, the constant parameter $C = 12$ in Chisholm's correlation was modified into a function of the volume concentration (v) of ethylene glycol/water mixtures, and Chisholm's correlation then becomes

$$\phi_{FL}^2 = 1 + \frac{12[1 - 2.8v(1-v)]}{X} + \frac{1}{X^2}$$

This correlation reduces to Chisholm's correlation for both pure water ($v = 0$) and pure ethylene glycol ($v = 1$). In Figure 5, the experimental data are compared with the predictions of the modified Chisholm's correlation. This modification improves the predictions both in values and trends.

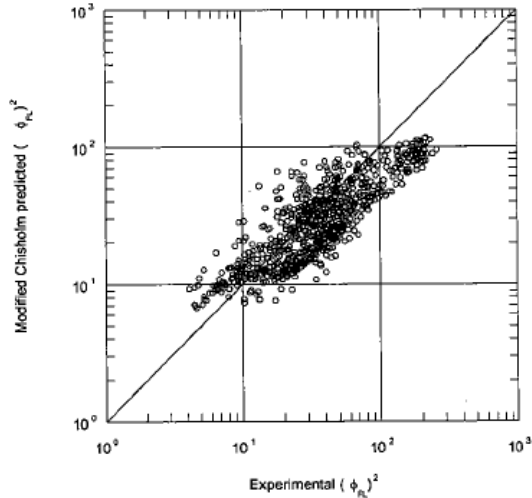


Figure 5. Two-phase frictional pressure gradient

Heat Transfer Coefficient. In the present study, the nucleation-dominant boiling data have the following characteristics.

(a) Although both convective heat transfer and nucleate-boiling heat transfer exist, the dominant

heat transfer mechanism is nucleate boiling. Since the nucleate-boiling heat transfer rate is much higher than the convective heat transfer, the latter can be neglected.

(b) As shown in Figure 3, the boiling heat transfer is dependent on heat flux but almost independent of mass flux. This finding means that, for a certain fluid, the boiling heat transfer coefficient can be expressed as a function of heat flux.

(c) The heat transfer coefficients have different dependence on heat flux for different fluids. Therefore, deriving a general correlation for boiling heat transfer coefficients requires fluid properties in the correlation.

(d) Argonne researchers employed the dimensionless parameter combination form of boiling number, Weber number, and liquid-to-vapor density ratio in developing different predicted correlations for boiling heat transfer coefficients with different fluids, and the predicted results are quite good.

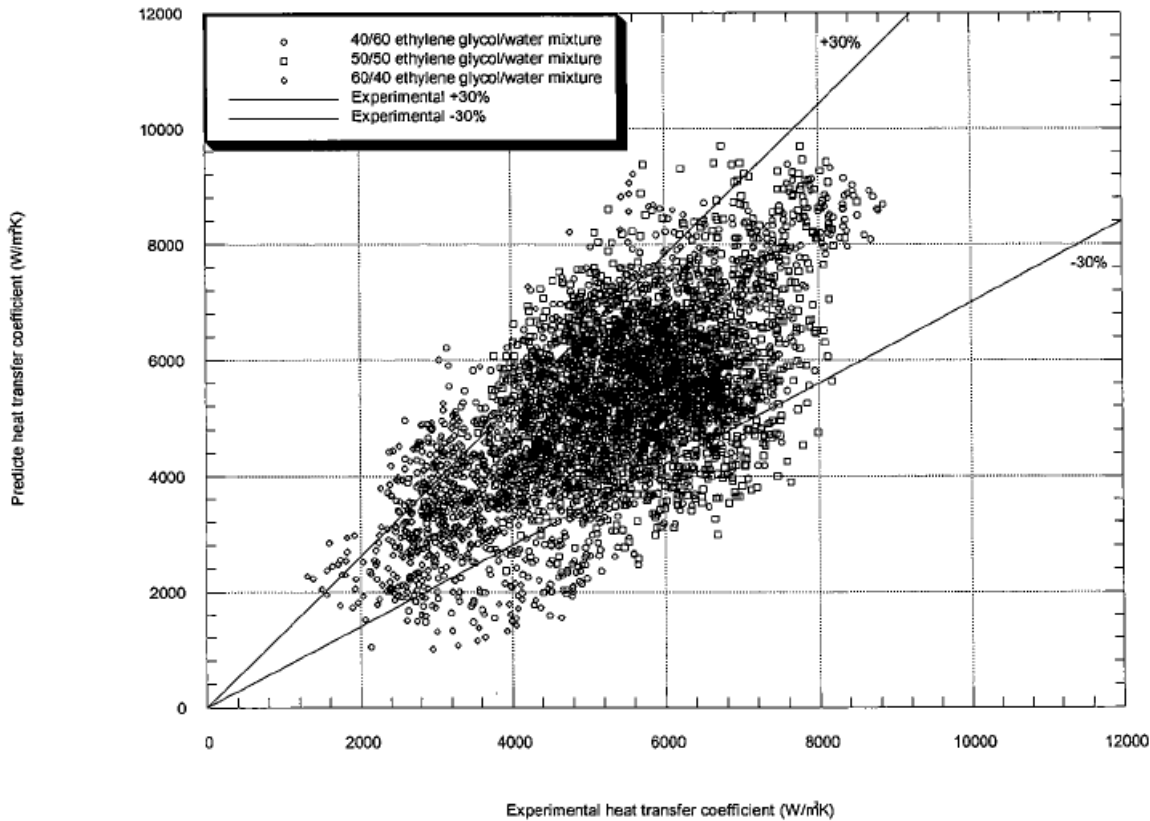


Figure 6. Heat transfer coefficient comparisons (nucleation-dominant-boiling region)

Based on the above facts, we extended the property term to include the liquid-to-vapor viscosity ratio and were able to correlate boiling heat transfer data (h) for water, 50/50 ethylene glycol/water mixture, refrigerant 12, and refrigerant 134a.

$$h = 135000(BoWe_l^{0.5})^{0.5}[(\rho_l/\rho_v)^{-0.5}(\mu_l/\mu_v)^{0.7}]^{1.5}$$

In the above equation, ρ is the density, μ is the viscosity, and the boiling number Bo and the Weber number We_l are defined, respectively, as

$Bo = q''/(Gi_{fg})$ and $We_l = G^2D/(\rho_l\sigma)$, where q'' is the heat flux, i_{fg} is the latent heat of boiling, G is the mass flux, D is the diameter, and σ is the surface tension. For this heat transfer equation to be used for the prediction of experimental data for ethylene glycol/water mixtures with concentrations other than 50/50, we further modified it with a concentration correction factor, which reduces to 1 for concentrations $v = 0$ and $v = 0.5$. The new correlation can be expressed as

$$h/h^* = [1 + 6v(v - 0.5)](BoWe_l^{0.5})^{0.5}[(\rho_l/\rho_v)^{-0.5}(\mu_l/\mu_v)^{0.7}]^{1.5}$$

where h^* is a characteristic heat transfer coefficient of $135 \text{ kW/m}^2\cdot\text{K}$ for all of the data.

Figure 6 shows the experimental data and the predicted values obtained with the correlation for ethylene glycol/water mixtures. The predictions are in good agreement with the experimental data, and most are within $\pm 30\%$ of the experimental data. Note that the comparisons are only for the data within the nucleation-dominant-boiling region. The success of the correlation in predicting the heat transfer coefficients of fluids boiling in small channels is directly related to the trend, as presented in Figure 3, that the heat transfer data are dependent on heat flux but not mass flux. The fact that the equation is also heat-flux but not mass-flux dependent is in accord with the experimental data.

Vertical Flow Boiling

In the application of engine cooling, both horizontal and vertical flows exist. Therefore, it is necessary to investigate the impact of vertical versus horizontal flows on two-phase heat transfer.

Experimental Test Section. The design of the vertical experimental test section is similar to the existing horizontal section. The instruments attached to the vertical test section include thermocouples and pressure transducers that were calibrated against a NIST-traceable thermocouple and a standard device to ensure accurate measurements of temperatures and pressures. The test facility and test-monitoring program were also modified to adapt to both horizontal and vertical flows. Figure 7 shows a picture of the vertical test section before it was insulated.



Figure 7. Vertical experimental test section

Single-Phase Calibration. Single-phase heat transfer for vertical flow has been carried out in the test facility, and the results are compared to the predictions of the Gnielinski equation in Figure 8. All experimental data are within the 20% range of the predictions. This agreement serves as a validation of the accuracy of the instrumentation, measurements, data acquisition, and data reduction procedures. These single-phase heat transfer tests are an “end-to-end” final validation of the test apparatus.

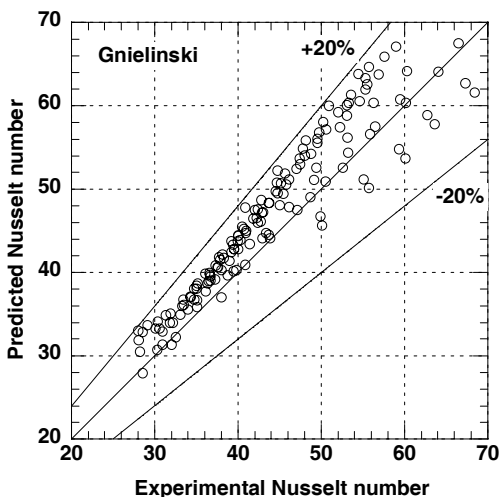


Figure 8. Single-phase Nusselt number

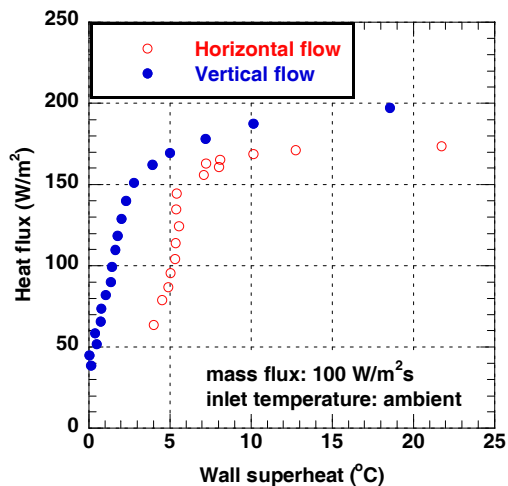


Figure 9. Horizontal and vertical boiling curve

Preliminary Boiling Tests. We plan to run systematic vertical flow experiments on two-phase boiling heat transfer with water and ethylene glycol/water mixtures. The tests are expected to provide essential information for the design of nucleate-boiling cooling systems. Preliminary vertical-flow boiling tests have been carried out, and the results are reported below.

Figure 9 shows the heat flux as a function of wall superheat for boiling of water with 100 kg/m²s mass flux and ambient inlet temperature, and also compares the vertical with horizontal flow boiling under the same test settings. As can be seen in the figure, the curve for vertical flow boiling follows the same trend as that for horizontal flow boiling. However, to reach the same wall superheat, the heat flux and, in turn, the critical heat flux, for vertical flow boiling are higher than for horizontal flow boiling. This result is expected because the vapor distribution for vertical flow boiling is more uniform than that for horizontal flow boiling due to the influence of gravity. This phenomenon is important for the design of nucleate boiling cooling systems. Because a practical cooling system usually contains both horizontal and vertical channels, the design of a nucleate boiling cooling system will be too conservative if based only on the horizontal-flow boiling data and too optimistic if based only on the vertical-flow boiling data.

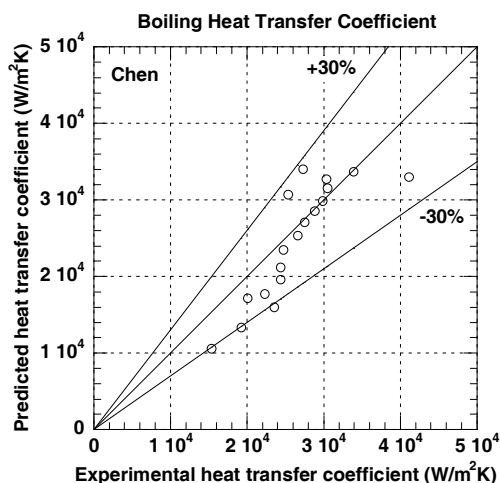


Figure 10. Heat transfer coefficient comparisons

Figure 10 compares the heat transfer coefficient data of the two-phase vertical flow boiling for 100 W/m²s mass flux and ambient inlet temperature with the predictions of the Chen correlation that was developed based on water boiling data. The limited data show a reasonable agreement between the experimental data and predictions, and most of the predictions are within ±30% of the experimental data. Note that the comparisons are only for the data within the nucleation-dominant-boiling region and that further experiments are necessary to confirm this trend.

Conclusions

Excellent progress has been made on the experiments and analysis for this project.

(a) A new procedure has been developed that can analytically calculate the boiling temperature along the test section and, subsequently, the local heat transfer coefficients by using ideal-mixture and equilibrium assumptions along with Raoult's law. This procedure can be easily used for designing cooling systems with flow boiling.

(b) Two-phase frictional pressure gradients of ethylene glycol/water mixtures follow similar trends as those of water. The results are in reasonable agreement with the predictions of Chisholm's correlation. A modification has been made to Chisholm's correlation, which reduces to Chisholm's correlation for concentrations $\nu = 0$ and $\nu = 1$. This modified Chisholm's correlation improves the predictions of pressure drop for ethylene glycol/water mixtures.

(c) The experiments show a high heat transfer rate with ethylene glycol/water mixtures, which is a positive result for engine cooling. We developed a general correlation based on data for water, ethylene glycol/water mixtures (concentrations 40/60, 50/50, and 60/40), and refrigerants. This correlation predicts the experimental data quite well, and most of the predicted values are within $\pm 30\%$ of the experimental data.

(d) It was found that the boiling heat transfer of ethylene glycol/water mixtures is mainly limited by flow instability rather than critical heat fluxes that usually constitute the limits for water boiling heat transfer. Tests show that stable, long-term, two-phase boiling flow is possible for ethylene glycol/water mixtures as long as the mass quality is less than a certain critical value (approximately < 0.2). The heat transfer rate at this mass quality is significantly higher than that of conventional, single-phase, forced-convective heat transfer.

(e) The single-phase tests on the vertical flow have confirmed the validation of the vertical test section and data reduction process. Preliminary experimental tests of vertical flow boiling to water show the same trend of wall superheat increasing with heat flux except that, to reach the same wall superheat, the heat flux for vertical flow boiling is higher than that for horizontal flow boiling. The results imply that the critical heat flux for vertical flow boiling is higher than that for horizontal flow boiling. The heat transfer coefficient data for vertical flow boiling are predicted reasonably well by the Chen correlation, and most of the predictions are within $\pm 30\%$ of the experimental data. These preliminary results will be verified by ongoing systematic tests of vertical flow boiling. We are planning on using water and ethylene glycol/water mixtures for two-phase boiling heat transfer experiments of vertical flows. The tests are expected to provide essential information for the design of nucleate-boiling cooling systems.

B. Nanofluids for Thermal Control Applications

Principal Investigator: W. Yu (coworkers: David France, Dileep Singh, and Roger Smith)

Argonne National Laboratory

9700 South Cass Avenue, Building 212

Argonne, IL 60439

(630) 252-7361, fax: (630) 252-5568, e-mail: wyu@anl.gov

Technology Development Manager: Lee Slezak

(202) 586-2335, e-mail: Lee.Slezak@ee.doe.gov

Technical Program Manager: Jules Routbort

(630) 252-5065, e-mail: routbort@anl.gov

Contractor: UChicago Argonne, LLC

Contract No.: DE-AC02-06CH11357

Objective

- Exploit the high heat transfer rates of nanofluids (nanoparticles suspended in liquids) by characterizing them in terms of thermal properties, physical attributes, and heat transfer rates for transportation and other commercial applications.
- Develop nanofluid technology for vehicle thermal control.
- Improve/optimize the efficiency of heavy-vehicle cooling systems, with the goal of a minimum cooling system size reduction of 5%.

Approach

- Measure the thermal conductivity and viscosity of nanofluids.
- Measure the heat transfer coefficient of nanofluids.
- Measure/determine nanofluid characteristics with regard to: particle suspension, particle agglomeration, particle size, and particle shape.
- Develop models of nanofluids for heat transfer fluid selection and for system design.
- Perform cooling system tests in collaboration with transportation companies.

Accomplishments

- Developed new capabilities to measure the heat transfer coefficient of nanofluids.
- Developed new capabilities to measure the thermal conductivity of nanofluids (from room temperature to 100°C).
- Added the capability of measuring nanofluid viscosity.
- Added the capability of making nanoparticle measurements in suspensions using laser scattering.
- Conducted single-phase tests with the pure base fluids of ethylene glycol and water in the Nanofluid Heat Transfer Test Facility. The measurements showed good agreement with the predictions of the Gnielinski equation. This agreement served as a final validation of the test section instrumentation and data reduction procedures, and the results provided baseline data for comparison with nanofluids using these two base fluids.

- Using two experimental techniques, X-ray small angle scattering and laser scattering, characterized several nanofluids with respect to particle size, shape, and agglomeration.
- Performed numerical simulations quantifying the effects of nanofluids used as engine coolants in over-the-road heavy vehicles.
- Published a comprehensive survey and assessment of the state-of-the-art for nanofluids with regard to production, thermal properties, heat transfer rates, and thermal property theories.

Future Directions

- Identify/develop well-characterized nanofluids with high thermal conductivity and good suspension properties.
- Conduct detailed nanofluid characterization tests to determine the physical structure of the nanoparticles in suspension.
- Conduct experiments to determine nanofluid properties of thermal conductivity and viscosity.
- Conduct experiments to quantify the heat transfer enhancement of nanofluids compared to their base fluids and to provide data and predictions necessary for industrial applications.
- Refine models of nanostructure-enhanced and nanoparticle-mobility-enhanced thermal conductivity of nanofluids for simulation of cooling system performance and develop comprehensive model of enhanced thermal conductivity.
- Conduct tests of cooling-system heat transfer in collaboration with the transportation industry.

Introduction

For engines in the transportation industry, the ever-increasing heat rejection requirements, due to trends toward higher power outputs and stringent emission levels, have brought the cooling issue to the forefront. Conventional cooling methods have been optimized to their limits, including design of the radiator air-side fin. However, engine fluids themselves, such as lubricants and engine coolants, are inherently poor heat transfer fluids and contribute to the limitations on engine cooling rates. Therefore, there is a strong need for higher performance coolants to be used in thermal control systems for vehicles.

A very promising approach to increasing cooling efficiency in heavy vehicles is the use of a relatively new class of fluids, nanofluids, as coolants. For more than a century, scientists have tried adding particles to fluids to improve thermal conductivity and heat transfer performance. However, studies of the thermal conductivity of suspensions have been confined to millimeter- or micrometer-sized particles. The major problem with the use of such large particles is the rapid settling of these particles in liquids. Other problems include abrasion and

clogging in cooling systems. To overcome such problems, Argonne National Laboratory has pioneered nanofluids by uniformly and stably suspending nanometer-sized particles in liquids. Nanofluids are nanotechnology-based heat transfer fluids engineered by dispersing a very small quantity (typically 1 to 4% by volume) of nanoparticles in conventional heat transfer fluids to achieve 10% to 40% enhancement in heat transfer performance.

The potential benefits to heavy vehicles of using nanofluids include:

- Improve heat transfer of engine coolants and oils.
- Reduce radiator and heat exchanger size and weight, thereby decreasing the vehicle frontal area, reducing the wind-averaged drag coefficient, and increasing fuel efficiency.
- Reduce heat transfer fluid inventory and coolant system size.
- Reduce coolant pumping energy.

A goal of this project is improve engine cooling thereby allowing reduction of the size and weight of heavy vehicle cooling systems (radiator, oil cooler, pump, etc.) by using nanofluids to replace traditional coolants. Such nanofluids are among the most

promising coolants for the transportation industry. However, the ways in which the nanoparticles in these nanofluids generate enhanced properties are not completely understood. To achieve the project goal, better understanding is required of the thermal enhancement and stability of nanofluids. To attain this understanding, we are conducting the following tasks: (1) explore and exploit the unique properties of nanoparticles to identify/develop heat transfer fluids with high thermal conductivity and heat transfer rates, (2) experimentally characterize nanofluid physical attributes, (3) determine the basic mechanisms of enhanced thermal conductivity and stability of nanofluids, (4) experimentally determine heat transfer rates and pressure drops in flowing nanofluids, (5) develop and validate new thermal models for nanofluids, (6) develop nanofluid technology for increasing the thermal transport of engine coolants and lubricants, and (7) conduct cooling tests in conjunction with industry.

Approach

The approach taken to overcoming the poor heat transfer rates of conventional heat transfer fluids used as engine coolants is to replace them with nanofluids, which possess much better thermal properties. Solids with thermal conductivities orders of magnitude higher than those of the base liquids are suspended in the base liquid to form the nanofluid. For example, the thermal conductivity of copper at room temperature is about three orders of magnitude greater than that of engine coolants and engine oils. A small concentration of such particles in the nanometer size range has been shown to significantly improve the thermal properties of the suspension. Although numerous theoretical and experimental studies of the effective thermal conductivity of dispersions that contain solid particles have been conducted since Maxwell's theoretical work was published about 100 years ago, most of them have been confined to millimeter- or micrometer-sized particles. The major problem with the use of such large particles is the rapid settling of these particles in fluids. Another problem is the abrasive nature of the suspension. In contrast, use of nanoparticles has the potential to produce the increased thermal conductivity sought in heat transfer fluids while minimizing the problems of settling and abrasion. Maxwell's concept of enhancing the thermal conductivity of fluids by

dispersing solid particles in them is old, but what is new with nanofluids is the idea that particle size matters for suspension stability (gravitational effects can be minimal) and for dynamic thermal interactions.

Argonne National Laboratory now has the capability to measure the most significant aspects of nanofluids, including some that are almost never measured by other researchers for lack of appropriate facilities. Using both high-intensity X-ray and laser scattering techniques, Argonne has measured particle size, shape, and agglomeration of nanoparticles while suspended in their base fluids. Argonne has successfully measured the thermal conductivity of numerous nanofluids by using a transient hot-wire apparatus.

Argonne has an operating facility for measuring pressure drops and heat transfer rates in flowing nanofluids. In addition, a viscosity measurement capability has recently been added, and scanning electron microscope use continues to be important. The newly acquired environmental SEM could also prove to be invaluable. All of these independent measurements form a full complement of nanofluid development techniques required to meet the project goal. This combined capability is unique to Argonne. Furthermore, recent studies have shown the importance of measuring nanofluid properties over a range of temperatures. Argonne has the capability of making most measurements over extended temperature ranges. For example, new capabilities are in place to measure the thermal conductivity and heat transfer rates of nanofluids from room temperature to 100°C.

The thermal conductivity of nanofluids has been, and continues to be, a major focus of nanofluid thermal property research and development. The thermal conductivity has been shown to be a good indicator of the heat transfer rate achievable with the fluid and is much easier to measure. Since this rate is the ultimate parameter defining heat transfer enhancement for flowing system applications, the Argonne project will be focused more in this direction in the future. In conjunction with heat transfer measurements, it is critical to physically characterize candidate nanofluids in terms of particle size, shape, and concentration. Unfortunately, this physical characterization is rarely found in the

engineering literature associated with the thermal enhancement of nanofluids. As a consequence, it is difficult to compare research results among experimenters and to know exactly what fluids were tested. All of the experimental capabilities discussed will be used at Argonne in the methodical development of nanofluid technology. In addition, we plan to collaborate with industry to conduct heat transfer tests in transportation systems to demonstrate nanofluid technology for vehicle thermal control applications.

Results and Discussion

Nanofluid Experiments

In addition to showing significant thermal enhancement, nanofluids that are candidates for commercial applications must be stable suspensions, producible in large quantities at reasonable cost, and amenable to pumping without adverse system effects. As part of the development of commercially viable nanofluids, thermal conductivity measurements were made on several of nanofluids having different particle materials, sizes, and concentrations. Shown in Figure 1 are the thermal conductivity results for silicon carbide nanoparticles suspended in a base fluid of water. The nanoparticles were in suspension in water with a 4% concentration of particles by volume. The particle size in the suspension was measured three ways. The X-ray small angle scattering technique yielded a mean diameter of 170 nm with significant dispersion in size. The laser scattering technique and scanning electron microscope images were in agreement with this mean value. Figure 1 shows that the thermal conductivity enhancement, defined as the ratio of the thermal conductivities of the nanofluid to the base fluid, varies between 1.2 and 1.1 as a function of temperature. The temperature trend has been shown to be reversed for other nanofluids, and some have produced even greater enhancement. Nonetheless, the SiC nanofluid has good potential for commercial application, and its development is being pursued further.

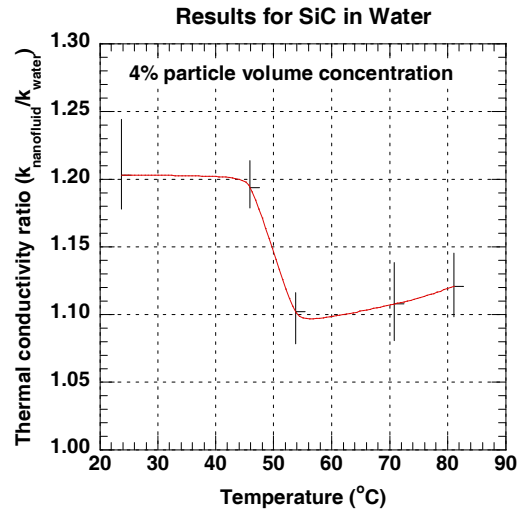


Figure 1. Thermal Conductivity Enhancement of SiC in Water

A second example of thermal conductivity enhancement is shown in Figure 2 for copper oxide nanoparticles suspended in a base fluid of ethylene glycol. Measurements were made at room temperature over a range of particle concentrations up to 0.85% by volume. The effect of increased thermal conductivity enhancement as particle concentration increases is evident in the Figure 2. This enhancement is expected to continue as particle concentration increases up to a limit, after which the trend might reverse.

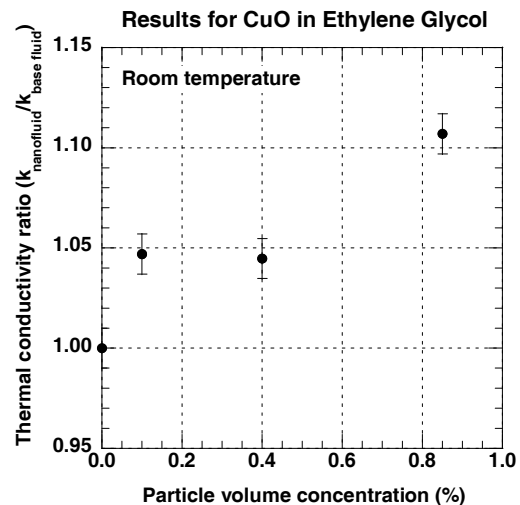


Figure 2. Thermal Conductivity Enhancement of CuO in Ethylene Glycol

Two nanofluids were subjected to preliminary heat transfer tests in an attempt to provide the final nanofluid measurements. However, in both cases, particle settling became an important issue, and experiments were terminated before completion. Effort is ongoing to identify and completely describe commercially viable nanofluids.

Nanofluid Literature Survey and Assessment

Nanofluid research and development efforts have been increasing around the country and the world since the inception of the technology over a decade ago at Argonne. The effort has been somewhat scattered in terms of types of nanofluids studied, but at this time there is sufficient published information to determine the state-of-the-art in terms of magnitudes and trends of nanofluid parameters and enhancement levels. To that end, Yu et al. [1] made a comprehensive survey and assessment of the engineering literature, concentrating on thermal conductivity measurements and theories, as well as heat transfer measurements and correlations. These areas are deemed key to the application of nanofluids in industrial systems. Over 150 publications were reviewed, and experimental results analyzed. The experimental results were presented in a variety of ways in the literature, and it was necessary to put all results into a consistent form for comparison purposes. Then eight key parameters were identified that have received attention from researchers with respect to their effects on thermal enhancement: (1) particle volume concentration, (2) particle material, (3) particle size, (4) particle shape, (5) base fluid material, (6) temperature, (7) additive, and (8) acidity. Thermal enhancement was graphed as a function of each of these parameters independently, while all other parameters were left unchanged. Consistency was investigated among experimenters with regard to magnitudes and trends of results. When repeatability was evident among experimenters, trends and magnitudes were identified as the state-of-the-art.

As an example, results are shown in Figure 3 for the effect of particle material on thermal conductivity enhancement. Results are presented from five research groups who ran tests with the particle materials of Figures 1 and 2, plus aluminum oxide. The consistency of the results in this case is substantial evidence of the insensitivity of the enhancement to these particle materials. (The

situation changes when metal particles are added with their higher thermal conductivities.)

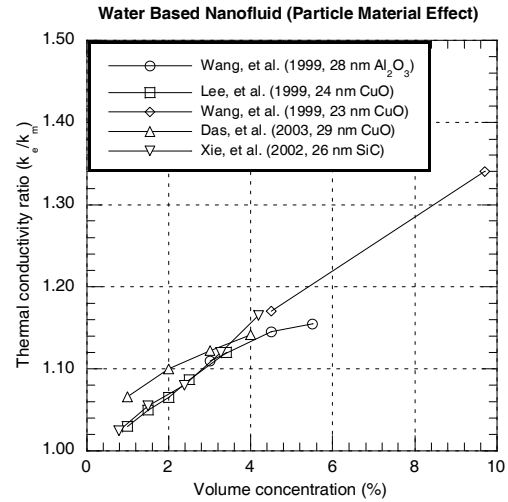


Figure 3. Particle Material Effect on Nanofluid Thermal Conductivity

An example of the enhancement in heat transfer rate enhancement for nanofluids is shown in Figure 4 in terms of Nusselt number enhancement for 55-nm-size copper oxide nanoparticles suspended in water. The results from convective heat transfer experiments are shown for a range of particle concentration, and the enhancement is found to increase monotonically with concentration. The results of Figure 4 are all from one research group, and similar results from other groups were used to establish the validity of this trend.

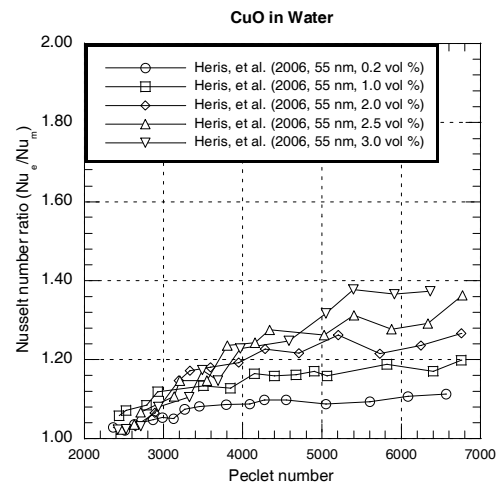


Figure 4. Particle Concentration Effect on Heat Transfer in Water

Numerical Simulations of Nanofluid Coolants in Truck Engine Cooling System

The engine coolant for a standard over-the-road heavy vehicle is a 50% by volume mixture of ethylene glycol and water. Replacing this standard coolant with a nanofluid would result in higher heat transfer rates in the engine, radiator, and cabin heater. Such a coolant gives the truck manufacturer many options in utilizing the thermal enhancement aspects of the nanofluid coolant. However, the

magnitude of the enhancement and the extent of the options depend on the engine and nanofluid coolant. To quantify these effects, we performed numerical simulations using a commercial code, Flowmaster. An engine and cooling system from a Class 8 truck were modeled, where the nanofluid consisted of CuO nanoparticles suspended in a base fluid of a 50/50 mixture of ethylene glycol and water. A diagram of the coolant system from Flowmaster is shown in Figure 5.

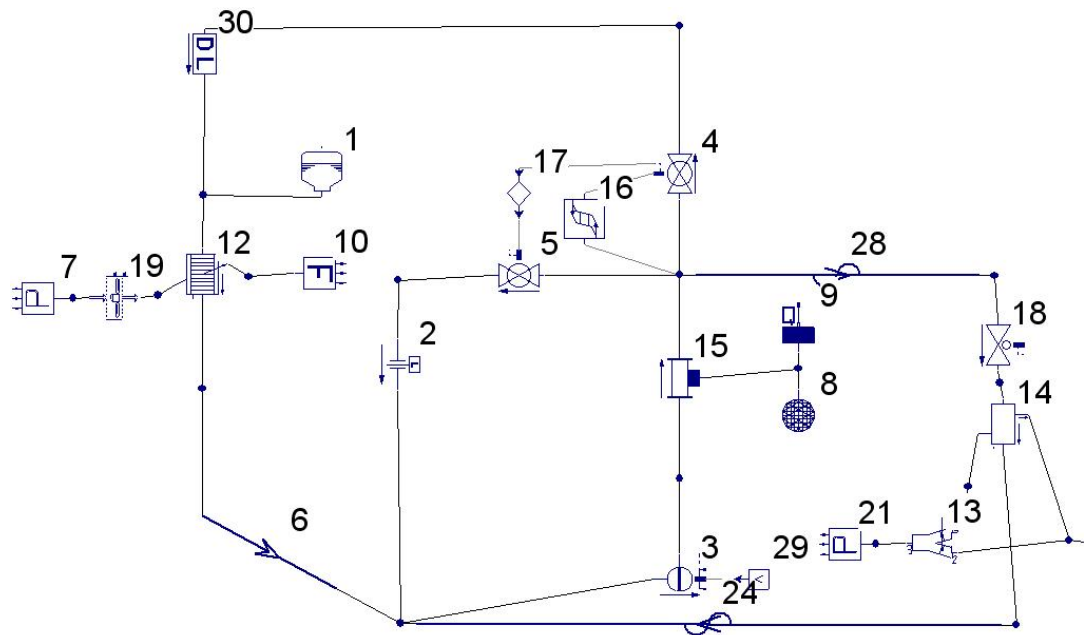


Figure 5. Model of Class 8 Truck Engine Cooling System: 1 Expansion tank; 2 Coolant recirculation path bypassing radiator; 3, 29 Coolant pump; 4, 5, 17 Thermostat flow control; 6, 24, 28 Coolant hose; 7, 10, 19 Engine cooling fan; 8, 9, 15 Heat source from engine to coolant; 12 Radiator; 13, 20, 21 Cabin air flow; 14 Cabin heater; 16 Thermostat; 18 Cabin heater flow control; 30 Coolant path pressure loss.

The coolant system model includes heat rejection from the engine to the coolant circuit and from the coolant to air through the radiator. The coolant pump drives the flow through the network, and the thermostat distributes the coolant to the radiator based on the actuation temperature. In Figure 5, the salient cooling system components are as follows:

Simulation results showed that the most significant system parameters using nanofluid coolants were the coolant and engine temperatures. The coolant mass flow rate and pressure were only slightly affected by the change in coolant, but the temperature changes were substantial. The average engine block

temperature decreased from 206°C with the base fluid alone to a minimum of 141°C with a nanofluid consisting of 4% nanoparticles by volume in the base fluid. This temperature reduction is due to the increase in the nanofluid heat transfer coefficient compared to the base fluid, and it allows for considerable flexibility in design of engine coolant passages and control of local temperatures. A large reduction in engine block temperature need not be taken. Instead, redesign can lead to more uniform engine block temperatures, more effective local cooling, optimum engine block temperature, etc. Other design flexibilities using nanofluid coolants

that were quantified in the study include radiator size, coolant pump size, and engine size. Results are being prepared for publication.

Future Directions

Future work will focus on the following three major tasks.

Identify, Develop, and Characterize Nanofluids in Terms of Physical and Thermal Properties

We will continue to use the full complement of experimental facilities available at Argonne in the development of commercially viable nanofluids and the theories needed to direct their application. Thermal conductivity measurements and theory development will continue to identify candidate fluids for specific applications. Fluid characterization by X-ray and laser scattering techniques will be used to identify the physical condition/state of the nanofluids, and viscosity measurements will be used to determine the potential pumping conditions.

Conduct Nanofluid Flow and Heat Transfer Experiments

We will explore the flow characteristic and measure the heat transfer coefficients of nanofluids. Control tests will be conducted with base fluids. Subsequently, nanofluid flow and heat transfer experiments will be conducted. We will then relate enhanced thermal conductivity and flow characteristics to enhanced heat transfer coefficients of nanofluids. The flow and heat transfer data for nanofluids will be used to determine the nanofluid enhancements over the base fluids and to provide a data base for developing the data correlation needed for system design.

Demonstrate Nanofluid Effectiveness in Industrial Systems

Once commercially viable nanofluids have been developed that are stable with good heat transfer enhancement and are producible in large quantities at acceptable prices, they will be used as working fluids in industrial systems. This phase of the program will provide operating system information as a final part of the process of nanofluid commercialization.

Conclusions

Argonne scientists are developing nanotechnology-based, next-generation fluids that may revolutionize heat transfer where liquid coolants are involved. By suspending nanophase materials like copper or various oxides in liquids such as water, ethylene glycol, or engine oil, researchers can improve the ability to transfer heat by up to 40% in many cases and potentially much higher in others. Improved oils and coolants would make possible more efficient engines and smaller and lighter cooling systems. Such engines and cooling systems would reduce aerodynamic drag and parasitic energy losses, improve fuel savings, and reduce environmental concerns.

Reference

1. W. Yu, D. M. France, S. U. S. Choi, and J. L. Routbort, *Review and Assessment of Nanofluid Technology for Transportation and Other Applications*, Argonne National Laboratory Technical Report, ANL/ESD/07-9, 78 pp., April 2007.

C. Erosion of Materials in Nanofluids

(This project is jointly funded by Propulsion Materials and Heavy Vehicle Systems Optimization)

Principal Investigator: J. L. Routbort and co-workers: D. Singh, Cinta Lorenzo-Martin, R. K. Smith, D. J. Cookson (APS) and Gang Chen (now at Ohio University)

Argonne National Laboratory

9700 S. Cass Avenue, Argonne, IL 60439-4838

(630) 252-5065, e-mail: routbort@anl.gov

Technology Development Manager: Lee Slezak

(202) 586-2335, e-mail: Lee.Slezak@ee.doe.gov

Contractor: UChicago Argonne, LLC

Contract No.: DE-AC03-06CH11357

Objective

- Determine if the use of fluids containing a variety of nanoparticles result in erosive damage to radiator materials.
- Develop models to predict the erosive damage.

Approach

- Develop an experimental apparatus to measure erosive loss.
- Conduct experiments to study erosive damage of fluids containing various types and sizes of nanoparticles on typical radiator materials.
- Develop methods to characterize nanofluids and analyze erosion results.

Accomplishments

- Little erosion damage to a typical radiator material, aluminum Al3003, was observed in experiments performed using CuO nanoparticles in ethylene glycol having impact angles of 30 and 90° and velocities up to 10m/s for impact for a total time of 3,620 hrs. Particle concentration varied between 0.1 and 0.85 vol. %.
- Utilized small-angle X-ray scattering technique to measure nanoparticle size, distribution, and shape.

Future Direction

- Erosion of typical radiator materials using fluids containing a variety of well-characterized nanoparticles will be measured, varying the angle, size of the nanoparticles, impact velocity, nanoparticle volume percent, and temperature.
 - If erosion occurs, a predictive model will be developed.
 - Initial friction and wear tests using nanofluids as lubricants.
-

Forward

Efforts have shifted away from the in-house production of nanofluids, to development of advanced characterization techniques and establishment of working relationships between companies that produce nanofluids. As commercial nanofluids become available, ANL will measure their thermal properties. Fluids that show promise from a heat transfer perspective will then be characterized using SAXS. Finally, liquid erosion tests will be performed to determine if the nanofluid will cause deleterious damage to radiator materials.

Introduction

Many industrial technologies face the challenge of thermal management. With ever-increasing thermal loads due to trends toward greater power output for engines and exhaust gas recirculation for diesel engines, cooling is a crucial issue in transportation. The conventional approach for increasing cooling rates is use of extended surfaces such as fins and microchannels. Reducing radiator size will reduce the frontal area and hence the aerodynamic drag. However, current designs have already stretched this approach to its limits. Therefore, an urgent need exists for new and innovative concepts to achieve ultra-high-performance cooling. Nanofluids seem to show enormous potentials as a coolant for radiators. Choi, et al. have shown that fluids containing 1 vol.% Cu nanoparticles increases thermal conductivity by 40% [1] while 1 vol.% carbon nanotubes increase thermal conductivity by 250% [2].

In order for the enhanced thermal conductivity to be utilized it must be shown that liquid erosion of typical radiator materials will be tolerable. If nanofluids result in excessive erosive wear, they cannot be used. Hence, the Office of Vehicle Technologies funded a program on liquid erosion of radiator materials using nanofluids.

Results and Discussion of Erosion

An apparatus was built and calibrated as described in the FY05 annual report. Baseline data was obtained

using a fluid consisting of 50% ethylene glycol and 50% water impacting a aluminum Al3003 target, typical of a radiator material. Results are tabulated in table 1. As can be seen, the liquid, over the entire range of angles and velocities, produced no erosive wear even for the conditions in which the maximum kinetic energy was transferred to the Al3003 target. It should be mentioned that typical flow velocities in truck radiators are about 1 m/s and hence 10 m/s would be expected to accelerate damage by a factor of 100.

Table 1. Erosion results on Al3003 measured using a baseline fluid, a mixture of 50% ethylene glycol and 50% water.

Impact Angle (°)	Velocity (m/s)	Time (h)	Weight loss (mg)
90	8.0	236	0 ± 0.2
90	10.5	211	0 ± 0.2
50	6.0	264	0 ± 0.2
50	10.0	244	0 ± 0.2
30	8.0	283	0 ± 0.2
30	10.5	293	0 ± 0.2

A previous series of experiments using a very low concentration of Cu (0.01 vol. %) nanoparticles in triethylene glycol reported in the FY6 annual report also showed no erosion of the aluminum target for long times at both 30 and 90° impact angles using velocities up to 9.6 m/s. The size, shape, and distribution of the nanoparticles were not known. It was also speculated that since the volume concentration of the nanoparticles was so low that one would not expect damage. Additionally, Cu is softer than the hardened Al3003 and hence might not be expected to cause damage

In order to determine whether the erosion rate is affected by the particle loading and or the particle type, a long (3620 hrs) series of experiments using various concentrations of CuO in ethylene glycol at two impact angles, 30 and 90°, at velocities up to 10m/s were performed. The results are tabulated in Table 2.

Table 2. Results of erosion of Al3003 using CuO in ethylene glycol.

Vol.%	V (m/s)	Angle (°)	Time (h)	Weight Loss (mg)
0.1	7.7	30	848	3.3 ± 0.2
0.4	7.7	30	643	0 ± 0.2
0.85	7.7	30	692	0 ± 0.2
0.85	10.0	30	771	0 ± 0.2
0.85	10.0	90	500	0 ± 0.2

The first test performed at 7.7 m/s and with an impact angle of 30° indicated a weight loss of 3.3 mg. This result is plotted in Figure 1. The rate of material removal is very small, $4 \times 10^{-2} \mu\text{m/hr}$, corresponding to a loss of 0.003 inches/year for a truck radiator. The results also looked as if there were a threshold.

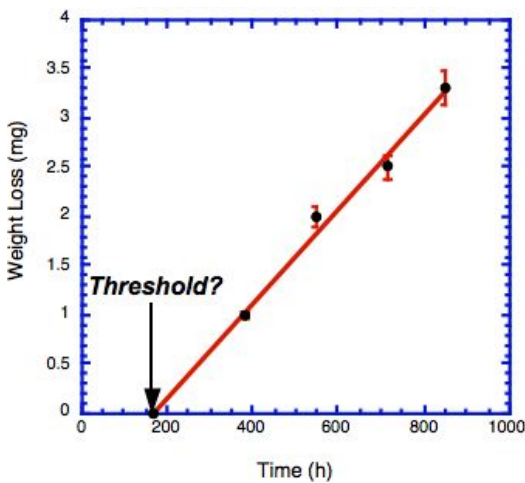


Figure 1. Weight loss vs. time for an impact angle of 30°, velocity of 7.7 m/s, using a 0.1 vol.% CuO nanoparticles in ethylene glycol.

However, closer examination with a scanning electron microscope revealed that the damage was highly localized. It looks as if there was a flaw in the original aluminum that was enlarged by the impact of nanofluid. The fact that the weight loss was not observed using higher velocities substantiates the fact that the weight loss, as small as it was, was an anomaly. Results of thermal conductivity enhancements for this nanofluid were presented in the previous chapter.

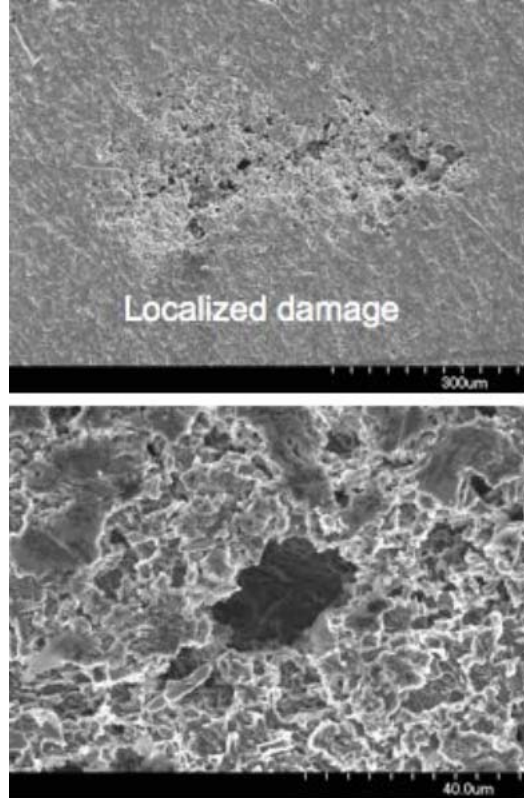


Figure 2. Scanning electron microscopy of the damage resulting from impacts of 0.1 vol.% CuO nanoparticles impacting at 7.7 m/s and 30°

While we have not observed erosive wear as a result of the CuO nanofluid, we have only begun to investigate the parameter space that would include nanoparticle material, concentration, shape, size, and size distribution. These are critical parameters. While the material and concentration can be controlled, the shape, size, and size distribution are generally not accurately determined. One might expect that since the thermal conductivity is such a strong function of nanoparticle size [3] and the kinetic energy imparted to the target by the nanofluid is proportional to the size, it is a very important parameter. The size of the nanoparticle also enters into all theoretical treatments of thermal conductivity. Shape is probably also important, as a sphere is less likely to cause damage than a nanoparticle with sharp edges. Furthermore, one might expect that more damage will result if the dynamic hardness of the nanoparticle is greater or equal to that of the target.

Typically nanoparticle sizes have been determined two ways. First, the particle size of the raw powder

is measured, typically, by microscopy, and it is assumed that when added to the fluid, remains the same. The second method uses laser scattering to measure nanoparticle size of a transparent nanofluid. Laser scattering emphasizes the large particles because of the dependence of the scattering factor on R^6 , where R is the particle radius. We have refined a much more accurate method of measuring the particle size, shape, and distribution, based on small angle X-ray scattering (SAXS) using high-intensity X-rays from the Advanced Photon Source at ANL.

In order to obtain a definitive result on the effect of particle size/distribution on thermal conductivity, we have chosen to use commercially available nanofluids, “Ludox” (W.R. Grace & Co., Columbia, MD), primarily used for coatings, metal casting, refractory products, and catalysts. It is a colloidal silica solution using a water-based fluid (buffered to $\text{pH} = 10$) containing amorphous SiO_2 particles. Ludox is available in three SiO_2 sizes.

SAXS on nanofluids was performed on beamline 15-ID-D (ChemMatCARS) at the Advanced Photon Source, Argonne National Laboratory. General description of the beamline setup can be found elsewhere [4]. The nanofluids were drawn in with a syringe pump to an open-ended 1mm glass capillary and irradiated with a $0.5 \times 0.3 \text{ mm}$ mono-chromatic X-ray beam ($\lambda = 1.5 \text{ \AA}$). X-ray scattering was measured with a charge-coupled device X-ray detector, with intensity calibrated from pure water measured in the identical capillary. All nanofluid SAXS profiles were background-subtracted using profiles obtained from pure buffer solution. For comparison purpose, we also measured the particle size with dynamic light scattering (DLS) using a lab-based instrument (Brookhaven Instruments Corp., Holtsville, NY).

Analysis of X-ray scattering from particles in a liquid can be complicated by interference between the X-rays elastically scattered from individual particles. This particle-particle interference becomes detectable at volume fractions larger than about 0.5%. Figure 3 shows the 1-D SAXS patterns of a silica nanofluid (i.e., Ludox SM) with three different particle volume fractions. The plot of X-ray scattering intensity versus scattering momentum change ($q = 4\pi \sin \theta / \lambda$), where θ is the scattering angle, and λ is the wavelength) on a log-log scale

provides information about the nanoparticles. The X-ray scattering intensity shows a maximum in the region $0.01 < q < 0.05 \text{ \AA}^{-1}$ for the 1 and 16 vol. % samples due to the interparticle interference effect [5]. The oscillations observed above 0.1 \AA^{-1} arise from the inherent form-factor scattering from the particles. These oscillations are often ‘washed-out’ by poly-dispersity in particles size. The fact that they are still intact for these fluids is due to the narrow size distribution of the nanoparticles. That no change in this oscillatory feature was observed in these three samples indicates that dilution does not affect the particle size distribution. To simplify the data analysis, we use data taken from the most diluted samples, where the effect of interparticle interference can be neglected.

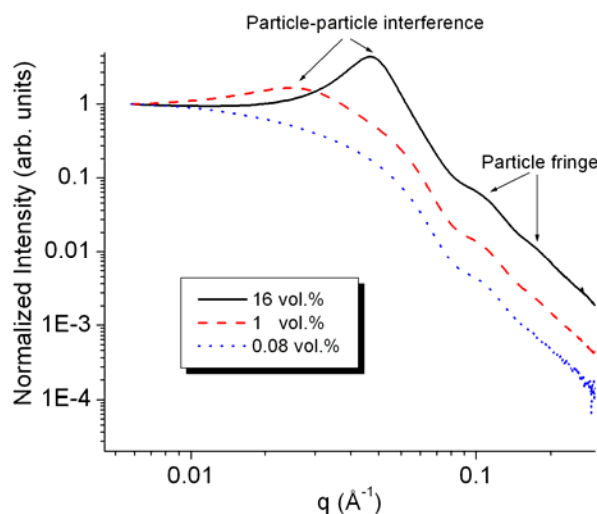


Figure 3. SAXS patterns of Ludox SM nanofluid with three different particle volume

Quantitative data analyses of the SAXS patterns were performed using solid-sphere form factors fitted with a variety of least-squares methods implemented in the program suite IRENA (Ilavsky et al. 2005). Figure 4 shows the 1-D SAXS pattern of a 0.02 vol. % silica nanofluid fitted with a maximum entropy algorithm [6]. This method assumes no particle-particle interference and apart from a non-negative criteria, imposes no further restriction on the resulting size distribution profile. Figure 5 shows the normalized particle size distribution of three diluted silica nanofluids. The concentrations of the samples SM, HS, and TM are 0.08, 0.02, and 0.02 vol. %, respectively. Only one major peak is observed in each of the size distribution profiles,

confirming the mono-dispersity of the nanoparticles. The presence of small satellite peaks in the distributions may be due to a small amount of aggregation – but are just as likely to be artifacts of the maximum entropy technique. Further analysis of the dominant peaks in these profiles shows that the peak centers (average particle sizes) are located at 107, 167, and 286 Å, and the corresponding full widths at half maximum are 49, 43, and 68 Å. In comparison, the average particle sizes measured by the DLS were 104, 174, and 303 Å that correlate well to the SAXS results.

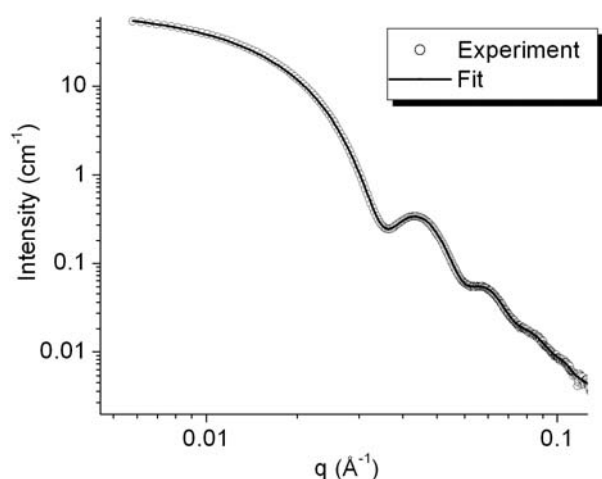


Figure 4. SAXS data of a 0.02 vol.% SiO₂ nanofluid and a fit using the maximum entropy method assuming spherical particles with an average diameter of 17 nm.

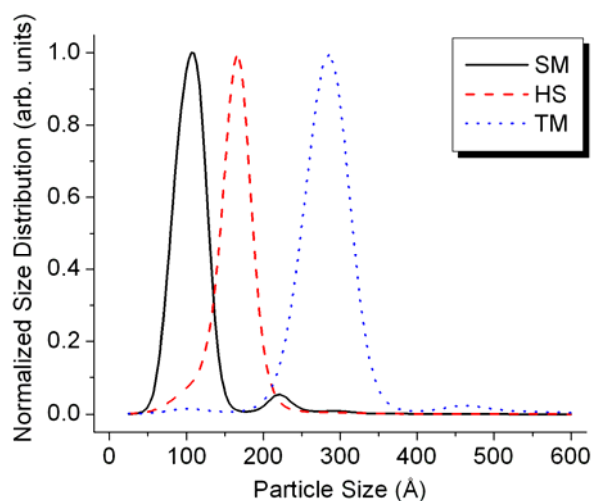


Figure 5. Particle size distribution of three silica nanofluid samples

In summary, the use of SAXS allows determination of nanoparticle size, shape, and distribution in all types of nanofluids. Therefore, it will be used to characterize all nanofluids that exhibit promising thermal properties. The accurate determination of particle size and shape combined with thermal conductivity, heat transfer, and erosion will allow a rigorous comparison with theoretical models and their extensions.

Issues & Future Direction

Understanding mechanism(s) of weight loss of target metal is vital to developing pre-dictive models to describe the erosion behavior from nanofluids. At the present time, it appears that erosion behavior by nanofluids is not severe. However, this observation is based on a limited set of data. We have not yet tested a wide-variety of nanofluids containing well-characterized, and controlled volumes of larger percentages of nanoparticles. For example, we have not tested the erosion of a nanofluid containing nanoparticles that are much harder than the target, such as Al₂O₃, or SiC and would be more likely to cause erosion. Similarly, we haven't tested nanofluids containing larger well-characterized particles and particle size distributions. We plan these tests in FY08.

Conclusions

Long-term liquid erosion tests using CuO nanoparticles whose vol. % varied between 0.1 and 0.85 in ethylene glycol, at 30 and 90° impact angles, and at fluid velocities of up to 10 m/s indicated that erosion of a typical radiator material, Al3003, was not a problem. However, it was felt that the soft CuO nanoparticle characterization (i.e. nanoparticle size) was not very adequate to describe the nanoparticle parameters in the fluid.

Therefore, we have refined a small angle X-ray scattering technique with X-rays from the Advanced Photon Source at ANL to measure the particle size, distribution, and even the shape. A model nanofluid, consisting of a water-based solution containing three different sizes of SiO₂ colloids was used to calibrate SAXS. The technique provides a wealth of information that will be used in the future to characterize nanofluids and hopefully, help to remove some of the ambiguities in the thermal property data that have resulted from poorly characterized nanofluids.

References

1. J. A. Eastman, S.U.S. Choi, S. Li, W. Yu, and L. J. Thompson, "Anomalously Increased Effective Thermal Conductivities of Ethylene Glycol-Based Nano-Fluids Containing Copper Nano-Particles," *Applied Physics Letters*, 78, 718-720 (2001).
2. S. U. S. Choi, Z. G. Zhang, W. Yu, F. E. Lockwood, and E. A. Grulke, "Anomalous Thermal Conductivity Enhancement in Nano-tube Sus-pensions," *Applied Physics Letters*, 79, 2252-2254 (2001).
3. W. Yu, D. M. France, J. Routbort, S.U.S. Choi, "Review and Comparison of Nanofluid thermal Conductivity and Heat Transfer Enhancements, *J. Heat Transfer*, in press
4. D. J. Cookson, N. Kirby, R. Knott, M. Lee, and D. Schultz, "Strategies for data collection and calibration on the small angle X-ray scattering camers at ChemMatCARS", *Advanced Photon Source. J. Synchrotron Rad.* 13, 440-444 (2006).
5. Y. Xu, P. L. Hiew, M. A. Klippenstein, Y. Koga, "Study of a commercial SiO₂ sol and gel by small angle X-ray scattering: effect of sample thickness and interoperation by means of Smoluchowski scheme", *Clays and Clay Minerals* 44, 197-212 (1996).
6. J. A. Potton, G. J. Daniell, B. D. Rainford, "Particle size distributions from SANS data using the maximum entropy method", *J. Appl. Cryst.* 21, 663-668 (1988).

D. Diesel Engine Underhood Thermal Analysis

Principal Investigators: Jimmy Chang and project manager: Tanju Sofu

Argonne National Laboratory

9700 S. Cass Avenue, Argonne, Illinois 60439

(630) 252-9673; fax: (630) 252-4500; e-mail: tsofu@anl.gov

Technology Development Area Manager: Lee Slezak

(202) 586-2335, fax: (202) 586-2476, e-mail: Lee.Slezak@ee.doe.gov

Contractor: Argonne National Laboratory

Contract No.: DE-AC02-06CH11357

Objective

- Develop a novel simulation technique to predict diesel engine thermal performance and to identify potential hot-spots in engine compartments of heavy-duty trucks.
- Optimize engine thermal system and cooling package leading to improvements in energy efficiency of heavy vehicle systems.

Approach

- Develop a conjoined 1-D thermal-fluid model and 3-D CFD model for a prototypical heavy vehicle underhood thermal system of a diesel engine.
- Build the underhood thermal model and predict engine compartment temperatures, flow field distribution, and engine thermal performance under the specified test conditions.
- Achieve fuel efficiencies through cooling system optimization and radiator size reductions.

Accomplishments

- A conjoint 1-D and 3-D underhood thermal simulation package of a diesel engine with exhaust gas recirculation (EGR) was developed.
- Thermal-fluid model was created with engine metal structure, underhood air, lubrication oil, and coolant circuits (cabin heater, EGR, and radiator subsystems).
- CFD model was developed to simulate the underhood air temperatures and the component surface heat transfer rates between ambient air and engine metal structure.
- Simulation package was validated for tests of engine speeds 1200 and 1700 rpm. The simulation package predicts the temperatures and distributed heat rejection rates within reasonable accuracy

Future Direction

- Thermal-fluid model needs to be improved by including air-conditioning loop and adding more components to the existing subsystems of cabin heater, EGR, radiator-fan, and charge air cooler.
 - CFD model needs to be refined to account for the local heat transfer effects from heat exchanger, radiator, and charge air cooler with fan under operation.
 - Combined use of thermal-fluid and CFD models should be expanded to study the sizes and the relative placements of radiator, charge air cooler and fan to maximize the cooling efficiency
-

Abstract

An optimal design of vehicle thermal system is important for energy efficiency since less than one-third of the total fuel energy provides useful mechanical work and the remainder is lost through the exhaust system and heat rejection. The objective of this work has been to develop a novel simulation technique based on combined use of 3-D computational fluid dynamics (CFD) and 1-D thermal-fluid models to predict diesel engine thermal performance and to identify potential hot-spots in engine compartments of heavy-duty trucks. This new technique is anticipated to be important for optimization of engine thermal system and cooling package leading to improvements in energy efficiency of heavy vehicle systems.

Introduction

As the diesel engine emission regulations becomes increasingly stringent, emission control technologies such as cooled exhaust gas recirculation (EGR) and after-treatment devices are applied. As a result, the engine heat rejection to both coolant and air increases substantially, causing generally higher underhood temperatures with potential hot spots. In addition, warm air from the radiator can further heat up as it passes over heat generating component surfaces. The combination of these effects can compromise the durability of certain temperature sensitive components under the hood, leading to reduced vehicle life, especially under extended driving conditions. To remedy the situation, OEMs often overdesign their cooling packages resulting in reduced energy efficiency. To address these challenges and shorten the design cycle, ANL had partnered with Cummins, Inc. under a CRADA to develop an integrated simulation technique for underhood thermal analysis and cooling package optimization for a conventional diesel engine.

The experimental effort by the Cummins team focused on conducting tests with controlled ventilation air flow rates at wind tunnel inlet and with controlled coolant temperature and flow rate at coolant pump to estimate the cooling needs for an enclosed truck engine. The purpose of the analytical studies by the ANL team (with modeling support from FLUENT Inc. and FLOWMASTER International) was to assess the various simulation methods that could be used to predict underhood

ventilation air temperatures and engine component surface temperatures. The work involved development and validation of combined 1-D and 3-D simulation models of the Cummins ISX diesel engine (rated at 500 ~ 565 HP) to evaluate engine cooling system. Although the separated cooling system compartments are unique to trucks, the Cummins tests and the ANL analyses provide an opportunity to understand the combined effect of coolant cooling and air cooling on engine performance for a wide range of heavy vehicles.

FLUENT is a three-dimensional computational fluid dynamics (CFD) solver which allows engineers to import the complicated underhood geometry and calculate the complex flows typical for vehicle underhood thermal analysis [1]. FLUENT solvers are based on the finite volume method with domain discretized into a finite set of volumes or cells, and with general conservation equations for mass, momentum, energy, and turbulence. With multiple solver options combined with a convergence-enhancing multigrid method, FLUENT provides an efficient and accurate solution for underhood thermal analysis.

FLOWMASTER is a one-dimensional fluid flow analysis program and allows engineers to graphically model complete fluid systems to predict pressure, temperature, heat flow, and fluid flow distribution in their systems [2]. The physical basis of FLOWMASTER is built on empirical correlations as well as analytical conservation equations for mass, momentum, and energy [3-4]. An extensive database is included with the software to describe the components of a system, such as pipes, pumps, heat exchangers, heat sources, and flow sources, etc. The user can also incorporate the performance characteristics of other components into the database.

Modeling Development

The 1-D thermal-fluid software Flowmaster is used to account for overall energy balance and simulate cooling system response. The 3-D CFD software Fluent is used to determine underhood air temperatures and component surface heat transfer. The developed 1-D model is composed of engine structure, air, oil, and coolant loops. The coolant loop includes exhaust gas recirculation, radiator-fan, and cabin heater subsystems to form a complete cooling package. The developed 3-D CFD model is

based on the finite volume method with domain discretized into a finite set of volumes or cells, and with general conservation equations for mass, momentum, energy, and turbulence. The thermal fluid model had been conjoined with the CFD model to manage the underhood thermal control and enhance the cooling performance.

Figure 1 shows the flow chart of the sequential analyses with the 1-D thermal-fluid model and 3-D CFD model. The 1-D model requires the coolant temperature and flow rate at the pump in the coolant system, air flow rates and air temperatures to the radiator, to the EGR, and to the cabin in the air passage system and oil pump speed in the lubrication oil system to account for the overall energy balance and predict the engine component temperatures.

In the 3-D thermal analysis, the 1-D model predictions are used to specify the surface temperature boundary conditions for various engine components, which allow the 3-D code to calculate the air temperatures at all underhood locations and the corresponding heat fluxes between the ventilation air and the surface of various engine components. The results of the 3-D CFD analysis are, in turn, sent back to the 1-D model to improve the component surface temperature predictions by modifying the heat transfer coefficients between the engine components and ventilation air. An iterative procedure was employed between the two models to obtain consistent solutions (Figure 1). For a vast majority of the components consistency between the 1-D and 3-D solutions was established after 4~5 iterations.

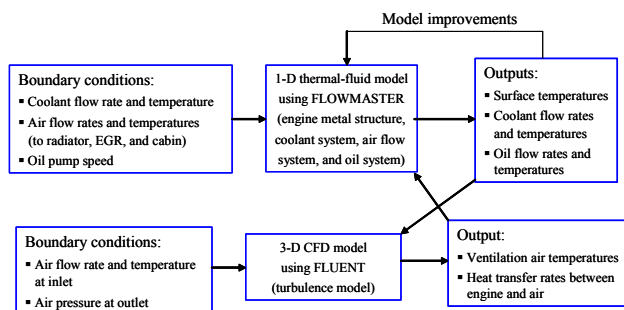


Figure 1. Flowchart of coupled simulations using CFD model (FLUENT) and thermal-fluid model (FLOWMASTER)

Results and Discussion

The desired flow rate through the wind tunnel was assured by imposing an air velocity at the inlet as the boundary condition. The tunnel outlet was considered with the pressure as the outlet boundary condition. The wall of the wind tunnel is initially set at room temperature (25°C) and exchanges the heat with the engine surface through the air convection heat transfer. The final CFD model consists of 0.80 million fluid cells, with a 4 mm thick extrusion layer surrounding the engine surfaces. The ventilation air flow field in the test wind tunnel and the convective heat transfer coefficient for the solid surfaces were obtained using the FLUENT CFD software. An initial parametric study of the effect of the buoyancy force in the thermal-fluid calculations revealed that the effect of density variations on the overall flow and temperature fields is negligible. Thus, the ventilation air flow field was simulated as a steady incompressible flow with energy equation using the k-epsilon two-equation turbulence model with standard wall functions. As the most basic two-equation turbulence model, k-epsilon is believed to provide a reasonable approximation of the time-averaged flow distribution over the surface of the engine and its components in the test wind tunnel. A set of transient calculations were also performed to investigate temperature fluctuations observed during the experiments and assure that the calculated flow field is steady with no oscillations. The results indicated negligible differences between the transient and steady state solutions. Two tests with different engine speeds, each having its own wind speed and heat rejection, were studied with the CFD model. The calculations were performed on a Linux cluster.

The thermal-fluid model FLOWMASTER simulates four possible heat and fluid paths - the coolant loop, the oil loop, the air passage, and the solid metal structure. The cooling water loop consists of the flow through the engine to remove the heat from engine, the flow through radiator to release heat to air, the flow through EGR to remove heat from exhaust gas, and the flow through the cabin heat exchanger to control temperature. The oil loop within the model contains the oil filter, ECM, oil pan and sump, passage through the turbocharger, cylinder head, cylinder block, oil pump, and oil cooler. The oil pump controls flow through the oil loop.

With air temperatures determined from CFD model, the “convection solid” component, used in the FLOWMASTER model, serves as the boundary temperature of engine metal structure and simulates the heat transfer across the various engine surfaces, gaining heat from the front, and then splitting heat to the left, right, top, and bottom of the engine. The final section of the thermal-fluid model is the solid metal structure of the engine block consisting of various “conduction” components. The metal structure network represents the interconnections of all solid sections of the engine and their interfaces with the other fluid flow paths.

The model provides predictions well within that range (Figures 2 and 3 for tests of engine speeds 1700 rpm and 1200 rpm, respectively). In fact, over 95% of the model temperature results are within 10% of the measured data. Although the discrepancies are generally small, the attempts to resolve them are part of the continuing modeling effort to provide a better description of the underhood thermal system.

Summary

A combined 1-D and 3-D simulation technique was developed to predict the underhood thermal performance of a diesel engine with exhaust gas recirculation system. The coupled calculations were performed for two engine speeds 1200 and 1700 rpm with the corresponding rejection heat, wind speed, fan speed, pump speed and coolant flow rate. The results indicate that the temperatures and distributed heat rejection rates can be estimated within reasonable accuracy when 1-D and 3-D models are used together. The developed model can help redesign underhood configuration while meeting new energy efficiency and emissions requirements. Through the simulations by using the developed model, significant fuel efficiencies can be expected from optimization of cooling system and reductions in radiator size.

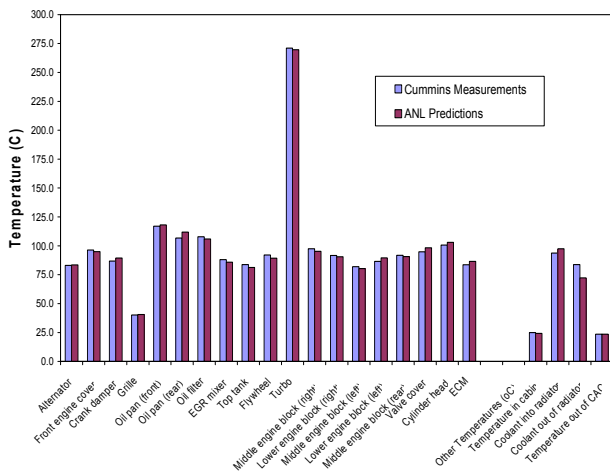


Figure 2. Comparison of temperatures between measurements and model predictions at engine speed 1700 rpm

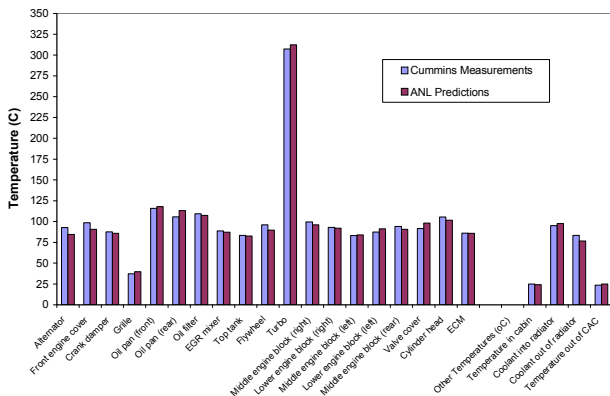


Figure 3. Comparison of temperatures between measurements and model predictions at engine speed 1200 rpm

References

1. *FLUENT Flow Modeling Software 6.2 Training Notes*, publication of FLUENT Inc., December 2005.
2. *Flowmaster – Cooling Systems Easy Start Guide*, Flowmaster International Ltd.
3. Fon-Chieh Chang, Tanju Sofu, John Hull, and David Weber, “Thermal Analysis of an Off-Road Machine with a Conjoint 3-D CFD and 1-D Network Simulation Package,” *Int. J. Heavy Vehicle Systems*, Vol. 14, No. 1, 2007.
4. Fon-Chieh Chang, Srinivas Malipeddi, Sudhindra Uppuluri, and Steven Shapiro, “Underhood Thermal Management using 1D-Network Simulations,” SAE paper 2003-01-3405.

III. FRICTION AND WEAR

A. Boundary Lubrication Mechanisms

Principal Investigators: O. O. Ajayi, C. Lorenzo-Martin, R.A. Erck, J. Routbort, and G. R. Fenske
Argonne National Laboratory
9700 South Cass Avenue, Argonne, IL 60439
(630) 252-9021; fax: (630) 252-4798; e-mail: ajayi@anl.gov

Technology Development Manager: Lee Slezak
(202) 586-2335, Lee.Slezak@hq.doe.gov

Technical Program Manager: Jules Routbort
(630) 252-5065, e-mail: routbort@anl.gov

Contractor: Argonne National Laboratory, Argonne, Illinois
Contract No.: DE-AC02-06CH11357

Objective

Develop a better understanding of the mechanisms and reactions that occur on component surfaces under boundary lubrication regimes with the ultimate goal of friction and wear reduction in oil-lubricated components and systems in heavy vehicles. Specific objectives are

- Determine the basic mechanisms of catastrophic failure in lubricated surfaces in terms of materials behavior. This knowledge will facilitate the design of higher power density components and systems.
- Determine the basic mechanisms of chemical boundary lubrication. This knowledge will facilitate lubricant and surface design for minimum frictional properties.
- Establish and validate methodologies for predicting the performance, and failure of lubricated components and systems.
- Integrate coating and lubrication technologies for maximum enhancement of lubricated-surface performance.
- Transfer the technology developed to OEMs of diesel engine and vehicle components and systems.

Approach

- Characterize the dynamic changes in the near-surface material during scuffing. Formulate a material-behavior-based scuffing mechanism and prediction capability.
- Determine the chemical kinetics of boundary film formation and loss rate by in-situ X-ray characterization of tribological interfaces at the Advanced Photon Source (APS) of Argonne National Laboratory (ANL).
- Characterize the physical, mechanical, and tribological properties of tribo-chemical films, including the failure mechanisms.
- Integrate the performance and failure mechanisms of all the structural elements of a lubricated interface to formulate a method for predicting performance and/or failure. This task will include incorporation of surface coatings.
- Maintain continuous collaboration with OEMs of heavy vehicle systems to facilitate effective technology transfer.

Accomplishments

- Conducted extensive characterization of microstructural changes during scuffing of 4340 steel, using scanning electron microscopy (SEM) and X-ray analysis.
- For metallic materials, developed a model of scuffing initiation based on an adiabatic shear instability mechanism and scuffing propagation based on a balance between heat generation and heat dissipation rates.
- Characterized the mechanical properties and scuffing resistance of a graded nanocrystalline surface layer produced by severe plastic deformation resulting from the scuffing process.
- Conducted preliminary evaluation of scuffing mechanisms in ceramic materials.
- Extended scuffing mechanisms study into ceramics and metals contact pairs.
- Using X-ray fluorescence, reflectivity, and diffraction at the APS, demonstrated the ability to characterize tribochemical films generated from model oil additives.
- Designed and constructed an X-ray accessible tribo-tester for in-situ study of boundary film formation and loss rates.

Future Direction

- Experimentally validate the comprehensive scuffing theory for various engineering materials, including ceramics.
- Develop and evaluate methods and technologies to prevent scuffing in heavily loaded oil-lubricated components and systems.
- Using X-ray based and other surface analytical techniques, continue to characterize tribochemical films formed by model lubricant additives.
- Characterize the physical, mechanical, and failure mechanisms of tribochemical films with nano-contact probe devices.
- Evaluate the impact of various surface technologies, such as coating and laser texturing, on boundary lubrication mechanisms.
- Develop a technique to measure real contact temperature needed for tribochemical film formation.

Introduction

Many critical components in diesel engines and transportation vehicle systems such as gears and bearings are lubricated by oil. Satisfactory performance of these components and systems in terms of efficiency and durability is achieved through the integration of materials, surface finish, and oil lubricant formulations often using Edisonian trial-and-error approach. Indeed, experience is likely the sole basis for new designs and methods to solve failure problems in lubricated components. Because of the technology drive to more efficient and smaller systems, more severe operating conditions are invariably expected for component surfaces in advanced engines and vehicle systems. The trial-and-error approach to

effective lubrication is inadequate and certainly inefficient. Departure from this approach will require a better understanding of the fundamental mechanisms of both boundary lubrication and surface failure in severely loaded lubricated components.

Another major technical thrust area for the Department of Energy in the development of diesel engine technology for heavy vehicles is emission reduction. Indeed, with the higher efficiency of diesel engines compared to gasoline engines, significant reduction in emissions will facilitate the use of diesel engine for automotive applications. Unfortunately, some essential components in oil lubricants and diesel-fuel additives (such as sulfur, phosphorus, and chlorine) are known to poison the

catalysts in diesel engine emission-reducing after-treatment devices. Reduction or elimination of these additives will make emission after-treatment devices more effective and durable; it will however make the surfaces of many lubricated components more vulnerable to catastrophic failure. There is, therefore, a need to develop effective replacement for these essential lubricant additives. Again, such an endeavor will require a better understanding of the mechanisms of boundary lubrication and the failures therein.

Increases in vehicle efficiency will require friction reduction and increase in power density in the engine and powertrain systems. Higher power density translates to increased severity of contact between many components. This, again, will compromise the reliability of various critical components, unless they are effectively lubricated. The efficacy of oil additives in reducing friction and in protecting component surfaces depends on the nature and extent of the chemical interactions between the component surface and the oil additives. In addition to reliability issues, the durability of lubricated components also depends on the effectiveness of oil lubrication mechanisms especially under boundary conditions. Components will eventually fail or wear out by various mechanisms including contact fatigue. Wear is the gradual removal of material from contacting surfaces, and it can occur in many ways, such as abrasion, adhesion, and corrosion. Repeated contact stress cycles, to which component contact surfaces are subjected, can initiate and propagate fatigue cracks and, ultimately, lead to the loss of a chunk of material from the surface. This damage mode by contact fatigue is often referred to as "pitting." Wear and contact fatigue are both closely related to boundary lubrication mechanisms. Antiwear additives in lubricants are designed to form a wear-resistant protective layer on the surface. The role of lubricant additives on contact fatigue failure is not fully understood, although it is clear that the lubricant chemistry significantly affects contact fatigue. Again, lack of a comprehensive understanding of the basic mechanisms of boundary lubrication is a major obstacle to a reasonable prediction of the durability of lubricated components and systems.

Significant conservation benefits would accrue by extending the drain interval for diesel engine oil, with an ultimate goal of a fill-for-life system. Successful implementation of the fill-for-life concept for the various lubricated systems in heavy vehicles requires optimization of surface lubrication through the integration of materials, lubricant, and, perhaps, coating technologies. Such an effort will require an adequate fundamental understanding of surface material behavior, chemical interactions between the material surface and the lubricant, and the behavior of material and lubricant over time.

Some common threads run through all of the challenges and problems in the area of effective and durable surface lubrication of efficient and high power density engine components and systems briefly described above. The two key ones are lack of adequate basic and quantitative understanding of the failure mechanisms of component surfaces, and lack of understanding of the basic mechanisms of boundary lubrication, i.e., how lubricant chemistry and additives interact with rubbing surfaces, and how this affects performance in terms of friction and wear. To progress beyond the empirical trial-and-error approach for predicting lubricated component performance, a better understanding is required of the basic mechanisms regarding the events that occur on lubricated surfaces. Consequently, the primary objective of the present project is to determine the fundamental mechanisms of boundary lubrication and failure processes of lubricated surfaces. The technical approach taken in this study differs from the usual one of posttest characterization of lubricated surfaces but, rather, will involve developing and applying in-situ characterization techniques for lubricated interfaces that will use the X-ray beam at the Advanced Photon Source (APS) located at ANL. Using a combination of different X-ray-based surface analytical techniques, we will study, in real time, the interactions between oil lubricants and their additives and the surfaces they lubricate. Such study will provide the basic mechanisms of boundary lubrication. In addition to surface chemical changes, the materials aspects of various tribological failure mechanisms (starting with scuffing) will be studied.

Results and Discussion

Efforts during the FY 07 were devoted to the study of scuffing mechanisms in ceramic materials and metal contact pairs. Such contact pairs are currently used to solve scuffing problems in components such as diesel fuel injectors [1, 2]. However, the mechanisms of scuffing in such contact pairs are still largely unknown. Study of scuffing in ceramic-metal contact pairs will provide significant input into the development of a comprehensive scuffing model that is applicable to all classes of engineering materials, including thin-film hard ceramic coatings. In view of the patchy nature of the tribochemical boundary films as shown in Figure 1, it is apparent that the knowledge of the temperature at the point of contact is essential in order to develop a model for the kinetics of film formation. Since the surface chemical reaction is thermally driven, the patchy morphology may be the result of difference in temperatures at the real areas of contact. Consequently, efforts during the FY07 were also devoted to explore means of measuring the contact temperature based on thermoelectric potential.

Scuffing ceramic/steel contact pairs

In the past years, a scuffing theory was developed for metallic materials based on experimental observations from hardened 4140 steel [3, 4]. Scuffing initiation occurs when the rate of thermal softening as a result of heat generated by plastic deformation at the real areas of contact exceeds the rate of work hardening due to an increase in dislocation density associated with plastic deformation. Under such condition, the real contact area plastic deformation process becomes unstable and a severe localized plasticity ensues, accompanied by a large amount of heat generation – scuffing initiation. Progression of scuffing to a catastrophic stage (in which the entire contact area becomes damaged) is dependent on whether its propagation occurs or not. If the rate of heat dissipation from the initiation site exceeds the rate of heat generation from continued deformation, then scuffing does not propagate. If the rate of heat generation exceeds the rate of heat dissipation, scuffing will propagate into a run-away thermal process, ultimately resulting in a catastrophic failure.

Structural ceramic materials are currently being used in some tribological systems to address scuffing problems in the lubricated components of such systems. For example, zirconia (ZrO_2) ceramic plungers have been successfully used in fuel injector systems for heavy duty diesel engines, primarily to address scuffing failures in low-lubricity diesel fuels [1, 2]. In this particular application, ceramic plunger slides against steel barrel. In many other similar applications such as hybrid bearings, ceramic materials are in sliding contact with steel material.

Scuffing tests were conducted with a block-on-ring contact configuration, with the ceramic material as the block and steel as the ring. Ceramic materials evaluated are commercially available polycrystalline zirconia; ZrO_2 (Y-TZP), silicon carbide (SiC) and alumina (Al_2O_3). The ceramic block is held stationary and loaded against a rotating steel ring partially submerged in poly-alpha-olefin (PAO) basestock lubricant, thereby creating a fully flooded and well-lubricated contact interface. A three-axis load cell allows measurement of normal, lateral, and traction forces. Loading and unloading are done by a fast-response pneumatic system attached to the load cell, enabling fast unloading when scuffing occurs.

Zirconia/steel: In yttria stabilized tetragonal polycrystalline zirconia (Y-TZP), material, scuffing did not occur until the maximum load capacity of the test rig, which is 1800 N (Figure 2a). Under similar test condition, steel-on-steel contact pairs typically scuffs at about 300 N. At the conclusion of the test, the damage in the Zirconia block material consisted primarily of polishing wear, shown in Figure 2b, and some area of microspalling. The occurrence of polishing wear in this material during scuffing test is expected to shift the lubrication regime from boundary to EHD/mixed as the ratio of lubricant fluid film thickness to the composite surface roughness (the so-called λ ratio) increases. Such transition in lubrication regime is probably responsible for the decrease in friction coefficient from the initial value of 0.14 (typical for boundary regime) to a steady value of 0.08 (typical for PAO lubricant under EHD) observed in the later stage of the test as shown in Figure 2a. Although the scuffing test in the ZrO_2 material was conducted at

ambient room conditions, the contact temperature at the conclusion of the test was very high as indicated by excessive smoking of the lubricant oil and the breakdown of the oil to form a tenacious carbon deposit layer at the edge of contact area (Figure 2b).

Alumina/steel: Results of the scuffing tests with alumina-steel contact pair is shown in Figure 3. In this material combination, scuffing occurred at a normal force of about 300 N (Figure 3a), which is also typical for steel-on-steel contact. The friction coefficient showed only a slight decrease from the initial value of 0.14 to about 0.12 before the sudden rapid increase typical for scuffing failure. Extensive metal transfer from the steel ring onto the Al_2O_3 block occurred during the scuffing test with this material combination (Figure 3b). The metal transfer patches are also severely deformed, perhaps indicative of shear instability of steel-on-steel contact pairs.

Silicon carbide/steel: Figure 4 shows the results of scuffing test with SiC-steel contact pairs. As indicated in Figure 4a, scuffing also occurred (at normal force of about 100 N) in the contact pair. Test started with relatively low friction of about 0.06, but increased to a near steady value of 0.08 before the sudden rise when scuffing occurred. Prior to scuffing, this material pair showed the lowest friction coefficient of all the material evaluated. In oil lubricated applications that do not involve severe sliding contact, SiC-steel pairs will be good material choice to minimize friction. As in Al_2O_3 , occurrence of scuffing is accompanied by extensive steel material transfer onto the SiC surface as shown in Figure 4b.

So far, results from our study of scuffing process in ceramic/steel contact pair clearly show that when there is no metal transfer, scuffing did not occur. It is not clear if the metal transfer is caused by scuffing or that the transfer is necessary for scuffing. The mechanisms of metal transfer and perhaps its prevention will be explored further in the coming year. Implication of this finding for ceramic coatings will also be examined, because the use of ceramic materials for scuffing prevention in vehicle components will best be implemented via thin-film ceramic coatings.

Contact Temperature Measurement

When two dissimilar metals are joined, as the temperature of the junction increases, an electric potential is established as a result of differences in the work functions of the two materials. The magnitude of the voltage from this potential difference is precisely dependent on the temperature. Consequently, measurement of the voltage provides accurate information on the temperature of the bimetallic junction. This is indeed the principle on which thin-wire thermocouple devices are based. Conceivably, the same principle can be applied to measure the temperature of real area of contact during tribo-interaction between two dissimilar metallic specimens as illustrated in Figure 5.

An attempt at the proof of this concept was made by putting a copper and steel blocks in a stationary contact as shown in Figure 6. A cyclic radiative heating test of the bimetal contact was conducted and the contact voltage continuously measured during the heating and the cooling cycles. The temperature of the joint was also measured by a thermocouple. Figure 7 shows the results of the measured temperature and voltage from the pulse heating experiment. Both measurements show excellent correlation. In the coming year, this technique will be refined for the dynamic sliding tribo-contact under both dry and lubricated conditions.

Conclusions

During FY2007, the efforts on this project were focused on the study of scuffing mechanisms in commercially available structural ceramic materials and metal contact pairs with particular emphasis on the scuffing mechanisms. In Y-TZP zirconia material, scuffing characterized by sudden rise in friction was not observed. Instead, polishing wear and local spallation was observed in the contact area. Occurrence of polishing wear aided the fluid film lubrication by increasing the lamda ratio. In both alumina and SiC materials, scuffing was observed and in both cases metal transfer from the steel counterface was observed as well. The connection between the scuffing process and the metal transfer will be investigated further – did transfer occur as a result of scuffing; or did the occurrence of transfer led to scuffing?

In view of the role of contact temperature in the formation and kinetics of tribochemical films formed during boundary lubrication, some effort was devoted to the development of a technique for contact temperature measurement. It was demonstrated that thermoelectric potential principle can conceivably be applied to measure the real contact temperature during a sliding contact.

References

1. D. K. Hickey et al., US Patent 6,149,073 (2000)
2. W. F. Mandler and T. M. Yonushonis, Proc. 6th Diesel Engine Emission Reduction (DEER) Conf. (2000).
3. O. O. Ajayi, J. Hershberger, J. Zhang, H. Yoon, and G. R. Fenske, *Tribology International*, Vol. 38 (2005), 277-282
4. J. Hershberger, O. O. Ajayi, J. Zhang, H. Yoon, and G. R. Fenske, *Wear*. vol. 258 (2005), 1471-1478.

Publications

1. C. Lorenzo-Martin, O. O. Ajayi, D. Singh, and J. L. Routbort, "Evaluation of Scuffing Behavior of Single Crystal Zirconia Ceramic Materials," *Wear*. vol. 263, (2007), 872-877..
2. O. O. Ajayi, A. Erdemir and G. R. Fenske, "Mechanisms of Scuffing in Ceramic Thin Film Coated Surfaces" Presented at 31st Intl. Conf. on Adv. Ceramics & Composites, Daytona Beach, FL, Jan. 21-26, 2007
3. C. Lorenzo-Martin, O. O. Ajayi, D. Singh, and J. L. Routbort, "Effect of Microstructure on Friction and Wear of Polycrystalline Zirconia Ceramic Materials" Presented at 2007 STLE Annual Meeting, Philadelphia, PA, May 6-10, 2007.
4. R. A. Erck, O. O. Ajayi, and G. R. Fenske, "Friction of Steel Sliding under Boundary Lubrication Regime in Commercial Gear Oils" Presented at 2007 STLE Annual Meeting, Philadelphia, PA, May 6-10, 2007.

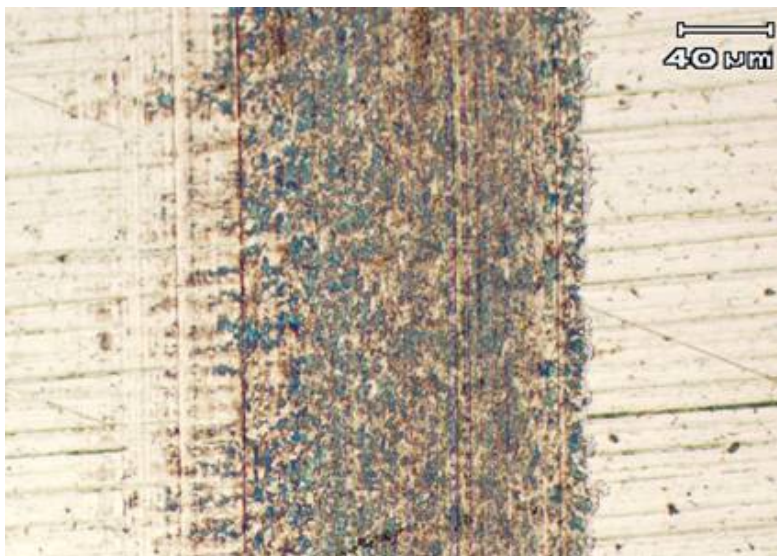


Figure 1. Optical micrograph showing the patchy nature of tribochemical films.

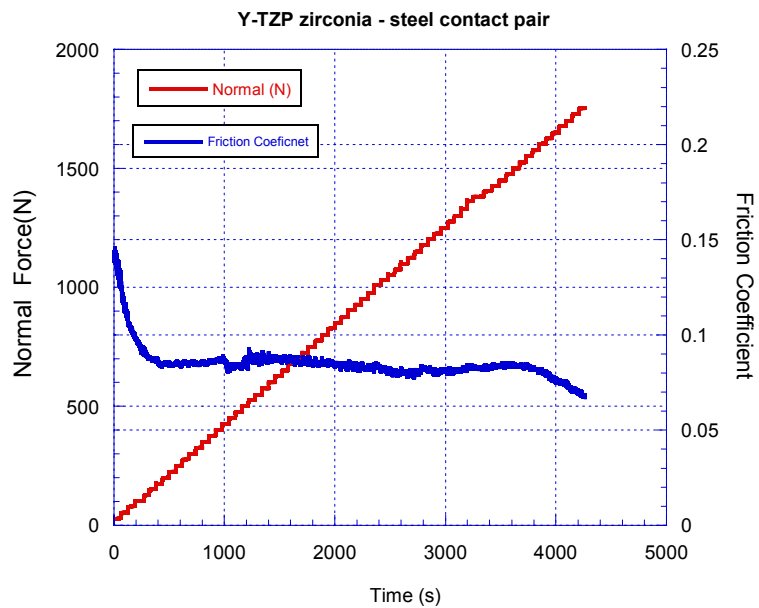


Figure 2a. Variation of friction with normal force during scuffing test with Y-TZP zirconia.

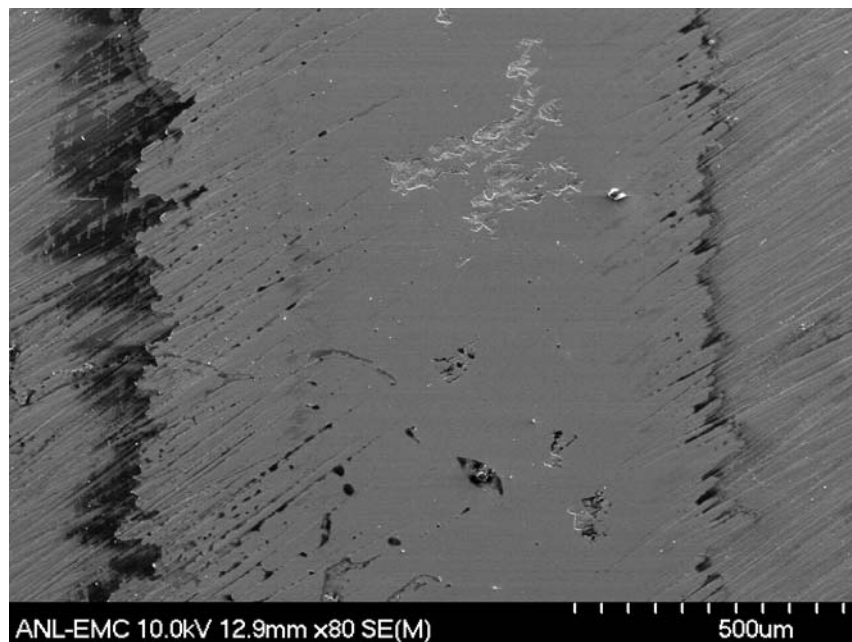


Figure 2b. SEM micrograph of contact area Y-TZP zirconia after scuffing test

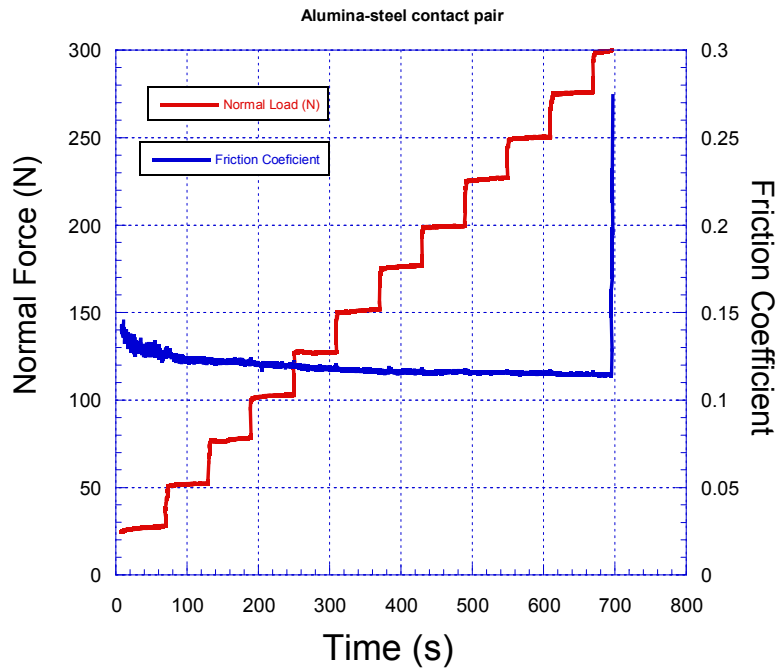


Figure 3a. Variation of friction with normal force during scuffing test with alumina

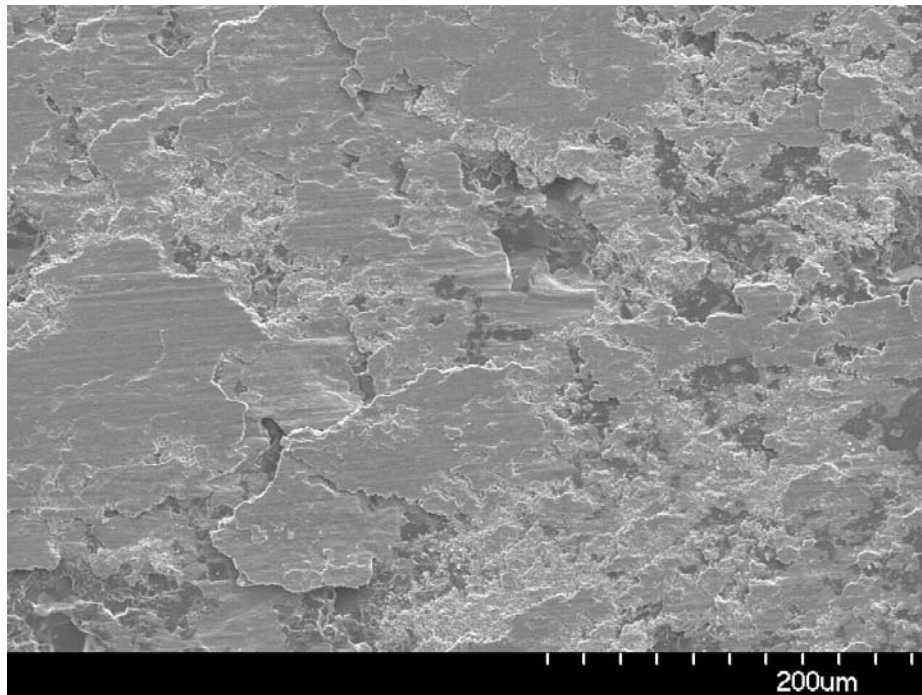


Figure 3b. SEM micrograph of alumina block after scuffing test showing extensive metal transfer

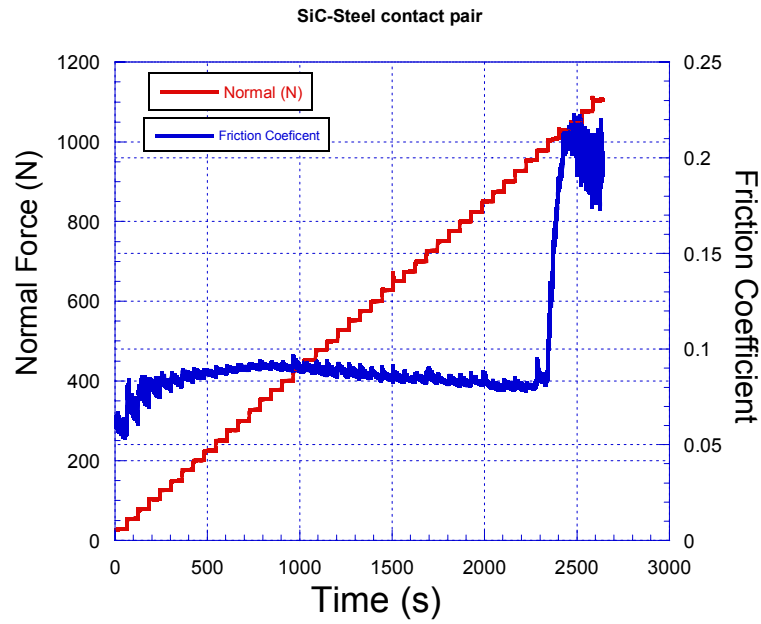


Figure 4a. Variation of friction with normal force during scuffing test with SiC

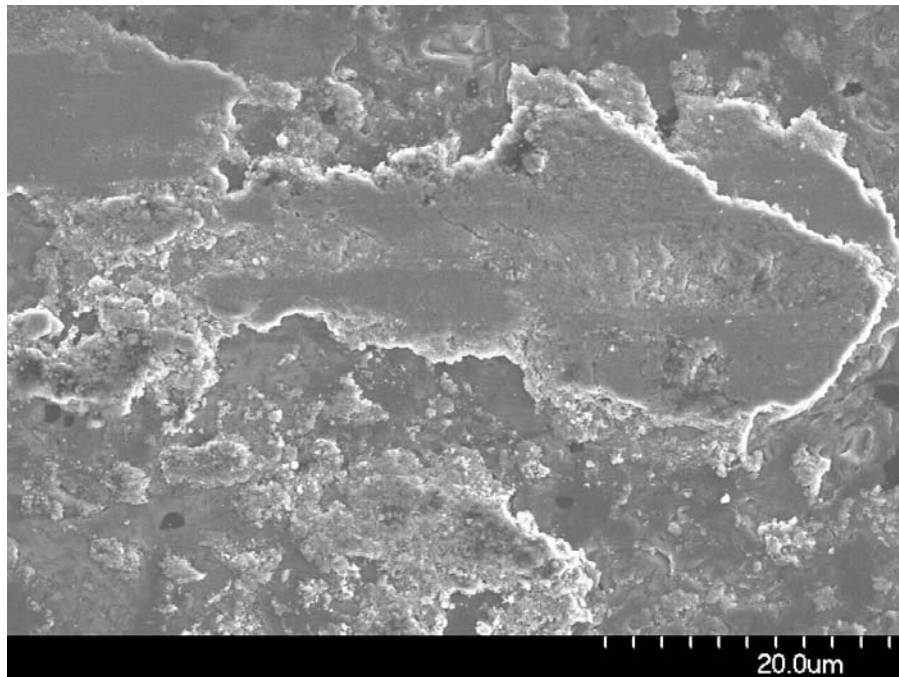


Figure 4b. SEM micrograph of SiC block after scuffing test showing metal transfer

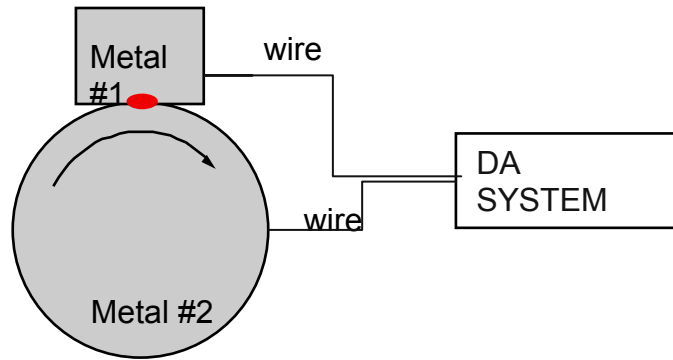


Figure 5. Schematic diagram of a possible approach to measure contact flash temperature by thermoelectric potential

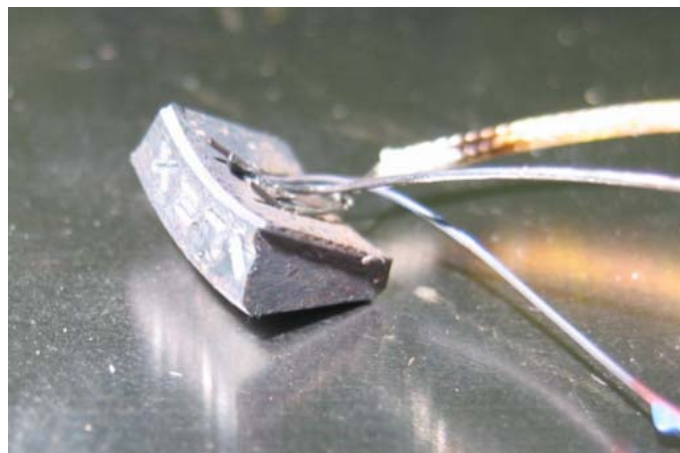


Figure 6. Picture of two dissimilar metal contact pair for a proof of concept.

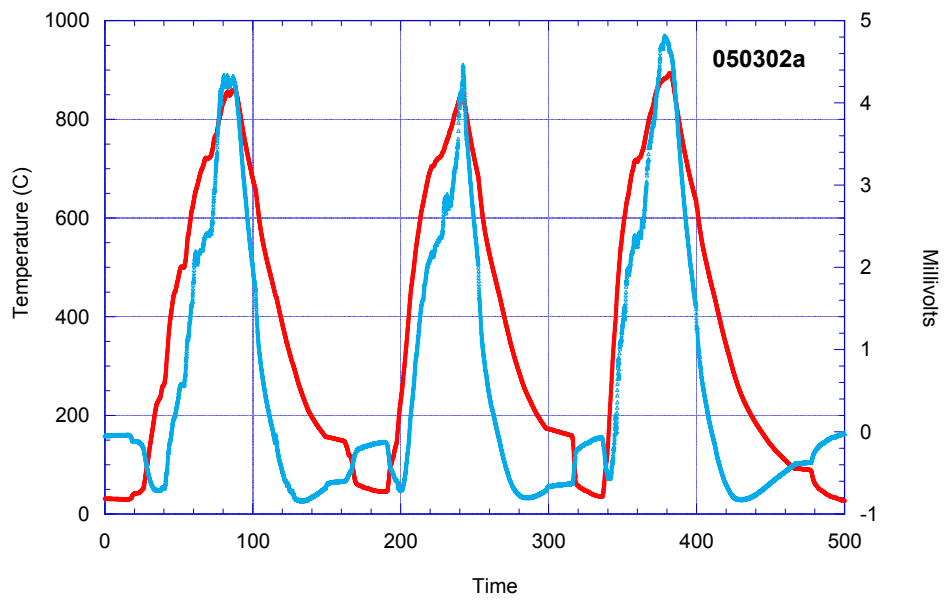


Figure 7. Graph from ramp heating test with the measured temperature (red) and millivolts output (blue)

B. Parasitic Energy Loss Mechanisms

Principal Investigators: George Fenske, Robert Erck, Ali Erdemir, and Layo Ajayi

Argonne National Laboratory

Argonne, IL 60439

(630) 252-5190, fax: (630) 252-4798, e-mail: gfenske@anl.gov

Technology Development Area Specialist: Lee Slezak

(202) 586-2335, fax: (202) 586-2476, e-mail: Lee.Slezak@hq.doe.gov

Field Project Manager: Jules Routbort

(630) 252-5065, fax: (630) 252-4798, e-mail: routbort@anl.gov

Participants

Robert Erck, Argonne National Laboratory

Layo Ajayi, Argonne National Laboratory

Ali Erdemir, Argonne National Laboratory

James Kezerle, Ricardo Engineering

Lee Oberto, Ricardo Engineering

Zoran Fillipe, University of Michigan

Contractor: Argonne National Laboratory

Contract No.: DE-AC02-06CH11357

Objective

- Develop and integrate mechanistic models of engine friction and wear to identify key sources of parasitic losses as functions of engine load, speed, and driving cycle.
- Develop advanced tribological systems (lubricants, surface metrology, and component materials/coatings) and model their impact on fuel efficiency with a goal to improve vehicle efficiency by 3% in FY12. Develop engine component maps to model the impact on fuel efficiency for use in analytical system toolkits.
- Develop database of friction and wear properties required for mechanistic friction and wear models –coatings, lubricant additives, and engineered surface textures.
- Validate mechanistic models by performing instrumented, fired-engine tests with single- and cylinder engines to confirm system approaches to reduce friction and wear of key components.
- Integrate models into vehicle system codes (PSAT).

Approach

- Predict fuel economy improvements over a wide range of oil viscosities using physics-based models of asperity and viscous losses.
- Model changes in contact severity loads on critical components that occur with low-viscosity lubricants.
- Develop and integrate advanced low-friction surface treatments (e.g., coatings, surface texturing, and additives) into tribological systems.
- Measure friction and wear improvements on advanced lab rigs and fired engines to confirm model calculations.
- Develop component maps of parasitic energy losses for heavy-vehicle system models.

Accomplishments

- Modeled the impact of low-friction coatings and low-viscosity lubricants on fuel savings (up to 4%) and predicted the impact of low-viscosity lubricants on the wear/durability of critical engine components.
- Developed experimental protocols to evaluate the friction and wear performance of advanced engine materials, coatings, and surface treatments under prototypical/piston/ring/environments.
- Initiated lab testing of surface modified ring and liner components to optimize treatments for single-cylinder engine tests.

Future Direction

- Apply superhard and low-friction coatings on actual engine components and demonstrate their usefulness in low-viscosity oils.
- Optimize coating composition, surface finish, thickness, and adhesion to achieve maximum fuel savings.
- Evaluate the impact of advanced lubricant additives on asperity friction.

Introduction

Friction, wear, and lubrication affect energy efficiency, durability, and environmental soundness of critical transportation systems, including diesel engines. Total frictional losses in a typical diesel engine may alone account for more than 10% of the total fuel energy (depending on the engine size, driving condition, etc.). The amount of emissions produced by these engines is related to the fuel economy of that engine. In general, the higher the fuel economy, the lower the emissions. Higher fuel economy and lower emissions in future diesel engines may be achieved by the development and widespread use of novel materials, lubricants, and coatings. For example, with increased use of lower viscosity oils (that also contain lower amounts of sulfur- and phosphorus-bearing additives) the fuel economy and environmental soundness of future engine systems can be dramatically improved. Furthermore, with the development and increased use of smart surface engineering and coating technologies, even higher fuel economy and better environmental soundness will be feasible.

Integration of advanced lubricant chemistries, textured/superfinished surfaces, and advanced component materials and coatings necessitates a systems approach. Changes in one system component can readily change the performance of other system components. For example, application of a hard coating on a liner to improve its durability may decrease the durability of the mating rings.

Also, lowering the viscous drag will cause certain components (e.g., bearings) to operate under boundary lubrication regimes not previously encountered, resulting in accelerated degradation. A systems approach is required to not only identify what are the critical components to address in terms of energy savings, but also to identify potential pitfalls and solutions.

The main goal of this project is to develop a suite of software packages that can predict the impact of smart surface engineering technologies (e.g., laser dimpling, near frictionless carbon, and superhard coatings) and energy-conserving lubricant additives on parasitic energy losses from diesel engine components. The project also aims to validate the predictions by comparison with experimental friction and wear data from Argonne National Laboratory. Such information will help identify critical engine components that can benefit the most from the use of novel surface technologies, especially when low-viscosity engine oils are used to maximize the fuel economy of these engines by reducing churning and/or hydrodynamic losses. A longer-term objective is to develop a suite of computer codes capable of predicting the lifetime/durability of critical components exposed to low-viscosity lubricants.

Since FY 2003, Argonne and Ricardo, Inc., have collaborated to identify engine components that can benefit from low-friction coatings and/or surface treatments. The specific components considered included rings, piston skirt, piston pin bearings,

crankshaft main and connecting rod bearings, and cam bearings. Using computer codes, Ricardo quantified the impact of low-viscosity engine oils on fuel economy. Ricardo also identified conditions that can result in direct metal-to-metal contacts, which, in turn, can accelerate engine wear and asperity friction. Efforts were also initiated to identify approaches to validate the predictions under fired conditions.

Argonne also worked on the development and testing of low-friction coatings under a wide range of sliding conditions using low- and high-viscosity engine oils. These coatings (such as near frictionless carbon) as well as laser-textured surfaces were subjected to extensive friction tests using bench-top rigs. The test conditions (i.e., speeds, loads, and temperatures) were selected to create conditions where direct metal-to-metal contacts will prevail, as well as situations where mixed or hydrodynamic regimes will dominate. Using frictional data generated by Argonne, Ricardo estimated the extent of potential energy savings in diesel engines and identified those components that can benefit the most from such low-friction coatings and/or surface treatments. Argonne developed a test rig to simulate engine conditions for piston rings sliding against cylinder liners – one of the major sources of parasitic energy losses identified in Ricardo's studies. Wear data generated by Argonne can be used to develop models and computer codes that predict the lifetime/durability of diesel engine components. Several techniques were surveyed to validate the models. A fired, single-cylinder, fixed-sleeve technique available at the University of Michigan was selected to provide in-situ friction force measurements between the cylinder liner and the piston/piston ring assembly – a major source of friction losses. Efforts also progressed on the development of a benchtop ring-on-liner rig for testing in the tribological conditions under which advanced surface treatments and additives optimally function.

During FY 2006, Ricardo and the University of Michigan completed design of the single-cylinder test bed and initiated fabrication of components necessary to measure combustion chamber friction forces under fired conditions. In addition, Argonne initiated benchtop tests on experimental and commercial-engine lubricant additives.

Results

Phase I and Phase II activities for this project focused on modeling the impact of low-friction surfaces and low-viscosity engine lubricants on friction losses and fuel economy. Figure 1 [1] summarizes the results of Ricardo's calculations on the impact of boundary friction and engine lubricant viscosity on the fuel economy of a heavy-duty diesel-powered vehicle. These curves are based on detailed calculations of the friction mean effective pressure (FMEP) for the piston rings and skirt, valve-train components, and engine bearings under a range of driving conditions. The results predicted fuel savings up to 4-5%, depending on lubricant viscosity grade and asperity friction.

Plans were established for a Phase III activity to validate the calculations using measurements with a fired diesel engine. Several approaches were considered, including a) direct fuel consumption measurements in a running, mass-production, diesel engine, b) friction force measurements in a running, mass-produced engine, and c) friction force measurements in a running, single-cylinder test engine. The last approach was selected due to considerations of simplicity and ability to accurately measure friction forces.

Three different methods were considered to measure forces during operation. A force-difference method based on cylinder-pressure and connecting-rod strain measurements and a floating liner method based on load cell measurements of liner forces were ruled out due to large statistical errors associated with the first method and gas leakage and structural vibration issues associated with the second method. In the end, a fixed-sleeve method (Figure 2) was chosen. The fixed-sleeve method employs strain gauges applied to a rigidly supported cylinder liner to measure the friction forces transmitted to the cylinder liner from the piston skirt and rings.

The fixed-sleeve method will be used with a Ricardo Hydra test engine installed at the University of Michigan. To this end, a sliding sleeve will be inserted inside a modified Hydra cylinder liner. The sleeve will be fixed radially near its top by a supporting wire and will be restrained axially by a locknut at its bottom. Axial forces on the sleeve will be transmitted through the locknut joint to the liner.

Friction forces will be calculated from the measured liner strain.

The contract with Ricardo and the University of Michigan has been established, and Phase III activities are underway. The first task of Phase III involves adapting the Hydra engine to accept an instrumented fixed sleeve (strain gauges and thermocouples). Figure 3 shows a photograph of the Hydra engine mounted on the Cussons-dyno test stand at the University of Michigan. Current activities for this task are focused on design, fabrication, and instrumentation of combustion chamber components (in collaboration with Ricardo and Mahle). The second task will involve establishing a baseline to compare the engine to obtain friction measurements at different engine conditions (speeds and loads) and lubricant viscosities. Part of this task will involve in-situ friction measurements of unformulated basefluids (at two viscosities) with and without low-friction additives. Subsequent tasks will concentrate on measurements using low-friction technologies (e.g., low friction coatings, superfinishing, textured surfaces, and low-friction additives).

Experimental activities at Argonne concentrated on the development of a ring-on-liner rig to measure friction in an effort to confirm/validate asperity friction values used in the Ricardo models, to measure the boundary friction of advanced low-friction technologies on prototype ring and liner components, and to integrate/optimize advanced technologies for rings, liners, and pistons. The test system uses segments of rings and liners obtained from standard rings and liners, currently 137-mm and 145-mm diameter liners – comparable to those modeled by Ricardo. The system is capable of applying loads up to 2000 N, speeds up to 10 Hz, strokes up to 37 mm, and temperatures to 300°C. Data recorded during the tests include friction forces, temperature, ring position, and contact resistance (between the ring and liner) at rates in excess of 2000 Hz. High data acquisition rates (above 2000 Hz) are used to obtain “flash shots” of the friction, position, and contact resistance during each stroke. Such information provides detailed data required to determine which lubrication regime (boundary, mixed, or hydrodynamic) is dominant during the stroke.

Figure 4 shows the friction as a function of time for a stock CrN-coated ring sliding against a stock liner with a commercial, formulated 10W-30 synthetic lubricant (top) and a concentrated commercial additive package (bottom). The tests in Figure 4 were performed with a load of 150 N at a reciprocating speed, 15 rpm, sufficiently low to ensure boundary lubrication over the entire travel or the baseline lubricant (top curve). At the point of stroke reversal where the speed is near zero with the baseline fluid, boundary lubrication is dominant with a friction coefficient around 0.12 to 0.15. As the velocity increased (near midstroke), the friction of the top curve remained high, indicating that the lubrication was dominated by boundary friction. The bottom curve in Figure 4 shows a significantly lower friction behavior than that of the baseline fluid – at reversal, the friction is around 0.09, but then rapidly decreases to around 0.05. The difference can be attributed to the high viscosity of the additive package (bottom curve). The high viscosity resulted in a rapid transition to mixed/hydrodynamic lubrication, thus providing lower friction. Overall, the friction was reduced by approximately 60%. At higher speeds (150 rpm), the friction was also reduced by 60% [2].

Other Phase III activities involve cost/benefit studies of treating specific engine components. Figure 5 shows cost/benefit analysis based on the Ricardo models. Fuel savings on the order of 100 gallons per 1000 hours of operation can be realized by using technologies (e.g., a low friction coating, low-friction additive, or surface texturing) that reduce boundary friction by 90% and a low-viscosity (e.g., SAE 20 wt) engine lubricant. At a price of \$3/gallon, one would realize a cost savings of \$300 per 1000 hours of operation, which should more than offset the cost of many low-friction coating treatments.

Summary

Computer simulation of parasitic energy losses in diesel engines indicate that fuel savings up to 5% can be achieved through the use of low-viscosity engine lubricants and low-friction surface treatments. Work is underway to experimentally validate the models by tests with a fired, single-cylinder diesel rig outfitted with an instrumented fixed-sleeve to measure the friction forces continuously as a function of crank angle.

A rig-on-liner test rig was developed and brought on-line to validate the friction coefficient data used to model the parasitic friction losses, as well as to optimize advanced surface modification technologies for engine applications. Tests are underway to evaluate two technologies: a boric-acid based lubricant additive and a surface texturing technique. Both technologies, in addition to the use of low-friction coatings, will be further examined and optimized in preparation for fired engine tests on the instrumented Hydra test engine in FY08.

Cost/benefit analysis indicated a saving at about \$300 per 1000 hours of operation with advanced tribological systems.

References

1. Fox, I., Numerical Evaluation of the Potential for Fuel Economy Improvement due to Boundary Friction Reduction within Heavy-Duty Diesel Engines, ECI International Conf. on Boundary Layer Lubrication, Copper Mountain, CO, Aug. 2003.
2. George Fenske, Parasitic Energy Loss Mechanisms: Impact on Vehicle System Efficiency, 2006 U.S. Department of Energy Heavy Vehicle Systems Review, April 18-20, 2006, Argonne National Laboratory, Argonne, Illinois.

Acknowledgements

Argonne is managed by U Chicago Argonne, LLC, for the U.S. Department of Energy under contract DE-AC02-06CH11357.

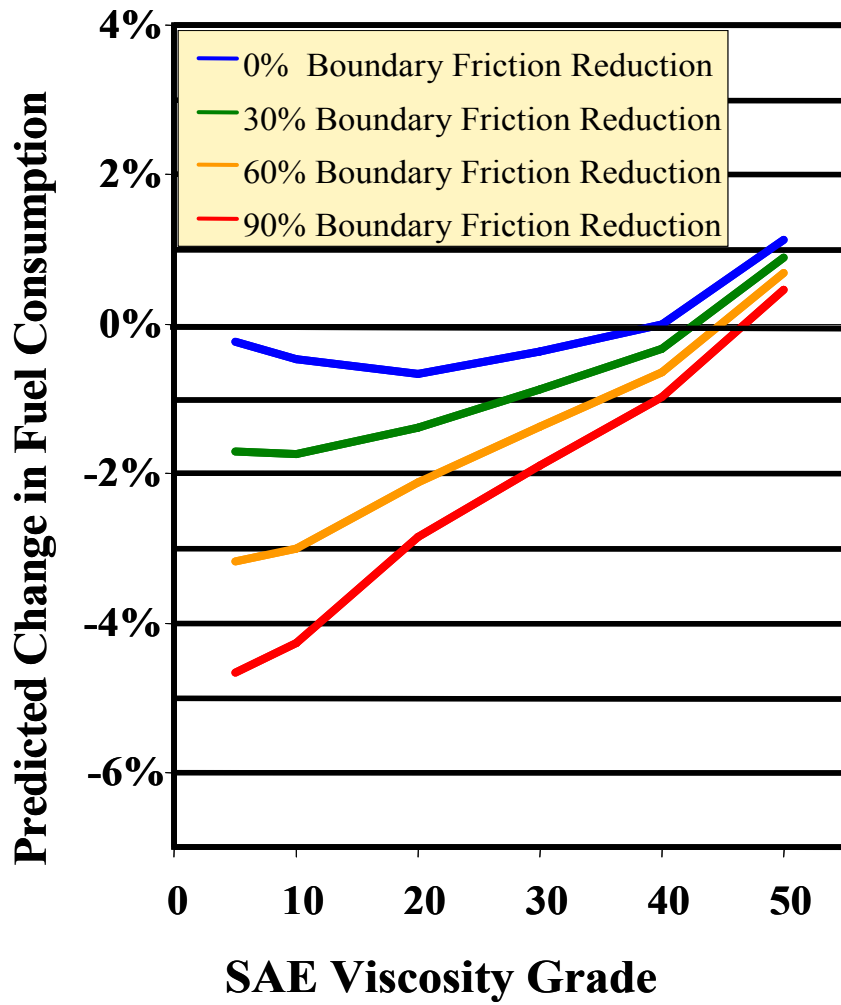


Figure 1. Predicted Change in Fuel Economy as a Function of Engine Lubricant Viscosity and Boundary Friction

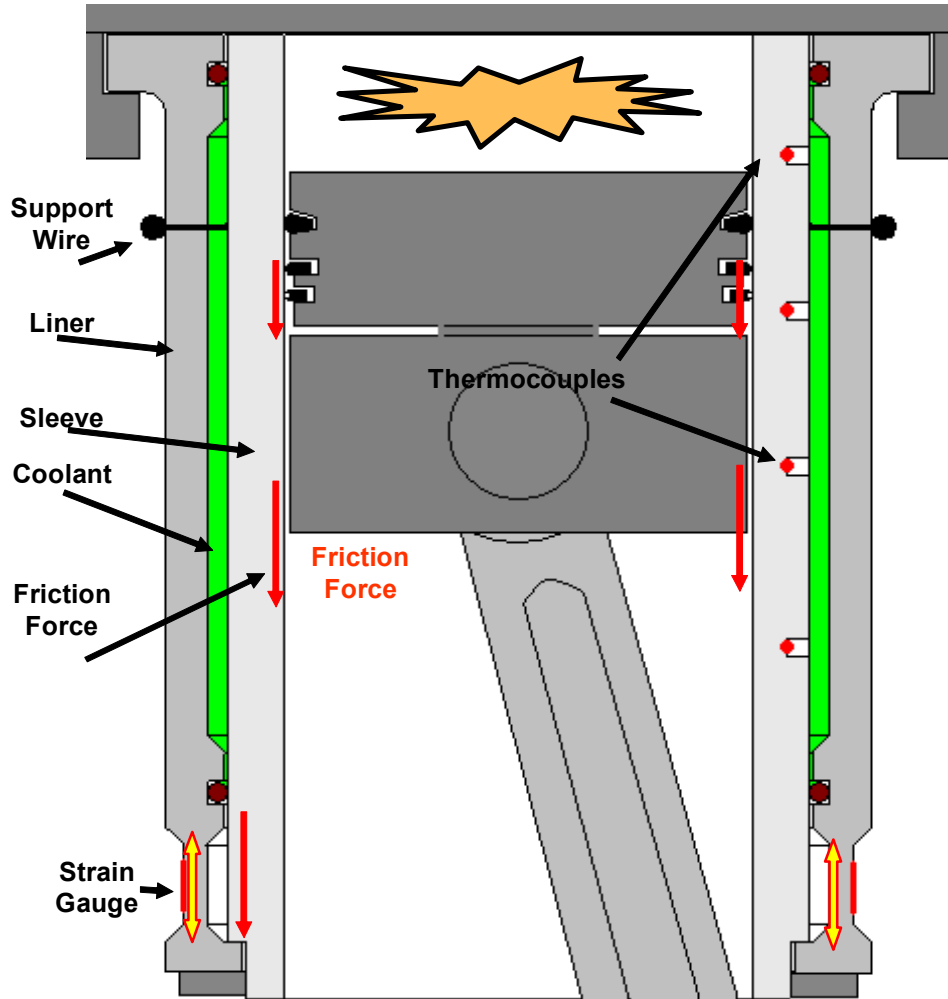


Figure 2. Schematic of Fixed-Sleeve Method. This method will be used to continuously monitor friction forces during fired operation of a single-cylinder diesel engine.

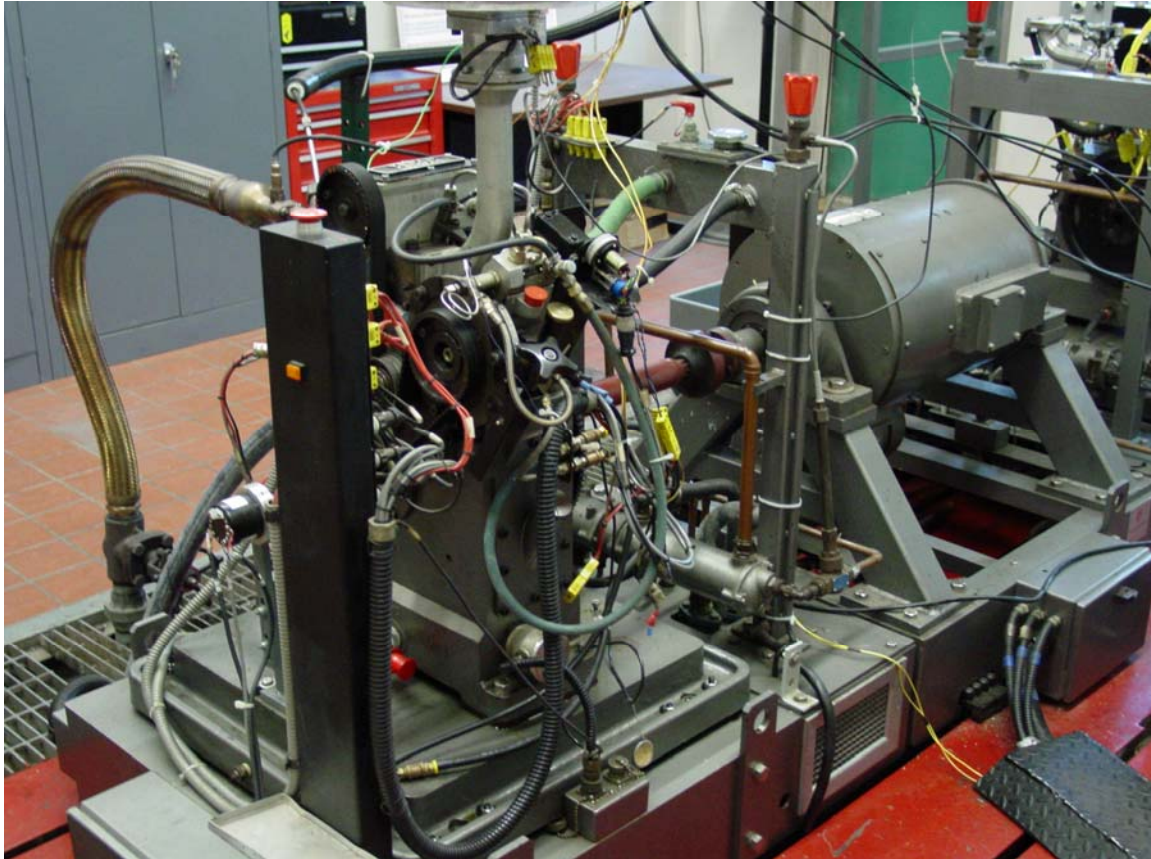


Figure 3. Photograph of the Ricardo Hydra Engine Under Modification for In-Situ Friction Measurements (University of Michigan)

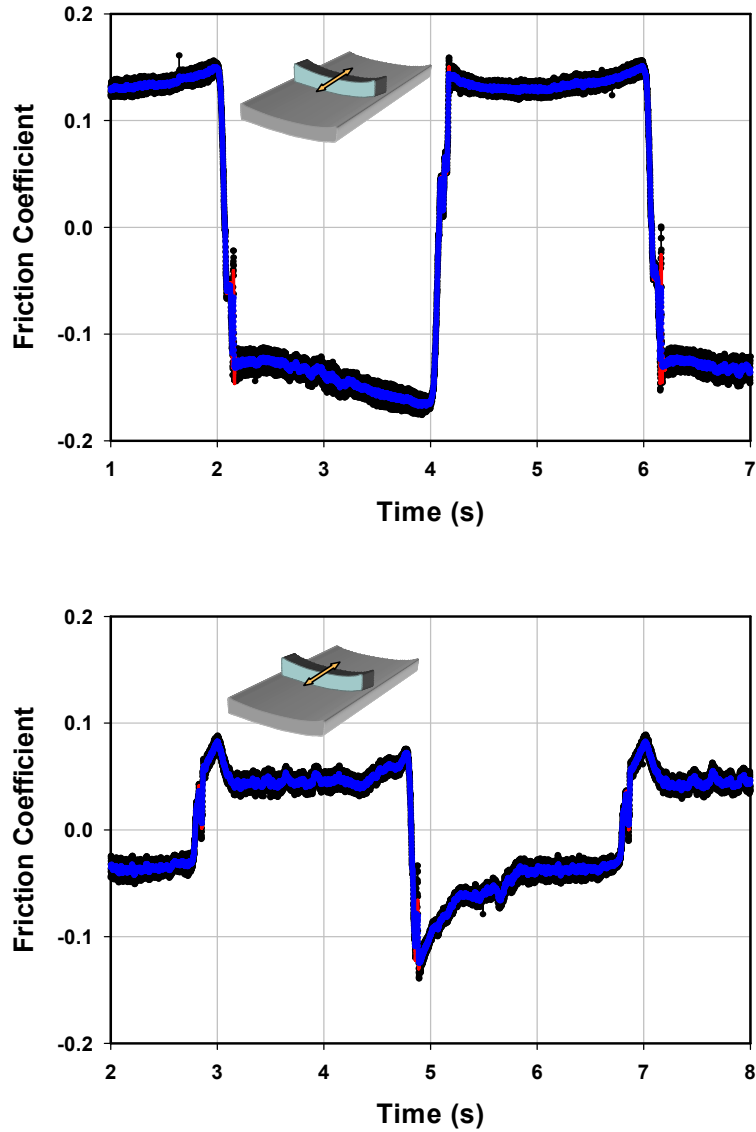


Figure 4. Friction as a Function of Time Obtained from High-Speed Ring-on-Liner Lab Tests (15 rpm, 150 N Load): Top - Baseline - Formulated 10W-30 Synthetic, Bottom - Commercial Low-Friction Additive.

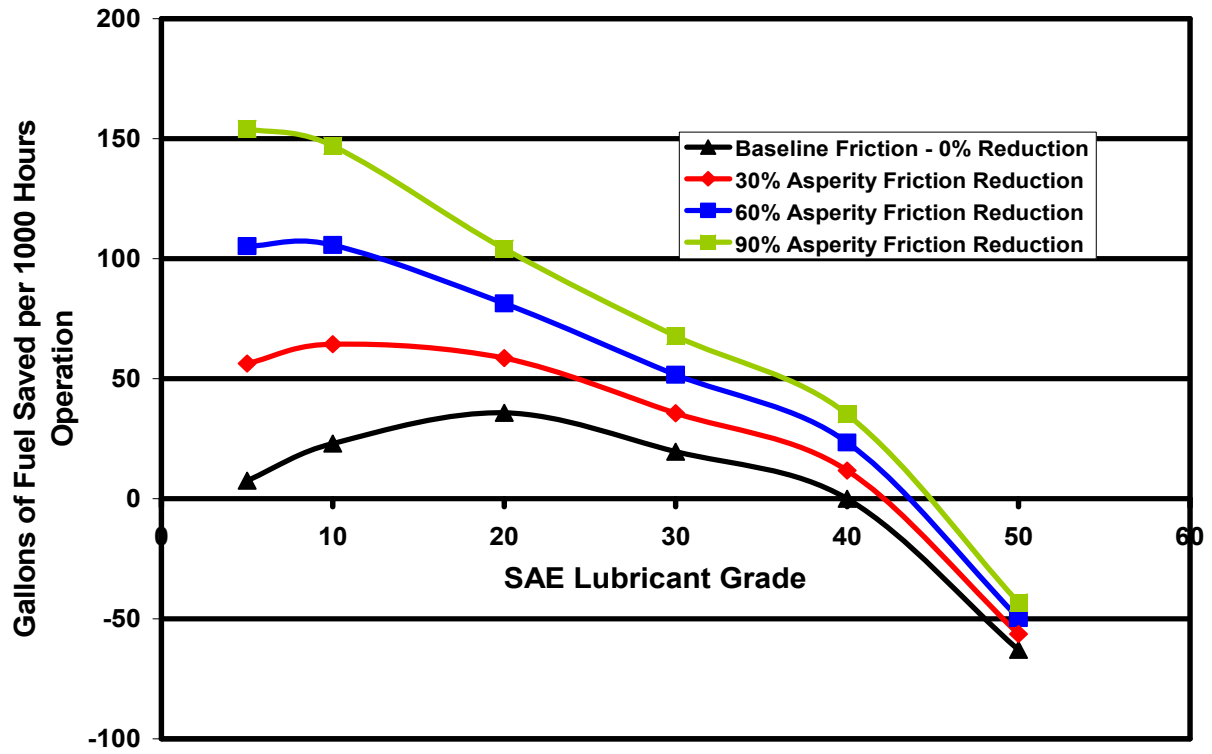


Figure 5. Fuel Saved by Reducing Boundary Friction of Piston Skirts as a Function of Lubricant Viscosity

C. Efficiency Improvement Through Reduction of Friction and Wear in Powertrain Systems

Principal Investigator: Michael L. Killian
Eaton Corporation
Innovation Center
26201 Northwestern Highway
Southfield, MI 48037
(248) 226-1766; fax (248) 226-7166; e-mail :mikelkillian@eaton.com

DOE Project Officer: John Jason Conley
National Energy Technology Laboratory
Morgantown, WV 26507-0880
(304) 285-2023; fax (304) 285-4403; e-mail: John.Conley@netl.doe.gov

DOE Technology Development Area Specialist: Lee A. Slezak
Office of Vehicle Technologies
U.S. Department of Energy
1000 Independence Ave., S.W.
Washington, D.C.
(202) 586-2335; fax (202) 586-2476; email: lee.slezak@ee.doe.gov

Field Technical Manager: Jules L. Routbort
(630) 252-5065; fax: (630) 252-4289; e-mail: jules.routbort@anl.gov

Participants
Jian Zhang, Diann Hua, Tom Beveridge, Caterpillar Inc.
Oyelayo Ajayi, George Fenske, Ali Erdemir, Jeff Hershberger, Argonne National Laboratory
Jane Wang, Leon Keer, Northwestern University
Dong Zhu, Alaa Elmoursi, Eaton Corporation, Innovation Center

Contractor: Eaton Corporation, 4201 North 27th Street, Milwaukee WI 53216
Contract No.: DE-FC26-04NT42263

Objective

- To reduce friction and parasitic energy loss by 30-50% in transmissions and axles used in class 3-8 trucks without compromising performance or durability is the objective of this project.
- During the first three (3) years, develop computer simulation tools for various contact geometries to predict friction, interface temperatures, wear, and other performance parameters for gears, bearings, seals, and oil churning losses. These simulation tools will be calibrated and validated utilizing coupon fixture testing and component bench testing.
- During the following two (2) years, integrate the various simulation tools into a design procedure and prove its utility by designing specific components for transmissions and axles and conducting limited testing on dynamometers and vehicles.
- Identify commercialization strategies for efficiency improvement methods in transmissions and axles.

Approach

- Reduction of boundary friction through development of boundary film technologies, which involves low friction materials, coatings and lubricant additives.
- Reduction of hydrodynamic friction and churning loss via advanced lubrication technologies, improved system design, lubricant properties and surface texturing.
- Optimization of design parameters, operating conditions and surface finish processes to minimize the severity of surface contact and to maximize hydrodynamic lubrication effectiveness through next-generation integrated design and analysis tools.
- Bench tests and dynamometer tests to investigate benefits from technical elements of the implementation strategy.
- Development of surface failure analysis and prediction tools and their correlation with experimental data to improve the component design for longer life and higher reliability.

Accomplishments

- Preliminary implementation strategies were prepared by Eaton and Caterpillar. Technical elements in the strategies to be addressed include churning, lubricants, surface roughness, coatings and surface textures.
- Initial dynamometer tests reveal that the dry sump (reduced fill) approach provides 40 to 55 percent reduction in parasitic loss. The dry sump reduces churning. Low viscosity lubricants also reduce churning.
- Eaton introduced a new transmission fluid, SAE 50 Revision 7 into the market in August 2006. The commercial release resulted in an immediate reduction in friction in user fleet transmissions. The reduction in friction coefficient, compared to a leading commercial fluid, exceeds 40 percent.
- Caterpillar and Eaton have demonstrated that further reductions in the friction coefficients of powertrain lubricants are possible. Experimental lubricants yielded friction coefficients 25 to 42 percent lower than Eaton's new Revision 7 lubricant.
- The integrated friction and wear model with surface evolution has been used to predict friction coefficients for specific cases of surface roughness and lubricant. A hobbed and shaved spur gear set lubricated with mineral oil was compared to a super finished gear set lubricated with synthetic oil containing friction modifier. The model predicted a 40 percent reduction in friction coefficient with the "super finish-synthetic oil" combination.

Future Direction

- Conduct bench tests and dynamometer tests to optimize lubricants for lowest friction coefficient, reduced churning loss and superior wear resistance.
 - Optimize dry sump design for minimal parasitic loss due to churning.
 - Develop gear coating that (a) provides very low friction when used with specific low friction lubricants and that (b) exhibits extreme durability.
 - Exploit the integrated design modules to predict friction coefficients and wear amounts for specific combinations of technical elements in the implementation strategies.
 - Prepare and dynamometer test transmission and axle prototypes incorporating optimized technical elements of the implementation strategies.
-

Introduction

This report is a third annual report on the project. Technical progress is reported under specific headings that correspond to the deliverables for Year 3, Budget Period 2. Project focus has shifted from modeling and analysis to strategies for implementation.

Implementation Strategies

A strategy for implementing efficiency improvements on heavy duty truck transmissions and axles has been formulated. The strategy identifies specific technical factors that can reduce friction and parasitic losses and, in turn, that can be exploited to reduce the US consumption of petroleum by trucks. Among the technical factors are the following:

1. Churning
2. Lubrication
3. Surface roughness
4. Coatings
5. Textures

The order in which the factors are presented, implying their relative importance, may be the subject of debate, but the items on the list remain firm. Previous work under this program identified a realistic target for fuel economy gains from the reduction of friction and parasitic losses in driveline components. The target is 2 to 4 percent more miles per gallons. Attainment of this goal requires reducing friction and parasitic losses in the driveline by 30 to 50 percent.

It should be remembered that the implementation strategy was formulated for heavy duty trucks. However, the approaches described also have applicability to light duty vehicles and to passenger vehicles.

Bench Test Results

Lubricants

An implementation of the lubricant strategy materialized in August 2006 with the commercial introduction of a new Eaton transmission fluid, SAE 50 Revision 7. The commercial release of this product, phasing out the former CD50 Revision 6 fluid, resulted in an immediate reduction in friction in user fleet transmissions. Figure 1 presents results from Falex four-ball testing of Roadranger Revision 7 lubricant along with another commercially available product Mobil SHC 50. Two

friction coefficients are shown for Mobil SHC 50, 0.119 and 0.123. Under similar test conditions Roadranger Revision 7 oil yields a friction coefficient of 0.066. The reduction in friction coefficient, one commercial transmission fluid compared to another, exceeds 40 percent.

While the reduction in friction is significant, this gain in efficiency would be an empty improvement if it was accompanied by increased wear. Fortunately, Roadranger Revision 7 reduces friction and produces a corresponding 30 percent decrease in wear compared to Mobil SHC 50.

An alternative path to friction reduction with transmission lubricants also was pursued. New formulations were evaluated by Falex four-ball testing. A commercial polyalphaolefin (PAO) base oil was selected. Adding a friction modifier and various anti-wear additives to the PAO base stock produced fluids that displayed significantly reduced friction and reduced wear even compared to the Eaton SAE 50 Revision 7 oil baseline, Figure 2. A friction coefficient of 0.038 was obtained, representing a 42 percent improvement. With this lubricant there was a corresponding 25 percent reduction in wear.

Churning

Churning is the turbulent circulation of oil in contact with rotating components in the transmission. Churning results from an excessive quantity of oil dragging against the surfaces of fast moving components. Sump design, lubricant foaming and viscosity also influence churning. To minimize churning loss, oil must be delivered precisely to the frictional contact interfaces in a quantity just sufficient to prevent wear. Establishing the optimal sump fill level and applying auxiliary spray tubes and lubricant injectors (some are electronic) are keys to minimizing churning loss.

The simplest approach to reduce churning is to reduce the sump fill level from the "full fill" level to a "reduced fill" level of 20 to 50 percent of the full fill level. This reduced fill method is referred to commonly as the "Dry Sump" concept.

The difficulty with the reduced fill or dry sump concept is the risk of damaging the gears,

bearings, bushings, shafts and other components under severe conditions of high loads, high torque and high environmental temperatures. If gears are starved for lubrication under severe operating conditions, the results are scoring, scuffing, micro-pitting, spalling, pitting, galling and wear. These undesired consequences lead to premature failure of transmission components.

Caterpillar measured the parasitic torque for four oils and two sump levels. Tests were conducted at 30 degrees C (86 degrees F) and at 90 degrees C (194 degrees F). The lower temperature simulated start-up or cold weather operation, while the higher temperature represented a typical operating condition.

Oil additives, Figure 3, seem to have little impact but viscosity seems to be a key in determining the churning loss at low temperature. Oil #20 having the highest viscosity (338 cSt @ 40 degrees C) exhibits the greatest parasitic torque for both sump configurations. Oils # 1, #11 and #18, with 40 degrees C viscosities ranging only from 183 to 215 cSt, clustered together for both full sump and dry sump conditions.

The dry sump system clearly shows reduced parasitic loss compared to the full sump (centerline fill). For high viscosity Oil #20, the reduction in parasitic torque due to the dry sump exceeds 30 percent (at 2000 and 3000 rpm). For lowest viscosity Oil #11, the reduction in parasitic torque approaches 35 percent. If a full sump with Oil #20, 338 cSt, is compared to a dry sump with Oil #11, 183 cSt, at a speed of 2000 rpm, the reduction in parasitic loss approaches 45 percent.

A higher temperature of 90 degrees C (194 degrees F) is investigated in Figure 4. Dry sump data clearly separates from the full sump (centerline fill) data. Separation by viscosity also is apparent. High viscosity lubricant gives high churning loss for each sump configuration.

At the increased temperature, the full sump (centerline fill) parasitic torque is much higher than the dry sump. For a speed about 2000 rpm, the dry sump used with Baseline Oil #18 (19 cSt viscosity at 100 degrees C) exhibits over 47 percent reduction in parasitic loss compared to the full sump. For the higher speeds of many off-highway applications, the benefit of dry sump is even greater, 55% at 3330 rpm.

Coatings

The following challenges have been identified when PVD (physical vapor deposition) processing is used for coating gears:

Gear geometry

The tip of a gear tooth, in comparison to the root, is a high electric field concentrator. As a result during RF etching and coating deposition, the charged species are attracted more to the tip than to the root. This has two major side effects:

1. RF etching becomes ineffective at the root
2. Non-uniform coating thickness from the tip to the root of the gear tooth.

Limited temperature processing due to substrate

Most commonly used transmission gear materials are the 4100 and 4300 carbon steels. These are typically carburized and tempered at 150 - 170°C. This sets a limitation to PVD processing since the best adhesion results are achieved at processing temperatures around 350 – 500°C. For coating gears, we are limited by not being able to exceed 150°C.

Surface finish

The best adhesion of PVD coating is achieved on smooth surfaces with surface roughness below 0.05 μm (2 μinch). The different finishes used today in transmission gears are: a) Hobbed and shaved attaining surface roughness of 45 μinch , b) CBN ground yields surface roughness of 22 μinch and c) Honing yields 15 μinch surface roughness. There is a current trend in the industry to adopt super finishes (isotropic finish) 2-4 μinch . As this occurs, surface finish may no longer be a limitation to implementing PVD coating on transmission gears.

Cost

Because of the large surface area of transmission gears and over all size of the gears, the numbers of gears processed per batch may be at best a few hundred, thus making the cost on the order of several tens of dollars per gear. This is probably the biggest challenge at this stage. However, a new trend in PVD processing is attempting to transition from batch processing to continuous feed.

Surface Design Model and Benefit Evaluation

Surface finishing processes, such as turning, milling, shaving, grinding, honing, lapping, polishing and dimpling, generate surfaces with 3-Dimensional topography of specific textures. For critical components, questions arise concerning the optimal topography/texture for the specific application. Unfortunately, no finishing process is universally good.

Surfaces usually are selected by trial and error.

To overcome this difficulty, a simulation-based procedure called “virtual texturing” has been developed. With this procedure, one can use either digitized real engineering surfaces or computer generated textures as input data for contact and lubrication analysis in order to predict the tribological performance and life.

One example for surface parameter optimization is given in Figure 5. During machining, it is better to make the machining tracks perpendicular to the motion direction for line contact applications such as gears and roller bearings.

This “Virtual Texturing” procedure is based on advanced mixed lubrication models and virtual surface generation as well as real surface digitization. With this procedure, “trial-and-error” will be minimized and surface design optimization computerized.

Advanced Wear Model with Surface Evolution

Sliding wear is one of the most important surface failure modes for powertrain components, such as gears, bearings, engine parts and seals, etc. Due to the difficulties in predicting “contact severity” in mixed lubrication, where most components operate, wear model development in the past has not been accepted readily. Available empirical formulae appear to be too simple, failing to reflect the true complexity of wear phenomena and often not giving an accurate prediction.

Based on the mixed lubrication model recently developed at Eaton, a deterministic simulation model has been developed. A numerical solution for the lubricated interface without consideration of wear is obtained as an initial value for the solution with wear. Based on an assumed or experimentally estimated wear coefficient, one can virtually remove material gradually and repeatedly from local spots where contact pressure exceeds the yielding limit, following the Archard Law. Surface topography is consequently changed gradually,

and the updated surface profile will be used for the solution at the next time step. The wear coefficient can be adjusted, if necessary, based on comparison to performance tests.

Modeling Friction in Gears

Modeling friction in gears is a complicated task, involving complex gear geometry, dynamically changed contact and lubrication conditions and effects of surface roughness and topography.

By integrating the mixed lubrication results into modified Helical Gear Code package, friction variation along each line of action has been calculated for sample gear sets, Figure 6. Note that at pitch position there is a minimal sliding so that the friction is close to zero. With the hobbed and shaved process and mineral oil without friction modifier, the maximum friction between gear teeth is about 0.092 for this spur gear set, while with polished surfaces and synthetic oil plus friction modifier, the maximum friction is reduced down to about 0.054, showing 40% reduction.

Summary

Results from bench tests, dynamometer tests and modeling have enabled an initial vision of the efficient powertrain assembly, whether a transmission or an axle. In terms of the technical elements of the implementations strategies, the efficient powertrain assembly includes a dry sump with precision oil injection to the gear mesh and to bearings. The lubricant for the efficient powertrain is low viscosity synthetic oil, heavily dosed with friction modifiers and anti-wear additives. Contact surfaces including gear teeth and rotating elements are super finished. Coatings applied to super finished surfaces have the potential to reduce friction and to reduce operating temperature. Durability remains an issue requiring further development and testing.

Conclusions

1. To reduce friction and parasitic loss in truck powertrain assemblies, the technical elements of greatest significance are churning, lubricant, surface roughness, coatings and surface texture.

2. To reduce parasitic loss due to churning, the best approach is to use a dry sump (reduced fill) with oil injected on the gear mesh and bearings. A reduction in churning parasitic loss exceeding 50 percent is possible.
3. To reduce churning and to reduce friction in the gear mesh and bearings, the best approach is to use a low viscosity, synthetic oil that is heavily dosed with friction modifiers and anti-wear additives. A reduction in gear mesh and bearing friction exceeding 40 percent is possible.
4. Super finishing of gears lowers friction and should improve durability. Super finished surfaces minimize the amount of gear wear and reduce the amount of hard, metallic debris circulated through the gear mesh.
5. Super finished surfaces are a precursor for coatings.
6. Liu, Y., Wang, Q., Hu, Y., Wang, W., and Zhu, D., "Effects of Differential Schemes and Mesh Density on EHL Film Thickness in Point Contacts," *Journal of Tribology*.
7. He, B., Chen, W., and Wang, Q., "Friction and Wettability of A Micro-Textured Elastomer: Poly(dimethylsiloxane) (PDMS)," *Tribology Letters*.
8. Xiong, S., Wang, Q., Lin, C., Liu, W., Zhu, D., "A Local Enrichment Approach for Texturing Journal-Bearing Surfaces," *Journal of Tribology*.
9. Liu, Y., Zhang, Y., Zhu, D., and Wang, Q., "EHL Experimental Techniques and Experimental-Numerical Result Comparisons," *J. of Tribology Presentations*

Publications

Publications and submissions for publications, and presentations, partially funded by this project, are identified below:

1. Bair, S., Liu, Y. and Q. Wang, "The Pressure-Viscosity Coefficient for Newtonian EHL Film Thickness with General Piezoviscous Response," *Journal of Tribology*.
2. F. Wang, L. M. Keer, and Q. J. Wang, "Analysis of 3D Elastic-Plastic Contact with Machined Rough Surfaces", submitted to *Journal of Tribology*
3. Liu, S., Chen, W.W, Hua, D., and Wang, Q., "Tribological Modeling: Application of Fast Fourier Transform," submitted to *Tribology International*.
4. Wang, F., Keer, L.M., and Wang, Q., "Analysis of 3D Elastic-Plastic Contacts with Machined Rough Surfaces," *Journal of Tribology*.
5. Martini, A., Velter, G., Keer, L.M., and Wang, Q., "Maximum Stress Prediction for Rough, Sinusoidal and Textured Surfaces," *Tribology Letters*.
5. D. Zhu, A. Martini, W. Wang, Y. Hu, B. Lisowsky, and Q. Wang, "Simulation of Sliding Wear in Mixed Lubrication," *ASME Journal of Tribology*, Vol.129, pp.544-552, 2007.
6. N., Ren, W., Chen, Y., Liu, D., Zhu, and Q., Wang, "A Three-Dimensional Deterministic Model for Rough Surface Line Contact EHL Problems," submitted to *ASME Journal of Tribology*.
7. A., Martini, D., Zhu, and Q., Wang, "Friction Reduction in Mixed Lubrication," to appear in *Tribology Letters*.
8. N., Ren, T., Nanbu, Y., Yasuda, D., Zhu, and Q., Wang, "Micro Textures in a Concentrated Contact Lubrication: Effect of Distribution Pattern," to appear in *Tribology Letters*, 2007.

Ann Arbor Testing & Development, Inc.				
FALEX FIXED 4-BALL TEST				
1200 rpm, 40 Kg load, 100 degrees C, 8.0 hours				
TEST NO.	LUBRICANT	FRICITION COEFFICIENT	WEAR SCAR DIAMETER	
		(average)	(mm)	
H142 Baseline	Eaton Roadranger SAE 50 Rev 7	0.066	0.44	COMMERCIAL (August 2006)
H143	R7L5	0.066	0.44	
H144	R7L6	0.066	0.43	
H145	R7L7	0.064	0.43	
H146	R7H7	0.079	0.45	
H147	R7H8	0.074	0.44	
C230	Mobil SHC 50 11/12/02	0.119	0.61	
H154	Mobil SHC 50	0.123	0.64	COMMERCIAL

High contact stress: >150,000 psi June 5, 2007

Figure 1. Falex four-ball test results for commercial and experimental oils.

TEST NUMBER	DESIGN CODE	LUBRICANT COMPOSITION	FRICITION COEFFICIENT	WEAR SCAR DIAMETER
				(mm)
H142	RFN4	Roadranger SAE 50 Rev 7 Baseline	0.066	0.44
H154	RFN4	Mobil SHC 50 tested 5/25/07 -42%	0.123	0.64 25%
H204	RFY4	PAO + CK3D + RFF2 + RFY2 + H121	0.038	0.33

Figure 2. Falex four ball test data. Note the reduced friction coefficient and reduced wear of RFY4 oil compared to the already low values of Eaton Roadranger Revision 7 lubricant.

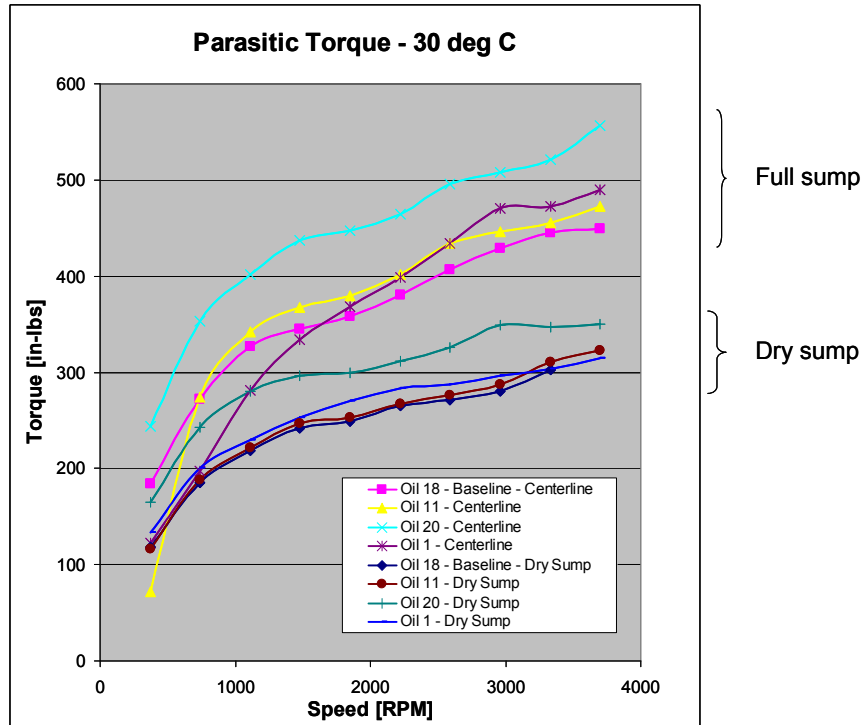


Figure 3. Parasitic torque for four Caterpillar oils tested at 30 degrees C (86 degrees F). For high viscosity Oil #20, the reduction in parasitic torque due to the dry sump exceeds 30 percent.

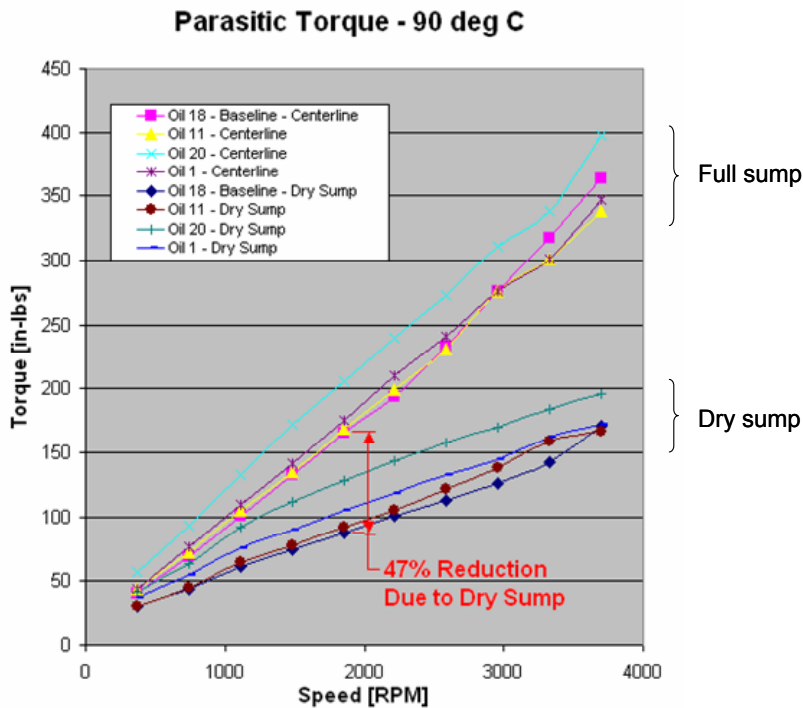


Figure 4. Dry sump data at 90 degrees C (194 degrees F). For Baseline Oil #18 run at 2000 rpm, the dry sump provides 47 percent reduction in parasitic loss.

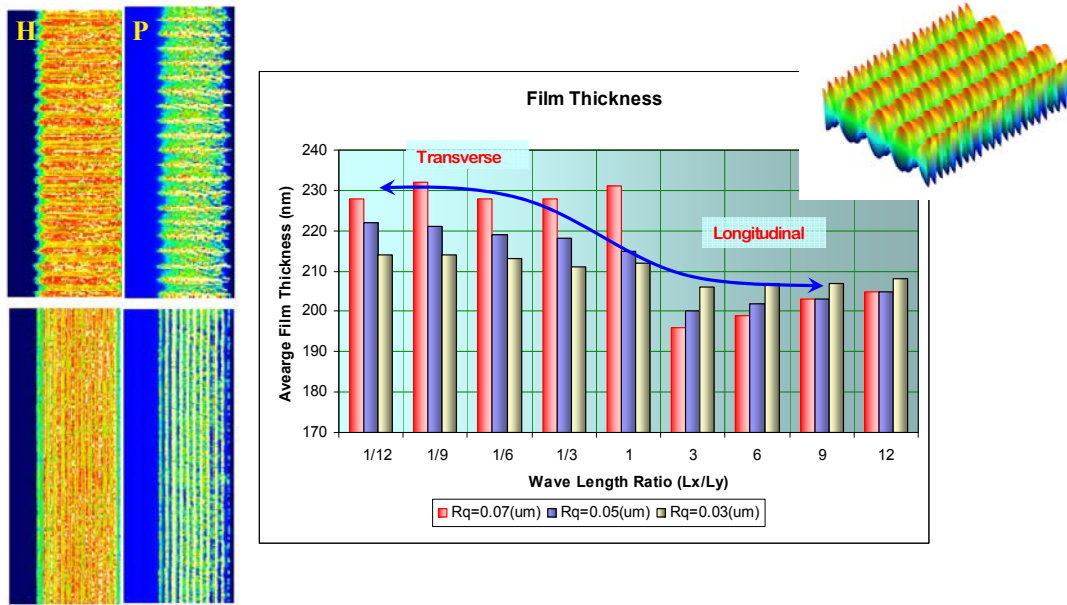


Figure 5. Sinusoidal wavy surfaces are generated by computer, and waviness in x- and y- directions as well as wave height are changed in order to study the topography effect on lubricant film thickness. Transverse roughness yields thicker EHL film than longitudinal in line contacts.

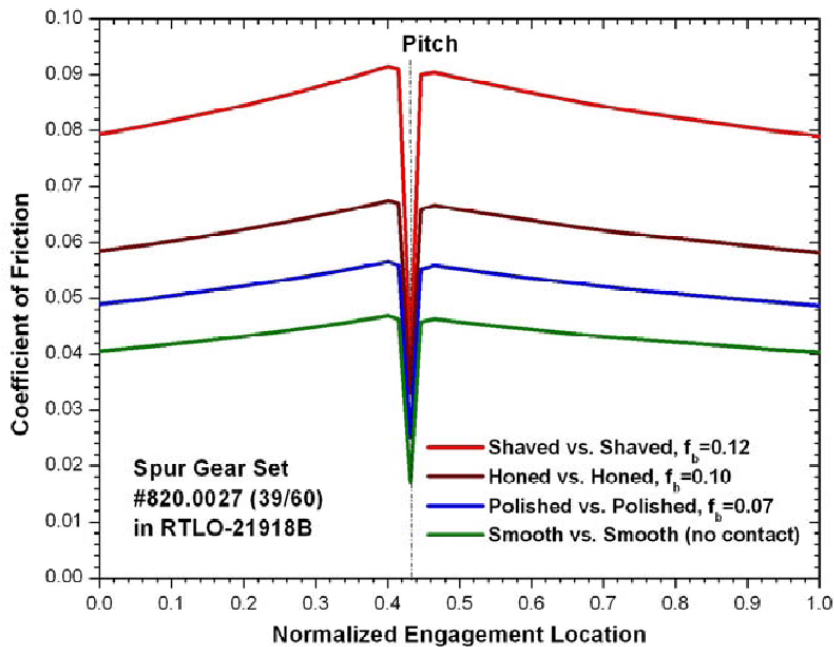


Figure 6. Maximum friction for hobbed and shaved gear teeth with mineral oil is about 0.092 for a spur gear set. For polished gear teeth with synthetic oil plus friction modifier, the maximum friction is reduced down to about 0.054, showing 40% reduction.

D. Superhard Coatings

Principal Investigators: A. Erdemir, L. Ajayi, and O. Eryilmaz

Argonne National Laboratory

Energy Systems Division, Argonne, IL 60439

(630) 252-6571, fax: (630) 252-4798, e-mail: erdemir@anl.gov

Technology Development Area Specialist: Lee Slezak

(202) 586-2335; fax: (202) 586-2476; e-mail: Lee.Slezak@hq.doe.gov

Field Project Manager: Jules Routbort

(630) 252-5065; fax (630) 252-4798; e-mail: routbort@anl.gov

Contractor: Argonne National Laboratory

Contract No.: DE-AC02-06CH11357

Objective

- Design, develop, and optimize low-friction, superhard, nano-composite coatings for advanced transportation applications.
- Demonstrate their durability and energy-saving benefits in actual diesel engine systems.
- Elucidate their friction and wear-reducing mechanisms.
- Explore large-scale production of such coatings in commercial-scale deposition systems.
- Implement demonstrated technology in engines in collaboration with industrial collaborators.
- Confirm performance under severe running conditions of fired engines.

Approach

- Obtain test samples and components, inspect and prepare for coating deposition.
- Optimize and employ deposition protocols that can consistently produce superhard coatings on these samples and components.
- Characterize coating adhesion, thickness, and uniformity and surface roughness.
- Optimize these superhard coatings to provide the lowest possible friction and wear coefficients and longest wear life.
- Test and demonstrate their superior friction and wear performance under a wide range of conditions using bench-top test machines and actual engines.
- Analyze test data and examine sliding surfaces.
- Determine friction and wear mechanisms.
- Prepare reports.

Accomplishments

- During FY07, we further upgraded our deposition system and optimized the deposition protocol.
- Using this system, we successfully produced a range of superhard coatings on test samples and actual engine components.

- We maximized the bonding strength of these coatings to steel substrates and determined the optimum thickness, and surface finish.
- Using coated test samples, we performed extensive wear and scuffing tests to further confirm their extreme resistance to scuffing and wear.
- We also evaluated their performance in a ring-on-liner test machine using cut segments of piston rings and cylinder liners.
- We demonstrated significant reductions in friction and wear under a wide range of speed and loading conditions.
- We ascertained their unique lubrication mechanisms using time-of-flight secondary ion mass spectrometry and X-ray photoelectron spectroscopy techniques.
- Galleon International and Hauzer Technocoat signed an option-to-license agreement for the commercialization of superhard coating technology.
- We worked very closely with several engine companies and OEMs (such as Burgess-Norton, Eaton, Mahle, and Caterpillar) and successfully applied superhard coatings on their engine components.

Future Direction

- Increase industrial collaboration with existing and other engine companies including Cummins, GM, Ford, and Federal Mogul.
- Finalize scale-up and commercialization activities with Hauzer Technocoat.
- Perform surface analytical and mechanical studies on as-deposited and friction- and wear-tested surfaces to understand the fundamental tribological mechanisms behind the superlow friction and wear of superhard coatings.
- Explore fundamental mechanisms that control superhardness and extreme resistance to wear and scuffing using advanced surface analytical tools.
- Explore new and better nano-structured coating architectures based on MoN-Sn, MoN-Sb, and MoN-C and demonstrate their performance.
- Continue to evaluate MoN-Cu and newer coatings with bench-top ring-liner and block-on-ring test machines.
- Determine their behavior as a function of temperature under lubricated sliding conditions.

Introduction

Increasing demands for higher efficiency, power density and reduced emissions in future transportation systems are pushing current materials and lubricants to their limits. In particular, higher loads and speeds and other harsh operating conditions are rendering current materials and lubricants essentially useless. Therefore, the development of novel materials (including hard coatings) and lubricants is extremely important for satisfying the increasingly more stringent application conditions of future engine systems. One of the major goals of this project is to design, develop, and optimize novel superhard and low-friction coatings for use in critical diesel engine parts and components that are subject to severe operating conditions.

Another important goal is to improve their performance, efficiency, and durability even under the most stringent operating conditions.

Synthesis of Superhard Coatings

In this part of our research, we have explored different ways of depositing MoN-Cu-based superhard coatings on a variety of test samples (pins, balls, flats, disks, ring and liner segments, etc) as well as actual engine parts (like tappets, piston rings, and piston pins). Several optimization steps and procedures were tried to achieve the best overall structure (that is extremely dense, free of pin holes and defects) and chemical composition (that is hard MoN phase is nearly stoichiometric, while soft Cu phase is homogeneously distributed). Our trial runs

have led to a structurally dense, superhard coating which was also very smooth and strongly bonded to the substrate materials. For the deposition of MoN-Sn, MoN-Sb, MoN-Ag, and MoN-C based superhard coatings, it is necessary to use Mo and other targets separately, since it might be very challenging to produce truly composite targets of these materials. When separate targets are used, deposition parameters might have an effect on the coating microstructure and chemistry, such as slow turning speeds may lead to layered (MoN, MoN-Cu rich or MoN, Cu layers) microstructure, or there is a possibility that some oxygen may enter into the films for the cases where a composite target is used. Before starting to synthesize any new coating system, it is very important to duplicate known MoN-Cu system by using separate targets.

The new sets of coatings also were synthesized in a commercial scale sputter ion plating system (CemeCon Model #CC800/9XL). This commercial unit has a three stage rotational capabilities with 6 satellite sample holders. Since Mo and Cu sputtering targets were placed at each corner of a cubic shaped vacuum chamber, it is obvious that slower rotational speed might lead to the development of a layered structure. Turning table at very high speeds may cause samples to move and take a different position with respect to the targets. The most important point is to find or select maximum safe turning speed during deposition. After series of deposition experiments 2 rpm was selected as a maximum safe rotational speed which would allow us to achieve a proper mixture of Mo and Cu in the coating.

In the second step, we have investigated the source and effect of possible oxygen contamination on film performance. The composite targets used in the previous studies were made by direct sintering of Mo and Cu targets. Since the surface of every target is covered with an oxide layer, depending on the powder sizes, there might be a considerable amount of oxygen in the total target system (which is always ignored by the manufacturers).

Flowing very small amount of oxygen into the chamber was another challenge since it needed equipment modification by installing a mass flow controller that can deliver 5 to 10 sccm max., and the integration of the new system into the deposition system's computer control unit. We found another

easy way of doing this by simply installing a needle valve to one of the port in the chamber. When the system reaches its ultimate pressure by adjusting the needle valve it was possible to control the partial pressure of air in the chamber by knowing the partial pressure of air, the oxygen partial pressure can easily be calculated.

Another important step for the deposition of high quality film was to adjust the amount of copper in the total MoN-Cu coating system. The amount of each ingredient can be adjusted by simply changing the power of each sputtering target. But the amount of sputtering rate was not directly proportional to the sputtering power and it was necessary to find optimized values experimentally.

After taking into account the steps mentioned above, several series of coatings have been deposited and tested. The deposition process parameters were optimized and it is found that 7% at. oxygen containing MoN-Cu system would not only give the lowest friction coefficient and very low wear rates, but also it was structurally very dense and nearly futureless as shown in Figure 1.

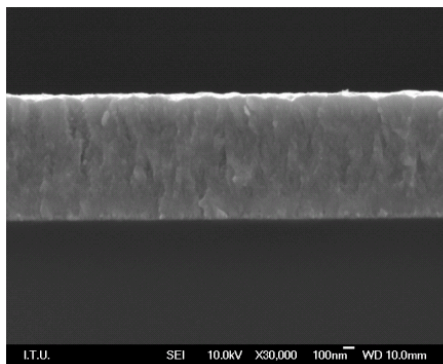


Figure 1. Cross sectional SEM image of MoN-Cu system coating containing 7% at. oxygen.

Figure 2 shows the XRD spectra of the MoN-Cu coating with varying degree of oxygen in the film. By the introduction of copper into the structure, a broadening in the peaks is observed which is indicative of grain size refinement. As expected, no peaks related to crystalline copper are present in the spectra. Some peaks that are related to molybdenum oxides were also present in the coatings with very high oxygen content.

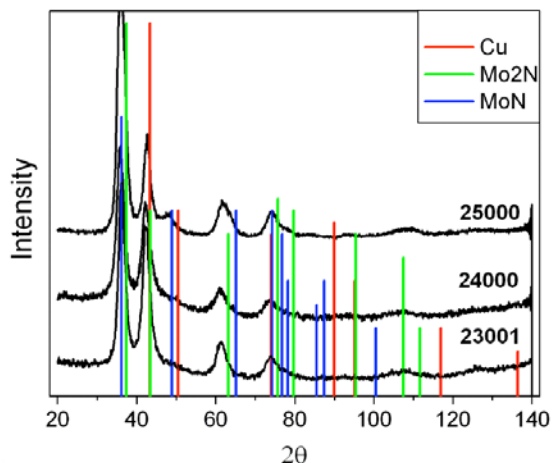


Figure 2. Glancing angle XRD diffractions of MoN-Cu superhard coatings with oxygen incorporation. (23001: 3.36 % at., 24000 : 7%at., 25000: 25% at.oxygen)

Tribological Tests

Tribological testing of superhard coatings was carried out with two types of test machines: a pin-on-disk tribometer for screening tests and a block-on-ring test machine for scuffing studies. All of the tests were performed under heavy loads and relatively low sliding velocities to create a boundary-lubricated sliding regime where direct metal-to-metal contacts occur.

Figure 3 shows the typical friction coefficient of new MoN-Cu-coated test pairs under lubricated sliding conditions. These tests were performed in the pin-on-disk tribometer. The lubricant used was an SAE 10W-40 grade formulated engine oil. As evident in Figure 3, the friction coefficient of the coated test pair is initially around 0.09 but decreases steadily to 0.05 after 100 m of sliding and finally stabilizes at around 0.06 toward the end. Such a reduction in friction is expected to result in increased fuel savings in actual engines. In addition to impressive friction test results, the wear of MoN-Cu coated surfaces was hard to measure.

Using the block-on-ring test machine, we performed a series of scuffing tests on the new MoN-Cu coated steel samples. Scuffing is a catastrophic failure of a lubricated surface subjected to severe loading and/or inadequate lubrication. It is a major problem in heavy duty engines. When such a test was run on uncoated or control samples, scuffing always occurred between 650 and 700 N loads. However,

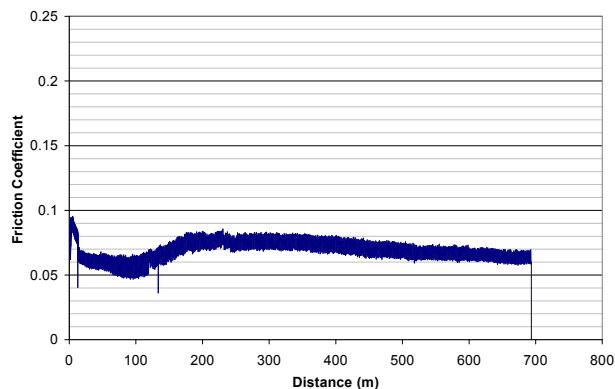


Figure 3. Friction coefficients optimized superhard-coated steel test samples under boundary-lubricated sliding conditions of a pin-on-disk tribometer in fully formulated Mobil 1 10W-30 oil.

for the MoN-Cu coated surfaces, scuffing did not occur even up to the load limit (1700 N) of this machine. Overall, the new superhard coatings developed under this program possessed exceptional resistance to scuffing. Such a property would be extremely useful for engine applications involving severe loading, high temperatures, low viscosity oils, and/or starved lubrication conditions.

Surface Analytical Studies

During FY07, we conducted numerous surface analytical studies on the sliding surfaces of MoN-Cu coated test samples. The main motivation was to elucidate the fundamental tribological mechanisms controlling the friction, wear, and scuffing behavior of these coatings. One of the tools we used was a time-of-flight secondary ion mass spectrometer (or ToF-SIMS), which is well-known for its surface sensitivity (capable of providing chemical information from surface layers that are a few Å thick). In support of the ToF-SIMS, we also used X-ray photoelectron spectroscopy (XPS).

The comparison of the depth profiles and ToF-SIMS images of the sliding surfaces of steel and superhard coated test samples (see Figures 4 and 5) clearly show that phosphorus and sulfur based compounds are considerably higher in the wear tracks formed on superhard coatings. This finding suggests that superhard coatings are very responsive to the additives in the oil and that the tribolayers formed on these surfaces are strongly bonded and durable. They do not wear off very quickly.

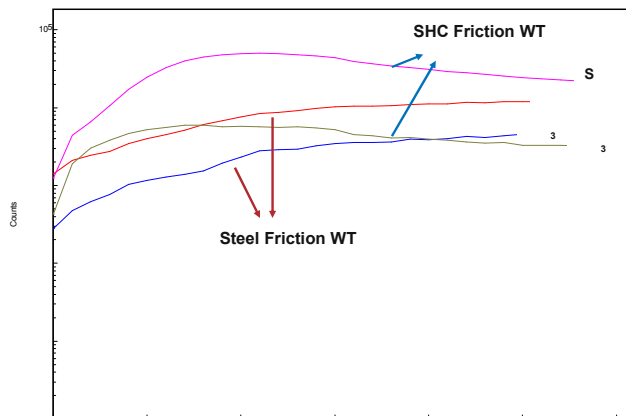


Figure 4. TOF-SIMS depth profile of sliding surfaces of superhard coating and steel in fully formulated oil.

XPS study of the same sliding surfaces yielded supporting information. Specifically, it suggested that sulfur existed in at least two reacted forms: MoS_x and CuS_x . Some FeS_x was also found on the sliding surfaces.

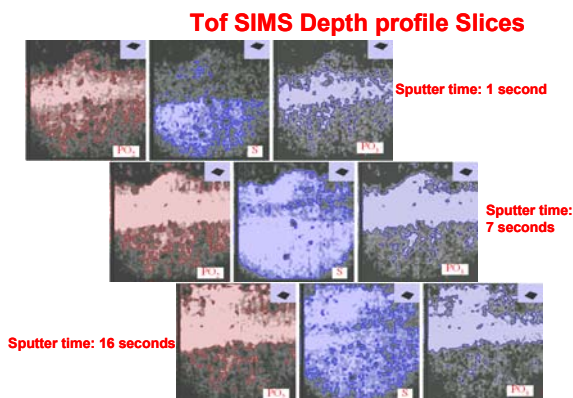


Figure 5. TOF-SIMS slices taken from different depths of sliding surfaces of superhard coating in fully formulated oil.

Since TOF-SIMS is a very surface sensitive technique, it also enabled us to do chemical mapping as a function of depth. With this information we have further scientific evidence of how the tribolayer functions in a given system. As it is clear from the depth profile slice pictures of tested coatings in Figure 5, PO based compounds stays on top of the surface and S based species are found underneath these PO-rich layers.

Conclusions

During FY07, we produced new and much improved versions of the superhard coatings on a number of test samples using a commercial-scale deposition system. We performed detailed systematic studies on their friction, wear, and scuffing performance. Friction and wear tests in a pin-on-disk machine confirmed significant reductions in friction, while wear was reduced to unmeasurable levels. These superhard coatings drastically improved the resistance of steel substrates to scuffing. Using a block-on-ring test machine, we could not scuff these surfaces up to the load limit of this machine. Detailed surface analytical studies with ToF-SIMS and XPS revealed high concentration of MoS_x and CuS_x (and some FeS_x) within the wear track, suggesting that these species were perhaps responsible for the exceptional scuffing resistance of these coatings.

Patents and Publications

During FY07, we filed one provisional patent and published and/or presented five new papers on the work that was performed under this project.

1. Comparative Tribological Behaviors of TiN-, CrN- and MoN-Cu Nanocomposite Coatings, A.Öztürk, K. V. Ezirmik, K. Kazmanlı and M. Ürgen, O. L. Eryilmaz, and A. Erdemir, Tribology International, in press, 41(2008)49-59.
2. “Effect of Copper Addition on the Temperature Dependent Reciprocating Wear Behaviour of CrN Coatings”, V. Ezirmik, E. Senel, K. Kazmanli, A. Erdemir, and M. Ürgen, Surface and Coatings Technology, 202(2007)866-870.
3. “Design of Novel Nanocomposite Films For Improved Boundary Lubrication and Scuff Resistance,” A. Erdemir, O. L. Eryilmaz, O. O. Ajayi, M. Urgan, and K. Kazmanli, presented at the Annual Meeting of the Society of Tribologists and Lubrication Engineers, Calgary, Canada, May 7-11, 2006.

4. “Multifunctional Nanocomposite Hard Coatings for Improved Boundary Lubrication,” A. Erdemir, invited keynote paper presented at Joint COST 532 & U.S. Dept. of Energy Conf. on Triboscience & Tribotechnology, Porto, Portugal, Oct. 12-14, 2005.
5. “Development of Multifunctional Nanocomposite Coatings with Extreme Resistance to Wear and Scuffing under Boundary Lubricated Sliding Conditions,” A. Erdemir, O. L. Eryilmaz, O. O. Ajayi, M. Urgan, and K. Kazmanli, presented at Intl. Conf. on Metallurgical Coatings & Thin Films ICMCTF 2006, San Diego, May 1-5, 2006.

E. Residual Stresses in Thin Films

(This project is jointly funded by Propulsion Materials and Heavy Vehicle Systems Optimization)

Principal Investigator: D. Singh (co-workers: J. L. Routbort, G. Chen, O. Eryilmaz, A. Erdemir)

Argonne National Laboratory

9700 S. Cass Avenue, Argonne, IL 60439-4838

630-252-5009 dsingh@anl.gov

Program Manager: Lee Slezak

202-586-2335 Lee.Slezak@ee.doe.gov

Contractor: Argonne National Laboratory

Contract No.: DE-AC02-06CH11357

Objective

- Measure residual stresses in thin films and coatings as a function of film thickness and relate stresses to film properties such as hardness, fracture toughness, and adhesion energy to relate to film processing variables and to predict durability

Approach

- Develop X-ray technique to measure change of lattice parameter of coating constituents as a function of depth and hence to calculate the lattice strains and stresses
- Develop indentation technique to measure hardness, fracture toughness, and adhesion energy of films and coatings
- Relate stresses, properties, and processing conditions to film durability

Accomplishments

- Advanced Photon Source (APS) used to measure stresses in 3- μm thick thin films of nanocrystalline MoN and MoCuN deposited on silicon and steel substrates as a function of depth
- Stresses were found to be sensitive to deposition conditions and thermal annealing
- A paper published in Applied Physics Letters
- Preliminary coating/film adhesion energies measured using indentation

Future Directions

- Continue to refine and improve resolution of X-ray technique
 - Develop indentation technique to measure film adhesion
 - Investigate stresses in superhard, nanocrystalline MoCuN films as a function of deposition conditions and Cu concentration on steel substrates as well as investigate other coatings systems applicable for engine applications
-

Introduction

Because of their unusual structural, mechanical, and tribological properties, superhard, nanocrystalline coatings can have an immediate and far-reaching impact on numerous advanced transportation applications including FreedomCar and 21st Century Truck Programs of DOE by reducing parasitic friction losses (hence increasing fuel economy) and wear (hence increasing durability/reliability). They can also be used to overcome toxic emission problems associated with exhaust gas recirculation in diesel engines. Durability of hard coatings is a critical property. The durability is determined by the surface adhesion energy, but is the result, in a large part, of the residual stresses that form as a result of materials, and processing parameters such as deposition bias voltage, ion flux, and temperature.

The approach for this effort is to use the high-brilliance X-rays produced by the Advanced Photon Source (APS) at Argonne National Laboratory, and a microfocus beam, to measure the residual stresses/strains of MoN thin films as a function of depth from the surface through the interface to the substrate. Subsequently, correlate the residual stress profiles with the film processing conditions and the resulting film/substrate adhesion and its tribological properties.

During the past year, focus has been on two coating/substrate systems: (a) MoN/Mo film on silicon (Si) single crystal wafer and (b) MoN/Mo film deposited on steel; latter system having a significant technological implication. In addition, effect of copper additions on the film was also investigated. MoN/Mo on Si system was used to measure residual stress/strains using two different approaches (edge scan and wire technique) to establish viability of each of the techniques and their pros/cons. Whereas, MoN/steel system was used for residual stress measurements and preliminary correlation of film/substrate adhesion energy to the residual stresses.

Experimental

(a) Coating/substrate systems

MoN/Mo on Si

MoN/Mo bilayer films were prepared by physical vapor deposition (PVD) using magnetron sputtering at temperatures between 250 and 300 °C. The substrate was p-type (100) single-crystal silicon wafer (cleaved into 3 cm × 3 cm × 0.1 cm pieces) with native oxide layer. Film deposition details have been described in FY 06 report and will not be repeated here. Figure 1 is a scanning electron microscopy (SEM) micrograph of the cross section of an as-deposited MoN/Mo film. The Mo and MoN layers show a dense columnar structure.

MoN/Mo on steel

MoN/Mo thin films on H 13 steel substrates (1” x 1” x 0.25” coupons) were also deposited by PVD process. Three samples were fabricated using slightly differing deposition conditions to investigate the effect of processing on film adhesion. In all the samples, initially a bond layer was deposited followed by MoN coating. The bond coat was either combination of Mo + Mo₂N or Mo₂N. Flowing nitrogen gas was used. Details for each of the samples are listed in the Table 1. Based on the deposition parameters, it is estimated that bond layer for all the samples would be approximately 100 nm. Figure 2 shows a SEM micrograph of a typical MoN/Mo film deposited on steel. The film thickness is approximately 4 μm and is dense.

Table 1. Deposition Conditions for the MoNCu/Steel Samples

Sample ID	Mo & Cu Deposition Power (kW)	Deposition Time (s)
C70109	Mo:8; Cu: 0	7200
C70110	Mo: 8; Cu: 0.5	6600
C61215	Mo: 8; Cu: 0.8	7200

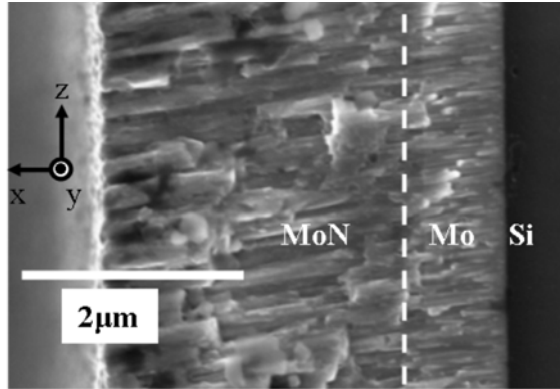


Figure 1. Cross-sectional scanning electron micrograph of MoN/Mo bilayer film deposited on Si substrate.

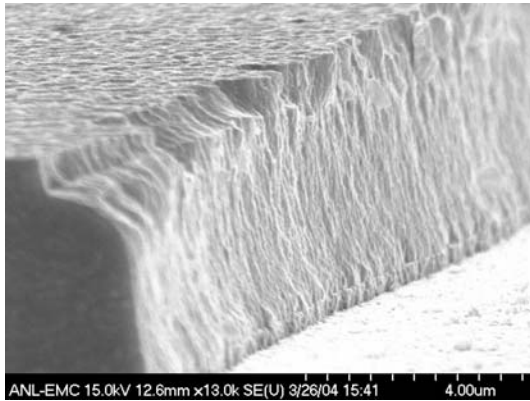


Figure 2. Cross-sectional SEM of a MoNCu/Mo film deposited on steel substrate.

(b) Residual stress measurements

X-ray microdiffraction was performed on beamline 34-ID-E at the Advanced Photon Source (Argonne National Laboratory) [1]. The X-ray beam was focused by Kirkpatrick-Baez mirrors down to 0.4 (horizontal) \times 0.6 (vertical) μm^2 . A high-resolution charged coupled device (CCD) X-ray detector was used to collect X-ray diffraction (XRD) patterns from the X-ray microbeam with energy of 8.9 keV (1.39308 Å). Strains and stresses were evaluated from the change in the lattice spacing determined from diffraction pattern of specific diffraction planes of coating and substrate materials and their respective stress free states. Two different

approaches, namely cross-section and wire techniques, were used for the measurement of stresses.

For the cross-section or edge technique, cross-section of the sample is examined, either by fracturing the sample or aligning the sample such that one of the edges is perpendicular to the X-ray beam. Schematic of the edge technique is shown in Figure 3(a). Sample was aligned by an X-ray fluorescence method so that the film surface (i.e., the yz plane in Figure 1) was parallel to the X-ray beam. The position of the X-ray beam was scanned along the film normal (x in Figure 1) direction with a step size of 0.25 μm . Similarly, by rotating the detector or the sample by 90° , out-of-plane strains can be determined.

Schematic for the wire technique is shown in Figure 3(b) and was originally developed by Larson et. al. [2] to study the strain tensors and orientations in three-dimensional crystals. When the X-ray beam hits a series of grains within the film, a Laue diffraction pattern is generated and captured by the CCD X-ray detector. This pattern contains information on grains along the X-ray beam direction. Unlike previous two-dimensional X-ray structural microscopy, this technique uses an X-ray absorption wire (a 50-micron platinum wire) as a differential-aperture (i.e. knife edge) slit to separate Laue patterns obtained from different grains along the sample depth. Thus, by comparing the shift in Laue patterns from grains, at a specific coating depth, to that of the unstrained grains, residual strains can be determined. Currently, this technique provides ~ 0.5 μm spatial resolution along the beam direction. However, by decreasing the beam size and the step size of the wire movement, it is possible to increase the resolution to ~ 0.1 μm . Thus, this technique can be extremely useful in stress profiling in thin films and coatings.

There are pros and cons associated with both the techniques. Edge or cross-section based technique is simpler in terms of conducting experiments and analyzing data; however, results from this technique could be affected by the edge effects. On the other hand, wire technique is more complex in terms of experimentation and analysis. At the present time, wire technique is set-up to only measure out-of-plane stresses/strains.

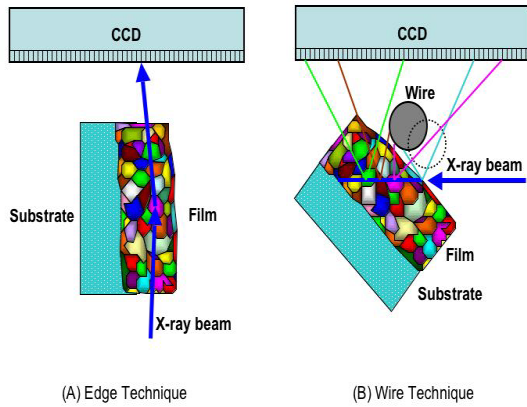


Figure 3. Experimental set-up used for stress evaluations: (a) Edge and (b) Wire techniques.

(c) Adhesion energy measurements

An indentation technique [3] was used to evaluate the film/substrate interfacial adhesion energy. Specifically, this technique is applicable for hard brittle films deposited on relatively ductile substrates, similar to the MoN/steel system used in our study. This technique assumes that upon application of an indentation load, the sub-surface stress is concentrated at the interface. At a critical indentation load, stress concentration becomes equal or greater than the film adhesion strength, thereby leading to delamination of the film. Typically, the extent of delamination can be observed by the formation of circumferential cracks in the film.

Accounting for the complex stress state developed during indentation, residual stresses, plasticity of the substrate material, and the extent of interfacial delamination, Kim et. al. [3] have developed a closed-form solution for the critical energy release rate ‘ G_c ’ or the adhesion energy given as:

$$G_c = \left(\kappa \frac{dP}{dc} + \lambda \right) t / \left(c - a \frac{da}{dP} \frac{dP}{dc} \right) \quad (1)$$

where, P is the indentation load, a is the indent radius, c is the delamination radius, t is the film thickness, and κ and λ are constants that include the material properties of the film and substrate materials and the residual stresses. Thus, by experimentally determining the variation of the indentation and delamination radii with the indentation loads (da/dP & dc/dP), material properties, and residual stresses in

the film, adhesion energy of the film can be calculated.

Results and Discussion

(a) Residual stress measurements in MoN/Mo on Si using cross-section technique

Results from this technique were reported in FY 2006 annual report. Highlights of the results were that MoN and Mo layers in the as-deposited film were found to be under in-plane compression, with large strain gradients as a function of depth (Figure 4). The observed strain profiles were explained in terms of atomic peening and void-induced strain relaxation. Annealing of the film caused significant strain relief possibly due to defect reduction in the MoN layer. In contrast, residual strain in the Mo layer was only slightly relieved, and the defect concentration increased after annealing.

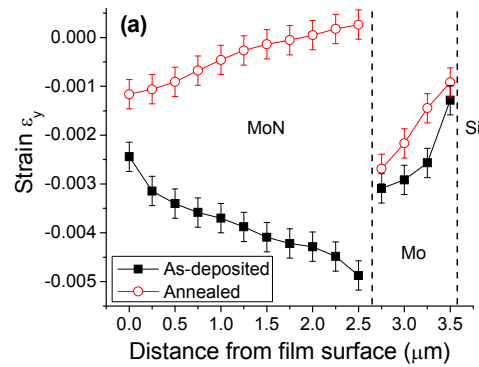


Figure 4. Depth-resolved residual strain for as-deposited and annealed MoN/Mo bilayer films as determined from cross-section technique.

(b) Residual stress measurements in MoN/Mo on Si using wire technique

Figure 5(a) shows the overall diffraction pattern of the MoN/Mo film, and Figure 5(b) shows the reconstructed patterns from different depths of the film, which were derived from the wire technique. The overall pattern shown in Figure 5(a) comes from both the MoN layer and the Mo bond layer. The latter shows a spotty diffraction pattern, indicating a relatively larger grain size than the MoN layer. The reconstructed patterns in Figure 5(b) indicate that the MoN layer is near the surface of the film while the Mo bond layer is near the substrate. Further analysis

of the diffraction patterns shows that there are shifts in the diffraction peaks (both MoN (402) and Mo (220)) as depth of film increases (Figure 6). The sharper peaks are the Mo and the broader peaks correspond to the MoN. The corresponding lattice parameter of the MoN (402) peak decreases from 1.1473 Å to 1.1411 Å. The corresponding lattice parameter of the Mo (220) also decreases from 1.1187 Å to 1.1174 Å. The strain free lattice parameters for MoN (402) and Mo (220) are 1.1405 Å and 1.1143 Å, respectively. Therefore, from these data, we can plot the depth-resolved out-of-plane strains for both MoN and Mo layers, as shown in Figure 7.

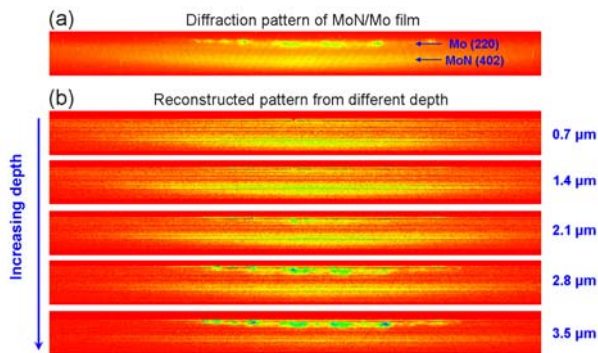


Figure 5. (a) Overall X-ray diffraction pattern of the MoN/Mo film and (b) reconstructed diffraction patterns from different film depths.

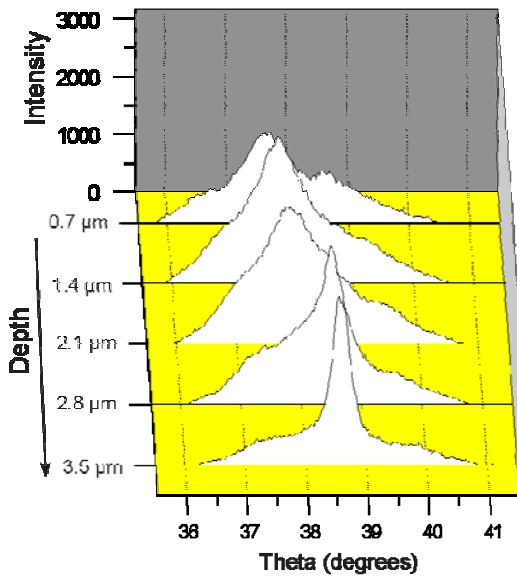


Figure 6. Shift in the diffraction peak as a function of depth indicative of variation of residual stresses as a function of depth.

Figure 7 also compares the out-of-plane strain measured by the wire technique with the in-plane strains measured by the cross-section technique. Because of the limitations in the current set-up for wire technique and associated software, independent measurements of the in-plane strains could not be made. Nevertheless, on estimating the in-plane strains based the out-of-plane strain measurements from the wire-technique gives values of in-plane strain that are significantly (20-40%) lower than those determined from the cross-section technique. This implies that sample sectioning or using the sample edge of as-deposited film/substrate, per the cross-sectional technique, alters the stress state. In this regards, cross-sectional technique should be best used for qualitative assessment of the residual stresses in thin films as opposed to accurate strain determinations.

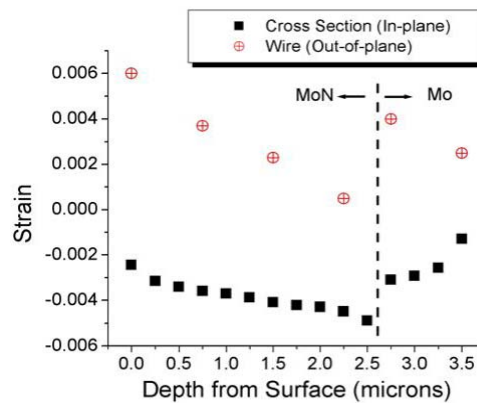


Figure 7. Depth resolved out-of-plane strain measured using the wire-technique in MoN/Mo film deposited on Si substrate.

(c) Residual strain measurements in MoN-Cu using the cross-section technique

Figures 8a-c show the measured lattice parameters of in-plane biaxial, out-of-plane, and strain free MoN 222 peaks as a function of the film depth in the MoNCu thin films deposited on steel substrates. Observations from three samples processed differently (Table 1) are quite similar; in-plane lattice parameters decrease with the film depth. Whereas, out-of-plane lattice parameters increase with the film depth. Strain-free lattice parameter is calculated from $\sin^2\psi$ approach [4]. These results indicate the

film is in in-plane compression and in tension out-of-plane.

Figure 9 shows the residual stresses for the three MoNCu/steel samples estimated from lattice spacing changes of Figure 8. In all cases, the in-plane residual stresses were compressive and increases in

magnitude with film depth. The magnitudes of the residual stresses were as high as 4 GPa. There was no clear correlation between the deposition conditions and the measured residual stresses for the three samples investigated. However, it appears that sample (C70110) with the shortest deposition time has the highest compressive residual stress.

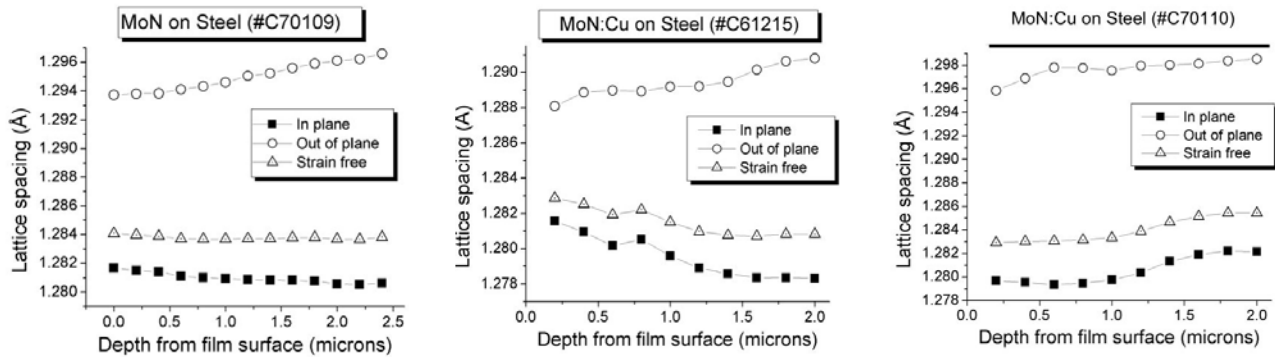


Figure 8. Lattice parameters of MoN 222 reflections for various stress-states as a function of film depth in MoNCu film deposited on steel.

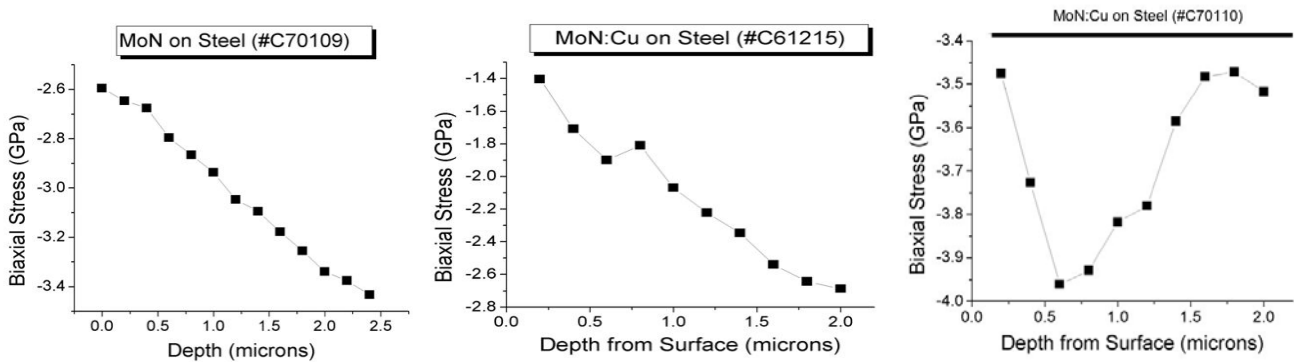


Figure 9. In-plane biaxial stress for various stress-states as a function of film depth in MoNCu film deposited on steel.

Residual strains in PVD coatings are very complex because they include both intrinsic and extrinsic strains [5]. The intrinsic strains are related to the microstructure of thin films, which varies with material as well as with film deposition conditions. Extrinsic effects refer to thermal strain caused by the thermal expansion coefficient mismatch between film and substrate. In PVD films, the intrinsic residual strain is strongly affected by deposition

conditions. Nonetheless, it is believed that compressive strains in thin films that have been subjected to ion or atom bombardment are caused by atomic peening [6], which is enhanced by low sputtering gas pressure and high substrate bias during deposition [6]. The case of the MoN layer is more complicated since N₂ was introduced during the film growth to form the metal nitride.

(d) Measurement of Thin Film Adhesion Energy

Spherical Brale C indenter was used to evaluate the adhesion energy of the MoN/Cu coatings deposited on steel substrate (sample C61215). Indentations were made at three different loads (P) ranging from approximately 600 N to 1600 N. Figure 10 is an optical micrograph of a typical indent showing the circular indent and on the sample. There is a large circular indent surrounded by a region where the film debonding and cracking occurs. Indent and delamination radii are depicted on the figure. The film debonding and cracking is symmetric around the indent. This indent was from an area of the sample away from the edge.

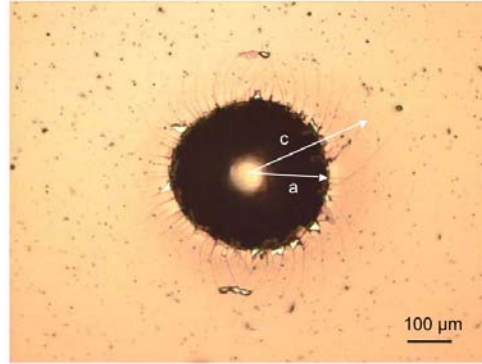


Figure 10. Optical micrograph of a 590 N indent on MoNCu/steel (C61215) sample away from the sample edge.

Figure 11 shows an indent on the same sample as in Figure 10, but near the sample edge. The indentation load was 590 N. Clearly, the cracking and delamination in this case is not symmetric to the indent made near the sample center (Figure 10).

Similar observations were made at all of the indentation loads. It is believed that the asymmetric nature of cracking and delamination is a direct consequence of asymmetric in-plane residual stress-state near the sample edge.

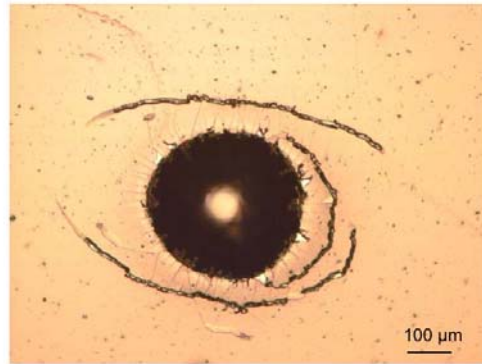


Figure 11. Optical micrograph of a 590 N indent on MoNCu/steel (C61215) sample near the sample edge.

Variations of the indent and delamination crack sizes as a function of indentation loads are plotted in Figure 12 and there is a linear dependence. The slopes of the linear curve fits to the data were used in the Eqn. 1, along with the material parameters, for the determination of the interfacial adhesion energy. The residual stress was assumed to be 2.5 GPa and the coating thickness was taken as 2.5 μm . The resulting value for the adhesion energy was determined to be 671 J/m^2 . High measured adhesion interfacial energy is consistent with experimental observation of short delamination zone. Similarly, adhesion energies for diamond like carbon (DLC) on steel (571 J/m^2 , ref. 3) and TiN/ZrN on steel (180 J/m^2 , ref. 7) have been reported in the literature.

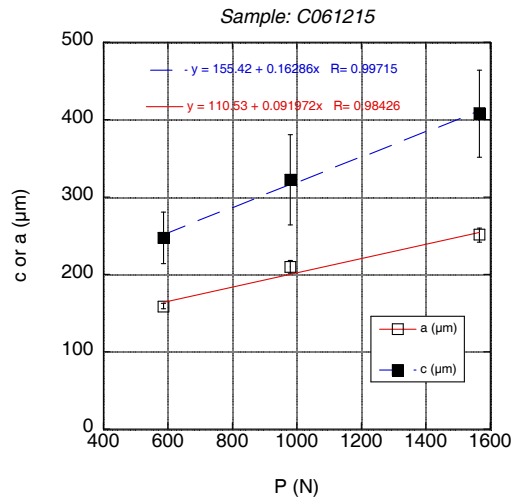


Figure 12. Plot of indentation and delamination crack sizes as a function of the indentation load for MoNCu/steel sample.

In conclusion, we have applied cross-section and wire techniques using X-ray micro-diffraction to study depth-resolved residual strain in MoN/Mo bilayer films deposited on Si and steel substrates. Preliminary evaluation of film/substrate adhesion energy made using an indentation method.

Future Direction

Residual stress measurements will be extended to superhard, nanocrystalline MoCuN thin films and to commercial films, namely Ni₃B, ZrN. The indentation technique will be further refined and exploited to measure the thin film or coating properties and the adhesion energy. The residual stress-states and adhesion energy will be related to the film deposition conditions to optimize the film tribological performance.

References

1. G. E. Ice, B. C. Larson, W. Yang, J. D. Budai, J. Z. Tischler, J. W. L. Pang, R. I. Barabash, and W. Liu, *J. Synchrotron Rad.* 12, 155 (2005).
2. B. C. Larson, W. Yang, G. E. Ice, J. D. Budai, and J. Z. Tischler, *Nature* 415, 887 (2002).
3. J. J. Kim et. al., *Thin Film Solids* 441, 172-179 (2003).
4. V. Hauk, *Structure and Residual Stress Analysis by Nondestructive Methods*, (Elsevier, Amsterdam, 1997), Chapter 2.
5. A. Misra and M. Nastasi, *Engineering Thin Films and Nanostructures with Ion Beams*, edited by E. Knystautas (Taylor & Francis, Boca Raton, FL, 2005), Chapter 7.
6. H. Windischmann, *Crit. Rev. Solid State Mater. Sci.* 17, 547 (1992).
7. S. V. Hainsworth, M. R. McGurk, and T. F. Page, *Surface and Coatings Technology* 102, 97-107 (1998).

IV. ANALYSIS

A. PSAT Heavy-Duty Vehicle Modeling and Simulation

Project Leader: Aymeric Rousseau

Argonne National Laboratory

9700 South Cass Avenue

Argonne, IL 60439-4815

(630) 252-7261; e-mail: arouseau@anl.gov

DOE Technology Manager: Lee Slezak

(202) 586-2335, Lee.Slezak@hq.doe.gov

Objective

- Develop heavy-duty PSAT capabilities.
- Gather component and vehicle data information.

Approach

- Collaborate with National Laboratories and Companies to collect component and vehicle data from existing projects.

Accomplishments

- Integrated component data from ORNL for several displacements.
- Collaborated with ORNL to define required vehicle instrumentation and testing to validate a Class 8 model of PSAT.
- Collaborated with West Virginia University to validate several heavy-duty and medium-duty vehicle classes based on dynamometer data.
- Supported OEMs by integrating specific drivetrain configurations in PSAT.
- Collaborated with the EPA as part of the SmartWay program to help companies evaluate the benefits of several advanced technologies.
- Started collaboration with NREL to evaluate the impact of several electrical accessories on fuel economy.
- Implemented co-simulation with ADAMS to model an HMMWV on different roads.

Future Directions

- Complete the validation of several heavy-duty vehicle classes based on West Virginia University and ORNL vehicle test data.
 - Extend collaboration with OEMs to support the 21 CTP activities.
-

Introduction

The goal of this task is to support the 21 Century Truck Partnership activities by extending the heavy-duty capabilities of the Powertrain Systems Analysis Toolkit (PSAT).

Integration of Component Data

Several component models were integrated into PSAT to simulate several technologies. Oak Ridge National Laboratory (ORNL) provided several engine maps, from 12 to 15.2 L, representing state-of-the-art technology from several manufacturers. In addition to the engine maps, several transmission and vehicle data were implemented in PSAT.

Model Validation

To validate a vehicle model, test data from dynamometer are required. Collaboration was initiated with West Virginia University to validate several vehicle classes based on previously collected data. Researchers from West Virginia University Center for Alternative Fuels, Engines, and Emissions (CAFEE) supported Argonne National Laboratory (ANL) in identifying and quantifying parameters that are critical to the accurate modeling of heavy-duty vehicle performance and fuel economy. Two vehicle classes are being considered: Class 8 and bus.

Discussions also have been ongoing with ONRL to gather information from the vehicle fleet testing that could be used to validate PSAT. Requested sensors as well as testing conditions have been provided to ORNL. The ability to easily integrate any drive cycle in PSAT was enhanced to facilitate the drive cycle analysis for ORNL.

Support of Existing Activities

Several powertrain configurations were added to support internal development from several manufacturers. Numerous questions from the PSAT users were answered regarding control strategy, graphical user interface usage, and component sizing.

Collaboration with the U.S. Environmental Protection Agency (EPA) was initiated to support the SmartWay activities. The main goal is to be able to quantify the benefits of a series of advanced technologies (i.e., aerodynamic, single tire, etc.).

Collaboration with the National Renewable Energy Laboratory (NREL) was initiated to evaluate the impact of accessory electrification. The list of required component data was defined.

Modeling of an HMMWV with ADAMS Co-simulation

The work performed advances the Virtual Prototyping agenda in the field of mechanical system simulation through a system-level simulation capability for engineering design of ground vehicles. The simulation capability integrates the vehicle, tire, powertrain, and terrain into a unified high-fidelity simulation environment that enables the on- and off-road study of areas such as vehicle performance and ride comfort, suspension design for improved ride, vehicle stability and maneuverability, and active control strategies. The vehicle considered is the U.S. Army High Mobility Multi-Wheeled Vehicle (HMMWV), modeled using MSC.Software 2005. Different tire are models available at various levels of fidelity (e.g., Fiala, Pacejka, FTire, and the fully nonlinear Finite-Element-based model). The PSAT is considered for the simulation of powertrain systems.

The flow of information between ADAMS and PSAT is defined in Figure 1.

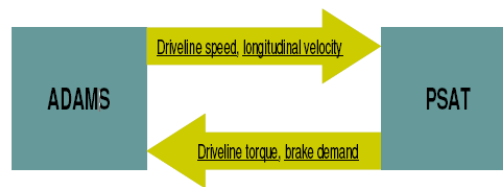


Figure 1. Linkage between ADAMS and PSAT

The powertrain system used in ADAMS/Car carries some limitations, as listed below:

- Only conventional powertrain systems,
- Unpredictable fuel economy,
- Low level of sophistication, and
- No extensive validation.

The PSAT offers the more sophisticated powertrain system. Therefore, the motivation is to perform the co-simulation of the ADAMS/Car vehicle model with the PSAT powertrain system. The PSAT powertrain system also offers prediction of fuel efficiencies within 1% to 5 % accuracy.

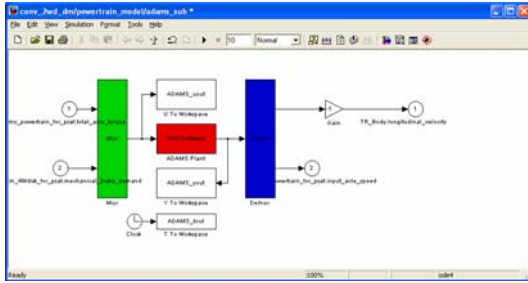


Figure 2. Sfunction Representing the ADAMs Model in PSAT

The linkage between both tools is performed by using an Sfunction, as shown in Figure 2.

Conclusions

Several component models and data have been integrated to meet the specific requirements of heavy-duty vehicles. The validation of several vehicle classes and powertrain configurations will continue to be an ongoing process.

B. Development of Medium and Heavy Truck Systems Models

Principal Investigator: K. Dean Edwards

Oak Ridge National Laboratory

National Transportation Research Center

2360 Cherahala Boulevard

Knoxville, TN 37932-6472

(865) 946-1213; e-mail: edwardskd@ornl.gov

DOE Program Manager: Lee Slezak

(202) 586-2335; e-mail: Lee.Slezak@ee.doe.gov

Objectives

- To support the Office of Vehicle Technologies Heavy Vehicle Systems activity and 21st Century Truck Partnership through the establishment of an updated medium and heavy truck (Class 3-8) dedicated model platform for PSAT-type simulations and evaluations.

Approach

- Engine maps of four 2004 emissions compliant, heavy-duty diesel engines have been developed for use in PSAT using data from engine dynamometer experiments.

Accomplishments

- Engine data necessary to produce the engine maps has been obtained from dynamometer evaluations of four, 2004 emissions compliant, heavy-duty diesel engines.
- A technique has been developed for producing the PSAT engine maps from the engine data.
- PSAT engine maps for the four engines have been completed and delivered to ANL for evaluation and implementation into PSAT.

Future Directions

- Obtain data and construct a PSAT map for a 2007 emissions compliant, heavy-duty diesel engine.
-

Introduction

Accurate systems simulations of the fuel efficiency and environmental impact of advanced vehicle propulsion and emission control technologies are vital for making informed decisions about the optimal use of R&D resources and DOE programmatic priorities. One of the key modeling tools available for making such simulations is the Powertrain System Analysis Toolkit (PSAT) maintained by Argonne National Laboratory (ANL). A distinctive feature of PSAT is its ability to simulate the transient behavior of individual drive-train components as well as their combined performance effects under realistic driving conditions. However, the accuracy and usefulness of PSAT simulations ultimately depend on the accuracy of the individual component sub-models or maps and the variety of systems which can be modeled.

Oak Ridge National Laboratory (ORNL) is a collaborator with ANL and is specifically tasked with providing data and models that augment PSAT's capabilities. Specifically, ORNL's role has focused on the experimental measurement of performance data from advanced diesel engines and emission control components and the incorporation of that data in the form of maps or low-order transient models into PSAT.

In addition to considerable effort on light-duty systems, near the end of FY2006, ORNL began efforts to expand PSAT capabilities on the heavy-duty side by providing engine maps based on engine dynamometer data from four, 2004 emissions compliant, heavy-duty diesel engines. These maps were completed in FY2007 and provided to ANL for evaluation and incorporation into PSAT.

Approach

The PSAT engine maps are generated from a small subset of data that is obtained through engine dynamometer experiments. Data is collected at a number of speed and load points with the engine operating at steady state conditions. Clearly, the accuracy of the maps is dependent upon the extensiveness of original engine data. It is important to have data that covers the entire speed-load range of the engine and that defines the torque curve.

The PSAT engine maps consist of $m \times n$ look-up tables with inputs of engine speed and torque. To generate the matrix used to populate the look-up table for each map, the sparse original data is fed into a Matlab routine which uses interpolation to fill in the missing regions of the speed-load range. The regions of the matrix that lie above the torque curve of the engine (where the engine cannot operate but which must be filled in with "dummy" values to complete the look-up tables) are filled in vertically using a "nearest-neighbor" extrapolation technique.

Results

The PSAT engine maps have been completed for the four, 2004-compliant heavy-duty diesel engines. The set of maps includes 12 look-up tables for fuel and exhaust flow rates, intake pressure and temperature, exhaust temperature, and engine out emission levels of NO_x, total hydrocarbons (THC), O₂, CO, CO₂, and particulate matter (PM). These parameters were chosen to provide information about the engine performance and to supply the necessary exhaust conditions to the aftertreatment models.

Maps of engine brake efficiency for the four engines are shown in Figure 1. For three of the engines, the brake efficiency peaks at approximately 43.5%; however, Engine A has a significantly higher peak efficiency of 45%.

NO_x emission maps (Figure 2) for all four engines are fairly similar in terms of the location of peak emission levels on the speed-load map, but the peak values vary widely from 325 mg/s for Engine B to 515 mg/s for Engine D. Peak PM emissions (Figure 3) also vary considerably from 9.3 mg/s for Engine D to 17.8 mg/s for Engine C. Although Engine D has the lowest peak PM emissions, this engine produces high PM emissions over a much wider range of operating conditions and at much lower loads than the other three engines.

Future Directions

Preliminary plans for FY2008 include acquiring data and producing similar information for a 2007 emissions compliant, heavy-duty diesel engine.

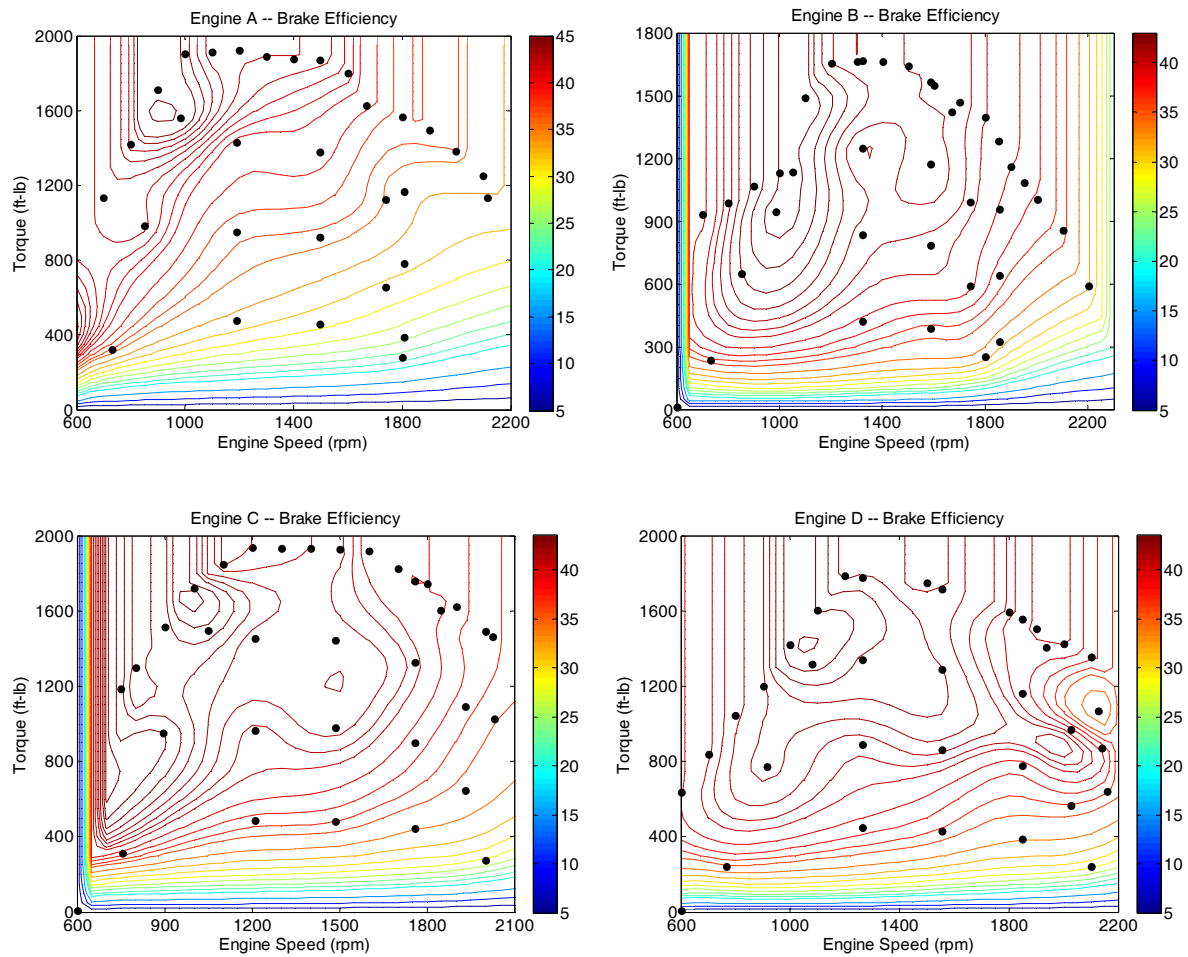


Figure 1. Graphical representation of the PSAT brake efficiency maps for four, 2004-compliant, heavy-duty diesel engines.

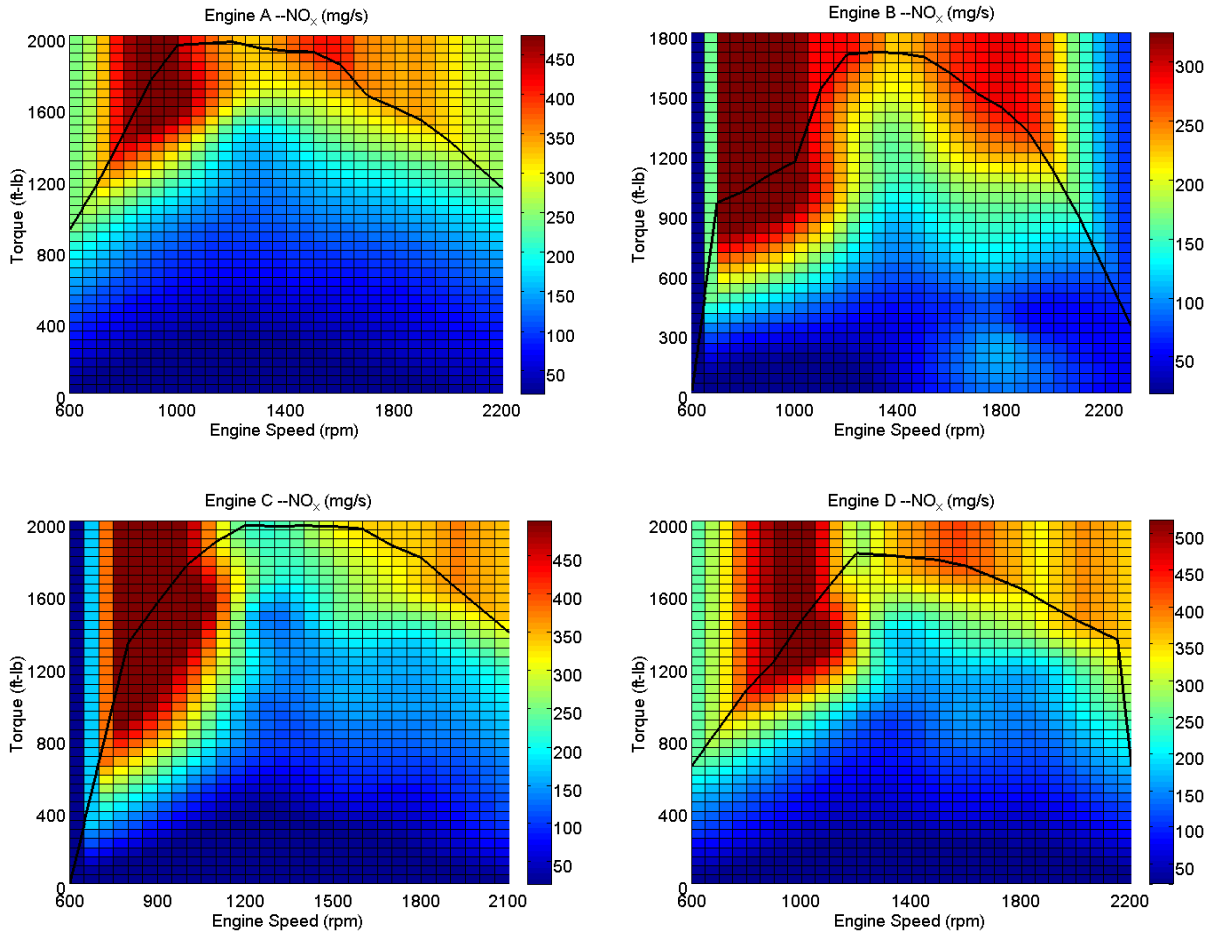


Figure 2. Graphical representation of the PSAT NO_x engine out emissions maps for four, 2004-compliant, heavy-duty diesel engines.

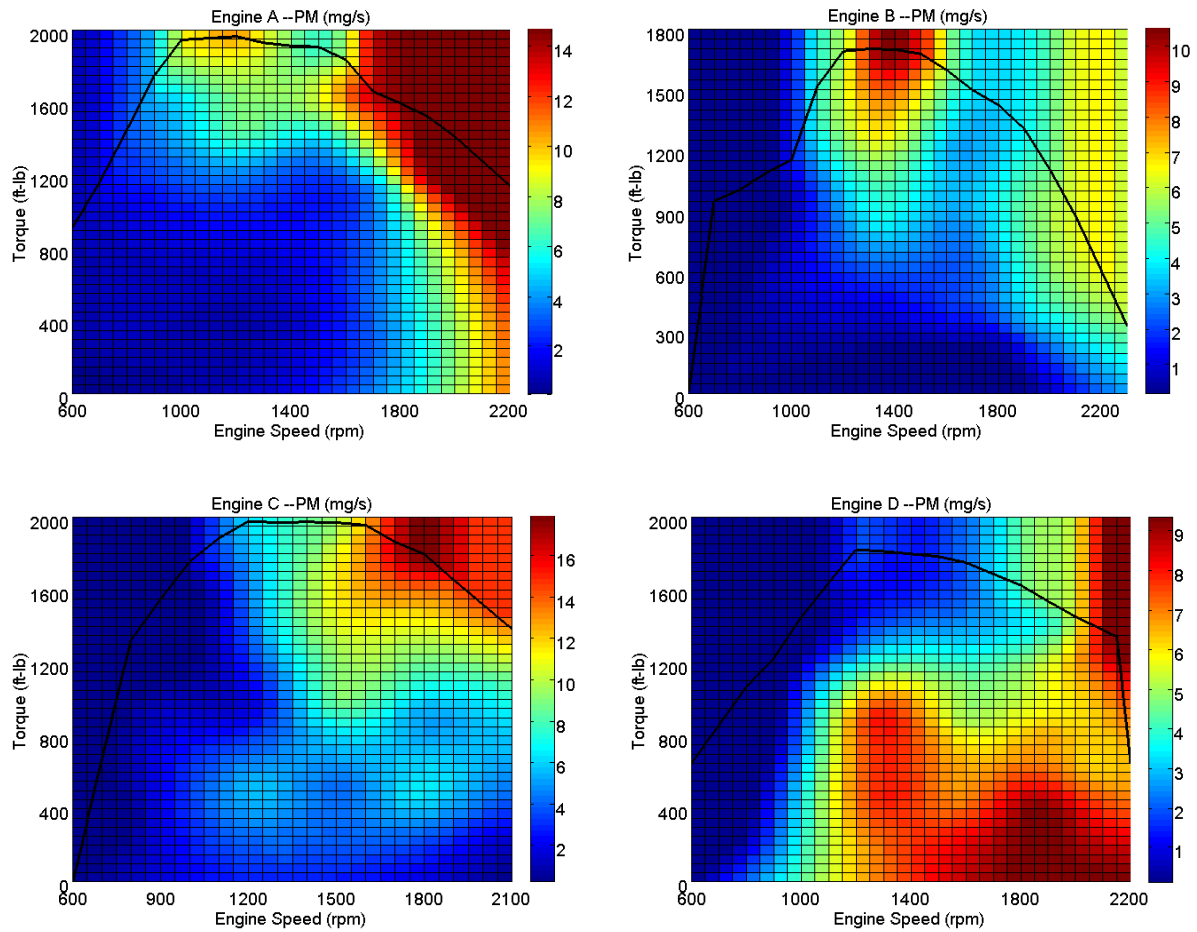


Figure 3. Graphical representation of the PSAT PM engine out emissions maps for four, 2004-compliant, heavy-duty diesel engines.

C. Heavy Truck Duty Cycle (HTDC) Project

Principal Investigator: Helmut E. (Bill) Knee

Oak Ridge National Laboratory

National Transportation Research Center

2360 Cherahala Boulevard, Room J-14

Knoxville, TN 37932-6472

(865) 946-1300, e-mail: kneehe@ornl.gov

DOE Program Manager: Lee Slezak

(202) 586-2335, e-mail: Lee.Slezak@ee.doe.gov

Objectives

The primary objective of this research is to collect real-world Class-8 (and in the future, Class-6) heavy vehicle performance data from instrumented tractor and trailers engaged in their normal vocational activities over a 12-month period of time. The data collected will involve not only velocity-time profiles, but tractor-trailer performance and situational data associated with such profiles that will allow for the calibration and independent evaluation of the Argonne National Laboratory-developed Class-8 PSAT (Powertrain Systems Analysis Toolkit) module. Such data includes gear ratio, engine torque, instantaneous fuel usage, location, highway grade, weight, time-of day, weather data, wind velocity and direction, etc. In addition, another primary objective is to develop a Duty Cycle Generation Tool (DCGenT) that will allow users to select from a number of duty cycle characteristics of interest, identify duty cycle segments that conform to these characteristics, and to statistically generate a single duty cycle that reflects is representative of the characteristics of the set. Lastly, one or more energy efficiency based studies related to the data collected in this effort will be conducted. It should be noted that one of the project partners is Michelin Tires (Greenville, South Carolina) who provided New Generation Single Wide-Based Tires (NGSWBTs) for half of the test fleet and new standard dual tires for the other half. An area of interest is to determine the fuel efficiency effects of the NGSWBTs compared to dual tires in real-world operations (it should be noted that in the pilot phase of this work, a 2.9% fuel savings for trans-America operation was experienced (the tractor, trailer, payload, route, and driver were the same, and the dates for the testing were in close proximity). It should be mentioned that Michelin has been a partner to ORNL in all phases of this research. Dana Corp. of Kalamazoo, Michigan was an industry partner during pilot testing, and Schrader Trucking of Jefferson City, Tennessee was a partner during the 12-month field test. Plans for collecting duty cycle information from Class-6 vehicles are being made.

Approach

This project was initiated by identifying the Class-8 truck performance and situational parameters that would be of interest to:

- The Department of Energy (DOE) to support decisions related to future technology research and investment (e.g., the study of the performance of heavy hybrids in real world environments),
- Developers of the Class-8 PSAT (C8PSAT) module to support its development and independent evaluation,
- Other federal agencies (e.g., the Environmental Protection Agency [EPA] and their interest in the development of a set of standard, but real-world based duty cycles; and the Department of Defense and their interest in duty cycles to reduce the fuel consumption of their truck fleet),
- The trucking industry to better understand how to improve the efficiencies and productivities of their fleets,
- Other heavy truck research communities who have virtually no good source of real-world operational/performance data for large truck fleets on which to base their research.

Pilot testing was conducted to: 1) confirm the list of parameters for which data was to be conducted in the Field Operational Test (FOT), 2) harden the data collection suite and the data acquisition system, and 3) to collect initial data to assess the impact on fuel efficiencies of NGSWBTs. Pilot testing was done with a partnership between ORNL, Dana Corp., and Michelin.

The FOT was initiated in October 2006 after six tractors and ten trailers from Schrader Trucking were instrumented. The FOT involved the phased “launch” of these instrumented tractor trailers for a period of 12-months. The FOT will continue through December 2007. As of the end of September 2007, more than 200Gbytes of compressed data have been collected, reviewed for validity, and placed into the Heavy Truck Duty Cycle (HTDC) data archive. Selected analyses of the data will be conducted along with the preparation of a final report (March 2008).

A Duty Cycle Generation Tool (DCGenT) will have been developed by early 2008 to support data analyses, and plans will be made to extend the data collection efforts to Class-6 vehicles.

Accomplishments in FY2007

- Completed the installation of six data acquisition systems, weather stations and other sensors on six tractors belonging to Schrader Trucking.
- Completed the installation of Air-Weigh sensors on ten box trailers belonging to Schrader Trucking.
- More than \$100,000 of equipment was installed on the test vehicles.
- Oversaw the installation of new tires (NGSWBTs and standard dual tires, both of which were donated by Michelin for this test) on the test tractors and trailers.
- Completed a media event at the National Transportation Research Center (NTRC) on October 26, 2006 for the signing of a Memorandum of Understanding (MOU) between DOE, ORNL and Schrader Trucking.
- Conducted a phased “launch” of the test vehicle during November/December 2006.
- Traveled to Jefferson City, Tennessee (headquarters of Schrader Trucking) weekly (on weekends) to download data from test trucks.
- Collected more than 200GBytes of compressed data during the FOT through September 2007.
- Addressed equipment problems related to the weather stations and other on-board equipment as they arose.
- Developed data viewing utility that would allow the research staff to visually see the data allowing quick identification of outliers, missing data, or erroneous data.
- Initiated the development of the Duty Cycle Generation Tool (DCGenT) which would allow users to specify characteristics of a duty cycle of interest, search the database for data that matches the selected characteristics, and to statistically integrate this data forming a duty cycle based on real-world data and reflective of the selected characteristics.
- Initiated data analyses on the fuel efficiencies of NGSWBTs compared to standard dual tires.
- Planned for the initial de-instrumentation of the first of the test vehicles in early FY2008.
- Planned for the completion of the DCGenT.
- Planned for the conduct of dyno testing (in early FY2008) using West Virginia’s portable dynamometer in order to generate wheel torque for a set of duty cycles including at least one from the collected real-world data.
- Worked with DOE, ANL and DSI (a Canadian firm) to identify a three-way evaluation of C8PSAT, ORNL’s real-world data and the Easy-5 code. An initial set of duty cycles were provided to DSI. Results of the comparison are expected in FY2008.
- Met with the DOE sponsor to plan the continuation of this research in FY2008 with planning for the collection of Class-6 duty cycle data.
- Initiated a dialogue with the Environmental Protection Agency concerning the collection of Class-8-based emissions data during dyno testing and from Class-6 vehicles during the FOT.
- Initiated writing of the FOT Final Report.

Future Directions

- Identify multiple Class-6 fleets for selected vocations for partnership purposes in the collection of Class-6 duty cycle data.

- Formulate and execute MOUs with selected vocational fleets.
- Re-evaluate data parameters for Class-6 data collection efforts.
- Seek sponsorship for Class-6 Duty Cycle effort from EPA.
- Work with EPA to define emission data collection requirements.
- Plan for 3-month data collection periods for selected Class-6 vocations.
- Initiate the collection of duty-cycle data on class-6 vehicles.
- As possible, refine the DCGenT.
- As possible, conduct specific data analyses for class-8 data.
- Compare ORNL Class-8 data to results from C8PSAT and Easy-5.
- Seek stronger alignment with the 21st Century Truck Initiative, the DOE “Super Truck” concept, and the National Transportation Research Center, Inc.’s (NTRCI’s) “Safe Truck” concept.
- Seek integrative energy efficiency and safety research including cross-agency research.
- Collect and analyze vehicle performance and duty cycle data on advanced vehicles.

Introduction

Nearly 80% of the U.S. domestic freight revenue involves the use of heavy trucks. Current trucking industry issues encompass a fine-balance of concerns related to the economical, safe, and secure operation of heavy trucks on our highways. In order to move toward an effective solution-set that optimally balances such concerns, a firm understanding of the nature and characteristics of heavy truck driving and their associated duty cycles in the US is critical.

The trucking industry in the U.S. involves considerable use of heavy trucks (Class-8 and Class 6 being the classes which consumes the most fuel), operates in relatively small fleets (50% of the fleets in the U.S. are less than 100 trucks, and 25% of the fleets in the U.S. are less than 10 trucks), operates on small profit margins, and is faced with considerable regulatory and economic pressures (e.g., issues related to hours-of-operation, and reduction of truck idling time). Making heavy trucks more efficient through new technologies or fleet management protocols is a goal that would contribute to larger profit margins and would also contribute to a reduced dependence on oil, and reduced emissions. Since efficient systems are also typically more inherently safe, lives could also be saved.

A practical dilemma involves knowing what the true benefits of new energy efficient technologies are.

Most benefit assessments are based on existing information on heavy truck operation. Much of this information is stylized and based on duty cycles that are meant to test various emission or fuel economy measurements. For example, the FTP Transient Cycle is a transient engine dynamometer cycle for heavy-duty truck and bus engines. It includes segments designed to simulate both urban and freeway driving and used for emission certification testing of heavy-duty diesel engines in the U.S. Another example is the Urban Dynamometer Driving Schedule (UDDS) which is an EPA transient chassis dynamometer test cycle for heavy-duty vehicles. While cycles such as these are based on an understanding of the vehicle technology and how best vehicles might be tested to assess emissions and fuel economy, they do not really reflect real world driving and the real demands placed on the vehicle, driver or vehicle systems.

Despite common beliefs, knowledge of how trucks actually operate on our highways is not well known. With hours-of-operation rules, recurring congestion in urban environments, anti-idling regulations, differing fleet management philosophies, weather, the need to deal with incidents of non-recurring congestion, and encountering various topological conditions, only the most highly experienced heavy truck driver has a true situational awareness of the characteristics of driving on our nation’s highways. A better understanding of the effects of these impacts

on driving, as captured via a field test of heavy vehicle driving would provide a valuable asset to DOE, other federal agencies, as well as the trucking industry in evaluating technologies for energy efficiency, safety, emissions, fleet management, etc.

For DOE, such data and information would provide a basis on which to make decisions related to new technologies being developed to reduce fuel consumption, provide alternative power sources (e.g., fuel cells and hybrid engine technologies), transition to alternative fuels, and to reduce emissions. In particular, a database that reflects true driving experiences across various parameters such as geographic terrain, fleet size, fleet type, driving environment, driving protocols, etc., can provide a rich source of information that could be utilized to make sound energy efficiency-based technology decisions.

These and similar complimentary data needs of various agencies of the Department of Transportation, the Environmental Protection Agency, and the trucking industry require data and information on how trucks are actually utilized and driven in real-world environments, the geography over which they are operated, information related to the driving situation and the protocols and regulations that govern their operation. In addition, much of the current thinking, and research related to long-haul and urban/city driving are based on anecdotal information. A quantitative profile of the driving behavior of heavy trucks does not currently exist. A thorough understanding of the operation of heavy trucks within duty cycles that reflect real-world conditions is an asset that would have great benefit to DOE, other federal agencies, and the overall trucking industry.

Approach

This project will involve efforts to collect, analyze and archive data and information related to heavy-truck (Classes 8 and 6) operation in real-world driving environments. Such data and information will be usable to support technology evaluation efforts, and provide a means of accounting for real-world driving performance within heavy truck analyses. Additionally, the data collected will generate data, information, and duty cycles that will support Argonne National Laboratory's (ANL's) development of a Class-8 module for their

Powertrain System Analysis Toolkit (i.e., C8PSAT). Industry partners to date have included Michelin Americas Research and Development Corp., of Greenville SC, Dana Corporation of Kalamazoo, MI, and Schrader Trucking of Jefferson City, TN. These partners are interested in the vehicle dynamics of real world long-haul driving in order to support research in vehicle stability, tire performance, tire-road interface and operational efficiency improvements. Significant in-kind contributions were provided in the pilot testing phase of this project (more than \$400K of in-kind resources were contributed by Dana and Michelin. Similar resource contributions were provided by Michelin and Schrader in the field test portion of this work). Figure 1 shows one of six Volvo tractors used in the field testing portion of the Heavy Truck Duty Cycle (HTDC) project. The project is being conducted in two phases. These phases are:

Phase 1: PILOT TEST - Design, Testing and Evaluation of a Duty Cycle Data Collection System (initiated in January 2005 and concluded in March 2006). Conduct initial runs utilizing New Generation Single Wide-Based Tires (NGSWBTs – see Figure 2) and compare fuel efficiencies for the same vehicle and route using standard dual tires.

Phase 2: FIELD OPERATIONAL TEST - Fleet Instrumentation, Data Collection and Analyses (initiated in March 2006 and will be concluded in March 2008). Continue to collect data on NGSWBTs and standard dual tires.



Figure 1. One of Six Class-8 Tractors Owned by Schrader Trucking, Used in the HTDC Field Test.

Pilot Test Overview

In the Pilot Test Phase of this work, about 150 different parameters were identified, a prototype data acquisition system was developed; a weather/wind station, emissions sensor, databus link, GPS, weight sensor, as well as other sensors were installed in a pilot test tractor-trailer donated for use in the pilot testing by Dana Corp. Data on 104 parameters were collected at 100Hz for two east-west trans-America runs (one with NGSWBS and the other with standard dual tires), and two north-south runs (again each with a different tire configuration).



Figure 2. Ms. Sue Nelson (Michelin) with a NGSBWT Mounted on One of the Schrader Instrumented Tractor-Trailers

This effort confirmed ORNL's capability to collect relevant data, allowed for the reduction of the parameter set to collect data from sensors that functioned adequately (the set was reduced from 104 to 60 parameters), allowed for the reduction of the data collection rate, allowed for the hardening of the data acquisition system, and provided data to conduct a preliminary analysis of the effect of NGSWBTs on fuel efficiencies. Overall, it reduced the risk of something going wrong in the much more expensive Field Operational Test. In addition, analysis of the fuel consumption data collected during the pilot testing indicated a 2.9% fuel savings when the same vehicle, with the same driver and the same payload traveled the same segments of highway, but utilizing NGSWBTs on one run, and new Michelin standard dual tires on another run. When this data was corrected for congestion effects, an 8.0% fuel savings was seen when the NGSWBTs were used.

Pilot testing was concluded by demonstrating the capability to generate duty cycle information that could be utilized by PSAT.

Field Test Overview

The Field Operational Test (FOT) involved the instrumentation of six tractors and ten trailers from the Schrader Trucking Company located in Jefferson City, TN. Instrumentation of the tractors and trailers was completed in October 2006, and data collection commenced with the signing of a Memorandum of Agreement (MOA) between DOE, ORNL, and Schrader Trucking. Figure 3 shows the signing of the MOA on October 26, 2006 at the National Transportation Research Center (NTRC).



Figure 3. HTDC Memorandum of Agreement Being Signed by (l-to-r) Dr. Dana Christensen (ORNL Associate Laboratory Director for Energy and Engineering Sciences), Mr. Phil Schrader (Co-Owner Schrader Trucking), Mr. Tom Hodge (Co-Owner Schrader Trucking) and Mr. Lee Slezak (DOE OVT).

The FOT collects 60 channels of data from each truck at 5Hz. This data relates to engine performance, vehicle performance, location, topology, weather conditions, and road conditions. The tractors and trailers engage in normal Schrader-based vocational activities, were donated for use to this test by Schrader at no charge to the project, and entered the field test in a staged manner to assure that there is no equipment or experimental weaknesses. Data for each tractor-trailer will have been collected for a period of 12 months. Half of the instrumented portion of the test fleet uses new Michelin NGSWBTs while the other half uses new Michelin standard dual tires. All test-vehicle tires were donated by Michelin at no charge to the project.

The routes traveled by Schrader trucking provide a diversity of topology (city, urban and rural highways) and have demonstrated various weather and road conditions. A data archive was developed to manage, cleanse, and archive the 200GBytes of compressed data (as of September 30, 2007) collected during the FOT. In addition, the development of a Duty Cycle Generation Tool (DCGent) was initiated that will allow for the generation of duty cycles based on a set of user-specified characteristics (e.g., grade, speed, time-of-day, urban/rural, weight, etc.). Over the past year, ORNL has been contacted by a number of private industry representatives concerning access to HTDC data. One firm, DSI of Ontario Canada was interested in duty cycle information to conduct simulations using their Easy-5 code. DOE agreed to allow ORNL to provide some subset of data to DSI in return for results of running Easy-5 on HTDC duty cycle data. The results of these runs will be compared to associated data in the HTDC data archive, and eventually with results of C8PSAT run on the same duty cycles. This work will be carried out in 2008.

Lastly, ORNL made plans to take one of the Schrader trucks used in the FOT to West Virginia University (WVU), to utilize their portable dyno to run three duty cycles (one of which will be a HTDC generated duty cycle, and the other two being (a) a duty cycle that will experience each of the ten gear ratios of the truck for two minutes, and (b) a standard duty cycle run by WVU for comparison of performance to the performance of other trucks on this cycle). The purpose of the dyno testing will be to generate drive torque data that can later be

extrapolated to other duty cycles not run on the dyno. In addition, emissions data will be taken to associate such data with the real-world duty cycles. Discussions with the Environmental Protection Agency (EPA) indicate a strong interest in real-world-based emissions data for Class-8 trucks and even a stronger interest in emissions data for Class-6 trucks.

Future Directions

This project will provide a valuable asset for making heavy truck energy efficiency technology decisions based on real-world performance data. In particular, it will provide input for developing, calibrating, testing and evaluating ANL's Class-8 module for PSAT, and will result in the development of a duty-cycle generation tool capable of generating custom duty cycles for various user-specified long-haul characteristics. Future directions for this work will be to enrich the database with data that provides greater breadth and depth to analysis capabilities. That is, to collect and analyze data on other vehicle types (e.g., Class-6 vocational applications), situational circumstances, operational protocols, etc. Such a capability would support the establishment of a national data archive for heavy truck performance data, and would be a valuable national asset for heavy truck energy efficiency research. Inclusion of safety data and information might also be a long-term goal that could receive cross-agency attention and support. Lastly, a future goal is to gain a deeper understanding of heavy truck operations on our nation's highways. The availability of a national archive of heavy truck performance data could support the establishment of a Center of Excellence in Heavy Truck Performance Research.

V. OFF-HIGHWAY

A. Hybrid energy storage and fuel optimization

Principal Investigator: Lembit Salasoo
General Electric Global Research
1 Research Circle, Niskayuna NY 12309
(518) 387-500; fax: (518) 387-6675; e-mail: salasoo@crd.ge.com

Field Project Manager: Christopher Johnson
National Energy Technology Laboratory
Morgantown, WV 26507-0880
(304) 285-4618; e-mail: cjohnson@netl.doe.gov

Technology Development Manager: Lee Slezak
(202) 586-4819; e-mail: Lee.Slezak@ee.doe.gov

Contractor: General Electric Global Research
Contract No.: DE-FC04-2002AL68284

Objective

- Develop and demonstrate locomotive system technologies targeting gross fuel efficiency gains
- Demonstrate a modular energy storage system for hybrid locomotive system on a hybrid locomotive platform
- Develop optimization software for minimizing fuel consumption in both hybrid and non-hybrid locomotives, and demonstrate the consist optimizer on the test track
- Demonstrate the combination of modular energy storage system and fuel optimizer on a hybrid locomotive with full-scale energy storage system

Approach

- Specify and develop advanced modular energy storage units and lab test prototype modules
- Design and bench test advanced hybrid locomotive energy management system (EMS) controls and demonstrate on a hybrid locomotive on a test track
- Develop suitable models for dynamic optimization of fuel use
- Develop practical robust fuel use optimization algorithms capable of locomotive implementation
- Demonstrate fuel use optimization algorithms in off-line interactive simulation environment
- Complete field demonstrations of selected fuel saving algorithms
- Fabricate and bench test full-scale energy storage modules and associated controls
- Integrate full-scale energy storage modules to hybrid locomotive
- Design, fabricate and bench test hybrid fuel optimizer controls
- Integrate fuel optimizer controls on hybrid locomotive, demonstrate on test track
- Measure and verify fuel savings benefit

Accomplishments

- GE unveiled the Evolution® Hybrid locomotive on May 24, 2007 at Union Station, Los Angeles, as part of its 2nd anniversary Ecomagination event
- Received subscale battery mockup with vibration-resistant features
- GE decision to re-engineer the battery case, by applying a combination of in-house and contracted expertise

Future Direction

- Re-engineer locomotive-worthy hybrid energy storage modules
- Design the integration of hybrid energy storage system to the hybrid locomotive platform
- Fabricate full locomotive set of hybrid energy storage modules, integrate system to the hybrid locomotive and track test
- On-locomotive test of hybrid fuel optimization controls
- Fuel performance of combined system will be measured and verified

Introduction

The 21st Century Locomotive Technology project was proposed by GE to improve locomotive efficiency with energy management and optimization technologies, and to develop advanced fuel injection and turbomachinery technologies for an emissions-compliant and fuel efficient power plant. The energy management and optimization technologies are projected to produce a combined 20% reduction in total fuel consumption with emissions at the baseline or lower. This annual report applies in particular to the progress for the two locomotive systems technologies of hybrid energy storage and fuel optimization.

GE unveiled the Evolution® Hybrid locomotive on May 24, 2007 at Union Station, Los Angeles, as part of its 2nd anniversary Ecomagination event. This development was enabled by the locomotive battery technology task of the 21st Century Locomotive Technology project. Simulation displays at Union Station and also Universal Studios showcased the operation and benefits of both the hybrid battery and fuel optimizer technologies addressed by this project.

Significant delays by a battery vendor to deliver a vibration-hardened hybrid locomotive energy storage battery module have led GE to plan an alternate approach to this task, by convening a new team for the re-engineering of the battery case.

Benefits for locomotives and road vehicles

The rail modality carries approximately 40% of US freight on a ton-mile basis, and in 2003, the Class 1

railroads consumed 3.85 billion gallons of fuel to move this freight. Application of the energy management and optimization technologies developed in this project to the whole locomotive fleet will save approximately 770 million gallons of fuel annually. Further, as fuel prices rise and global oil supply tightens, increasing railroad fuel efficiency makes transfer of freight transportation mode from less fuel-efficient modalities to rail increasingly attractive on an economic basis, producing significant impact on the national strategic imperative to reduce dependence on foreign oil. That is, the increase in railroad fuel efficiency will naturally provide the market-based signals to transfer freight transportation to rail from modalities with significantly lower fuel efficiency.

Reducing the energy expended in completing a mission reduces fuel use and emissions production. Optimization algorithms developed manage how the train is driven to meet travel time objectives, subject to track and train constraints, with the least fuel possible. While the precise variability is still being quantified, savings exceeding 4% have been demonstrated in several test runs. The advanced fuel optimizer and modular hybrid energy storage technologies developed in the 21st Century Locomotive Technology project have the potential to be applied for fuel efficiency improvement of on-the-road vehicles.

GE unveils Hybrid Locomotive and Fuel Optimizer technologies, acknowledges DOE

GE unveiled the Evolution® Hybrid locomotive on May 24, 2007 at Union Station, Los Angeles, as part of its 2nd anniversary Ecomagination event in California (Figure 1). In a 6-minute segment titled “The Right Track” on the NBC Today Show, GE CEO and Chairman Jeff Immelt, standing in front of the Evolution Hybrid Locomotive (Figure 2), emphasized that the Hybrid Evo technology would deliver 10% emissions and fuel savings, of particular importance to California since the bulk of US Pacific trade is shipped through California’s ports. The blue-and-green hybrid carried US DOE decals to acknowledge the technology contribution of the 21st Century Locomotive Technology and the Hybrid Mine Truck projects to the success of the Hybrid Locomotive and Trip Optimizer technologies at the demonstration.



Figure 1. GE Evolution Hybrid demonstrator locomotive on display at Union Station, Los Angeles.



Figure 2. NBC Today Show live interview of GE CEO Jeff Immelt & LA Mayor Antonio Villaraigosa.

A GE Transportation and GE Global Research team designed and built the hybrid demonstrator locomotive, as well as stationary simulation consoles to explain and

demonstrate the operation of hybrid technology and trip optimizer technology. The Union Station location hosted visitors from GE’s railroad customers and federal, state, regional and local government agencies in order to present the range of GE’s locomotive emissions and fuel reduction technologies, including Trip Optimizer and the Hybrid Locomotive. Due to other commitments, DOE Undersecretary Karsner and other officials were unable to attend. The stationary simulation consoles enabled the visitors to drive a locomotive in simulation, view the accumulating fuel and emissions savings, the operation of the hybrid energy storage, and compare manual and optimized driving strategies. A particular hit was the Trip Optimizer Challenge, where guests drove a locomotive to meet speed limits and a target trip time while trying to beat the optimized fuel consumption target.

Advanced modular energy storage system

A hybrid locomotive will store otherwise-wasted locomotive braking energy and reuse this energy for traction, thereby reducing fuel consumption 10-15%, while keeping emissions at the baseline or lower. The energy storage system (ESS) is the core part of the overall hybrid locomotive system. In previous years, sodium nickel chloride technology was selected for the hybrid locomotive, battery module voltage was set and an upgraded battery module cooling system design was developed. Three accelerated vibration tests were performed on the existing module design to identify failure modes to be addressed by locomotive-specific module redesign. A test program quantified the effects of connecting a cold battery to the locomotive system.

In FY2007, the battery vendor delivered a subscale “mockup” battery to validate the vibration performance of an improved design developed by the vendor. The delivery occurred after significant delays arising due to nontechnical issues at the vendor. To recover project momentum and ensure technical success, GE has decided to take an alternate approach to this task and convene a new team for the re-engineering of the battery case. It is planned to have the first re-engineered vibration-hardened battery ready by the end of FY2008.

Conclusions

The GE project team looks forward in FY2008 to developing locomotive-hardened advanced hybrid energy storage modules and fully developing fuel optimization technology that utilizes the additional

degrees of freedom presented by locomotive hybridization. The combination of these technologies will yield double-digit percentage reduction in fuel usage in freight haulage applications, a significant benefit to one of the dominant US freight transportation modalities.

B. Advanced Hybrid Propulsion and Energy Management System for High Efficiency, Off Highway, 240 Ton Class, Diesel Electric Haul Trucks

Principal Investigator: Tim Richter

*GE Global Research, 1 Research Circle, EP110C, Niskayuna, NY 12309
(518) 387-5670; fax: (518) 387-6675; e-mail: tim.richter@ge.com*

Technology Development Area Specialist: Lee Slezak

(202) 586-2335; fax: (202) 586-1610; e-mail: lee.slezak@ee.doe.gov

Field Project Manager: Chris Johnson

(304) 285-4718; fax: (304) 285-4403; e-mail: Christopher.Johnson@or.netl.doe.gov

Participants

Lauren Richards, GE Global Research

Kevin Gavel, GE Global Research

Gary Kilinski, GE Global Research

Dwight McCormick, GE Global Research

Henry Young, GE Transportation

Bertrand Bastien, GE Transportation

Tim Brown, GE Transportation

Allen Randolph, GE Transportation

Lori Kieklak, GE Transportation

Kim Byard, Komatsu America Corp.

Dan Funcannon, Komatsu America Corp.

Contractor: GE Global Research

Contract No.: DE-FC04-2002AL68080

Objective

The objective of this project is to reduce the fuel consumption of off-highway vehicles (OHVs), specifically large tonnage mine haul trucks. A hybrid energy storage and management system will be added to a conventional diesel-electric truck that will allow capture of braking energy normally dissipated in grid resistors as heat. The captured energy will be used during acceleration and motoring, reducing the diesel engine load, thus conserving fuel.

Approach

The project will work towards a system validation of the hybrid system by first selecting an energy storage subsystem and energy management subsystem. Laboratory testing at a subscale level will evaluate these selections and then a full-scale laboratory test will be performed. After the subsystems have been proven at the full-scale lab, equipment will be mounted on a mine haul truck and integrated with the vehicle systems. The integrated hybrid components will be exercised to show functionality, capability, and fuel economy impacts in a mine setting.

Accomplishments in FY 2007

- Sub-scale 4-pack battery hybrid operation
- All hybrid components integrated on vehicle
 - 8-pack battery enclosure

- 4-pack battery enclosure
- Inductors
- Power Electronics
- Controls
- User Interface
- Full-scale charge cart assembled and operational
- Successful initial full-power hybrid operation in fuel saving and performance modes.

Future Direction

The above accomplishments demonstrated on-truck hybrid capability at full power ratings. Shortly after the initial tests were complete, product test demands required reallocation of hybrid engineers and test facilities delaying further testing of the vehicle. The team will restart truck systems in FY 2008 for a planned demonstration to the Department of Energy in January 2008.

During initial testing of the hybrid systems on the vehicle, the battery components were of primary interest. Throughout the duration of the testing, the batteries performed well during discharge events but showed higher than expected resistance during charge events. This high resistance limited charging capability and will have a direct impact on fuel savings. Several characterization tests were run to better understand the nature of the resistance rise and efforts are continuing to link observed behavior to battery physics.

Based on experience in FY 2007, the team believes that efforts in FY 2008 should focus on diving more deeply into fundamental battery capability with specific effort on the transient nature of the OHV application. In addition, the team will complete testing on the hybrid OHV and demonstrate hybrid operation to the DOE. Further testing will drive additional data that will be used to validate and finalize the vehicle system model and assist in correlating laboratory battery testing to application-specific cycles and installations.

Introduction

The conventional mine haul truck, also referred to as an Off-Highway Vehicle (OHV), uses a diesel engine to turn an alternator that generates alternating current (AC) electricity. The electricity is rectified to DC voltage that is applied to the main electrical bus called the DC Link. Power electronics convert the DC link voltage to variable frequency, 3-phase AC that drives the wheel motors during motoring. When braking is required, the wheel motors function as generators and electrical power is directed to the Braking Grid Resistors, also known as the “Grid Box,” to be dissipated as heat. In addition to traction motors, the diesel engine must power auxiliary loads such as radiator cooling fans, operator air conditioning, steering, hydraulics, and control circuits. These auxiliary loads are powered by mechanical means and with a smaller, second alternator connected to the vehicle’s 24V battery system.

Figure 1 shows a block diagram of the hybrid vehicle system. Three primary components will be added to the conventional OHV: Hybrid Vehicle System Controls, Energy Management System, and Energy Storage System. Each component plays a specific role in the recovery of braking energy.

The Hybrid Vehicle System Controls perform the high-level supervisory functions of the hybrid vehicle, primarily controlling the balance of engine power, grid dissipation and battery charging or discharging. Performing these functions requires intimate connections to all of the truck systems.

The Energy Management System (EMS) acts to convert electrical power on the DC link into levels compatible with the Energy Storage System. The EMS is essentially a high power DC-DC converter. The Energy Storage System (ESS) consists of the batteries and manual disconnects, fuses and related safety and protective components.

The hybrid system can operate in three modes: baseline, fuel saving, and performance. The baseline mode simply disables the hybrid system. The fuel saving mode uses the diesel engine and hybrid power to provide rated power to the wheels. This mode results in fuel savings as the engine is providing less than rated power; however, productivity is reduced because of the hybrid weight overhead. The performance mode utilizes full engine power supplemented with hybrid power for extra speed on grade, increasing productivity. This mode can realize simultaneously realize fuel savings as the engine is running for less time during uphill hauls.

Full-scale Laboratory Evaluation

GE Transportation (GET) operates a 3500hp dynamometer for functional and performance testing of OHV propulsion systems. The facility can emulate all vehicle systems in a controlled environment allowing instrumentation of the system for analysis and troubleshooting. The entire battery system, with all control components and software, was assembled for evaluation prior to the truck integration. The facility is shown in Figure 3.

The full-scale battery test facility consists of twelve batteries connected with a CAN communication system. Each battery has a management controller on the CAN network and is capable of communicating status messages, such as temperature and state-of-charge (SOC), and receiving commands from the system controller. The GET team has fully integrated and tested CAN communication between all components, including the high voltage batteries. Galvanic isolation was installed on the CAN bus from the batteries to prevent damage or hazards in the control groups.

The power electronics unit found on production trucks is used to provide wheel motor and braking grid power control, as well as perform some hybrid power management. The standard propulsion system controller has been adapted to interface with the hybrid controller to enable smooth response of diesel engine and battery power to the wheels based on driver commands.

The full-scale laboratory has proven very useful for software code development and testing throughout the integration period. As demonstrated by the successful maiden test of the hybrid truck, the full-

scale laboratory configuration enabled a “build once” and operate system that provide functional capability with no redesign and minimal debugging.

Vehicle Integration

Four primary hybrid equipment groups are located on the vehicle: two battery enclosures, one hybrid control group, and one inductor group, shown in Figure 4. The batteries are mounted in two separate enclosures. These enclosures mount on the right-front upper deck and front bumper. The front bumper enclosure includes receptacles for off-truck battery charging and monitoring, when needed. Each enclosure is vibration isolated from the truck’s frame to minimize the risk of mechanical battery failure. The battery enclosures also host appropriate support components, such as disconnect switches and cooling fans.

The battery enclosures are designed to be compact, reducing weight overhead and affording visibility for the driver when possible. Visibility is a concern for the enclosure on the upper right-front deck. Two visual aids, additional mirrors and a camera system have been installed to improve the driver’s view of objects around the truck. The enclosures are air-cooled using filtered air and include means to quickly charge one or more batteries using off-board factory chargers to verify SOC and other diagnostic features.

The Hybrid Control Group (HCG) contains support and interface components for hybrid equipment and was one of the first components installed. It is located behind the operator’s cab and houses power supplies (DC-DC converters), fuses, contactors and other auxiliary equipment. Reinforcements to the deck were designed and provided by Komatsu to shore up mounting locations for the HCG.

Smoothing reactors have been mounted between the frame rails in the rear of the vehicle. Komatsu supplied modifications to support the two iron-core inductors with a simple cross-member type mounting structure. A sheet metal cover provides protection from water and excessive dirt.

As reported in the 2006 annual report for this project, all of the hybrid components except for the battery packs had been installed. The four-pack battery enclosure was installed and a maiden test of this sub-

scale battery system was successfully performed in December 2006. The eight-pack battery was installed on the truck later in December and the completed vehicle is shown in Figure 2.

The first full-scale hybrid test run was performed in February 2007. The system successfully passed functional tests on 10% grades and representative mine haul conditions. One of the tests from the 10% grade is shown in Figure 5, below. The test consists of an uphill climb, turnaround and downhill descent.

After several days of testing and minor software changes, the system was parked for the summer as Komatsu and GE needed to support product testing requirements, putting the hybrid effort on hold. During this down time, the data collected from the initial test runs was compared against model predictions. Upgrades to the software were also made. The software upgrades will be uploaded to the hybrid demonstration truck in FY 2008 pending functional testing on the Building 50 sub-scale system. The data analysis is described in the next section.

The vibration isolation system has performed well and the team has not experienced any faults or failures directly attributable to vibration at this point. General operation of the hybrid system is transparent to the driver and there are no noticeable surges, step changes, or unpredictable behaviors from the hybrid system.

On-vehicle System Validation

The initial tests were performed at the Komatsu Proving Grounds, near Tuscan, AZ. An aerial photo of the mine is shown in Figure 6 with notations of possible test roads that can be used to test actual mine operation and steady-state operation using a constant 10% grade.

Limited data has been collected from the full-scale on-truck hybrid system during operation on 10% grades and mine haul roads. The data was compared to the system model and shows good agreement in general. One gap that has been identified is in the battery model. The dynamic resistance of the battery has enough significance to warrant additional detail in the system model; however, the fundamental cause of such behavior needs to be identified.

The battery model in the current system model is a simple voltage source with series resistance. This model works well for quickly sizing the battery and understanding basic losses associated with charging and discharging the battery. After reviewing actual test data, it is clear the battery model requires additional capability to more accurately predict performance and additional effort will be required to perform further testing, modeling and analysis.

When the vehicle is restarted in Fall 2007, additional tests with more rigorous test protocols will be run to generate sufficient data to establish baseline versus hybrid performance. The current data does not contain enough repeated runs to afford statistical significance to improvement measurements.

Battery Testing and Performance

Sub-scale battery testing was not performed in 2007; all testing was performed on-truck. Limited data is showing there is a need to better understand and characterize sodium batteries as applied to mine haul trucks. As described above, the initial data from the full-scale system showed a deviation from the simple battery model used for system studies, primarily differing on cell resistance.

The 12 batteries that were installed on the truck are still operational after several hundred hours of on-truck testing. One battery is reporting a single cell failure. That failure is a short-circuit failure. The battery continues to operate as expected, except the open circuit voltage is 2.58V lower than a full string.

For 2008, a no-cost project extension will be filed with the DOE requesting scope change from battery teardown to battery characterization. This work would exercise the batteries to understand cell performance with specific regard to representative OHV haul cycles. GE's related project, the 21st Century Locomotive, has an operating environment similar to OHV (high temperature, high vibration, etc), but the battery cycle requirements are much more severe in OHV applications. The charge current dominates battery stress and transients are more prevalent than in locomotive applications.

Conclusions

A full-scale working prototype has been built and put through initial tests. The initial performance and results are sufficient to show feasibility; however,

additional testing is required to produce meaningful performance benefits. The expected demonstration in 2007 was pushed into 2008 and GE will be proposing a continuation of the project through 2008. This continuation will perform further research on battery characterization to better understand the life and degradation modes of sodium batteries specific to the OHV cycle and installation.

As with nearly every hybrid vehicle project, it is clear that the battery aspect is the limiting technology in realizing a commercially viable system. GE is investing considerably in advanced battery technologies for hybrid locomotives and this same technology could be utilized on the OHV,

breaking the barrier of entry for this energy saving configuration. GE is proposing to utilize the remainder of this DOE project to pursue better understanding of battery technologies to specifically address the needs of OHV.

GE will complete testing of the hybrid OHV in 2008 and transition the system model and technology to GE Transportation. GE Transportation will move forward beyond this DOE project by looking at new hybrid system designs and analyzing specific mine profiles to tailor the hybrid design for future commercialization.

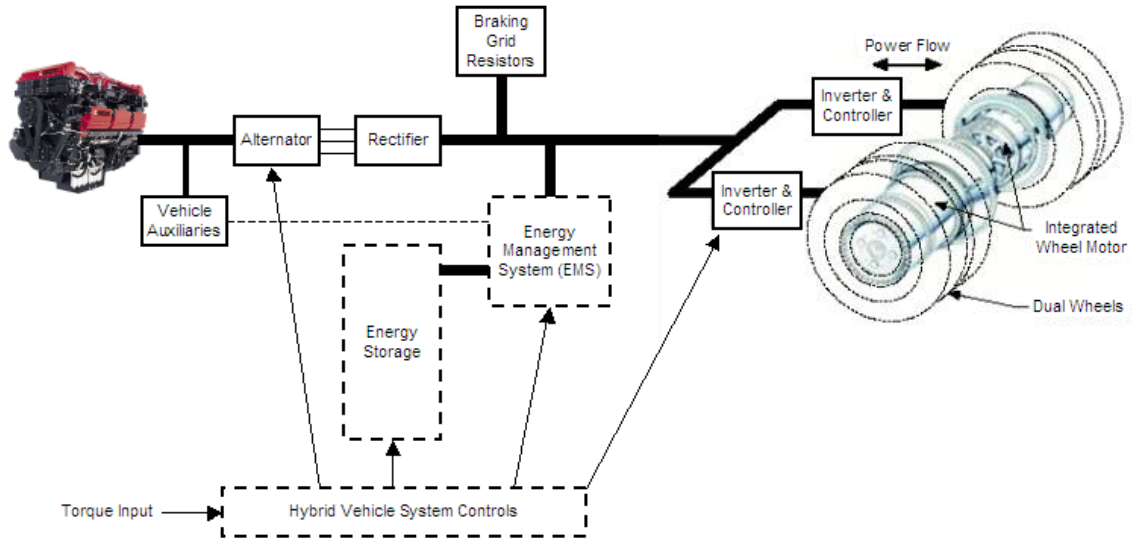


Figure 1. Hybrid Electric System Block Diagram



Figure 2. Komatsu 830E-AC Hybrid Mine Haul Truck

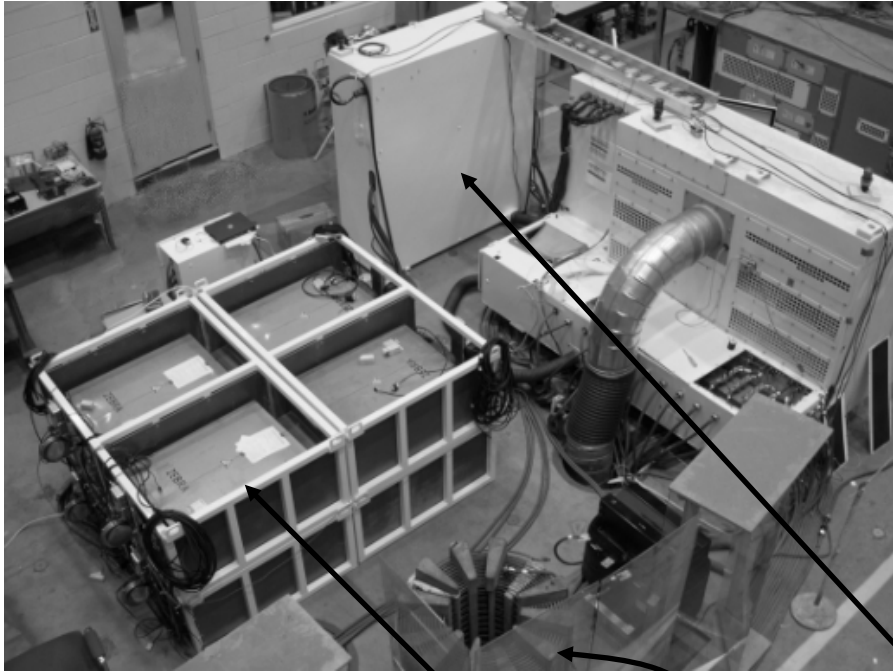


Figure 3. Full-scale test configuration

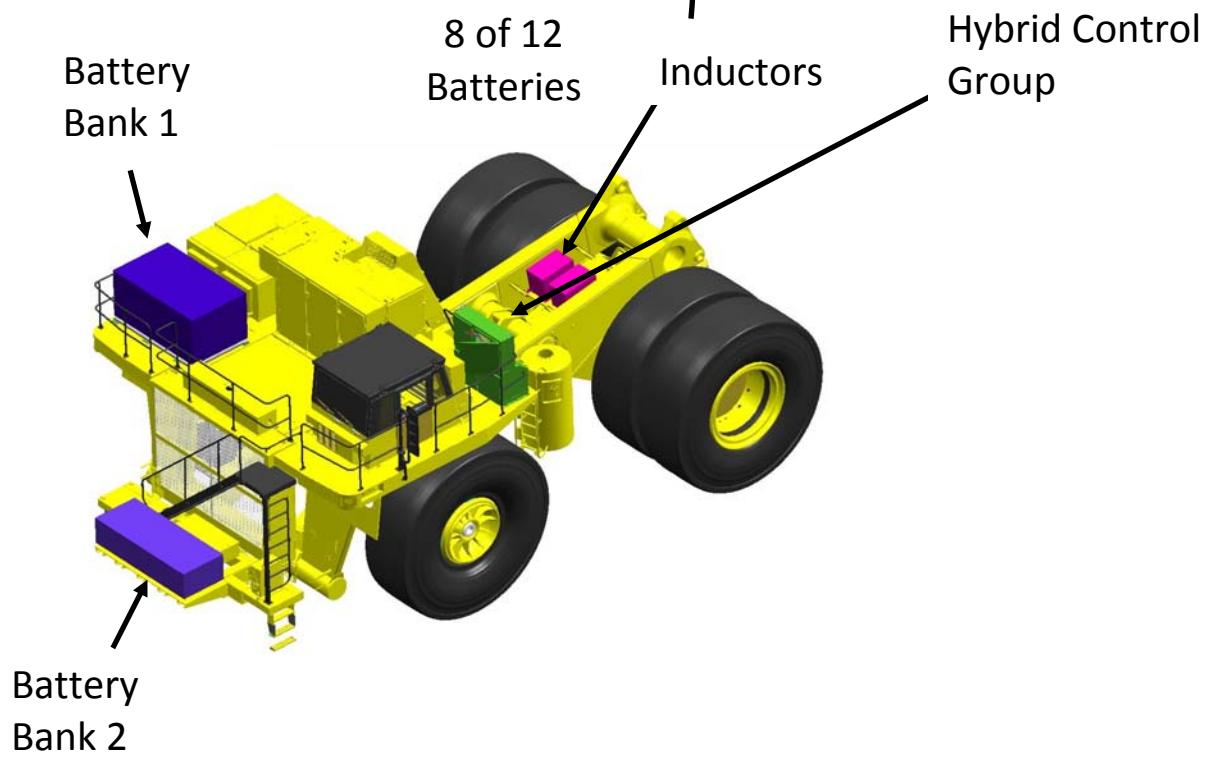


Figure 4. Hybrid Equipment Groups

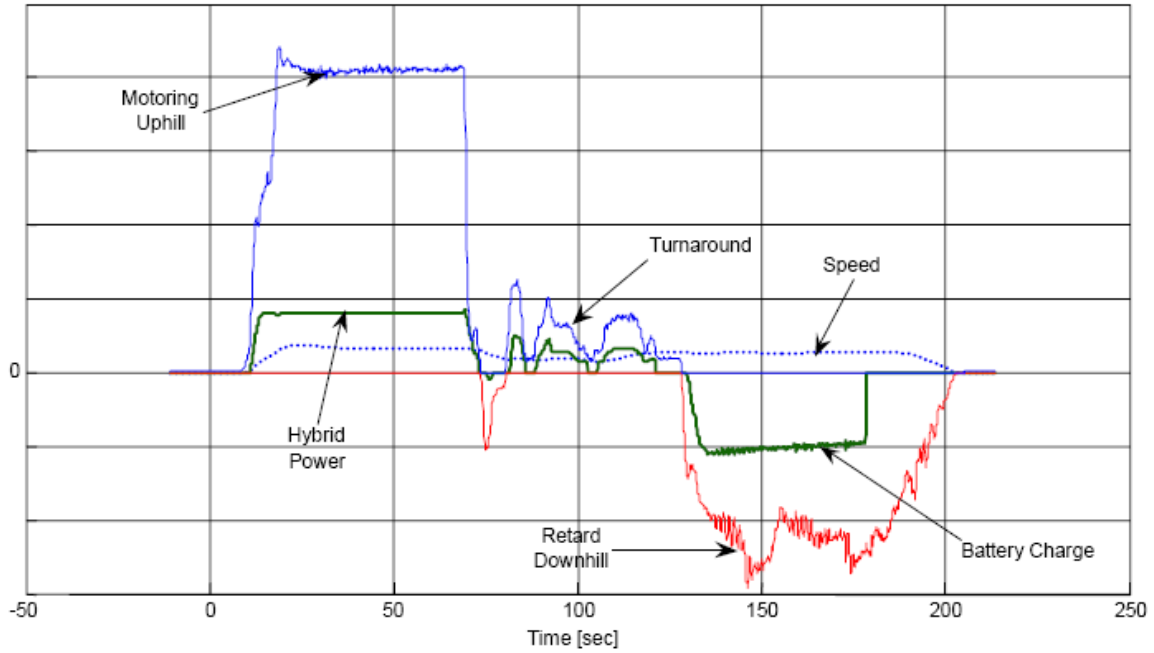


Figure 5. 10% Grade Hybrid Performance



Figure 6. Komatsu Proving Grounds, Green Valley, AZ

VI. EFFICIENCY IMPROVEMENTS FOR HEAVY VEHICLES

A. Truck Essential Power Systems Efficiency Improvements for Medium-Duty Trucks

*Principal Investigator/Technical Manager: Larry M. Slone
Caterpillar Inc. – Technology & Solutions Division
(309) 578-0243, fax: (309) 578-6285, e-mail: slone_larry_m@cat.com*

*Program Manager: Jeffrey F. Birkel
Caterpillar Inc. – Technology & Solutions Division
(309) 636-1077, fax: (309) 636-2567, e-mail: birkel_jeffrey_f@cat.com*

*Assistant Contract Administrator: Pamela J. Breen
Caterpillar Inc. – New Technology Division
(309) 578-9955, fax: (309) 578-2834, e-mail: breen_pamela_j@cat.com*

*Technology Program Manager: Lee A. Slezak
U.S. Department of Energy – Office of Vehicle Technologies Program
(202) 586-2335, fax: (202) 586-2476, e-mail: lee.slezak@hq.doe.gov*

*Contractor: National Energy Technology Laboratory.
Contract No.: DE-FC26-04NT42258*

This report was prepared with the support of the U.S. Department of Energy, under Award No. DE-FC26-04NT42258. However, any opinions, findings, conclusions, or recommendations expressed herein are those of the author(s) and do not necessarily reflect the views of the DOE.

Objectives

The goals of the Truck Essential Power Systems Efficiency Improvements for Medium-Duty Trucks (TEPS) project are:

- Develop a medium-duty generator package and energy storage system for sales to a broad, medium-duty (Class 4-7) truck market.
- Develop electrical alternatives to the use of the belts and gears in the medium-duty truck engine compartment.
- Develop a computer supervisory controller and algorithms to demonstrate fuel savings by taking advantage of electrification.
- Demonstrate reduction of fuel consumption during idle conditions and evaluate the possibility of charging the energy storage system during vehicle braking.
- Provide electricity for auxiliary equipment use in the field.

Approach

The team has completed component integration on the TEPS test chassis. The TEPS test chassis is a Class 6 Gross Vehicle Weight Rating (GVWR) truck with a Caterpillar C7 engine outfitted with a utility body and an automatic transmission.

In the last months of this period, the TEPS team will focus on testing the components integrated into the truck and analyzing the results.

Accomplishments

- Baseline chassis dynamometer fuel economy testing and coastdown testing are completed.
- Major components of TEPS have been integrated into vehicle platform, including cooling module, energy storage system (ESS), integrated starter/generator (ISG), and the power converter for the ISG.
- Supervisory controller for the ISG is complete and the controls software is installed and tuned.

Introduction

During budget period 3 (BP3), the team has brought closure to the bench testing and procurement work outlined by Task 102 (Bench Testing) and transitioned to Task 103 (Vehicle Integration and Testing). The team completed the remaining bench testing and started integration of components to the test bed chassis.

The team at Caterpillar continued to refine their existing plant models and received baseline testing data to aid in incorporating additional fidelity into the model. Component integration began after the completion of baseline testing and the return of the truck chassis to Caterpillar. Implementation of the TEPS components lasted several months due to the substantial changes to the vehicle architecture. System tuning followed the component installation, refining the overall vehicle operation in anticipation of final testing.

The second round of testing is currently underway at Transportation Research Center in Ohio and will be done by end of November 2007. Results from this set of tests will be compared to the original baseline testing to quantify the improvements yielded by the integration of the TEPS components. Both on-road and dynamometer testing are being employed to demonstrate the fuel economy gains of the enhanced chassis.

Bench Testing

A few bench testing tasks carried over into the first quarter of 2007. The ePTO drive controller was assembled. The ePTO power supplies, sensors, and CAN communications were also tested. The bench testing of this hardware also benefited the transmission oil pump, as similar hardware and software were used for that application as well.

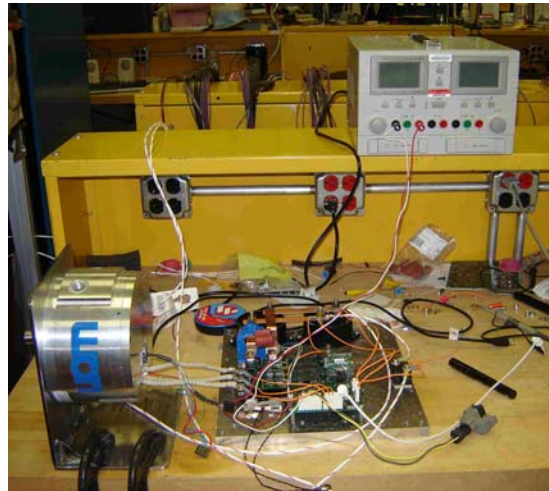


Figure 1. ePTO Bench Testing Set-up

Bench testing of the power inverter was successfully completed early in the quarter. The power inverter facilitates a project goal by providing electrical power to devices in the field. Figure 2 shows an example of this during bench testing of the inverter by powering a small drill. The red ellipse highlights the inverter.



Figure 2. Power Inverter Bench Testing Set-up

The high voltage distribution box and battery mount drawings were completed and sent to fabricators. Meanwhile, the high voltage distribution box was assembled and laboratory tested. The high voltage distribution box contains the majority of the critical high voltage hardware including the ISG controller as well as all of the fuses and relays for the system.



Figure 3. Inside of High Voltage Distribution Box

Other components were received and bench tested for communications and performance, including the cooling components from EMP and the nickel-metal hydride (NiMH) battery pack. EMP provided the six fans for the front cooling module as well as the jacket water pump and a secondary pump for the low temperature coolant loop. All of these components are commanded via CAN communications and all but the secondary pump draw power from the high voltage buss.

Controllers developed by Caterpillar drive the high voltage cooling components. The controllers are water cooled and tightly integrated to facilitate coolant access and minimize space claim. Caterpillar was able to develop a flexible controller that maximized common hardware for fans and pumps, requiring little more than software modifications. These controllers communicate via CAN and were bench tested in the laboratory prior to installation on the vehicle.



Figure 4. Bench Test of Cooling Controllers

Vehicle Integration

In January 2007, Caterpillar took delivery of the ISG machine and controller. Caterpillar tested the ISG controller communications to the supervisory controller. Establishing communications with the ISG controller enabled the team to move forward with integration and facilitated upgrades to the ISG software.

After demonstrating communications, the ISG was installed on the vehicle. The team was then able to demonstrate the ISG starting functionality for the first time -- a milestone success. Figure 5 depicts the installation of the machine onto the truck. In this case, the stator is shown sliding into the custom flywheel housing that has been bolted to the engine. Following stator insertion, the rotor is affixed to the crankshaft and then the transmission fitted to the rotor and flywheel housing.



Figure 5. ISG Stator Installation in Truck

The abilities to generate power and move the truck using stored energy were added to the ISG software in the second quarter of 2007. Improvements to the ability to start the diesel engine via the ISG were added to the software module during this upgrade as well. Testing of the software for full functionality with the other system components was performed successfully. Figure 6 shows an example of a vehicle launch assisted by the ISG. The plot illustrates how the ISG utilizes battery power to spin the engine and begin the process of vehicle acceleration.

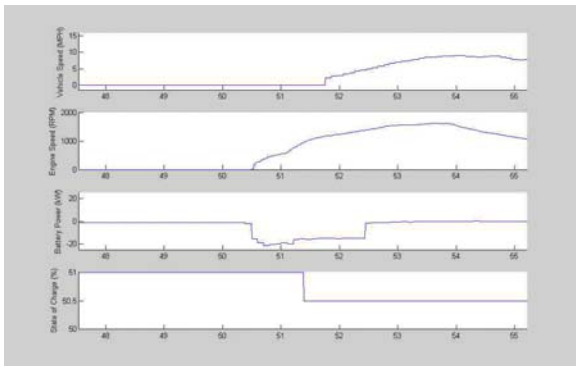


Figure 6. Plot of Vehicle Launch Using ISG

Energy storage and the wiring to carry the energy to the components were installed in addition to a DC-to-DC converter. These installations enabled the integration of the cooling packages and other subsystems for testing. The high voltage box, battery, and DC-to-DC converter were tested on the vehicle through on-road vehicle testing inside the Caterpillar Technical Center. The photo in Figure 7 shows how the high voltage distribution box and the ESS are integrated into the steps of the vehicle. The lower box with the centrally located red handle is the high voltage distribution box while the top box houses the ESS.



Figure 7. Integration of Components in Vehicle Steps

The team found issues with the DC-to-DC converter hardware and collaborated with the converter supplier to exchange the converter for a newer model based on an updated design. The new unit was installed and successfully tested on the truck.

The jacket water engine cooling system, including a water pump, fans, and electric thermostat valve, was installed. A low-temperature cooling system comprised of a water pump, heat exchanger, and second electric thermostat valve was installed and the coolant lines were routed on the truck. Additionally, the utility body was fitted and attached to the truck.



Figure 8. Truck with Utility Body Installed

High voltage accessories such as the electric air conditioning compressor, cooling fan controllers, and power inverter were installed on the truck and successfully demonstrated. The air conditioning compressor was charged and immediately put to use during preliminary testing and tuning. The fan controller box, meanwhile, comprises six controllers for the high voltage fans, a single controller for the high voltage water pump as well as a spare position for expansion. The box represents a compact packaging configuration that employs single-pass liquid cooling through the middle cool plate with four controllers mounted on either side.



Figure 9. Cooling Fan Controller Box

Development and installation of thermistor hardware for collecting temperature signals throughout the chassis and cooling system was also completed. The Caterpillar-developed device collects the analog data and routes it to the CAN network. Having the data on the CAN network allows the data to be more easily utilized for controls and data collection purposes. Moreover, duplicates of the original device have been reapplied around the truck for collecting a variety of other analog signals.



Figure 10. Caterpillar-developed Thermistor Device with CAN Connections

Baseline Testing

Prior to vehicle component integration, the Ford F-750 test bed chassis was tested in an OEM-like baseline state at the Transportation Research Center (TRC) in Ohio. A Caterpillar CX28 transmission was installed before testing commenced. The CX28 replaced the transmission that was originally installed on the truck from the factory. A truck similar to the specifications for the TEPS test truck platform was acquired to serve as a control vehicle for the testing. The control truck will be used to compare fuel economy at each stage of the test truck's lifecycle.

Both trucks were sent to TRC for a series of tests to analyze the truck's efficiency. These tests included a fuel economy test, a dynamometer cooling test at steady state, coastdown testing, and acceleration testing. Both trucks were ballasted to 19,210 pounds for the duration of testing to approximate an average load for a Class 6 vehicle.

Fuel Economy - The fuel economy test was conducted within requirements set forth in the SAE J1321 test procedure in order to provide a baseline with which to compare the performance of the TEPS electrified truck for percent improvement in fuel economy.

The test route featured 6 laps of a 7.5-mile track, a distance of 45 miles. The tests were broken up into sets of 3 laps with time in the middle to allow cycling of some equipment on the truck. Each driver remained paired with the same truck and the drivers tested the trucks at speeds ranging from 10 mph to 35 mph, simulating a nominal medium-duty truck cycle. Fuel volume was measured by weighing gravimetric tanks.

The TEPS test and control trucks were tested together on the track under the same conditions. The test and control trucks ran through a minimum of 3 runs for each test segment. In order for the run sets to be considered successful, the test to control (T/C) ratio of each run needed to be within 2 percent of the other runs in that set. Also, over the course of the 3 runs, the trucks could not have a variation in run times of greater than +/- 0.5%. Run data that was not within those parameters was disregarded and the run was repeated.

The overall results showed that the baseline Ford F-750 gave an average T/C ratio of 1.1800 with an average mpg of 7.82.

Steady State Dynamometer Cooling Test - A steady state dynamometer cooling test was performed to establish a baseline for the performance of the medium-duty truck across a range of loads, engine speeds, and ambient temperatures. The truck was equipped with fuel flow meters and thermocouples in its cooling heat exchangers to gather data about fuel usage and heat rejection. The data gathered in this test will be compared to data gathered from an electrified TEPS equipped truck.

Coastdown Test - A coastdown test was performed in accordance with SAE J1263 to determine the forces required of the vehicle to maintain a steady state speed on a level roadway under no wind conditions and to determine the coefficient of aerodynamic drag (CD) of the truck under the same conditions. The front area of the truck was measured in preparation for the test. Tests were

conducted in evening or at night when weather forecasts indicated wind speed would be minimal (not in excess of approximately 2 mph). The truck was driven approximately 30 miles at 60 mph on the test track to bring all systems to operating temperatures. The test truck was then driven into a two-mile long straight area of the track at a speed of 65 mph and shifted into neutral and allowed to coast. Data was continuously recorded using a data acquisition system. One run was done moving in a northbound direction and one was completed in a southbound direction. The procedure was repeated until the team had 7 run pairs completed. After the test was complete, the vehicle with the driver in it was weighed and the post-test weight was used for data analysis.

The CD indicates the relative rate of aerodynamic drag the vehicle produces. A lower CD value indicates greater efficiency. Our baseline truck, without TEPS components, produced a CD of 0.772.

Table 1. Medium-Duty Truck Coastdown Results Summary

Truck ID	Test ID & Date	A0 Coefficient	A2 Coefficient	CD	Horsepower Required at Speed			
					50 MPH	60 MPH	70 MPH	80 MPH
C1	C1A 10/25/06	0.1587743	0.1282783E-03	0.772	557.7	866.3	1282.2	1823.5

Acceleration Test - An acceleration test was run in compliance with SAE J1491 to determine the maximum road grade the vehicle can climb at a certain target speed. The truck was driven around the test track to bring all systems to operating temperatures. Five runs were made for each measurement until three in each direction were completed. Compromised runs and their paired run were excluded and another pair of runs completed. Test results represent the average of six measurements that met the variability requirements of SAE J1491.

The team found that the maximum road grade that the vehicle can climb at 40 mph was 5.5% on the southbound route and 5.9% on the northbound route. The average time it took for the vehicle to reach 40 mph was 36.62 seconds.

As previously mentioned, the results of the baseline testing were compared and integrated into the plant model to improve its fidelity. The team has continued to use the plant model as a means to predict performance and examine new control strategies.

Conclusion

The TEPS project will demonstrate an integrated system of electric accessories and truck electrification to potentially improve fuel economy. The heart of the system is the ISG, which starts the engine and generates all on-board electric power. The machine presents a significant improvement in efficiency compared to a conventional alternator and offers an opportunity to provide additional power to the driveline.

ISG power generation to the 340 VDC buss enables the use of high voltage, high efficiency electric accessories. The accessories can operate in a more “on-demand” or variable fashion and offer more efficient operation in addition to packaging flexibility. Extensive supervisory control algorithms harness the capability of the ISG, energy storage, and electric accessories. Simulation results obtained by coupling a dynamic plant model with control algorithms suggest significant fuel consumption reductions on the order of 10 percent for virtually any medium-duty application or driving cycle. Applications with extended idle periods would benefit from additional savings.

A final report with data and analysis comparing the second round of on-road fuel economy and chassis dynamometer testing to the initial results will be prepared and presented in completion of the deliverables for this effort.

B. Advanced Electric Systems and Aerodynamics for Efficiency Improvements in Heavy Duty Trucks

Principal Investigator: Larry M. Slone
Caterpillar Inc. – Technology & Solutions Division
(309) 578-0243, fax: (309) 578-6285, e-mail: slone_larry_m@cat.com

Caterpillar Program Manager: Jeffrey F. Birkel
Caterpillar Inc. – Technology & Solutions Division
(309) 636-1077, fax: (309) 636-2567, e-mail: birkel_jeffrey_f@cat.com

Project Manager: Ralph D. Nine
National Energy Technology Laboratory
(304) 285-2017, fax: (304) 285-4469, e-mail: ralph.nine@netl.doe.gov

Technology Program Manager: Lee A. Slezak
U.S. Dept. of Energy - Office of Vehicle Technologies Program
(202) 586-2335, fax: 586-2476, e-mail: lee.slezak@hq.doe.gov

Contractor: Caterpillar Inc.
Contract No.: DE-FC26-04NT42189

This report was prepared with the support of the U.S. Department of Energy, under Award No. DE-FC26-04NT42189. However, any opinions, findings, conclusions, or recommendations expressed herein are those of the author(s) and do not necessarily reflect the views of the DOE.

Purpose

- To improve the fuel efficiency of heavy-duty trucks through improvements in cooling system performance, air system management, and advanced power management.

Objectives

- Analyze, design, build, and test a cooling system that provides a minimum of 10 percent greater heat rejection in the same frontal area with no increase in parasitic fan load.
- Realize fuel savings with advanced power management and acceleration assist by utilizing an Integrated Starter/Generator (ISG) and energy storage devices.
- Quantify the effect of aerodynamic drag due to the frontal shape mandated by the area required for the cooling system.

Major Accomplishments

- Heavy-duty truck MEI/Driveline simulation model completed, along with analysis of drive cycles and advanced power management strategies.
- Electric thermostat valve and drive electronics design and fabrication completed and delivered to Cat from EMP. Valve bench testing for operation and communications complete, electrical integration of valve to MET complete. Valve installation and testing on More Electric Truck (MET) complete.
- Two prototype 20kW electric cooling fan motors specified, designed, and fabricated. Fan motor dynamometer testing and characterization complete, motors on-site at Caterpillar, motor drive communication testing complete. Fan supervisory control algorithms complete.

- ISG sensorless algorithms and dynamometer testing complete, fully characterized for engine assist operation over 0 to 2400 rpm range. ISG supervisory control algorithms complete. A 2007 emissions-compliant engine coupled with the ISG and a diesel particulate filter (DPF) was installed in the MET platform.
- Fabrication, assembly, and integration of a modular engine cooling system for the truck platform were completed. The system consists of a main radiator core, electric cooling fan, engine oil auxiliary radiator, and high temperature charge air cooler.
- Prototype high efficiency cooling fan blades and shroud were designed, fabricated, and performance tested in a lab setting. These components were installed into the test platform as part of the aforementioned modular engine cooling system.
- Truck underhood computational fluid dynamics (CFD) cooling analysis was completed. In addition, Argonne National Laboratory (ANL) completed CFD trials on the truck frontal area to examine the effect on drag coefficient of changes to the radiator tilt and/or size.
- An energy storage system consisting of nickel-metal hydride (NiMH) batteries, high voltage bus interconnect, liquid cooling loop, and CAN communication was implemented on the vehicle.
- Truck controls functionality was exercised and controls were tuned in order to provide the best configurations for fuel economy.
- Dynamometer tests for fuel economy as well as cooling package performance were performed on the Kenworth T2000 test truck to quantify the impact of electrification. Test configurations included a baseline employing mechanical accessories as well as multiple degrees of accessory electrification.
- Road testing using the Kenworth T2000 test truck and a Kenworth T800 control truck was completed utilizing a protocol similar to the SAE J1321 specification.

Introduction

The Advanced Electric Systems and Aerodynamics for Efficiency Improvements in Heavy Duty Trucks program (DE-FC26-04NT42189) focused on areas that will primarily benefit fuel economy and improve heat rejection while driving over the road. The program effort consisted of modeling and designing components for optimum fuel efficiency, completing fabrication of necessary components, integrating these components into the chassis test bed, completing controls programming, and performance testing the system both on a chassis dynamometer and on the road.

Emission control measures for heavy-duty engines have resulted in increased engine heat loads, thus introducing added parasitic engine cooling loads. Truck electrification, in the form of thermal management, offers technology solutions to mitigate or even neutralize the effects of this trend. Thermal control offers opportunities to avoid increases in cooling system frontal area and forestall reduced fuel economy brought about by additional aerodynamic vehicle drag.

Advanced power management, in the form of continuously optimized and controlled power flow between electric components, offers additional fuel economy benefits to the heavy-duty trucking industry. Control software for power management brings additional value to the power distribution and energy storage architecture on board a truck with electric accessories and an ISG.

The research team has built upon a previous truck electrification project, formally, “Parasitic Energy Loss Reduction and Enabling Technologies for Class 7/8 Trucks”, DE-FC04-2000AL6701, where the fundamental concept of electrically driven accessories replacing belt/gear-driven accessories was demonstrated on a Kenworth T2000 truck chassis. The electrical accessories, shown in Figure 1, were controlled to provide “flow on demand” variable-speed operation and reduced parasitic engine loads for increased fuel economy. These accessories also provided solutions for main engine idle reduction in long haul trucks. The advanced components and systems of the current project have been integrated into the same Kenworth T2000 truck platform.

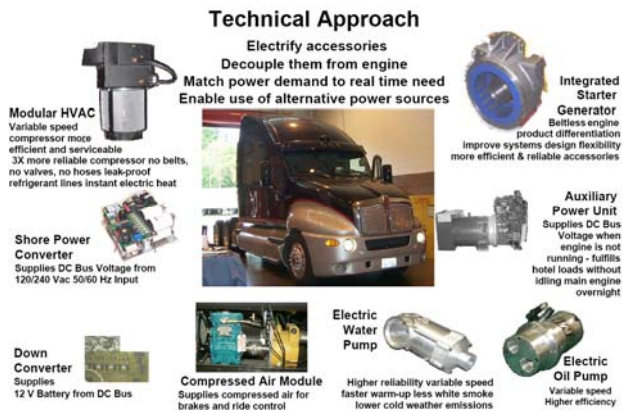


Figure 1. More Electric Truck

Reducing parasitic engine loading by decoupling accessory loads from the engine and driving them electrically has been a central concept of this project. Belt or gear-driven engine accessories, such as water pump, air conditioning compressor, or air compressor, are necessarily tied to the engine speed dictated by the current vehicle operating conditions. These conventional accessory pumps are sized to provide adequate flow or pressure at low idle or peak torque speeds, resulting in excess flow or pressure at cruising or rated speeds. The excess flow is diverted through a pressure-minimizing device such as a relief valve thereby expending energy to drive unnecessary and inefficient pump operation. This inefficiency causes an increased parasitic load to the engine, which leads to a loss of usable output power and decreased fuel economy.

Using variable-speed electric motors to drive accessory pumps and controlling the speed to provide only the required flow or pressure of a particular accessory system can yield significant increases in fuel economy for a commercial vehicle. Motor loads at relatively high power levels (1 – 5 kW, or higher) can be efficiently provided current from high-efficiency generators or batteries with system voltages in the range of 250 to 360 volts DC (VDC).

In the previous project, the electric accessories could be powered from one of three sources: an AC voltage source (“shore power”), an on board diesel generator (auxiliary power unit), or an ISG located in the flywheel housing and driven by the main engine. The electric accessories and power sources, including the ISG, have remained in place for the current upgrade of the research platform vehicle. In

this project, more emphasis has been placed on determining the best way to use the ISG to power the vehicle and accessories.

The transition to broad commercial applications of these technologies in the trucking industry should lead to significant gains in performance, reliability, serviceability, and system design flexibility. The Class 8 truck sector may benefit the most due to their higher average speed, the large number of vehicles produced yearly, and the high number of miles per year accumulated by each vehicle. Better fuel economy can accompany emissions reduction and could encourage customers to purchase the vehicles as an improved capital investment. These technology enhancements show the potential to be directly beneficial to mobile construction equipment, a variety of commercial and marine engine markets, and powertrains used by a wide variety of U.S. military mobile equipment as well.

Analysis and Design

Cooling Module

In alignment with the project goal of controlled thermal management for cooling system performance improvements, the electric cooling fan, radiator coolant bypass control valve, and oil cooler were identified as having the potential to increase cooling system heat rejection and improve fuel economy. Simulation analysis showed the AES cooling system with thermal management is capable of 335 kW heat rejection under worst-case ambient condition of 43 °C for both peak torque and rated speed conditions. This includes 227 kW from the water/glycol system and 108 kW from the charge air cooler. Figure 2 is a schematic of the fluid flow through the system.

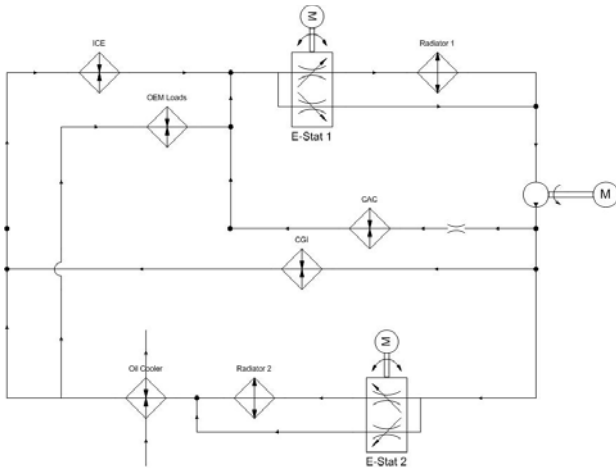


Figure 2. AES Water Cooling Circuit

Electric Cooling Fan

Conventional engine cooling fans on heavy-duty trucks range in size from about 28 inches to 32 inches in diameter and can consume up to 50 kW under conditions of full engine speed and low vehicle speed, especially as engine-to-fan belt pulley speed ratios have increased to about 1.4:1. The fan is belt driven through an on-off clutch on the front of the engine. For a long haul truck, average fan on-time as a percentage of truck operation is about 6 percent with half of that time attributable to air conditioning demands. The cooling fan is typically sized to deliver adequate cooling air flow at a peak torque engine speed of 1200 rpm resulting in excess air delivery at higher engine speeds with a cubic exponential increase in parasitic power draw from the engine. Electrification of the fan allows fan speed to be matched proportionately to cooling system load.

For the electric cooling fan, the space constraints for installation in the current platform were a determining factor in the decision to use a puller-type fan, as hood profile and mounting considerations of truck frame rail ends would have otherwise required a difficult redesign of major structural components. Future designs using an electric pusher fan with the electric motor in front of the heat exchangers have potential to benefit from increased fan efficiency due to the fan blades blowing colder, denser air. Air cooling of the fan motor may also be more feasible with a pusher design, as the motor would be located in cooler air upstream from the heat exchangers.

For the current puller design, fan motor power was specified to 20 kW continuous at 2000 rpm. Thermal challenges in the form of 80°C air temperatures and 100°C coolant temperatures combined with space claim constraints to limit fan motor continuous power to about 20 kW. This matches the 20 kW mechanical fan power at 1800 rpm engine speed and 30 mph ram air for a conventional belt-driven fan. With a higher efficiency fan and shroud, the same fan power will give more airflow and yield higher heat rejection.

Switched Reluctance Drives Ltd, a subsidiary of Emerson Electric Co., designed, developed, and tested the prototype electric fan motor shown in Figure 3. The motor design is switched reluctance technology with an 18/12 stator/rotor pole structure and peak continuous power rating of 20 kW at 2000 rpm. Motor operation allows the reversal of the fan, perhaps unneeded in an on-highway application but potentially useful in an off-highway machine to facilitate cleanout of debris from the heat exchangers. Motor physical size is approximately 300 mm in diameter by 200 mm in axial length. Electric current commutation is provided by position sensors mounted to the motor front interfacing with slotted tabs on the fan hub. Fan motor/drive efficiency of over 90 percent was demonstrated in dynamometer testing over most of its operating speed and power range.



Figure 3. 20kW Cooling Fan Motor

Primary cooling of the motor stator windings is accomplished with engine coolant, while an aft-to-fore air-cooling stream through openings in the motor endplates provides secondary rotor/stator cooling. Radial vanes on the fan hub provide a negative pressure zone at the motor front, enabling cooling airflow through the rotor.

The fan hub, Figure 4, was designed to wrap around the motor and provide mounting for the base of nine individually molded blades. This wraparound design allowed the fan blade leading edge to be located

100 mm from the radiator core, improving efficiency of the airfoil shaped blades and permitting space for the inlet radius of a type II shroud. Centrally locating the fan relative to the radiator core and a tight tip to shroud clearance allowed a fan diameter of 864 mm in contrast to the 812 mm diameter of the baseline system of the MET.



Figure 4. Fan Hub and Blade Design

The AES cooling module consists of the electric fan mounted to the aft side of the radiator frame and the auxiliary oil cooler and charge air cooler mounted to the front of the radiator frame. The electric cooling fan and motor were designed to integrate with the cooling module through cross frame tubing supports mounted to each corner of the radiator frame. Mounting to the radiator frame allowed close tip-to-shroud tolerance (8mm) since there is no need to account for engine movement on flexible mounts. Mounting the cooling fan and motor to the radiator frame also permitted a completely modular cooling package design for easy assembly and service. This cooling module can be assembled as a unit and then mounted as one piece to the truck frame.

To verify operation of the fan motor in a controlled environment, the cooling module was mounted to a bedplate and operated in a test cell. Operation of the fan mounted to the radiator frame was validated to 1500 rpm and 15 kW of electrical input power. System control and communications with the fan drive were verified. The fan was tested for excessive vibrations at natural frequencies that could cause damage to the fan or frame. The design and mounting were found to be robust and ready for integration to the vehicle with no excessive vibrations throughout the speed range of the fan.

Computational fluid dynamics analysis for T2000 underhood cooling airflow was performed for both the baseline conventional cooling components and the new AES components. Figure 5 shows velocity vectors in a horizontal plane view of the engine

compartment – one of many CFD snapshots captured.

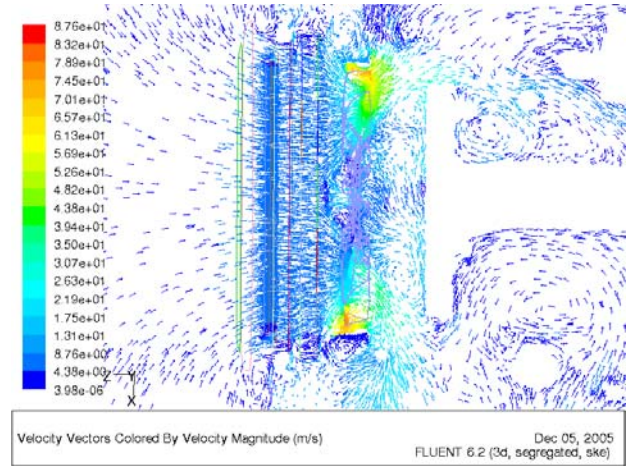


Figure 5. Horizontal Plane Velocity Vectors of Baseline Configuration

Results of the underhood CFD cooling analysis using AES components (see Table 2) showed an overall 14-33 percent efficiency gain (fan power (kW) per fan flow (kg/s)) with the AES fan and shroud design. The range stems from analysis at different design points with variable fan and vehicle speeds. Most significant is the 33 percent efficiency gain at the worst case cooling point of full fan speed (2000 rpm) and low ram air speed (30 mph) where the fan delivers 10.3 kg/s airflow with a mechanical input power of 28.9 kW (power to flow ratio 2.81). This compares favorably to analysis of the vehicle baseline belt-driven fan (see Table 1) delivering 12.0 kg/s at 2520 rpm with an input power of 50.0 kW (power to flow ratio 4.17).

Table 1. Baseline Conventional Cooling Components

	Fan speed (rpm)	Ram air (mph)	Grill flow (kg/s)	Fan flow (kg/s)	Fan power (kW)	Fan power /Fan flow (kJ/kg)
Baseline	1680	0	4.5	6.7	13.0	1.94
Iteration 1	1680	30	6.7	7.8	14.6	1.87
Iteration 2	1680	60	10.3	9.4	17.8	1.90
Iteration 3	2520	30	9.1	12.0	50.0	4.17

Table 2. AES Cooling Components

	Fan speed (rpm)	Ram air (mph)	Grill flow (kg/s)	Fan flow (kg/s)	Fan power (kW)	Fan power /Fan flow (kJ/kg)
Baseline	1500	0	4.8	7.2	12.1	1.68
Iteration 1	1500	30	6.6	7.6	12.2	1.60
Iteration 2	1500	60	9.9	8.6	12.5	1.46
Iteration 3	2000	30	8.2	10.3	28.9	2.80

Laboratory airflow tests were conducted with the newly fabricated fan blades, hub, and type II venturi shroud. These components were mounted in the fan laboratory air testing plenum, where variable restriction was used to develop static pressure. The fan was driven by an electric motor and a transducer was used to measure torque. Figure 6 shows the test pressure curves versus airflow for various fan speeds, while Figure 7 shows the mechanical power measured to produce the pressure and flow of Figure 6.

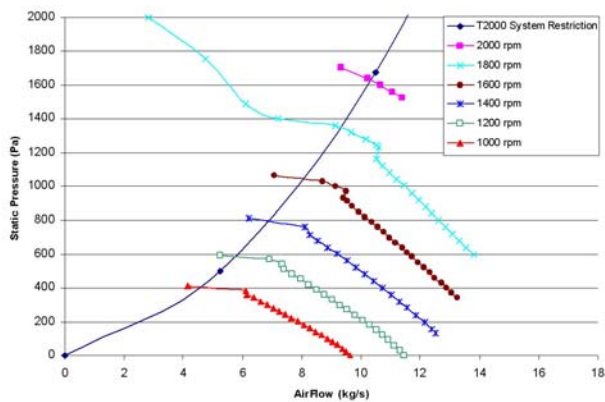


Figure 6. AES Fan Pressure versus Airflow

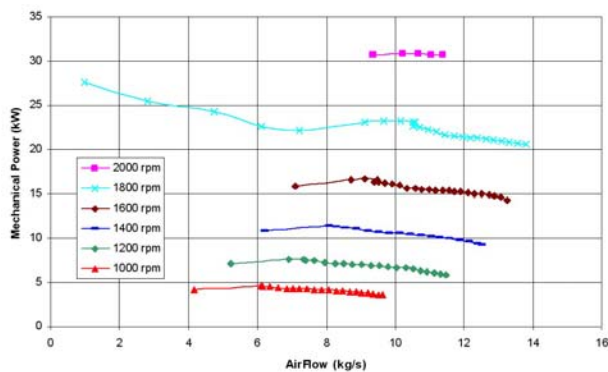


Figure 7. AES Fan Mechanical Power versus Airflow

Using fan curves obtained for the 812 mm T2000 baseline fan and the T2000 restriction curve from Figure 6, flow and power curves versus speed were developed for the baseline fan. Figure 6 and Figure 7 were used to construct similar curves of flow and power versus speed for the AES fan design. Figure 8 shows a comparison plot of the baseline fan versus the AES fan. The results showed a 7 percent increase in airflow for the same mechanical input power, 23.1 kW. It was also noted that the AES fan, at a larger

(864 mm) diameter than the baseline fan, is a more aggressive design, and will produce equal airflow at lower rotational speeds. To produce similar airflow, 9.3 kg/s, the AES fan required 23.1 kW, while the baseline fan needed 28 kW of mechanical input power, translating to a 17.5 percent increase in efficiency with the new AES design versus the baseline fan. This efficiency increase is important, since the energy conversion of mechanical to electrical power from the ISG and back to mechanical power in the fan motor increased the overall parasitic power load to the engine. Using the 90 percent efficiency of the ISG and fan motor obtained during testing resulted in 28.5 kW of engine power required to drive the electric fan at full power. This compared favorably to the 28 kW mechanical input power at 2100 rpm, where additional engine power (2-5 percent) would be lost through the belts driving the fan.

The 23 kW mechanical input power on the plot of Figure 8 is significant, as this is about the maximum that the fan motor is capable of producing at this speed, 1800 rpm. Given the system restriction curve shown in Figure 6, the electric fan would be power limited to about 1800 rpm, even though it was characterized and tested to 2500 rpm (at constant 23 kW power over the 1800 to 2500 rpm range).

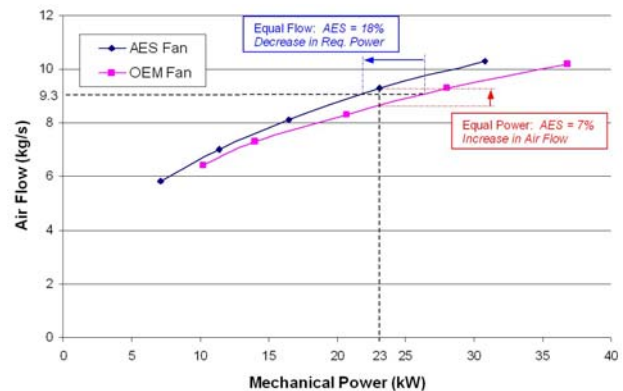


Figure 8. Comparison of Baseline and AES Fan Power and Flow

The above analysis encompasses worst-case operational conditions for the cooling fan at maximum heat rejection load. The real advantage of the electric fan is its variable speed operation, so that at normal operating conditions where less heat rejection may be required from the cooling system, the fan motor is controlled to a speed proportional to

the heat rejection load. Since the power draw of a fan is proportional to the cube of speed, the electric fan significantly reduces the parasitic engine load for a majority of the operational conditions compared to an on/off clutch, belt-driven fan.

Table 3 shows a comparison of the energy consumed during an hour of operation for both an on/off clutched belt drive fan operating at a 5 percent on-duty cycle at 1980 rpm and an electric fan operating at 100 percent on-duty cycle at 500 rpm. The electric fan moves 3.5 times the air mass while using less than half the energy. The constant speed electric fan would also result in a more consistent coolant temperature. This scenario of lower heat rejection requirements may occur during highway cruising or lower speed urban operation of a Class 8 truck.

Table 3. Comparison of Fan Drive Energy

Fan Drive	Duty Cycle (%)	Power (kW)	Energy Used over 1 Hr (kWh)	Airflow (kg/s)	Air Mass Moved over 1 Hr (kg)
Belt Drive Fan	5%	28	1.40	9.3	1674
Electric Fan	100%	0.62	0.62	1.6	5760

System controller and fan motor drive communications occur over a controller area network (CAN) using SAE J1939 specifications and proprietary network identifiers (IDs). Supervisory control algorithms for speed control of the cooling fan motor were developed to provide the temperature differential across both radiator and engine to within an 8°C range. The fan only operates when the bypass valve is routing all coolant to the radiator. This ensures the diverter valve primarily controls coolant temperature, as this is the control actuation with the least energy cost. The fan then operates in variable speed mode to control the temperature differential across the radiator.

Radiator Coolant Bypass Control Valve

An electrically-actuated valve was supplied by Engineered Machined Products, Inc. to control the coolant flow between the radiator and radiator bypass loop of the coolant circuit. Replacement of a conventional wax-type thermostat allowed for variable set point engine coolant temperatures. During periods of light to moderate engine load, the reference temperature can be increased, thus

allowing less heat absorption by the coolant from the engine and permitting higher exhaust temperatures for better passive regeneration of the DPF. The increased exhaust energy can also be used to power more boost from the turbocharger. Higher coolant temperature can also result in elevated cylinder wall temperature, increasing combustion efficiency. As engine load increases, the temperature set point can be decreased to provide adequate cooling of exhaust ports and other areas of high heat concentration.

Figure 9 shows the valve installation in the research platform integrated with the C15 engine. The control valve consists of a linearly-actuated flow diverter contained in a cylindrical nylon and aluminum housing driven by a stepper motor. A small drive electronics box with CAN communication and current drivers for the valve motor/actuator runs from the vehicle 12 V power. The 2.4-inch valve with 1-inch bypass provides 100 gallons per minute (gpm) flow with a 1-psi pressure drop, 300 gpm with a 5-psi pressure drop, and goes from closed to full open in 16 seconds. As with the fan, communication between the supervisory controller and the valve electronics is established via CAN using SAE J1939 specifications and proprietary network IDs.



Figure 9. Radiator Coolant Bypass Valve Installation

The design requirements for the valve included:

- Reference temperature easily adjusted
- Engine coolant temperature (ECT) controlled to +/- 5°C around the reference temperature

- System heat rejection maximized solely through valve actuation, minimizing the water pump and fan usage
- Small unnecessary movement of the valve (valve hunting) minimized
- Warm up time of the engine decreased
- ΔT of the coolant temperature across the block minimized to a maximum of 9°C

Proportional and proportional plus integral feedback control systems based on engine coolant temperature and artificial neural network control algorithms were designed and tested against both virtual truck/engine system models and on the actual T2000. Control challenges for a feedback control system include coolant transport delay and temperature sensor delay, which lead to potential system instability. With these delays, it is difficult to achieve reasonable system response times without having high control gain levels that make the system unstable. The neural network algorithms for this application were based on engine torque levels to help give the control system more of a predictive response.

Auxiliary Oil Cooler

The elevated engine coolant temperature made possible by the radiator coolant bypass control valve necessarily results in increased radiator outlet temperature, or bottom tank temperature, since a temperature differential of 8°C or less must be maintained across the engine. Since it is the coolant from the radiator outlet that is used to absorb heat in the oil cooler (oil to coolant heat exchanger), an increase in the bottom tank temperature may result in an inadequate temperature gradient across the oil cooler to effectively cool the engine oil. To mitigate this effect, the concept shown in Figure 10 was implemented to provide supplementary cooling of the coolant entering the oil cooler. The liquid-to-air heat exchanger is integrated into the vehicle cooling module with the radiator and charge air cooler.

The auxiliary oil cooler control valve shown in Figure 10 provides control over the temperature of the coolant entering the oil cooler. In principle, by using the proportional flow control valve, the engine oil temperature, and ultimately the temperature dependent viscosity of the oil, can effectively be controlled. In this way, during times of light to

moderate engine loading and especially at low ambient temperatures, the oil temperature can be increased to reduce oil viscosity and parasitic friction. For periods of high engine loading, the oil temperature can be decreased to provide adequate oil pressure for journal bearing flotation and critical cooling of engine components by the engine oil.

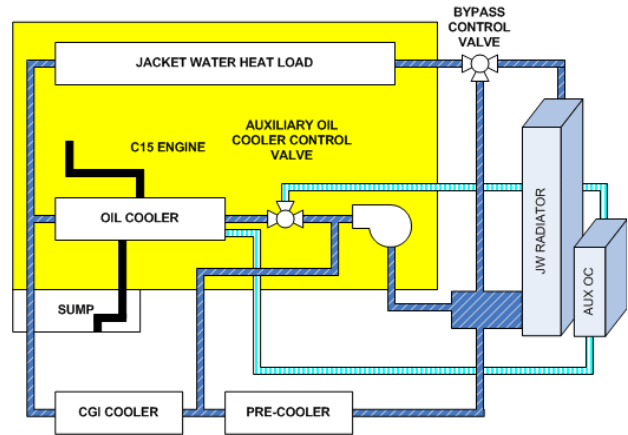


Figure 10. Oil Cooling System

High Temperature (Hi-Temp) Aftercooler

The original intent of the project’s high temperature aftercooler design was to have copper fins brazed to brass tubes, as the copper and brass material possessed high strength over the operating temperature, and high thermal conductance. The development of the copper/brass aftercooler was abandoned due to condensation of acidic exhaust components in the charge air and the relatively low resistance of brass and copper to corrosion caused by the acidic condensate. The prime path for the aftercooler design called for corrosion resistant stainless steel.

The aftercooler was designed according to the following constraints:

- Emissions requirements have resulted in higher charge air temperature, due to recirculation of clean exhaust gases, and increased heat removal necessary from charge air.
- Current aluminum aftercooler does not have material properties to withstand higher temperature, so air to jacket water pre-cooler required.

- Pre-cooler adds restriction and results in increased pumping losses to both air and coolant.
- Stainless steel material properties of aftercooler allow it to withstand higher temperatures.
- More efficient aftercooler design can further reduce parasitic pumping losses and increase heat rejection per unit area. Highly optimized turbulator design gently rolls charge air, avoiding stratified temperature differential of laminar airflow, yet preventing highly turbulent flow that would cause an excessive pressure drop across the aftercooler.
- Increased heat rejection per unit area can result in reduced frontal area of aftercooler, reducing overall vehicle drag.

Conventional design of tube-fin extended surfaces consists of flat tubes with internal turbulators (offset strip fins, v-shape) for charge air and external fins for cooling air (wave type fins). The new hi-temp aftercooler employs a primary surface tube with external fins - narrower flat tubes with internal dimples/ribs (no fins) as a primary heat transfer surface for charge air and with conventional external fins for cooling air. A significant advantage of the design was a reduction in charge air tube width by as much as 50 percent, for increased surface area/volume ratio, providing increased heat transfer. This results in equal rate of heat transfer from charge air (compared with conventional charge air cooler on unit area basis), with less charge air pressure loss, increased heat transfer to cooling air, and decreased cooling air pressure loss. The design also allowed for higher strength tubes to withstand higher temps and pressures. Overall, the hi-temp aftercooler permitted elimination of the charge air pre-cooler, lower parasitic charge air pressure loss, and increased cooling airflow.

Aerodynamic Drag Study

Argonne National Laboratory (ANL) also conducted research related to the cooling package. ANL studied the effects of small changes in radiator configurations on the aerodynamic performance of an aerodynamic tractor-trailer truck. These effects were quantified through a series of parametric engineering design studies using CFD simulations. A nominal geometry based on the Generic Conventional Model (GCM) was developed and the modified geometries were defined by altering the

dimensions of the GCM using commercial CAD software. This approach has been developed as part of Argonne's contributions to the U.S. Department of Energy's Heavy Vehicle Aerodynamic Working Group.

This study considered 4 different configurations for the radiator with different conditions to test for each configuration. The analysis included changes to grill/radiator height, grill/radiator width, grill/radiator surface area (maintaining the aspect ratio for the surface), and grill/radiator tilt with respect to the vertical axis of the vehicle. The primary radius of curvature between the hood panels and between the top of the hood and the grill was maintained in all cases. Grill height was reduced 10 percent and increased by both 5 percent and 10 percent with no effect on the total amount of drag force but a change in the distribution of the force across the grill/radiator area. Grill width was reduced 10 percent and increased 10 percent with no effect on the total amount of drag force but a change in the distribution of the force across the grill/radiator area. When reducing the surface area of the radiator/grill area by 10 percent without changing the ratio of height to width, no significant change was found in the total amount of drag force but there were changes to the distribution of that force across the grill/radiator area.

Based on the study results, the ANL team concluded that small changes in radiator size, either reduction or expansion, did not affect the fuel economy in any significant way if the vehicle was reasonably aerodynamic already. Small changes in radiator tilt also had a limited effect for reasonably aerodynamic vehicles. The ANL team goes on to suggest that these small changes might have more fuel economy effect for tractor-trailer vehicles that are not already optimized for aerodynamics.

Advanced Power Management

Management of the ISG and energy storage system (ESS) wields significant influence over the improvements wrought by an electrified architecture. The project explored advanced power management of electrified accessories and hybrid operation with electric energy storage. Proper use of the ISG and ESS during acceleration and deceleration offer the potential to increase fuel economy significantly depending on the drive cycle the vehicle undergoes.

Initially, a Dynasty/Simulink model of the MEI truck was used in a comparative evaluation of a possible power-management control. In this acceleration assist scheme, the ISG acted as a motor when the engine was under heavy load (greater than 80 percent of maximum torque). The ISG and other accessories ran off the high-voltage battery during this time. When the engine load decreased, or if the battery charge fell below a lower limit (70 percent of maximum charge), the ISG switched back to generator mode and recharged the battery.

The following table compares the fuel usage results of the simulation for the MEI truck traveling on a sinusoidal (hilly) road profile for a distance of 100 km. The elevation frequency is the distance between peaks along the route. Table 4 suggests that the fuel savings are highly dependent on the road profile, with this particular strategy even demonstrating a decrease in fuel economy for some road profiles. Nevertheless, these results are unique to the control strategy described above, and later efforts continued to examine methods to better match the control strategy to various road profiles.

Table 4. Simulated Fuel Usage with a Motor/Generator Power-Management Control

Maximum Grade (%)	Elevation Frequency (km)	Fuel Usage w/o Pwr Mgmt (liters)	Fuel Usage w/ Pwr Mgmt (liters)	Difference (%)
4	5	56.3	55.0	-2.31
2	5	41.5	39.9	-3.86
4	10	52.7	52.0	-1.33
2	10	39.2	39.6	+1.02

In addition, modeling and simulation with the objective of using the ISG for launch assist of the truck was undertaken. The truck’s motion in terms of velocity, acceleration, and jerk at start-up in 2nd, 4th, and 6th gears was evaluated. The analysis suggested that with the engine at warm temperature (coolant above 70 °C), the ISG would have the torque capability to launch the truck, even fully loaded, on level ground, with clutch engaged, while concurrently bringing the engine up to starting speed. This capability is a key enabler of start/stop operation and further increases the overall value of an ISG to the end customer, in terms of increased functionality and overall fuel savings opportunities.

In response to the desire for launch assist, an algorithm to simultaneously launch and start the

engine during periods of frequent stop-and-go traffic was refined and demonstrated on the truck. This new functionality permits idle stop, or shutdown of the engine, saving fuel and reducing emissions. In addition to restarting the engine, the ISG also provides initial propulsion of the truck as soon as the driver pushes the accelerator pedal. Acceleration assist and cruise assist then proved to be natural extensions of the launch assist algorithms. Acceleration assist provides power when increased vehicle speed is desired. Cruise-assist capability was next added to the power management algorithm. Cruise assist switches the ISG from generating to motoring to help maintain a constant travel speed during times of increased engine load, such as when going uphill. As noted in Table 4, simulation analysis indicated that fuel savings of 1-4 percent were possible with a cruise-assist control, depending on the spacing and steepness of the hills

To make use of the assist algorithms, motoring capability was added to the internal algorithms of ISG. Sensorless control algorithms for the ISG were developed for motoring operation over the 0 to 2400 rpm range by Emerson’s Switched Reluctance Drives (SRD) division. Peak torque of 1200 Nm was achieved from 0 to 160 rpm and constant power of approximately 25 kW was achieved from 500 to 2400 rpm with 84 percent to 90 percent efficiency.

Figure 11 shows a plot of an engine off stop/start operation with the ISG. With the sizeable peak torque capability of the ISG, simultaneous engine starting and vehicle launch from a vehicle stop is possible, even with a fully loaded trailer and gross vehicle weight (GVW) of 80,000 lbs. Idle stop and launch assist for heavy-duty applications have the potential to provide increased and smooth vehicle acceleration and to reduce clutch wear. Engine load transients can be reduced during launch assist, providing possible reduction in emissions. Collateral benefits such as these may increase the customer value of an ISG, stepping up acceptance of the technology, while also providing critical fuel savings.

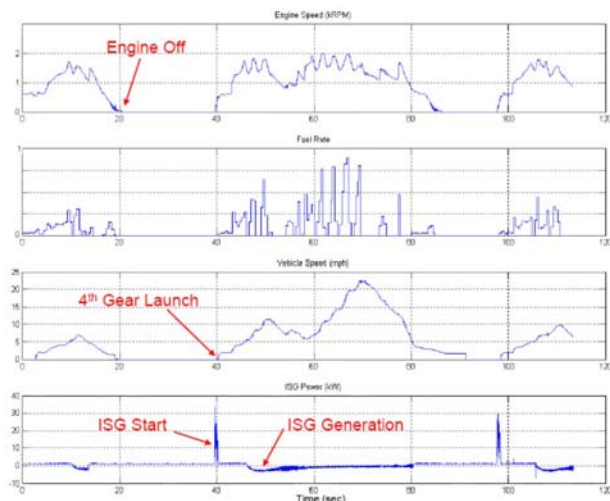


Figure 11. ISG Plots showing Engine Stop/Start Assist

The vehicle operations and assist modes described previously clearly rely on energy storage to add mechanical power to the driveline. An electrical energy storage system (ESS) using nickel-metal hydride batteries was specified for typical heavy duty over the road drive cycles. Key factors of life cycle versus depth of discharge, peak power delivery and absorption, and charge/discharge efficiency were used for system sizing. The 4.8 kWh system was initially specified to allow 100 seconds of acceleration or deceleration with a 20 percent depth of discharge although subsequent testing has revealed that the battery pack could be downsized for many applications. Because the ISG and other MEI components draw power from the batteries while the ISG is motoring, one supervisory algorithm monitors the state of the charge of the batteries to ensure that the system is not overdrawn. If the voltage or state of charge of the battery system falls below the allowed limit, then the ISG is switched back to the generating mode.

Engine Upgrade

A 2007 emissions-compliant, pre-production Caterpillar® C15 engine has been procured and installed in the T2000 vehicle test platform. This C15 ACERT™ engine, rated at 550 HP and 1850 ft-lb of torque, includes a DPF and a Caterpillar Regeneration System (CRS). The decision to upgrade to the 2007 engine was made in order to demonstrate the electric accessory and power management technology on an engine with 2007 representative heat loads and heat load splits.

Testing and Results

Chassis Dynamometer Testing

Chassis dynamometer testing was performed in May and June 2007 in laboratory facilities at Caterpillar Inc. The objectives of the chassis dynamometer testing were to:

- Verify the fuel consumption of the Kenworth T2000 test truck in a baseline test chassis configuration (without use of cooling system electrification).
- Evaluate fuel economy improvements resulting from truck electrification and running at elevated top tank temperatures as compared to the baseline test chassis configuration.
- Evaluate and document vehicle ambient capability for full AES configuration and baseline test chassis configuration at 1500 rpm and 1350 rpm.

The baseline test chassis was the Kenworth T2000 truck equipped with a pre-production 2007 Caterpillar 550 hp C15 engine and the initial 2002 cooling system from the More Electric Truck project. This configuration included a mechanical water pump, mechanical fan, and mechanical thermostat. The AES test chassis configuration comprised the aforementioned modifications including an electric water pump, electric cooling fan, electric thermostat valve, and a newer cooling module.

The tests included analyzing the baseline test chassis configuration and the AES fully electrified configuration for both fuel economy and ambient capability. The baseline test chassis configuration was tested for fuel rate and those numbers were compared to manufacturer specifications. The baseline test chassis configuration fuel consumption was within 2 percent of the nominal values across the lug curve provided by the engine manufacturer.

Chassis dynamometer testing determined that the top tank ambient capability for the baseline test chassis configuration was 36.3 °C. The fully integrated AES configuration top tank ambient capability was 42.7 °C. Additionally, the full electric accessories configuration produced a 2.7 percent maximum fuel efficiency improvement. This improvement is realized not only through increased efficiency, but also through additional control opportunities. The

electric accessories, for instance, also offer the ability to more tightly control top tank temperature. As such, test runs were performed at a top tank temperature of 110 °C. Figure 12 shows a comparison of the chassis dynamometer fuel economy results for various configurations at 50 percent load compared to the baseline test chassis configuration. This increase clearly demonstrates the increased capability and performance improvements of the AES configuration.

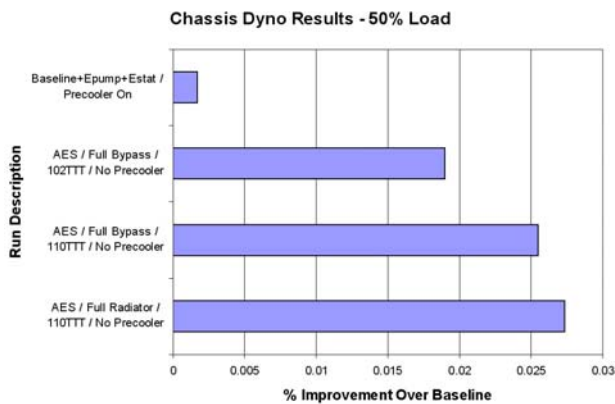


Figure 12. Chassis Dynamometer Results for AES Testing at 50% Load

Road Testing

Road testing was completed in August 2007. The objective of the road test was to conduct fuel economy testing within requirements set forth in both SAE J1321 test procedure type II and “The Fleet Manager’s Guide to Fuel Economy” in order to discover the best controls scenario(s) to optimize fuel economy and quantify the percent improvement in fuel economy.

Testing took place on an interstate route in central Iowa. The test route featured two laps of a 58-mile (one way) route for a total of 232 miles. A test run took just under 4 hours. Each driver remained paired with the same truck and speed was maintained at 65 mph using cruise control to reduce variability. Air conditioning was turned off for each run.

Fuel volume was measured using the procedures outlined in SAEJ1321. A thermometer and hydrometer were used to measure the temperature of the fuel and the fuel specific gravity. A correction factor was applied to the fuel volume based on those measurements.

The road test consisted of testing the AES test truck under three different control modes: baseline (maintaining battery charge), using regenerative braking with no propulsion assist, and using regenerative braking and assisting propulsion during medium-load conditions when battery state of charge (SOC) was sufficient. The test and control trucks ran through a minimum of three runs for each control scenario. In order for the run sets to be considered successful, the test to control (T/C) ratio of each run needed to be within 2 percent of the other runs in that set. Run data that was not within that 2 percent band was disregarded and the run was repeated.

Results shown in Figure 13 illustrate a 2.3 percent improvement in fuel economy when using regenerative braking and a 0.8 percent improvement in fuel economy when using both regenerative braking and the ISG propulsion assist.

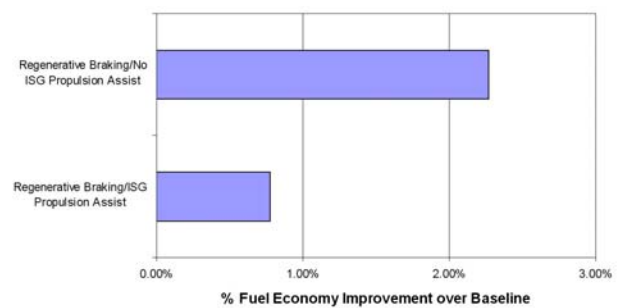


Figure 13. Percent Fuel Economy Improvements over Baseline

The reduction in fuel economy improvement when using additional assistance for the propulsion of the vehicle may, at first, seem counterintuitive. Nevertheless, a few plausible explanations may be found in the fuel consumption characteristics of the engine as well as the nature of vehicle momentum and the impact of the drive cycle on power management logic and fuel savings. In many instances, the addition of ISG power to the driveline reduces the load on the engine. For the same road speed, in the same gear, this reduced engine load can result in decreased efficiency. This phenomenon can be observed in a plot of brake specific fuel consumption (BSFC). BSFC measures the mass of fuel used per unit of mechanical energy out of the engine. Using the ISG assist reduces the engine power operating point by about ~26kW (~35 hp), raising the engine's BSFC, thereby lowering engine

fuel efficiency. Figure 14 illustrates the reduction in engine fuel efficiency in a graph of the engine speed versus power output for the engine during this test run.

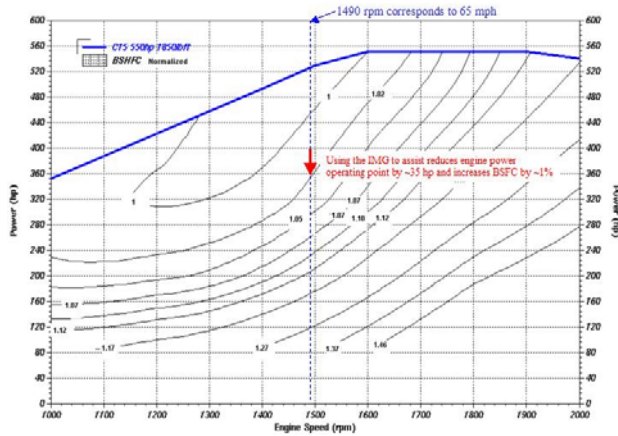


Figure 14. BSFC Map Showing the Impact of ISG Assist

An additional consideration is the interdependence of the control strategy, cruise control, and the terrain. The testing was conducted with the cruise control set to 65 MPH on rolling terrain. Typically, cruise control functions in a “soft” fashion, allowing the vehicle to exceed the setpoint during downhill coasting. The regenerative braking/propulsion assist algorithms may function a bit more aggressively than cruise control during downhill runs to satisfy state of charge conditions for the energy storage system. The assist algorithms use the stored energy much more rapidly, thus the system uses the downhill portions to restore the charge. In these cases, the truck may not accrue as much momentum, due to the increased duration of regeneration, and thus might incur additional load to traverse the next uphill slope, resulting in additional fuel consumption. This situation will occur if the potential energy the truck can capture during downhill sections of road is more efficiently stored as kinetic energy in the form of momentum rather than storing the energy in the battery packs. Figure 15 shows the increased time of regeneration and the subsequent loss of vehicle speed in the assist and regenerate configuration.

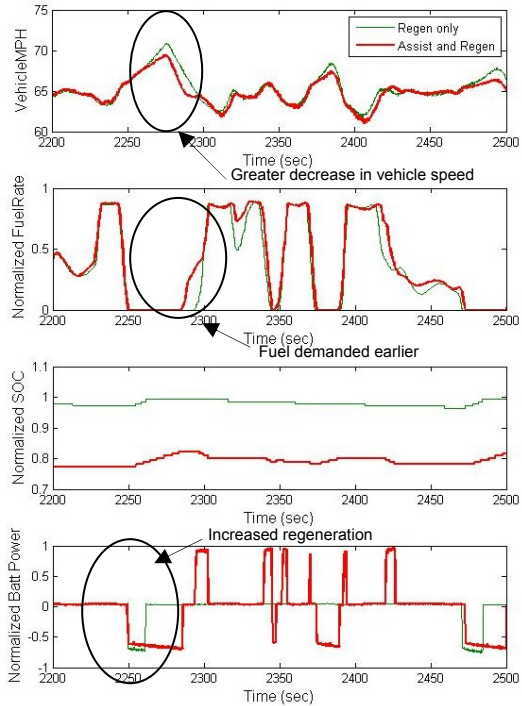


Figure 15. Control Strategy Impact in Hilly Terrain

The plot above shows the vehicle speed along with normalized fuel rate, state of charge (SOC), and battery power over the same section of road for both the regenerate-only and assist configurations. This plot portrays an example of increased regeneration on the downhill slope reducing the momentum available for the following hill ascent. The reduced momentum causes the vehicle to drop below the set speed earlier, which leads to a net increase in fuel consumption, as fuel is demanded earlier to compensate for the loss in speed.

Figure 16, on the other hand, highlights the SOC for both the regenerate-only and assist configurations over the course of an entire test run. The SOC starts at the same level for both configurations, but it can be seen that in the regenerate-only configuration, the SOC will increase and maintain a level close to the maximum, due to the relatively low accessory load on the truck. The energy used in powering the accessories is easily recaptured through short periods of regeneration on a downhill grade. In the assist configuration, however, the SOC increases a small amount and maintains a level only slightly above the minimum due to the increased energy used to assist. In both configurations, the complete depth of discharge is not utilized suggesting that additional

optimization of the strategies would benefit the overall consumption.

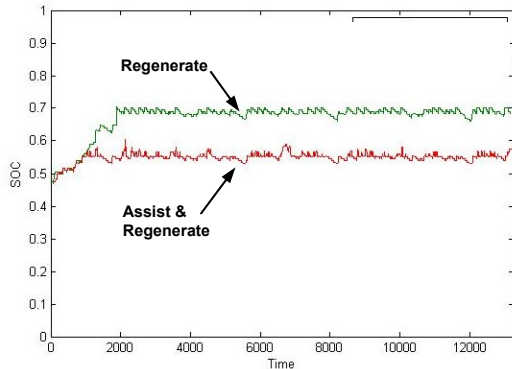


Figure 16. SOC Data for One Test Run

Due to the known dependence of drive cycle on the fuel consumption results, the road profile was scrutinized in additional detail. The following figure shows the profile of the route in terms of elevation from point A to point B. It shows that there is a net loss in elevation of approximately 250 ft when traveling from point A to point B over the first leg of the test route. Due to this, the fuel consumption when traveling from point A to B was compared to the consumption when traveling from point B to A, which has a net gain in elevation. The reliance of energy regeneration on gravitational potential energy suggested that there would be potential effects depending on the direction of travel.

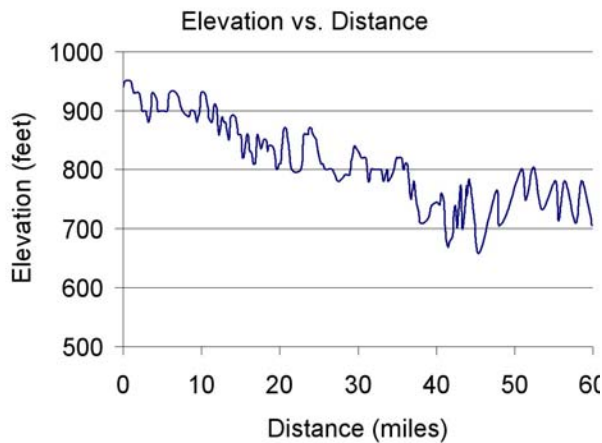


Figure 17. Elevation Plot of One Leg of the Test Route (Point A to Point B)

To look more closely at this, the ECM calculated fuel rate signal was used to indicate the relative amount of fuel consumed across the different configurations. The data was first normalized for all runs and configurations. Each run was then broken down into 4 sections, each representing one 58-mile leg of the run, with 2 of the legs making up one lap. Figure 18 shows the vehicle speed plot for one lap of the run, covering the same stretch of road in alternating directions. The truck begins at point A and turns around at point B. Each leg was analyzed from the point the truck reached the set speed until demand was cut at the turn-around. This provided the additional benefit of looking at the performance during steady-state operation without having to consider the fuel used while turning around.

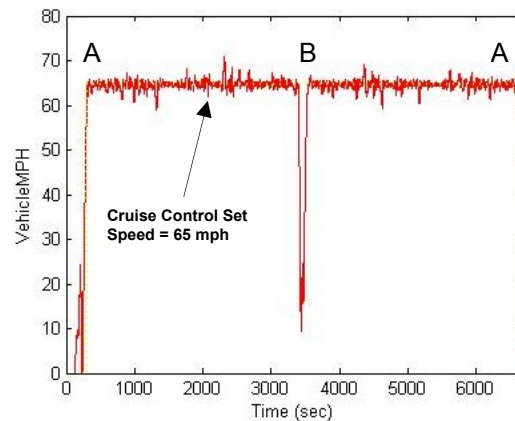


Figure 18. Vehicle Speed Plot for One Lap of Test Route

The chart in Figure 19 summarizes the results of fuel consumption relative to the direction of travel on the route, A to B being the direction resulting in a net loss of elevation or ‘downhill’, B to A being the opposite, ‘uphill’. The data is normalized to the average baseline fuel consumption in both directions. Consistent with the composite test data, both the regenerate-only and propulsion assist configurations provide a fuel consumption benefit. For this route, the regenerate-only configuration provided greater overall than the propulsion assist configuration. This figure highlights the source of the benefit to an additional level of detail.

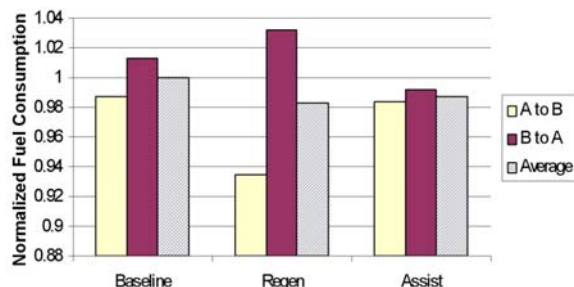


Figure 19. Normalized Fuel Consumption Dependent on Direction and Configuration

The data suggests that in all configurations, more fuel is consumed on the uphill portion of the run than on the downhill, which is consistent with the work energy theorem relative to gravitational potential energy. An interesting result is that the regenerate-only configuration appears to actually increase the fuel consumption on the uphill portion of the run relative to the baseline. The net improvement then comes as a result of the improvement on the downhill portion, which is most likely a result of the reduced amount of regeneration (relative to assist) on the downhill portion leading to increased energy stored in vehicle momentum. On the net uphill portion, when gravity is doing counterproductive work on the vehicle, there is much less energy to be gained over the run. In this case, the regeneration and subsequent slight loss in momentum may be the cause of the increased fuel consumption.

The propulsion assist configuration appears to have achieved a better balance in the fuel consumption between the different directions, with the uphill portion only requiring on slightly more fuel than the downhill portion. This averages to a small improvement over the baseline data, however, not as significant an improvement as the downhill portion for the regenerative braking only configuration. Similar to a previous observation, the increased regeneration proved to provide only a small advantage over the baseline. The data shows that in the downhill direction, relative to the regenerative braking only configuration, the propulsion assist configuration is decidedly worse. Conversely, the propulsion assist configuration does provide the best fuel consumption on the uphill portion. These results suggest that further optimization and customization of the controls could provide additional improvements.

Comparison to Original Simulations

Looking at the road profile for the fuel economy testing, the profile was determined to have a maximum grade of 4.05 percent with an average elevation frequency (peak-to-peak) of approximately 3.3 km. Referring back to Table 4, the original simulation data suggests a reduction of fuel consumption greater than 2.3 percent (assuming an increasing trend with respect to a constant 4 percent grade and decreasing elevation frequency). The measured results of a 2.2 percent improvement, while not an exact match for the simulation data, do corroborate the predicted results.

The differences between the measured results and the simulations can be attributed to a combination of differences between the power management algorithms and the hill profiles. The original simulations included a different depth of discharge and SOC limits for the batteries. The simulations also utilized different parameters in the power management strategy such as the range of engine torque where the ISG would assist. Considering the road profiles, the simulations used a sinusoidal profile with no net change in elevation. The hills were uniform in the simulations while the actual road profile for testing had a varying elevation frequency and grade. The simulated numbers themselves show dramatic differences in results with changes in the road profile. The combination of these disparities between the road tests and the initial simulations explain any small differences in the exact magnitude of the gains.

Conclusion

During 2007, the team completed integration of the electric cooling fan, stainless steel aftercooler, and energy storage system into the MET platform. Component integration enabled thermal performance testing utilizing the newly installed 2007 engine on the chassis dynamometer. Capitalizing on the increased robustness in temperature control offered by the electric components and new cooling module, the team investigated fuel economy improvement opportunities in addition to capability enhancements. The reworked cooling system demonstrated the ability to reduce fuel consumption by 2.7 percent during typical steady state conditions. Furthermore, the system increased the ambient capability of the system by more than 6 °C.

Following chassis dynamometer testing, the team performed on-road testing of mild-hybrid operation with the ISG providing regenerative braking and cruise assist. These functions yielded a 2 percent increase in fuel economy during on-road testing. The improvements seen on the chassis dynamometer and during on-road testing are believed to be largely additive because of their natural independence. Chassis dynamometer testing made no allowance for regenerative braking or cruise assist. Conversely, the on-road testing only examined the impact of control algorithms that make use of the ISG and the energy storage system in different manners. This suggests

that the technologies implemented during this program offer the opportunity to improve fuel economy by greater than 4 percent, a substantial savings for long haul applications. Previous work in this program suggests that each 1 percent improvement in fuel economy might equate to approximately \$2300 of present value to the operator. As such, the technologies evaluated during this program would not only reduce fuel consumption and emissions, but also do so in a value-added fashion, facilitating adoption through a variety of markets.

VII. ULTRALIGHT TRANSIT BUS SYSTEM

A. The Vehicle System Optimization Of A Lightweight Stainless Steel Bus

Principal Investigator: J. Bruce Emmons

Autokinetics Inc

1711 West Hamlin Road

Rochester Hills, MI 48309-3368

(248) 852-4450, fax: (248) 852-7182, e-mail: jbemmons@autokinetics.com

Technology Development Managers: Sid Diamond and Lee Slezak

(202) 586-2335, fax: (202) 586-2476, e-mail: Lee.Slezak@hq.doe.gov

Field Technical Manager: Jules Routbort

(630) 252-5065, fax: (630) 252-4798, e-mail: routbort@anl.gov

Contractor: Argonne National Laboratory

Contract No.: 4F-02161

Objective

- The intent of this project is to perform the integration and optimization of a hybrid or battery/electric propulsion system, and various vehicle subsystems into a lightweight bus body.
- Autokinetics will use as much off the shelf technology as possible. Optimization of the propulsion and vehicle systems will primarily be through careful selection of appropriately sized components.
- This project will result in a single "Proof-of-Concept" prototype bus, suitable for testing and evaluation of performance under controlled conditions.
- A further objective of the project is to identify one or more paths to rapid commercialization of the technology.

Approach

- Conduct ADVISOR and GREET computer simulations of a number of different types of propulsion systems to predict performance and energy efficiency.
- After identifying the most promising propulsion system architecture, use computer simulations to evaluate and select the individual components with the best combination of performance and affordability.
- Design, integrate and install the propulsion system.
- Design or select optimized vehicle subsystems such as seats, glass, air conditioning, etc.
- Purchase or fabricate and install all vehicle subsystems.
- Evaluate the performance and make modifications, if necessary.
- Perform initial testing.

Accomplishments

- Cables and connectors
- Low voltage system
- Progress towards commercialization

Future Direction

- Design, fabricate and install vehicle subsystems.
- Test the propulsion system.
- Perform FMEA (failure modes and effects analysis).
- Perform limited testing and development of the complete vehicle.
- Continue commercialization efforts.

Introduction

The intent of this project is to perform the integration and optimization of a hybrid or battery/electric propulsion system and various vehicle subsystems into a lightweight bus body. Off the shelf technology will be used wherever possible. Optimization of the propulsion and vehicle systems will primarily be through careful selection of appropriately sized components.

This project will result in a single “Proof-of-Concept” prototype bus, suitable for testing and evaluation of performance under controlled conditions. The design will not necessarily be ready for mass production, nor will it include trim and appearance items.

The completed prototype will include the primary body structure, suspension, glazing, driver’s station, electric wheel motors, inverters, and energy storage system. It will also include regenerative braking, limited lighting, bumpers, and full seating.

Cables and Connectors

As reported previously, the energy storage system for the propulsion system was developed and installed into the prototype vehicle. With this step complete, the wiring of the propulsion system began in earnest during this reporting period. The various circuits were laid out. Routing and enclosure systems have been developed. The main power cables were installed and batteries connected. Considerable

progress was made toward installing necessary wiring for the sub-systems such as chargers, cooling fans, and fuse boxes.

It is anticipated the wiring of the controls system will be completed soon allowing the propulsion system to be energized and tested in the very near future.



Figure 1. Main Cables and Battery Connections

Low Voltage System

In addition to the propulsion system a separate low voltage system was installed into the prototype vehicle. This system supplies the non-propulsion energy needs for the vehicle such as lighting, doors, compressor, etc. and consists of standard 24 volt marine type energy storage and a special dedicated charging system.

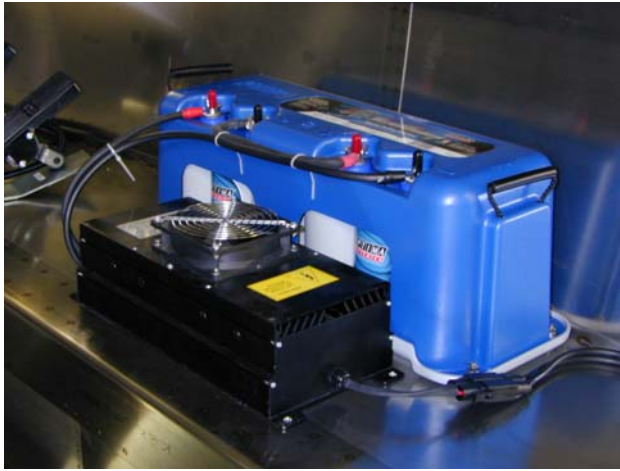


Figure 2. Low Voltage Energy Storage and Charger

Conclusions

With the prototype build near completion and most high-risk milestones successfully achieved, much of the focus during this period was aimed at commercialization of the technology. Many potentially useful contacts have been developed and various paths to commercialization have been identified and investigated.

The remaining project tasks, expected to be completed by June 2008, primarily involve lower risk subsystems such as seats, HVAC, doors, and ADA compliance. In light of this, Autokinetics continues to be confident that the improvement in fuel economy for this vehicle will be at least 300%, as predicted. It is anticipated that performance testing of the completed vehicle in the not too distant future will bear this out.

VIII. APPENDIX A

Investigation of Tractor Base Bleeding for Heavy Vehicle Aerodynamic Drag Reduction

Jason Ortega, Kambiz Salari, Bruce Storms

Abstract One of the main contributors to the aerodynamic drag of a heavy vehicle is tractor-trailer gap drag, which arises when the vehicle operates within a crosswind. Under this operating condition, freestream flow is entrained into the tractor-trailer gap, imparting a momentum exchange to the vehicle and subsequently increasing the aerodynamic drag. While a number of add-on devices, including side extenders, splitter plates, vortex stabilizers, and gap sealers, have been previously tested to alleviate this source of drag, side extenders remain the primary add-on device of choice for reducing tractor-trailer gap drag. However, side extenders are not without maintenance and operational issues. When a heavy vehicle pivots sharply with respect to the trailer, as can occur during loading or unloading operations, the side extenders can become crushed against the trailer. Consequently, fleet operators are forced to incur additional costs to cover the repair or replacement of the damaged side extenders. This issue can be overcome by either shortening the side extenders or by devising an alternative drag reduction concept that can perform just as effectively as side extenders. To explore such a concept, we investigate tractor base bleeding as a means of reducing gap drag. Wind tunnel measurements are made on a 1:20 scale heavy vehicle model at a vehicle width-based Reynolds number of 420,000. The tractor bleeding flow, which is delivered through a porous material embedded within the tractor base, is introduced into the tractor-trailer gap at bleeding coefficients ranging from 0.0–0.018. To determine the performance of tractor base bleeding under more realistic operating conditions, computational fluid dy-

Jason Ortega

Lawrence Livermore National Laboratory, P.O. Box 808, L-644, Livermore, CA 94550, e-mail: ortega17@llnl.gov

Kambiz Salari

Lawrence Livermore National Laboratory, P.O. Box 808, L-644, Livermore, CA 94550, e-mail: salaril@llnl.gov

Bruce Storms

NASA Ames Research Center, Moffett Field, MS-260, CA 94035, e-mail: bstorms@mail.arc.nasa.gov

namics simulations are performed on a full-scale heavy vehicle within a crosswind for bleeding coefficients ranging from 0.0–0.13.

1 Introduction

During the 1970s and 1980s, a number of first-generation drag reduction devices were designed to reduce the aerodynamic losses of heavy vehicles [5]. The result of this effort led to the development of a number of devices (front-end rounding, tractor aero-shields, body molding, and cabin side extenders) that improved the aerodynamics of heavy vehicle tractors. Additionally, a number of second-generation devices (tractor-trailer gap sealers, trailer side skirts, and boattails) were developed. Unfortunately, these devices did not enter into the market on a wide-scale basis, which was due not to their ineffectiveness in reducing drag, but rather to operational, maintenance, and, ultimately, economic concerns. However, with rising fuel costs and potentially unstable fuel supplies, there is a renewed objective to further reduce heavy vehicle aerodynamic drag.

On a modern heavy vehicle, one of the main sources of aerodynamic drag is tractor-trailer gap drag, which occurs when the vehicle is operating in a crosswind and free-stream flow is entrained into the tractor-trailer gap. This flow entrainment imparts a momentum exchange to the heavy vehicle in the direction opposite of travel, resulting in a drag increase. Presently, cabin side extenders, which are 0.46-0.51m wide vertical plates attached to the tractor base, are routinely utilized on modern heavy vehicles to mitigate flow entrainment into the gap. Wind tunnel measurements have shown that side extenders, when used in conjunction with a rooftop aero-shield and tractor side skirts, reduce the wind-averaged drag coefficient, $C_{d_{avg}}$, by about 0.15 [6]. Other devices, such as gap sealers and fillers are also effective in reducing tractor-trailer gap drag and provide additional reductions in the wind-averaged drag coefficient ranging from about 0.03-0.06 [6]. However, due to maintenance and operational issues, these devices are not commonly installed on modern heavy vehicles.

Despite their widespread use, side extenders are often damaged during routine shipping operations. Commercial fleet owners frequently comment that the large structural surfaces comprising the side extenders are easily bent or crushed when the tractor pivots too sharply relative to the trailer during loading maneuvers. When such damage occurs, the commercial fleets are forced to take the tractor out of operation for service and either remove or replace the side extenders, a task which can become extremely costly when such repairs are required for several thousand tractors in the larger shipping fleets. Consequently, there is a need to devise alternate drag reduction concepts that can both alleviate flow entrainment into the tractor-trailer gap and be less prone to damage during vehicle articulation. One such concept recently developed are side extenders that are about 38% shorter than those presently used and still provide nearly the same aerodynamic benefit [7].

Another proposed concept is tractor base bleed, in which a stream of low-speed flow is injected into the tractor-trailer gap at a velocity, U_b , over a large surface area, A_b , on the tractor base. Base bleed has been previously studied as a means of reducing the drag of bluff bodies, such as ballistic shells [18], blunt-base airfoils [28], backward facing steps [16], and circular cylinders [23]. The typical values of bleeding flow, defined by the bleeding coefficient, $C_\mu = U_b A_b / U_o A_o$, range from 0.0-0.28, where U_o is the free-stream velocity and A_o the characteristic area of the body. Bearman [3], Michel & Kost [20], and Wood [28, 29] showed that base bleed increases the pressure over the bleeding surface, thereby reducing the overall drag of the bluff body. When sufficient bleeding flow is injected into the separated wake, Bearman [3], Schumm, *et al.* [23], and Wood [28, 29] demonstrated that the strength of shed vortex street can be reduced. In addition, base bleeding displaces the separated wake in the downstream direction [3, 24, 29, 30]. Further increases in bleeding can suppress vortex shedding entirely. Yao & Sandham [30] showed that bleeding over a large area at a low velocity is more effective in reducing the drag than bleeding over a small area at a high velocity. Base bleed has also been shown to influence the stability characteristics of the separated wake [11]. Arcas & Redekopp [1], Hammond & Redekopp [10], Huerre & Monkewitz [11], and Sevilla & Martinez-Bazan [24] observed that, at a critical bleed rate, the wake transitions from being absolutely unstable to convectively unstable. And, Koch [14, 15] showed that the transition from absolute to convectively unstable flow occurs slightly downstream of the region of reverse flow in the separated wake.

Although the previous studies elucidated the flow physics and drag reduction capability of base bleeding, the types of bluff bodies used were either two-dimensional or axisymmetric. In addition, the bluff bodies were isolated from the influence of other bodies and were oriented at zero degrees yaw with respect to the free-stream flow. It is therefore difficult to determine from these previously published results as to whether or not base bleeding is an effective means of reducing the drag of a tractor-trailer gap, which is surrounded by both a highly asymmetric, three-dimensional geometry and a moving ground plane and which is typically oriented at a finite yaw angle. Thus, the purpose of this study is to investigate base bleeding as means of reducing tractor-trailer gap drag. In particular, we wish to answer the following questions. Does tractor base bleeding reduce the drag of a heavy vehicle? How much bleeding flow is required to produce a modest drag reduction? How is the flow within the tractor-trailer gap altered as a result of base bleeding? How do the gap flow physics and the reductions, if any, in drag due to tractor base bleeding compare to those of traditional side extenders?

2 Wind Tunnel Measurements

As a first step in providing answers to these questions, we perform wind tunnel measurements on a 1:20 scale heavy vehicle model that employs tractor base bleeding. The model tractor, which is a detailed representation [27] of a Freightliner

Columbia [8], is fabricated using a rapid prototyping technique (Fig. 1a) [25]. The engine grill and the air inlets on the bumper are sealed since Leuschen & Cooper [17] measured very little difference in the drag coefficient when the cooling airflow through these two regions was blocked. To prevent laminar flow separation, several lengths of 4×10^{-4} m diameter wire are laid over the leading edges of the tractor and 4.6×10^{-4} m diameter glass beads are bonded to the tractor nose, visor, aero-shield, window pillars, door columns, and engine grill. The tractor is attached to a 0.69m long model freight van that includes cross members and a landing gear on the trailer underside. The trailer body is constructed from 0.006m thick sheets of acrylic, while the trailer wheels are fabricated in the same manner as that of the tractor. The tractor-trailer gap is adjustable and, for this study, is set to 0.038 and 0.076m. Force measurements are made by suspending the entire tractor-trailer model on a six-component force balance (Northrop MK XVA 0.75") that is positioned near the upstream end of the trailer. The signals from the force balance are digitized and stored on a computer using BDAS 9.3 data acquisition software [4]. The resulting drag coefficients, $C_d = D / \frac{1}{2} \rho U_o^2 A_o$, are obtained to within $\pm 1.69 \times 10^{-3}$, which includes both the balance accuracy and the average measurement repeatability, where D is the drag force along the body axis, x_a , of the model, ρ the density of air, and $A_o = 2.47 \times 10^{-2} \text{m}^2$ the characteristic area of the model.

Tractor base bleeding is provided by directing a compressed air supply into two 0.019m NPT air supply lines that are connected to two smaller 0.006m internal diameter tubes, which enter the model through the trailer underside (Fig. 1b). The bleeding flowrate is measured with a pneumatic in-line flowmeter (Omega FL7722A). Since the 0.006m internal diameter tubes pass from the non-metric to the metric portions of the force balance, a service loop is incorporated into the tubing before it exits the upstream end of the trailer underside and is attached to two ports on the tractor underside. These ports direct the airflow into a plenum that comprises the entire model tractor cabin. On the base of the tractor cabin are threaded holes to which several different rapid-prototyped pieces can be affixed. For base bleeding configurations, perforated tractor bases with and without 0.02m wide side extenders are employed. On these pieces, the bleeding surface area is about 19% of the characteristic area, A_o , of the model tractor. For cases in which there is no bleeding flow, aluminum duct tape is placed over the perforated holes or a separate non-perforated tractor base piece with or without side extenders is fixed to the tractor base. Within the plenum, 0.051m thick packing foam is positioned against the perforated tractor base to provide a pressure drop for the bleeding flow as it exits the plenum, thereby ensuring a more uniform bleeding velocity profile. Four bleeding flowrates, corresponding to base bleeding coefficients of 0.0, 0.008, 0.013, and 0.018, are used in this wind tunnel study. Velocity measurements made in the gap using a multi-hole pressure probe (Cobra, Turbulent Flow Instrumentation) with no tunnel velocity demonstrate fairly uniform bleeding velocity (Fig. 2).

The drag coefficient measurements are made within the NASA Ames Fluid Mechanics Laboratory open-circuit wind tunnel, which has a contraction ratio of 9:1, a test section size of 0.813m \times 1.219 m, and a free-stream turbulence level of 0.15%. The wind tunnel is operated at a nominal dynamic pressure and tunnel speed of

Investigation of Tractor Base Bleeding for Heavy Vehicle Aerodynamic Drag Reduction

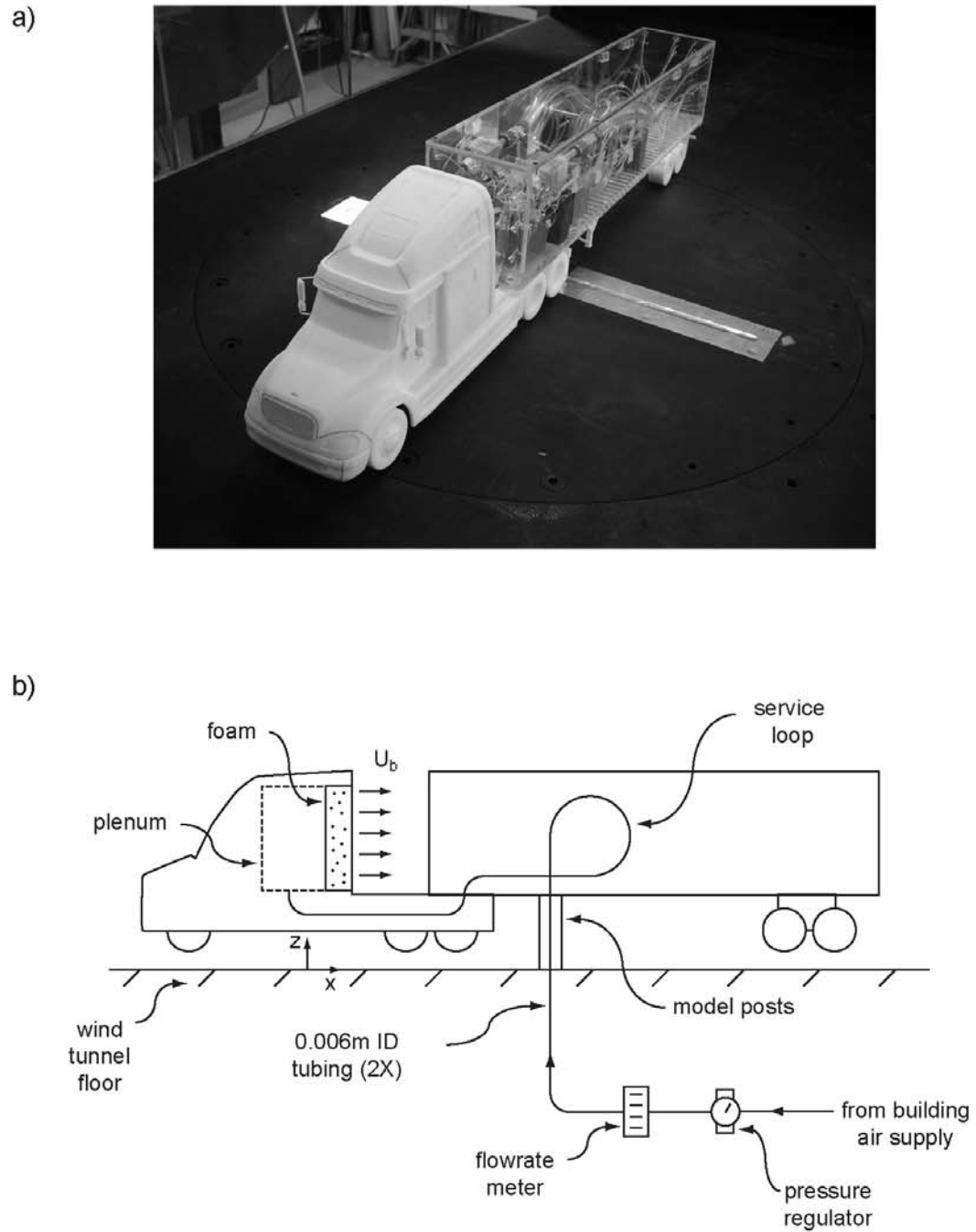


Fig. 1 a) 1:20 scale heavy vehicle model model in the low-speed NASA Ames wind tunnel. b) Details of the tractor base bleeding system.

6

Jason Ortega, Kambiz Salari, Bruce Storms

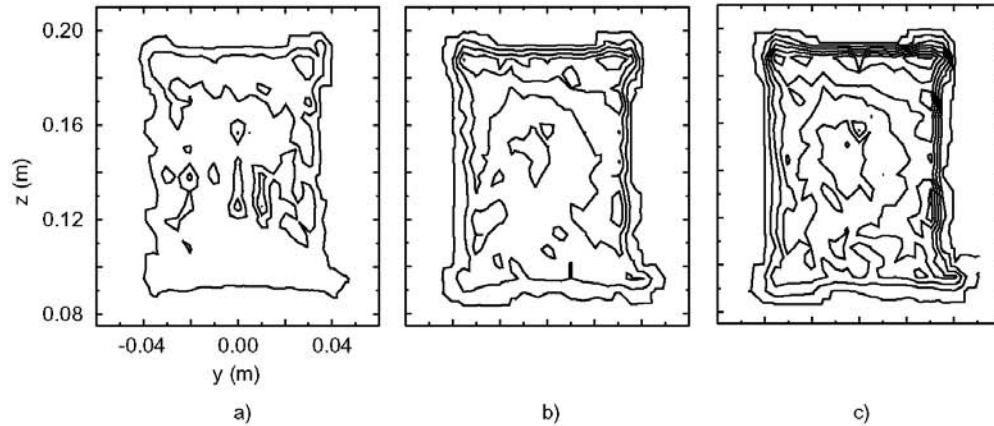


Fig. 2 Bleeding velocity contours in the x -direction made 0.019m downstream of the tractor base for C_μ equal to a) 0.008, b) 0.013, and c) 0.018 for a tractor-trailer gap distance of 0.076m with no tunnel velocity.

1420N/m² and 48.95m/s, respectively. The resulting width-based Reynolds number, $Re_w = U_o w / \nu$, of the model is 420,000, where $w = 0.13$ m is the model width, and ν the kinematic viscosity of air. The percentage of blockage of the model in the tunnel test section is 2.5% at 0° yaw. The model is mounted at height about equal to the boundary layer displacement thickness ($\approx 5.0 \times 10^{-3}$ m) above the tunnel floor on a turntable that is driven by a computer-controlled servo motor (Parker Compumotor), which can rotate the model to within $\pm 0.05^\circ$. For each model configuration, force measurements are made at yaw angles ranging from $\pm 8^\circ$. To assess the repeatability of the measurements, as well as hysteresis in the flow patterns over the model, the data are acquired on selective configurations for both increasing and decreasing yaw angle directions and are observed to show negligible hysteresis effects. Since the tractor bleeding flow generates forces on the model due to the effects of thrust and the expansion of the 0.006m internal diameter tubing within the trailer, force measurements are first made at a zero tunnel velocity at each non-zero bleeding coefficient value. These forces are then subtracted from the subsequent measurements made at the corresponding bleeding coefficient values.

While the C_d data at each yaw angle is useful for evaluating the tractor base bleeding concept, it is somewhat cumbersome since the C_d distribution does not summarize the drag reduction performance into a single quantity that can be easily compared with that of other devices, such as side extenders. Taking the mean value of C_d over all measured yaw angles is also insufficient since it does not account for the fact that the crosswind velocities cause a vehicle traveling at a particular speed to experience certain yaw angles more than others. A quantity that resolves both of these issues is the wind-averaged drag coefficient, $C_{d\text{avg}}$ [12], which is computed for each base bleeding configuration (Fig. 3). It is apparent that the drag coefficient decreases as the bleeding coefficient is increased for both gap distances. However, a greater reduction in drag is observed for the larger gap distance both with and without side extenders. When $C_\mu > 0.006$, tractor base bleeding with no

side extenders at the larger gap distance yields a greater reduction in drag than that of side extenders alone with no bleeding flow. It should also be noted that the wind-averaged drag coefficients for the larger gap are greater than those of the smaller gap, indicating the presence of a larger amount of entrained flow into the tractor-trailer gap. Similar trends in the dependence of the drag coefficient upon gap distance, d_{gap} , were observed by Hammache & Browand [9], who investigated tractor-trailer gap flow dynamics on a simplified tractor-trailer geometry at a comparable Re_w of 270,000. At a critical gap distance of $d_{gap}/\sqrt{A_o} \approx 0.5$, Hammache & Browand showed that the total vehicle drag increases sharply. In the present study, the values of $d_{gap} = 0.038$ and 0.076 m are below and about equal to the critical gap distance, respectively.

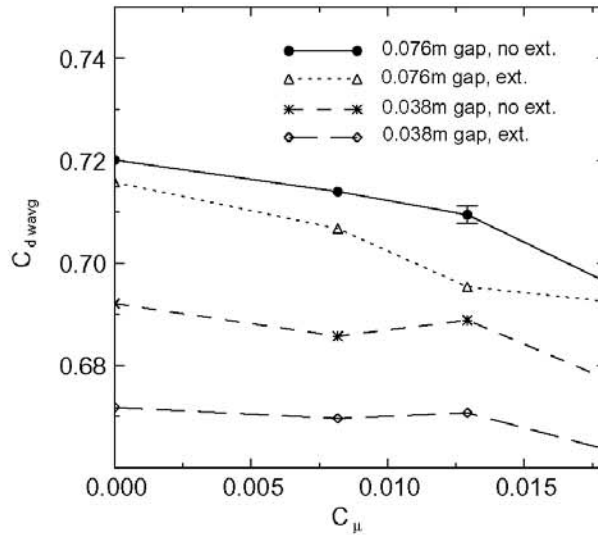


Fig. 3 Wind-averaged drag coefficient, $C_{d,wavg}$, as a function of the tractor base bleeding coefficient, C_μ , for two tractor-trailer gap distances with and without side extenders.

3 CFD Simulations

While the wind tunnel measurements demonstrate that tractor base bleeding can indeed reduce the drag of the heavy vehicle model, further investigation is needed both to demonstrate the effectiveness of this concept at a full-scale Reynolds number and to understand the changes in the gap flow physics arising from the base bleeding. For these reasons, we perform computational fluid dynamics (CFD) simulations on a full-scale Freightliner Columbia operating at highway conditions within a crosswind. The tractor-trailer gap distance is set to 1.02m and a 13.6m long freight van is attached to the tractor.

The simulations are performed within a computational domain that is $98\text{m} \times 49\text{m} \times 128\text{m}$ (Fig. 4), such that the heavy-vehicle cross-sectional area is 0.2% of that of the domain. To model the crosswind velocity, U_w , which is typically 3.1m/s

at vehicle mid-height [22], while the vehicle travels at a ground speed of $U_g = U_o = 29.1\text{m/s}$, the vehicle is yawed to $\theta = \tan^{-1}(U_w/U_g) = 6.1^\circ$ and a velocity of $\sqrt{U_g^2 + U_w^2} = 29.3\text{m/s}$ is specified at the inlet to the computational domain (Fig. 4). The resulting width-based Reynolds number is 5,000,000. Beneath the vehicle, a no-slip, moving ground plane boundary condition is prescribed at a velocity of U_g and a yaw angle of 6.1° . The no-slip surfaces of the tractor and trailer tires, which rotate at an angular velocity of 53s^{-1} , intersect the ground plane, producing a tire contact patch that has a swept angle of 20° [2]. A slip boundary condition and a zero gradient boundary condition are specified along the walls and outlet, respectively, of the computational domain. To produce the tractor base bleeding flow, an inlet velocity boundary condition ($U_b = 0.0\text{--}0.2U_o$, $v_c = 0$, $w_c = 0$) is defined across the tractor base, which has an area that is 65% of that of the vehicle cross-section, $A_o = 9.87\text{m}^2$. The corresponding bleeding coefficients range from 0.0–0.13. The other variables on the bleeding inlet boundary are computed by assuming a zero gradient normal to the inlet, such that the variables on the inlet nodes are extrapolated from the values of the interior nodes. To provide a performance comparison for the base bleeding concept, side extenders, which have a length of 0.38m, are modeled in one vehicle configuration and compared with the baseline case. A finite-volume code [26] is used to solve the Reynolds averaged Navier-Stokes (RANS) equations for the flow about the heavy vehicle. The spatial fluxes are discretized with a second-order monotone advection and reconstruction scheme (MARS) [26] and the $k - \omega$ SST turbulence model [19] with a wall function is used to solve for the turbulent kinetic energy and dissipation fields. A previous validation study by Pointer [21] demonstrated that this turbulence model can adequately capture the value of C_d at a Re_w on the order of 10^6 . The cell height adjacent to the vehicle is chosen to be $3.3 \times 10^{-3}\text{m}$, yielding a nominal value for y^+ [13] of 90 over the entire tractor-trailer surface. Meshes with about 25×10^6 cells are used in this study. The simulations are typically run for about 10,000–20,000 iterations in order to obtain statistically converged average drag coefficients, which tend to oscillate by about ± 0.007 due to the inherent unsteady nature of the three-dimensional flow field about the heavy vehicle.

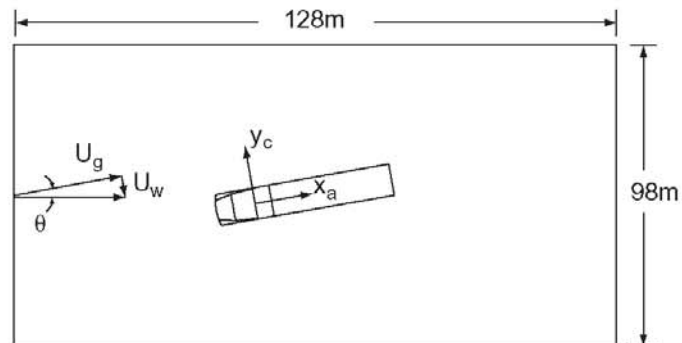


Fig. 4 Computational domain used for the full-scale CFD simulations.

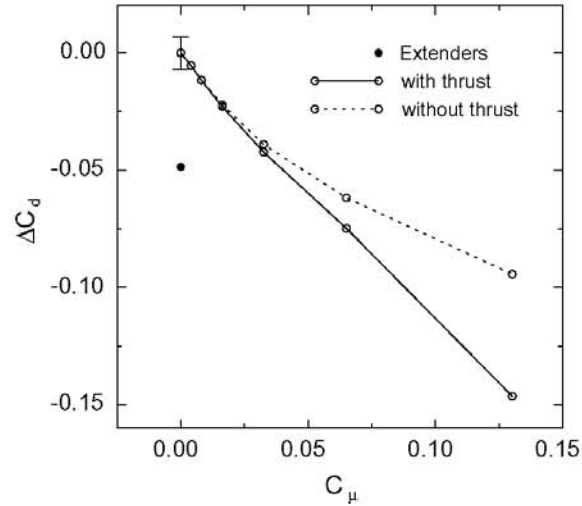


Fig. 5 Change in the drag coefficient as function of the bleeding coefficient for the CFD simulations.

A plot of the drag coefficient as function of the bleeding coefficient (Fig. 5) reveals that, in much the same manner as that of the wind tunnel measurements, increases in bleeding flow decrease the drag coefficient. In addition, the drag reduction of $\Delta C_d \approx 0.025$ observed for $C_\mu \approx 0.018$ is about equal to that seen experimentally ($\Delta C_d \approx 0.02$) at 6° yaw for the larger gap distance despite the relatively large difference in Re_w . For the computational results, the drag coefficient decreases in a nearly linear fashion for the largest bleeding coefficients, values of which were not attainable in the wind tunnel measurements. The largest reduction in drag ($\Delta C_d = 0.146$) occurs at the maximum bleeding coefficient of 0.13. It is also evident bleeding coefficients greater than 0.06 provide a larger reduction in drag than that of the side extenders ($\Delta C_d = 0.049$). Obviously, a portion of the drag reduction produced by base bleeding is due to the thrust,

$$T = \int_{A_b} \rho U_b \mathbf{u} \cdot \mathbf{n} \, dA, \tag{1}$$

of the bleeding flow and not to modifications of the tractor-trailer gap flow physics, where \mathbf{u} is the fluid velocity vector and \mathbf{n} the unit normal vector of the vehicle surface. Removing this thrust contribution from the data in Fig. 5 demonstrates that, for the bleeding coefficients evaluated in this study, a significant drag reduction occurs solely due to changes in the gap flow physics.

One of the changes to occur is in the amount of free-stream fluid entrained into the tractor-trailer gap. The entrainment rate is computed by defining a rectangular control surface that encompasses the volume of the entire tractor-trailer gap (Fig. 6), but not the bleeding area over the tractor base. The entrainment flowrate,

$$Q_e = \int_{A_{in}} \mathbf{u} \cdot \mathbf{n}_{cs} \, dA, \tag{2}$$

is calculated over the control surface to determine the amount of fluid entering the gap from the free-stream, where \mathbf{n}_{cs} is the normal vector of the control surface and

the integration area, A_{in} , indicates that the integral is computed over those portions of the control surface in which $\mathbf{u} \cdot \mathbf{n}_{cs} < 0$. Without any base bleeding, the gap entrains free-stream fluid at a rate of $0.085U_oA_o$, where a large portion of the entrainment occurs on the windward-downstream and bottom-upstream areas (Fig. 6) of the control surface. When side extenders are placed on the tractor base, $Q_e = 0.072U_oA_o$. Due to the highly three-dimensional nature of the velocity field in the gap, the flow exits through distinct patches spread over the leeward and upper areas of the control surface. When $C_\mu > 0$, the bleeding flow reduces the amount of free-stream fluid entrained into the tractor-trailer gap (Fig. 7). (Note that the asymptotic decay of Q_e to what appears to be a value greater than 0 is a result of the manner in which the control surface geometry is defined. The value of Q_e will likely be greater than zero for all C_μ because free-stream fluid will continue to enter the control surface through the upstream, vertical face.) A comparison of the contour plots of $\mathbf{u} \cdot \mathbf{n}_{cs}$ (Fig. 8) reveals that base bleeding significantly reduces the entrainment of free-stream fluid on the windward and bottom areas of the control surface and produces an exit flow pattern that is more uniformly distributed over the downstream areas of the control surface.

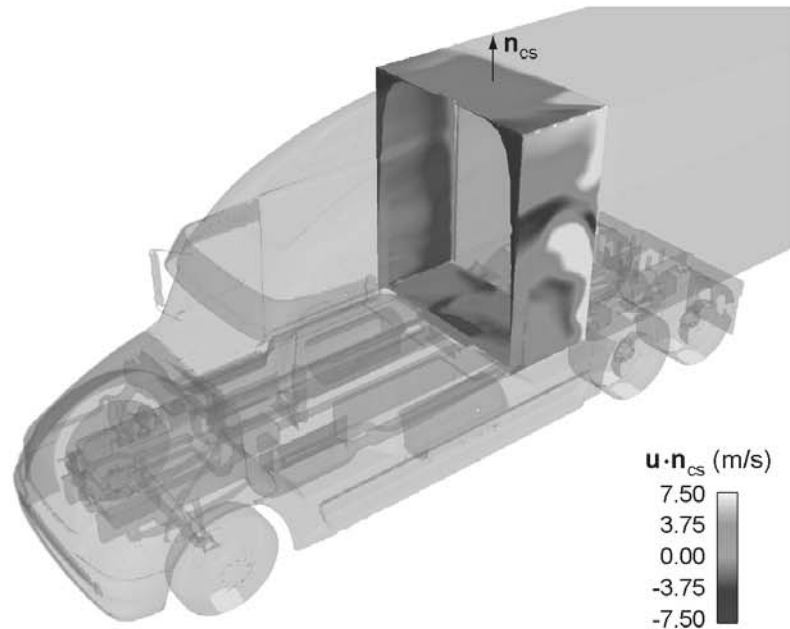


Fig. 6 Control surface defined for computing the flow entrainment rate, Q_e , into the tractor-trailer gap. The color contours on the surface denote the values of $\mathbf{u} \cdot \mathbf{n}_{cs}$ for $C_\mu = 0.0$.

The specific manner in which fluid entrainment is altered as a result of base bleeding can be understood by investigating the velocity field within the tractor-trailer gap. Prior to base bleeding, the windward shear layer separating from the tractor base impinges upon the trailer frontal face, producing a cross-stream flow in

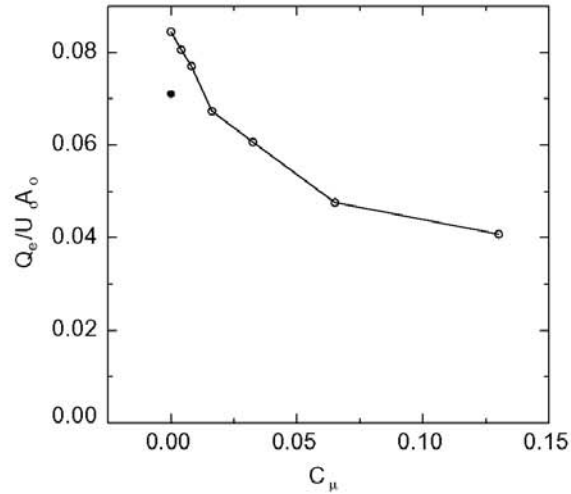


Fig. 7 Non-dimensional flow entrainment rate into the tractor-trailer gap as function of the bleeding coefficient. The symbol • denotes the configuration with side extenders ($C_\mu = 0.0$).

the form of a wall jet that spans the entire gap width (Fig. 9a,c). At the centerline of the gap, this wall jet has a maximum magnitude that is about $0.75U_o$ (Fig. 10). Since the flow recirculates within the gap, a positive cross-stream velocity is present near the tractor base. As the amount of base bleeding is increased, the strength of the wall jet decreases. In addition, the cross-stream velocity profile becomes linear with the gap distance near the tractor base and the peak velocity of the positive-valued recirculating flow diminishes. At a bleeding coefficient of $C_\mu = 0.13$, the cross-stream velocity profile is linear throughout the entire tractor-trailer gap centerline, except within a thin boundary layer on the trailer frontal surface. Plots of the velocity field (Fig. 9b,d) show a relatively uniform gap flow, where the regions of large cross-stream flow are confined to the outer extents of the gap. It should also be noted that side extenders reduce the strength of the cross-stream flow, such that the maximum magnitude of the wall-jet is reduced to a value about equal to that which occurs when $C_\mu \approx 0.033$ (Fig. 10).

The shear layer that produces the wall jet within the gap leaves a distinct high pressure signature as it impinges upon the trailer frontal face (Fig. 11a). Away from this impingement zone, the pressure is considerably lower in magnitude, except for a region on the leeward side of the gap. When bleeding flow ($C_\mu = 0.13$) is applied to the tractor base, this high pressure signature is diminished (Fig. 11b) and replaced with a more uniform pressure distribution that extends over nearly the entire trailer frontal face. The application of side extenders also reduces the pressure signature from the windward shear layer (Fig. 11c), though not to the extent seen for $C_\mu = 0.13$.

Plots of the pressure coefficient acting in the body axis-direction, $C_{pa} = |\mathbf{n} \cdot \mathbf{n}_a|(P - P_o) / \frac{1}{2}\rho U_o^2$, (Fig. 12) along the vertical centerline of the tractor base and trailer frontal face demonstrate that the pressure increases on both surfaces as the bleeding coefficient is increased, where P is the fluid pressure, P_o the freestream pressure, and \mathbf{n}_a is the unit body-axis direction vector. Calculating the average value

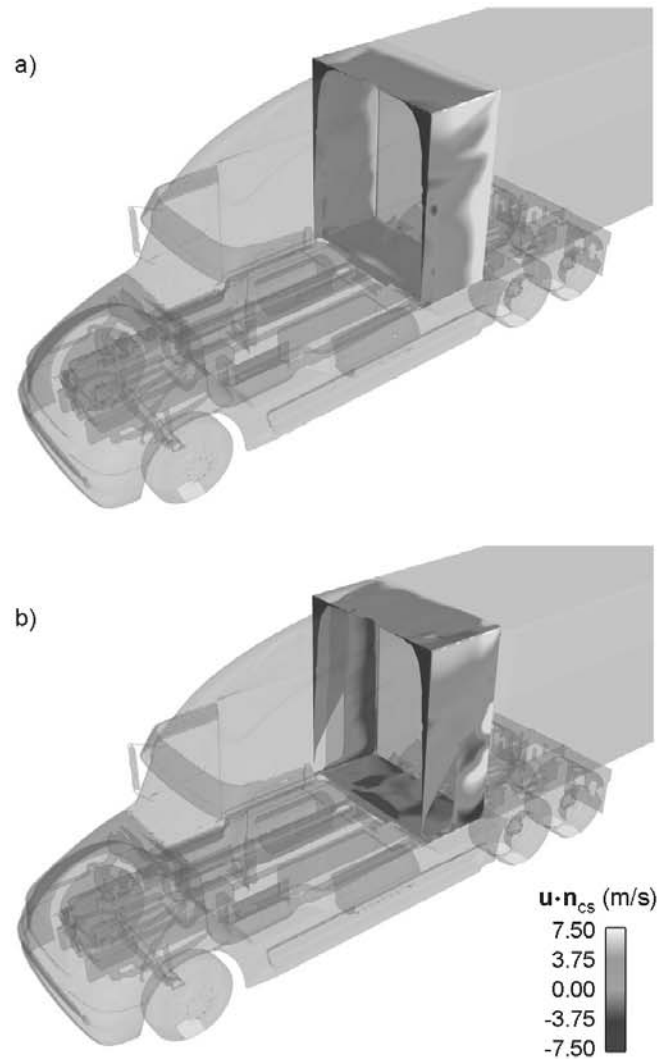


Fig. 8 Contours of $\mathbf{u} \cdot \mathbf{n}_{cs}$ over the control surface for a) a bleeding coefficient of $C_\mu = 0.13$ and b) for side extenders ($C_\mu = 0.0$).

of C_{pa} over the tractor base, trailer frontal face, and trailer base shows that the average pressure coefficient acting in the body-axis direction on the tractor base increases more rapidly than that on the trailer frontal face as C_μ is increased (Fig. 13). This subsequently reduces the difference between the average pressure coefficients on the tractor base and trailer frontal face, which is, in turn, responsible for the reduction in drag on the entire vehicle. In fact, for $C_\mu > 0.053$, the average pressure coefficient on the tractor base is greater than that of the trailer frontal face. The side extenders reduce the difference between average pressure coefficients over the tractor base and trailer frontal face, as well. However, the average pressure coefficient on the trailer base exhibits little sensitivity to either the bleeding flow or the side extenders.

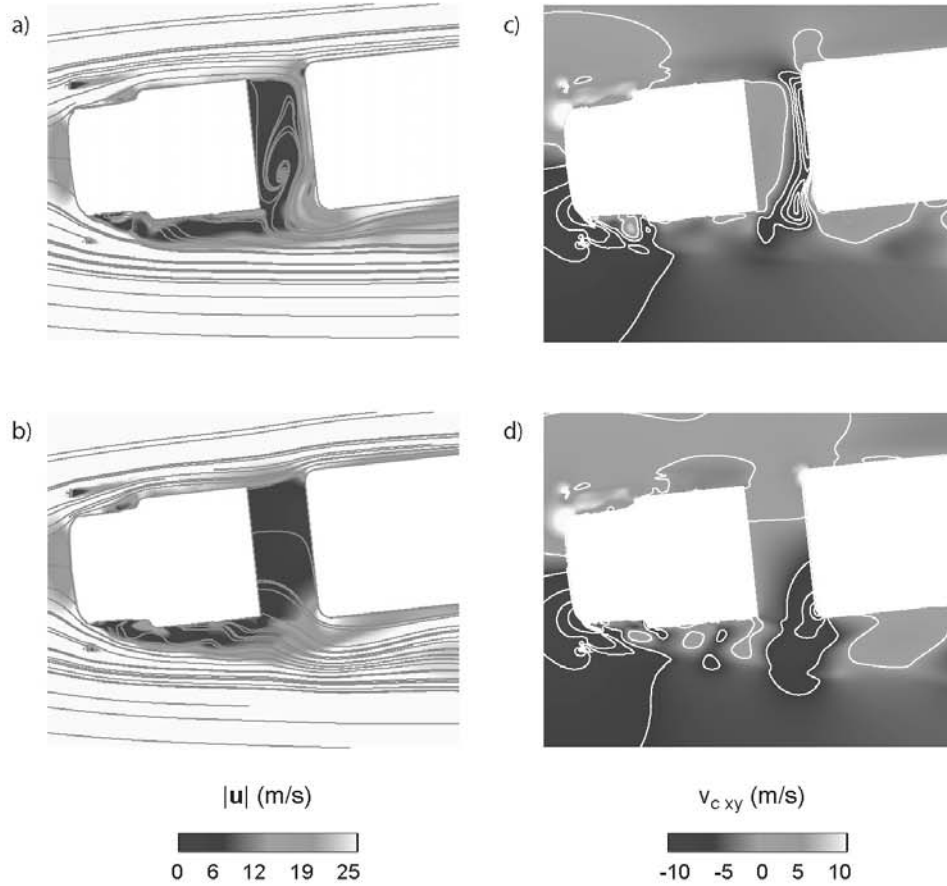


Fig. 9 a-b) Velocity magnitude and streamlines and c-d) cross-stream velocity at the mid-height of the tractor-trailer gap for C_{μ} equal to a,c) 0.0 and b,d) 0.13. Note that additional negative-valued contours are applied in c-d) to highlight the cross-stream gap flow.

4 Conclusions

Through this investigation, we have studied the drag reduction capability of tractor base bleeding. Both the 1:20 scale wind tunnel measurements and full-scale CFD simulations demonstrate that tractor base bleeding reduces the drag coefficient of a heavy vehicle. For bleeding coefficients greater than 0.06, the simulations show a reduction in the drag coefficient that is greater than that of side extenders. The simulation results also highlight the flow physics within the tractor-trailer gap that contribute to this drag reduction. As the bleeding coefficient increases, the rate of fluid entrainment from the free-stream into the gap decreases, which reduces both the pressure signature of the impinging windward shear layer on the trailer frontal face and the strength of the cross-stream wall jet within the gap. Lastly, tractor base bleeding reduces the difference between the average pressure coefficients on the

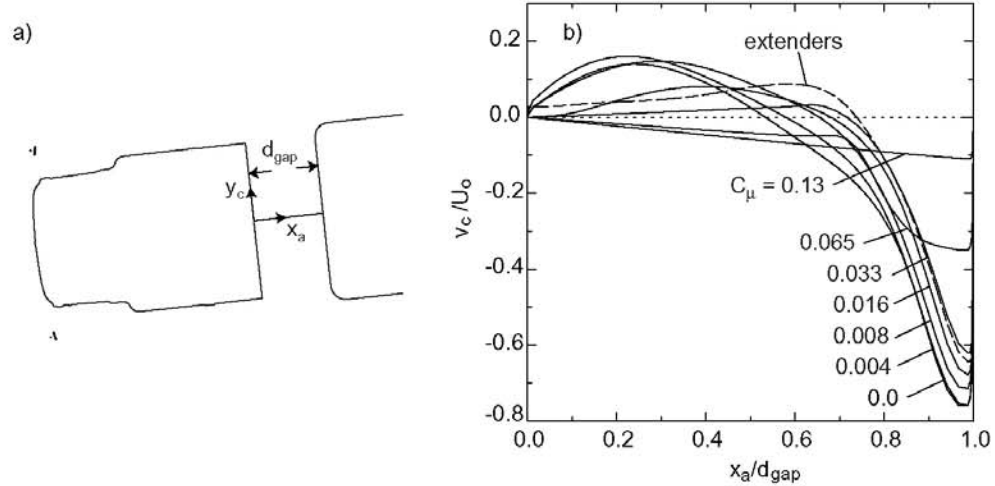


Fig. 10 a) Horizontal cross-section at the mid-height of the tractor-trailer gap. b) Non-dimensional cross-stream velocity through the gap as function of the bleeding coefficient.

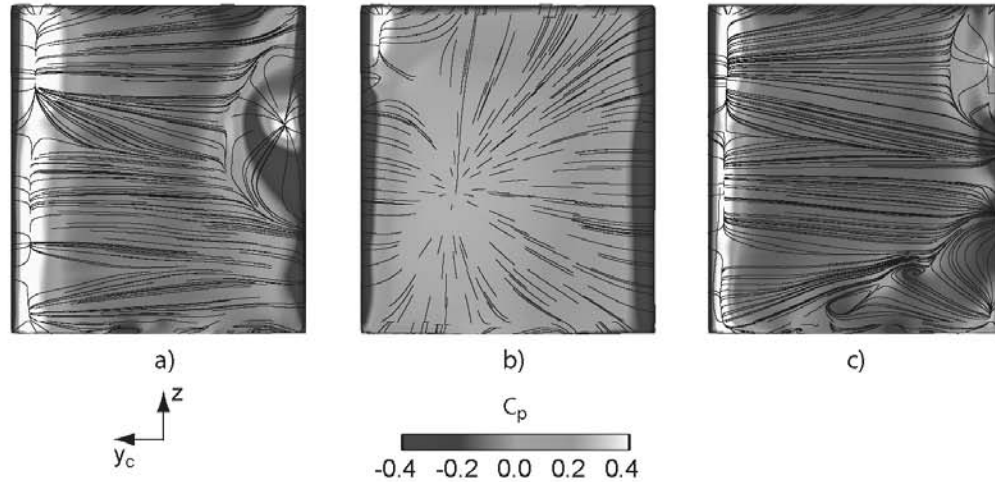


Fig. 11 Pressure coefficient and surface streamlines on the trailer frontal face for C_μ equal to a) 0.0 and b) 0.13 and c) side extenders.

tractor base and trailer frontal face, which is the mechanism responsible for the drag reduction.

The purpose in selecting tractor base bleeding as a drag reduction concept is to alleviate the maintenance and operational issues that often arise with conventional side extenders. It is evident through the results of this investigation that tractor base bleeding may, in fact, offer an alternative means to side extenders in reducing tractor-trailer gap drag. However, the base bleeding concept is not without its own

Investigation of Tractor Base Bleeding for Heavy Vehicle Aerodynamic Drag Reduction

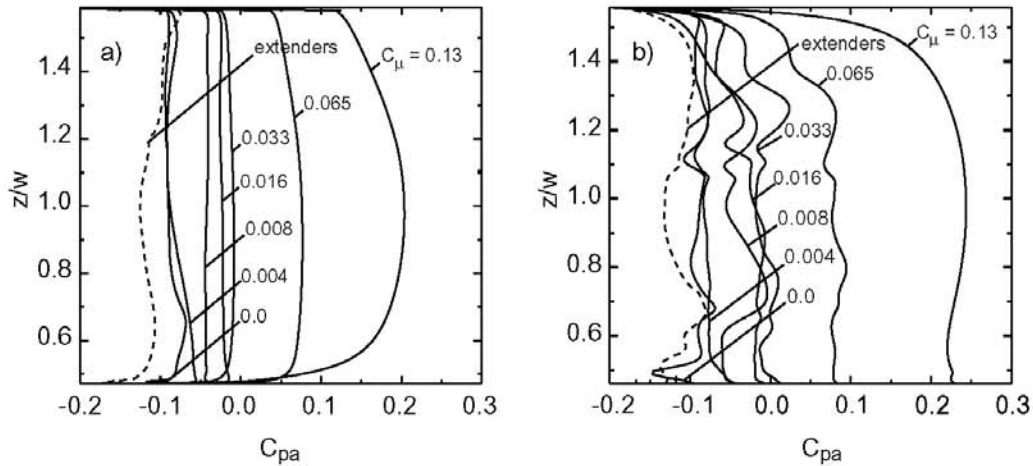


Fig. 12 Pressure coefficient in the body-axis direction on the a) tractor base and b) trailer frontal face centerlines as a function of the bleeding coefficient.

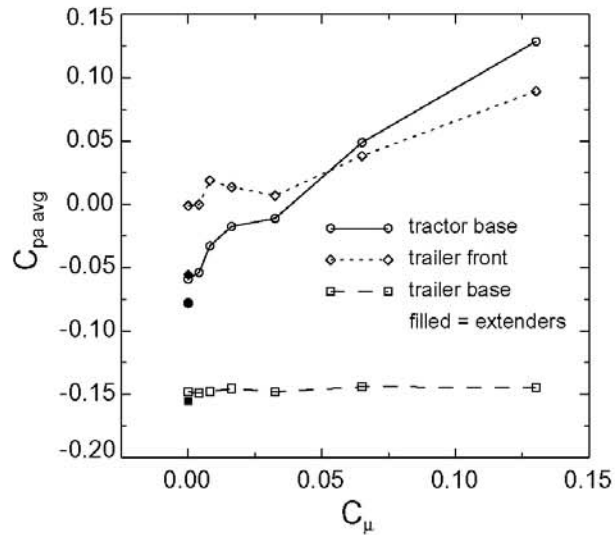


Fig. 13 Average pressure coefficient in the body-axis direction over the tractor base and trailer frontal surface and base in the body-axis direction as a function of the bleeding coefficient.

set of concerns and a number of questions remain unanswered regarding its feasibility, some of which are: how much power is required to produce the bleeding flow? Would it be more efficient to utilize solar energy or energy stored from regenerative braking to produce the bleeding flow? Can a base bleeding system be designed robustly enough so as to require a minimum level of maintenance? Under normal operating conditions, does tractor base bleeding provide a net reduction in fuel usage? Lastly, how much would a bleeding system add to the price of a tractor? Obviously, we are not in the position to answer these important questions at the present time. However, if these questions can be adequately and cost effectively addressed, tractor base bleeding may, in the future, offer commercial fleets a viable drag reduction alternative.

Acknowledgments

The authors would like to thank Dennis Acosta and Kurt Long of NASA Ames Research Center for their assistance in performing the wind tunnel measurements. This work was performed under the auspices of the U.S. Department of Energy by the University of California, Lawrence Livermore National Laboratory under Contract No. W-7405-Eng-48.

References

1. Arcas, D.R., Redekopp, L.G.: Aspects of wake vortex control through base blowing/suction. *Phys. Fluids* **16**(2), 452–456 (2004)
2. Axon, L., Garry, K.P., Howell, J.: An evaluation of CFD for modelling the flow around stationary and rotating isolated wheels. SAE 980032, SAE International Congress and Exhibition, Detroit, Michigan, February 23–26 (1998)
3. Bearman, P.W.: The effect of base bleed on the flow behind a two-dimensional model with a blunt trailing edge. *Aero. Quart.* **18**, 207–224 (1967)
4. BDAS 9.3 Software Package, Aerospace Computing, Inc. (2006)
5. Cooper, K.R.: Truck aerodynamics reborn lessons from the past. SAE 2003-01-3376, SAE International Truck and Bus Meeting and Exhibition, Fort Worth, Texas, November 10–12 (2003)
6. Cooper, K.R.: Commercial vehicle aerodynamic drag reduction: historical perspective as a guide. In: McCallen, R.C., Browand, F., Ross, J. (eds.) *The Aerodynamics of Heavy Vehicles: Trucks, Buses, and Trains*, pp. 9–28. Springer, Heidelberg (2004)
7. Gill, R.: Freightliner, LLC, private communication (2007)
8. Freightliner, <http://www.freightlinertrucks.com/trucks/find-by-model/columbia/> (2007)
9. Hammache, M., Browand, F.: On the aerodynamics of tractor-trailers. In: McCallen, R.C., Browand, F., Ross, J. (eds.) *The Aerodynamics of Heavy Vehicles: Trucks, Buses, and Trains*, pp. 185–205. Springer, Heidelberg (2004)
10. Hammond, D.A., Redekopp, L.G.: Global dynamics of symmetric and asymmetric wakes. *JFM* **331**, 231–260 (1997)
11. Huerre, P., Monkewitz, P.A.: Local and global instabilities in spatially developing flows. *Ann. Rev. Fluid Mech.* **22**, 473–537 (1990)
12. Ingram, K.C.: The wind-averaged drag coefficient applied to heavy goods vehicles. Transport and Road Research Laboratory Supplementary Report 392 (1978)
13. Kays, W.M., Crawford, M.E.: *Convective heat and mass transfer*. McGraw-Hill, Inc., New York (1993)
14. Koch, W.: Organized structures in wakes and jets—an aerodynamic resonance phenomenon? In: Bradbury, L.J.S., Durst, F., Launder, B.E., Schmidt, F.W., Whitelaw, J.H. (eds.) *Turbulent Shear Flows 4*, Springer (1983)
15. Koch, W.: Local instability characteristics and frequency determination of self-excited wake flows. *J. Sound Vib.* **99**, 53–83 (1985)
16. Leal, L.G., Acrivos, A.: The effect of base bleed on the steady separated flow past bluff bodies. *JFM* **39**(4), 735–752 (1969)
17. Leuschen, J., Cooper, K.: Full-scale wind tunnel tests of production and prototype, second-generation aerodynamic drag-reducing devices for tractor-trailers. SAE Paper 06CV-222, (2006)
18. MacAllister, L.C.: The aerodynamic properties and related dispersion characteristics of a hemispherical-base shell, 90-mm, HE, T91, with and without tracer element. BRL Memo. Report 990, Aberdeen Proving Ground, MD (1956)

Investigation of Tractor Base Bleeding for Heavy Vehicle Aerodynamic Drag Reduction 17

19. Menter, F.R.: Zonal two equation $k-\omega$ turbulence models for aerodynamic flows. Paper No. AIAA 93-2906, Proc. 24th Fluid Dynamics Conf., Orlando, Florida, USA, 6-9 July (1993)
20. Michel, G.W., Kost, F.H.: The effect of coolant flow on the efficiency of a transonic HP turbine profile suitable for a small engine. ASME 82-GT-86 (1982)
21. Pointer, W.D.: Evaluation of commercial CFD code capabilities for prediction of heavy vehicle drag coefficients. Paper No. AIAA-2004-2254, 34th AIAA Fluid Dynamics Conference and Exhibit, Portland, Oregon, 28 June–1 July (2004)
22. SAE wind tunnel test procedure for trucks and buses. SAE J1252, SAE Recommended Practice (1979)
23. Schumm, M., Berger, E., Monkewitz, P.A.: Self-excited oscillations in the wake of two-dimensional bluff bodies and their control. JFM **271**, 17–53 (1994)
24. Sevilla, A., Martínez-Bazán, C.: Vortex shedding in high Reynolds number axisymmetric bluff-body wakes: local linear instability and global bleed control. Phy. Fluids **16**(9), 3460–3469 (2004)
25. Solid Concepts, Inc., www.solidconcepts.com (2006)
26. STAR-CD v. 3.24-3.26. CD-Adapco Group, www.cd-adapco.com (2007)
27. Turbo Squid, www.turbosquid.com (2006)
28. Wood, C.J.: The effect of base bleed on a periodic wake. J. Roy. Aero. Soc. **68**(2), 477–482 (1964)
29. Wood, C.J.: Visualization of an incompressible wake with base bleed. JFM **29**(2), 259–272 (1967)
30. Yao, Y.F., Sandham, N.D.: Direct numerical simulation of turbulent trailing-edge flow with base flow control. AIAA J. **40**(9), 1708–1716 (2002)

IX. APPENDIX B

Experiments on Spray from a Rolling Tire

Charles Radovich and Dennis Plocher

Department of Aerospace & Mechanical Engineering
University of Southern California, Los Angeles, CA 90089
radovich@alumni.usc.edu, plocher@usc.edu

Abstract A novel laboratory apparatus has been built to understand the key mechanisms behind spray emerging from a rolling tire. Water leaving the tire from a single circumferential groove is analyzed using high-speed imaging. Visualizations reveal the formation of thin sheets of water connecting the roadway and the tire that eventually break into a droplet field. It is proposed that sheet breakup is the result of hydrodynamic instability. There is a preferred wavelength for disturbances on the sheet. After breakup, this preferred wavelength is preserved in slender ribs (or ligaments) that continue downstream until they disintegrate into droplets. Weber numbers based on the water density, tire circumferential speed and groove width vary in the range 1800 – 58000. The transition from sheet to spray is accelerated with increasing Weber number. Farther downstream, it is shown that droplet size and velocity distributions can be quantified as a function of Weber number.

1 Introduction

Tires moving through standing water create splash and spray which can decrease visibility and prove hazardous for other vehicles. Spray is defined here as water that has been forced through the tread pattern in the tire patch (contact patch between the tire and the pavement), thus, “processed” by the tire.

Our visualizations show that tires produce water spray as a result of the formation and breakup of thin sheets of fluid. An example image is shown in Figure 1.1, taken using a laser sheet for illumination (~10 nanoseconds exposure time). The tire on top (in the image) has a single rectangular circumferential groove 10.6 mm wide by 5.5 mm deep. The bottom tire has no groove. The peripheral speed of the tires is about 12 m/s, and the volume flow of water delivered upstream of the tire contact patch is just sufficient to fill the circumferential groove.

2

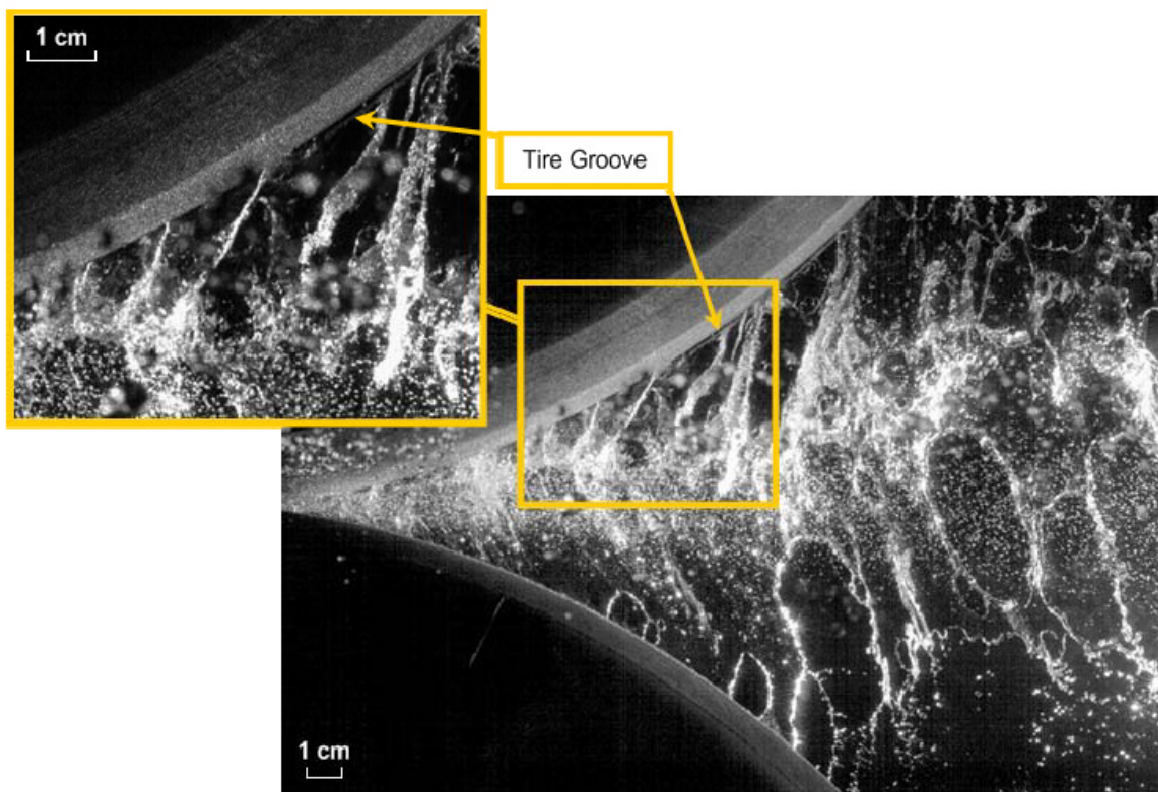


Fig. 1.1. Spray image using laser sheet illumination (~ 10 ns pulse time)

The laser illuminated image contains bright, irregular regions containing water that has left the circumferential groove. These irregular regions appear attached to the tires by ligaments and by thin sheets of water occupying the regions between the ligaments. There are breaks in the sheets and the smallest droplets appear to form along these rupture boundaries. Referring to the water leaving the circumferential groove as the central “jet,” the droplet formation process appears to be the combination of the instability and breakup of this central jet and the breakup or tearing of the thin sheets connecting the central jet to the tires.

Downstream from the contact patch, the spray ultimately disintegrates into a droplet field. Information on the distribution of sizes and velocities of these droplets is desired. This paper details the steps taken towards imaging and analyzing the spray immediately leaving the contact patch and the droplet field farther downstream. In brief, droplet size estimates come from counting the number of pixels a droplet occupies in an image. After determining the size distribution, images are “filtered” for specific size ranges and digital particle image velocimetry (DPIV) is used estimate droplet velocities as a function of droplet diameter.

2 Description of the Experiment

2.1 Justification for the two-tire geometry in the laboratory

In order to correctly model a tire rolling over a wet road, the physics of the tire patch must be understood. There are two reference frames applicable, as shown in Figure 2.1. In the first reference frame, an observer watches a tire roll along the wet pavement at a velocity U_{truck} . In the second reference frame, the observer rides with the rotating tire and sees water coming at the tire with velocity U_{truck} . Now, using the principle of symmetry, a second tire represents the road, as shown in Figure 2.2. This principle of symmetry and a reference frame riding with the car is used to model the tire/water interaction in the laboratory.

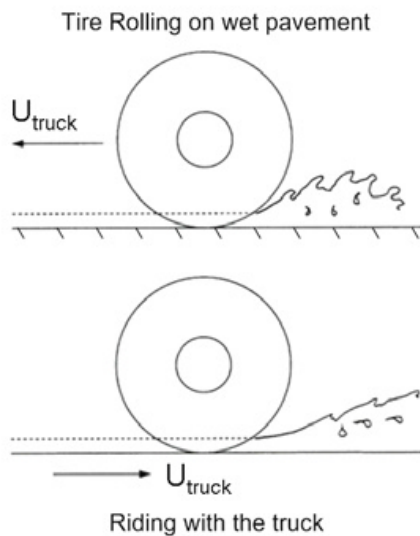


Fig. 2.1 Two reference frames for a tire rolling over wet pavement

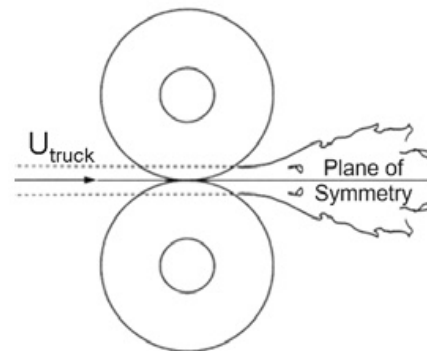


Fig. 2.2 Using principle of symmetry, a second tire represents the pavement

2.2 The Tire Spray Simulator

The apparatus for studying tire spray is shown in Figure 2.3. It consists of two rotating tires pressed together to form a tire patch, a system to deliver water at the peripheral speed of the tires and a means for visualizing spray coming from the tire patch.

Two wheels are suspended by swinging arms with tires touching. The tires (P-175/70 R13) are pressed together to form the contact patch and are held in place

4

by a spring-shock that is positioned using a stepper-motor-controlled lead screw. A Sensotech load cell measures the force between the tires. The left-most wheel in Figure 2.3 rotates by means of a chain drive and a Leeson DC electric motor and motor-controller. The tire to the right is driven by contact at the tire patch.

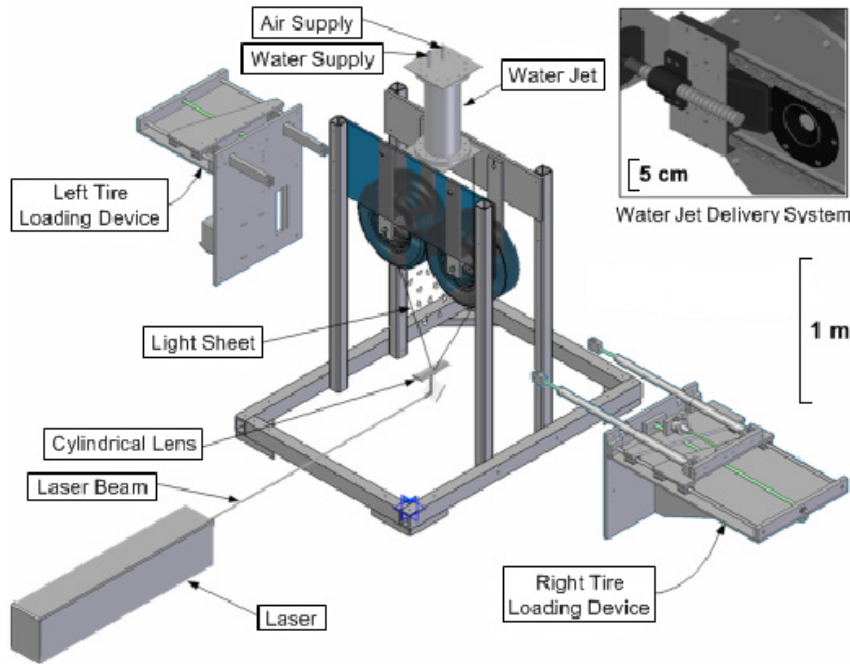


Fig. 2.3 The tire spray simulator

Wheel speed can be set in the range 3 m/s – 25 m/s. Precise wheel speed is measured by counting time intervals between pulses produced by a (stationary) Hall-effect pick-up and a toothed ring mounted on each wheel hub. The measured circumference of the grooved (g) and non-grooved (s) tires was $C_g = 1778 \pm 5$ mm and $C_s = 1810 \pm 5$ mm. Since the uncertainty in the time interval is on the order of microseconds, error in the estimate of tire speed, $\Delta U/U$, comes from uncertainty in knowledge of the tire circumference and is of the order 3×10^{-3} or less.

Visualizations of the tire spray are captured using a video camera set to record at 1600 fps and 5 μ s exposure time. Recorded images are 400 by 1260 pixels in resolution. The spray field can be illuminated using either a laser sheet or back-lighting. Laser sheet illumination allows for sharp, detailed images; however, pixel intensity information is often lost due to camera saturation as a result of specular reflection of light from the water surface. A more suitable means for imaging, and the method used for the remaining results in this paper, is backlighting. Figure 2.4 displays a side view of the experimental setup showing the orientation of the camera, tires, frosted (diffusive) glass and light source.

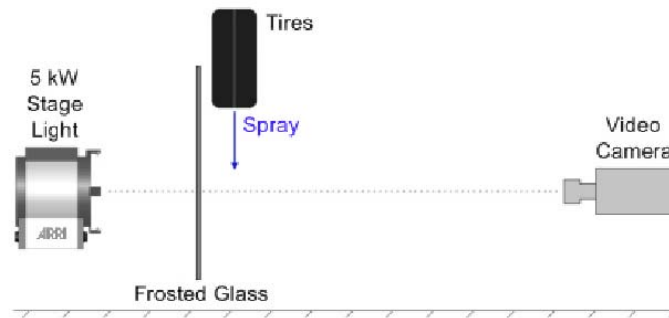


Fig. 2.4 Experimental setup for backlight imaging

2.3 Droplet Size Calibration

A series of calibration images were taken to verify that droplets of various sizes could be identified at all locations in the image field. A syringe pump, fit with a 21G hypodermic needle, delivered a single water droplet of a known size to the image field. A variation in droplet sizes was simulated by moving the camera farther from (or closer to) the free falling droplet. For each image of a droplet, a background image was recorded just before the droplet entered the field of view. This background image is used to account for and to correct any non-uniformities in the backlighting. Figure 2.5 shows an image of the prescribed droplet paired with its background image.

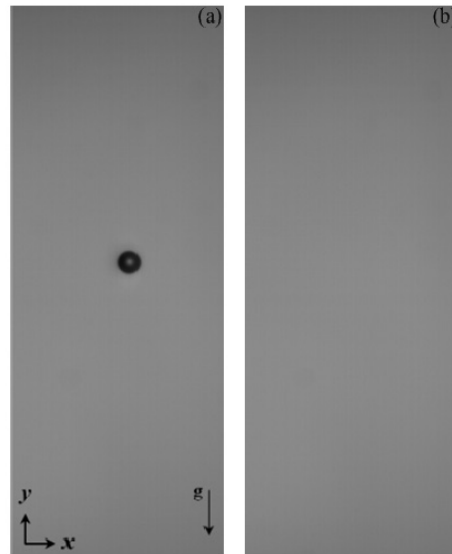


Fig. 2.5 (a) Image of a freefalling water droplet ($D = 2.83$ mm), (b) Background image, taken just before the droplet entered the field of view

Figure 2.6a shows a surface map of the image intensities recorded for a single droplet. Intensity values are expressed as a fraction of the average background intensity. The curvature of the surface is evidence of a non-uniformly lit background. In order to correct for this gradient, a linear gain correction matrix, $G(i,j)$, based on the background image was calculated and applied to the original intensity map $I'(i,j)$. Indices i and j refer to each pixel in the image field. Figure 2.6b shows the gain corrected intensity map $I_c(i,j)$. The final image used for analysis, $I(i,j)$, is obtained by subtracting the average background intensity from I_c and performing an inversion of the intensity map; Figure 2.6c. Equation Set 1 outlines the gain correction procedure.

$$\begin{aligned}
 G(i,j) &= BG(i,j) / \overline{BG} \\
 I_c(i,j) &= G(i,j) * I'(i,j) \\
 I(i,j) &= -1 * (I_c(i,j) - \overline{BG})
 \end{aligned}
 \tag{1}$$

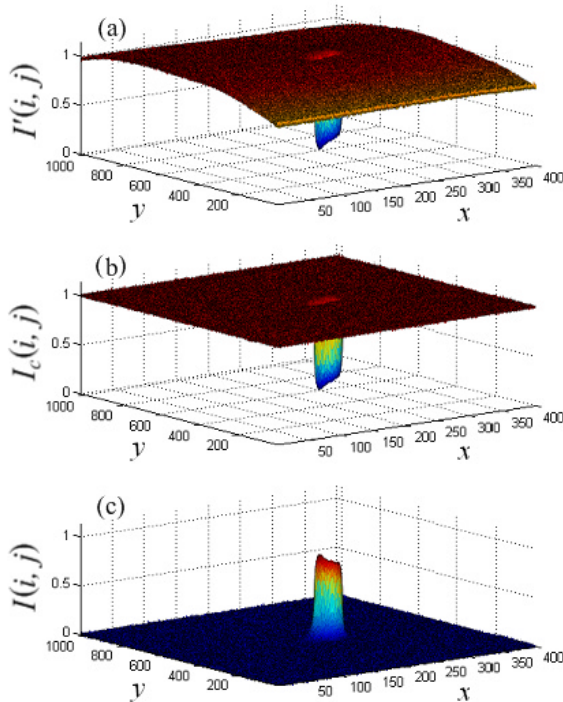


Fig. 2.6 Image intensity maps for (a) the raw image, (b) gain corrected image, (c) gain corrected and inverted image used for analysis

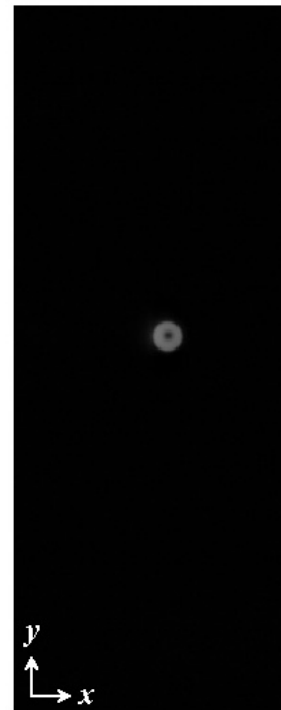


Fig. 2.7 Gain corrected and inverted image of a water droplet

An example of a gain corrected and inverted image is shown in Figure 2.7. This figure has a single droplet near the center of the camera field of view. Back-lighting transmitted through the droplet contributes to the dark spot in the center

of the inverted droplet image (seen as a bright spot in Figure 2.5a). Droplets can pass through any part of the image during a tire spray experiment. In order to verify that droplets are identifiable at all locations in the image, the calibration procedure was repeated for droplets located at the top and bottom of the image field.

The ability to resolve droplets of various sizes was also verified. The presence of smaller (larger) droplets was simulated by using the same 21G syringe pump and moving the camera farther away from (closer to) the apparatus. At each camera location, the prescribed droplet occupied a certain number of pixels. Observed droplet sizes ranged from 55 to 1380 pixels in area.

Figure 2.8 shows the intensity surface maps for four different droplet sizes at the top, center and bottom of the image field. This figure is a composite surface map with each droplet coming from a separate test. The presence of a droplet creates an intensity “mountain” with a broad base and narrow peak. The number of pixels retained in this mountain leads to the droplet size estimate. The black plane represents a cutoff threshold that determines which pixels to keep or to discard. Pixels with an intensity value at or above the threshold will be retained. Increasing or decreasing the threshold value will change the number of preserved pixels and subsequently alter the droplet size estimate.

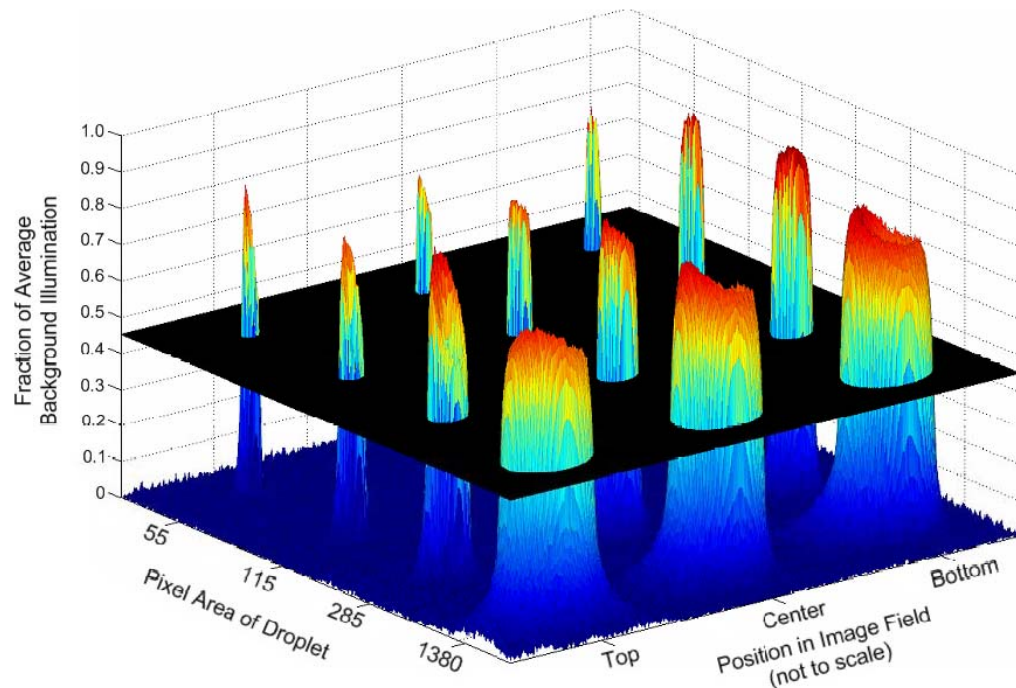


Fig. 2.8 Image intensity maps of four droplet sizes at the top, center and bottom of an image

Figure 2.9 illustrates the steps taken to estimate droplet size by counting the number of pixels a droplet occupies. Gray-scale images are reduced to black and white (binary) images after applying a threshold; Figure 2.9a. Pixels that are pre-

served are turned white (1) and everything else is set to black (0). Large droplets often allow a partial amount of light to transmit through, resulting in a “hole” at the center of the droplet. If a hole exists, it must be filled before counting pixels and determining the droplet size; Figure 2.9b. Once all droplets have been filled, the remaining pixels can be counted; Figure 2.9c.

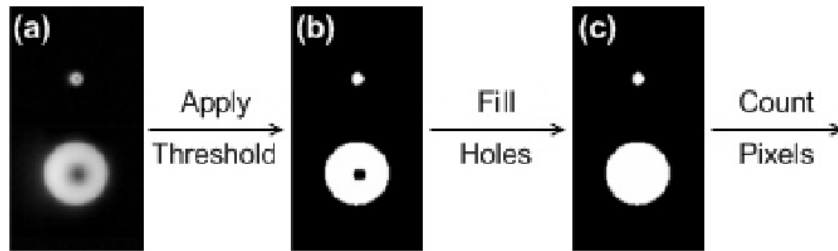


Fig. 2.9 Image processing used to determine the size of a droplet

Figure 2.10 shows the effect on the droplet diameter estimate when various threshold values are used. The abscissa represents the droplet area in terms of pixels; the ordinate is the estimated diameter calculated using $D = \sqrt{(4A/\pi)}$ and the appropriate mm/pixel factor for each camera location tested. The size of the droplet is 2.83 ± 0.01 mm in diameter, based on the average weight measured for a series of droplets. The experimental results provided in this figure clarify what threshold value is needed to estimate a droplet diameter within 5%, and to what extent various droplet sizes can be resolved with a single exposure. There is an increased sensitivity to minor changes in the threshold value for smaller droplets since these images have fewer pixels compared to the larger droplets. For all droplet sizes tested, an accurate estimate of the diameter was achieved using a threshold value equal to 45% of the average background illumination.

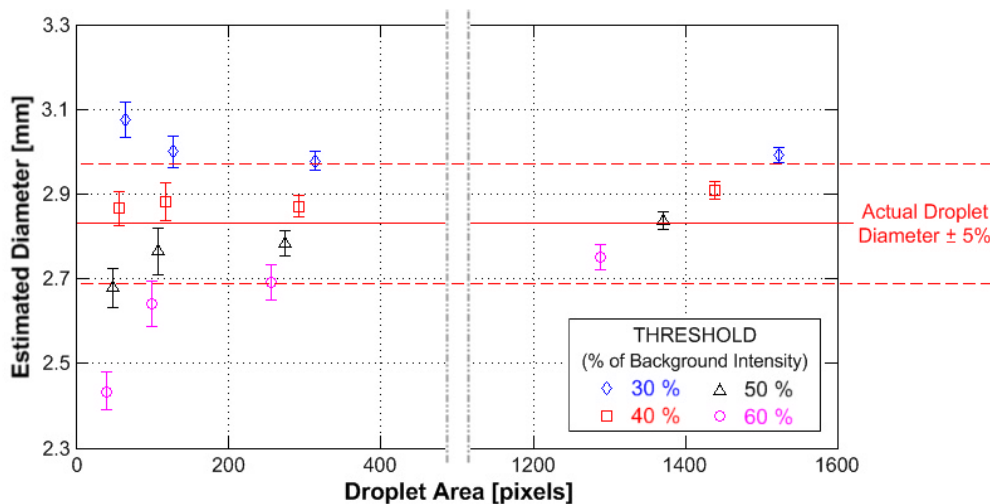


Fig. 2.10 Droplet diameter estimates for several droplet sizes and various threshold values

It was also observed that, in the spray plane, droplet images have a high contrast ratio compared to images outside of the focal plane. During the initial water delivery, spray may fall outside of the contact patch or create water spots on the frosted glass plate. These artifacts are undesirable for analysis as they are outside of the spray plane (the region downstream of the contact patch where the camera is focused). Therefore, applying an intensity cutoff threshold to the image retains pixels within and discards artifacts away from the region of interest. Previous works by Marmottant and Villermaux [1] and by Eastwood *et al* [2] illustrate a similar effort towards droplet detection and sizing.

3 Results

3.1 Sheet Formation and Break-Up

The Weber number is the most important parameter governing the formation of the water sheet and subsequent decay into a droplet field. This quantity is a ratio of the distorting force associated with fluid inertia to the (largely) restoring effect of surface tension (Equation 2). The Weber number is defined using the width of the tire groove ($h = 10.6$ mm), the density of water ($\rho = 998$ kg/m³), the speed of the water jet (U) and surface tension for water against air ($\sigma = 0.073$ N/m).

$$We = \frac{\rho h U^2}{\sigma} \quad (2)$$

A backlit image of the spray field produced at $U = 6$ m/s ($We = 5200$) is shown in Figure 3.1; the direction of flow is from left to right. The upper tire has a single circumferential groove; the lower tire has a buffed smooth surface. The field of view in this image is approximately 26.1 by 8.3 cm with the end of the contact patch visible on the left edge. Fluid leaving the contact patch remains attached to both tires and forms a thin sheet as the tires separate. The thickness of the sheet was not measured directly, however, it is estimated to be on the order of <1 mm. There are waves on the sheet that appear as dark rib structures. These ribs exhibit a periodic nature, suggesting a natural instability in the fluid flow. The sheet ultimately breaks up into a droplet field as it moves away from the contact patch.

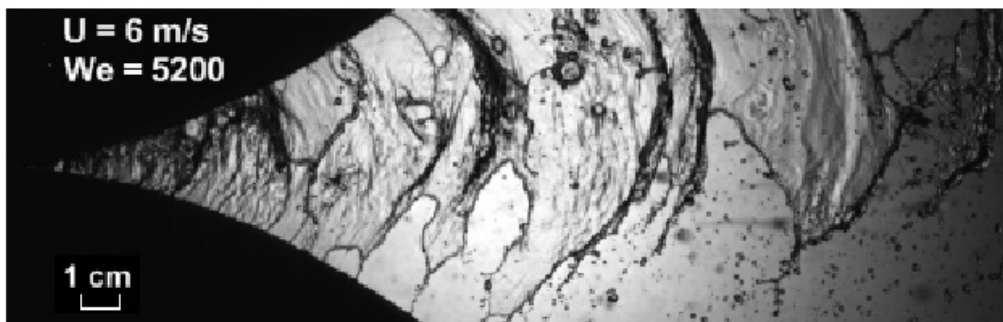


Fig. 3.1 Tire spray pattern at $U = 6 \text{ m/s}$, $We = 5200$

The development of the liquid sheet is sketched in Fig. 3.2, as it would appear at several cross planes looking upstream. The water passes through the tire patch inside the groove. At the downstream end of the tire patch the treads begin to move apart following the arc of the rotating tires, with the water exiting the tire patch as a jet attached to the groove on one side and to the smooth tire on the other side. The groove begins to drain and air flows in to fill the developing void. Sheets connect the jet to the smooth tire and to the water remaining in the groove. The jet takes on a sinuous shape (instability) as can be seen at the extreme left in Figure 3.1. Farther downstream, the sheet begins to separate from the surfaces of the tires. As breaks appear in the sheet, the sinuous jet forms into slender ribs (ligaments) orientated cross-stream to the flow.

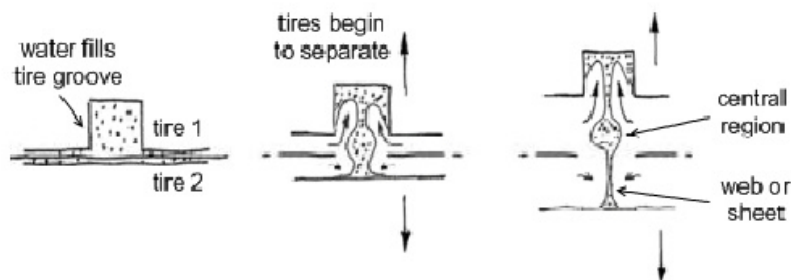


Fig. 3.2 Expected behavior of water as it leaves the tire groove at the contact patch

Eventually, ribs and sheets become a droplet field having a distribution of droplet sizes. At places where the sheet is thinnest, small droplets form along the edges of breaks and holes in the sheet. Where the broken sheet is thicker, the water within the contracting sheet is incorporated into the rib structure. Larger droplets are produced with the break-up of the periodic rib structure.

The patterns of sizes produced from a rolling tire are dependent on the Weber number. As described by Lefebvre [3], the development of a liquid sheet into a droplet field is governed by the fluid properties and initial velocity of the flow. Given that the groove width and properties of water are fixed, specific Weber

numbers are achieved through changes in the tire speed (and jet velocity). Figure 3.3 shows images taken at $We = 1,800$ and $47,000$. At low Weber number (Figure 3.3a), the flow field is heavily influenced by surface tension as edges of the broken sheet are rapidly pulled in towards the rib structures and little or no sheet remains. The majority of the droplet field at low We results from the break-up of the rib structures, thus, larger droplet sizes are expected. At higher Weber number (Figure 3.3b), the flow is driven by the fluid inertia and more liquid remains in the sheets. The breakup of these thin sheets tends to produce smaller droplets.

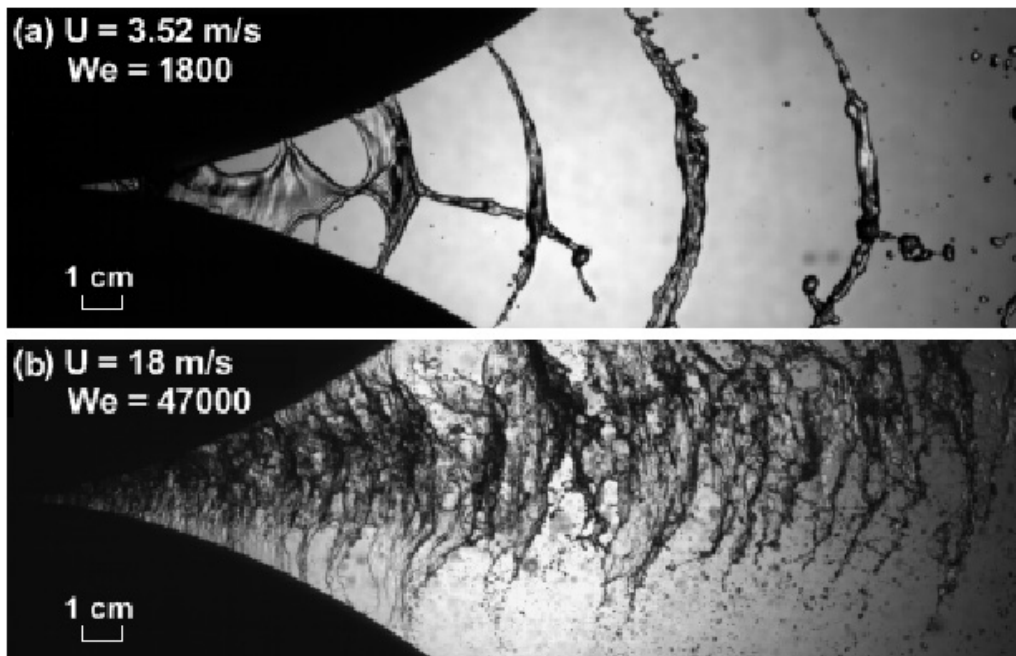


Fig. 3.3 Spray pattern variation with Weber number

3.2 Droplet Field Size and Velocity Estimates

Figure 3.4a is a single image from the video showing a portion of the droplet field produced by tires rotating at $U = 6$ m/s. The direction of flow in these images is from top to bottom. The center of the image field is one meter downstream from the end of the contact patch and the field of view is approximately 13 by 4 cm. Figure 3.4a reveals various droplet sizes as well as several “fuzzy” spots due to spray that fell outside of the contact patch at the start of the experiment. Figure 3.4b shows the gain corrected and thresholded image with only droplets in the spray plane remaining.

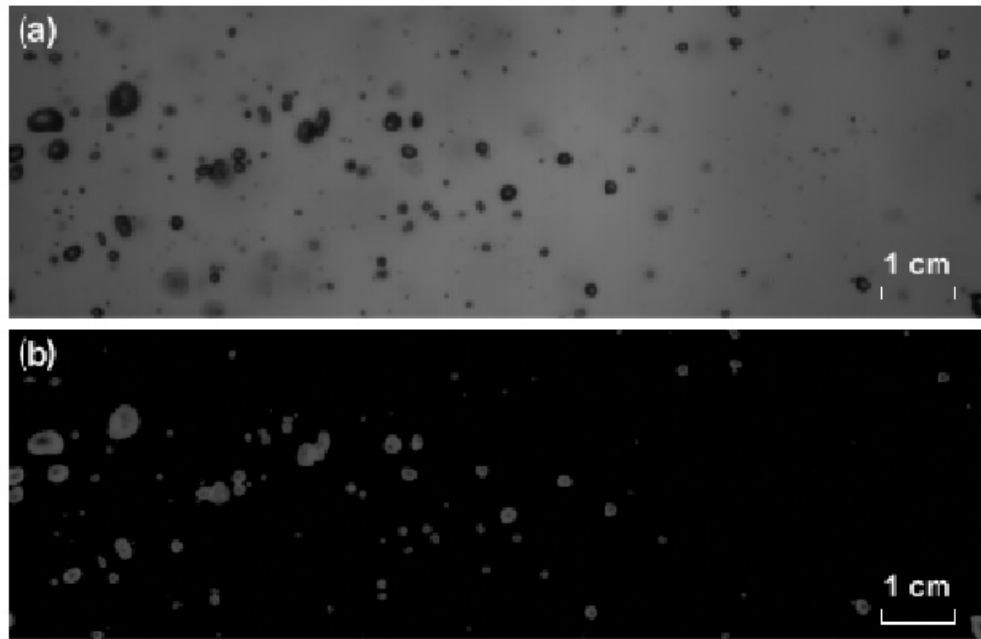


Fig. 3.4 Droplet field at $U = 6 \text{ m/s}$, $We = 5200$: (a) raw image, (b) gain corrected and thresholded image

Figure 3.5 displays the distribution of sizes for the droplets detected in this video frame. A total of fifty-eight (58) droplets were detected, ranging from 0.8 to 4.4 mm in diameter. This distribution is derived from the single image presented in Figure 3.4. Statistically more reliable distributions can be built up by adding contributions from multiple (hundreds of) frames.

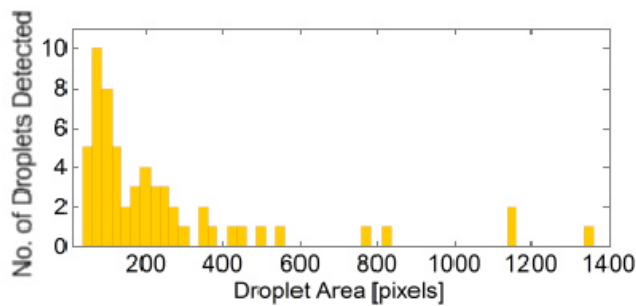


Fig. 3.5 Distribution of droplet sizes

Given a distribution of droplet diameters, images can be “filtered” for specific droplet sizes and DPIV performed to estimate droplet velocities as a function of diameter. Figure 3.6 represents a filtered version of Figure 3.4b with only droplets from 1.65 to 2.33 mm in diameter shown. This image and a successive image taken 625 μs later were processed using DPIV to obtain the velocity vectors for

each droplet in this size range. The DPIV process tracks the motion of a droplet by cross-correlating the two images. What makes this application of DPIV different from the standard technique is that only regions adjacent to particle centroids in the first image are interrogated in the second image. This greatly increases the efficiency of the DPIV algorithm. Typical particle displacements in the image pairs are on the order of forty pixels. The velocity estimate for droplets in this size range was 6.85 ± 0.5 m/s. The two droplets presented without a velocity vector had moved out of the image view before the second image was recorded.

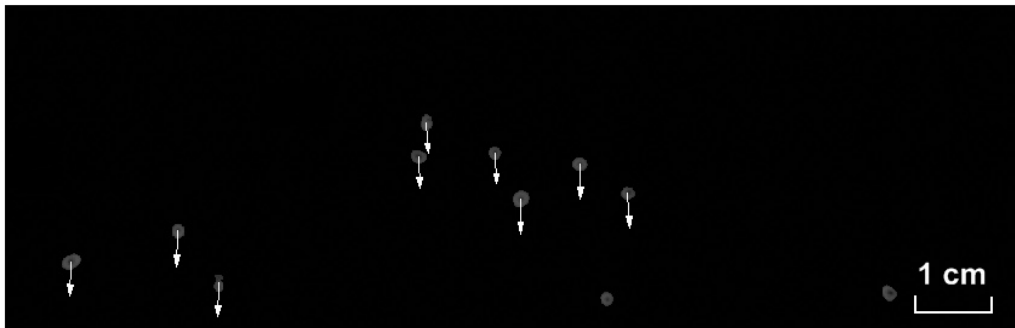


Fig. 3.6 $U = 6$ m/s spray field, filtered for droplets between 1.65 and 2.33 mm in diameter

The DPIV process was repeated for a smaller set of droplets with diameters between 1.16 and 1.65 mm. The estimated velocity for this size range was 6.15 ± 0.3 m/s. The spatial location, with respect to the contact patch centerline, and velocity vectors for these two droplet diameter ranges is presented in Figure 3.7. A divergence away from the contact patch centerline is evident by the direction of the velocity vectors. This behavior is due to the tendency of water to attach to the surface of a tire and the ability of a tire to carry water laterally away from the plane of symmetry.

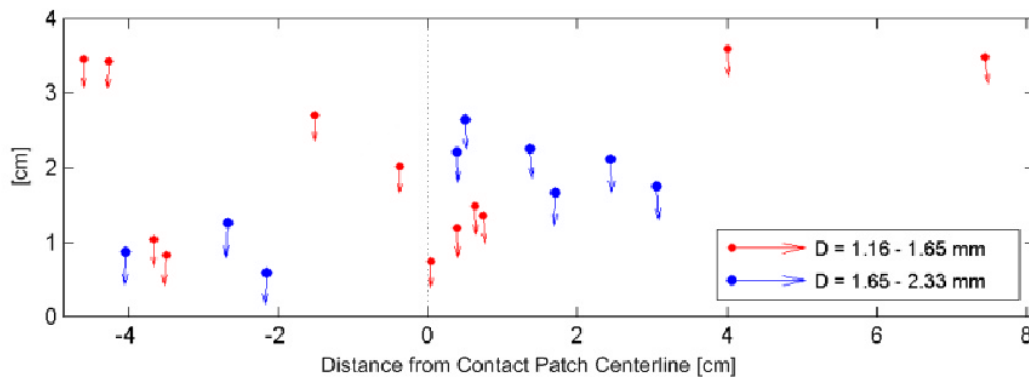


Fig. 3.7 A demonstration of DPIV results for two droplet size ranges

4 Conclusion

The operation of a tire spray simulator has been demonstrated. Video of the developing spray was captured in the region just downstream of the tire patch. From this video the flow was qualitatively described as a jet exiting the tire patch that spreads out into a sheet which spans the distance between the two tires. The sheet, thickened by the central jet, is unstable and forms sinuous waves that break into a cross-stream rib structure. Ultimately, the entire flow disintegrates into a droplet field.

A technique for isolating and measuring the size and velocity of individual droplets has been developed and calibrated. The ability to detect droplet sizes a factor of 5 different in diameter using a single exposure was demonstrated, with the lower limit of detection approaching 50 pixels in area. It is possible that this lower limit can be further relaxed.

Acknowledgments

The authors would like to acknowledge the continued financial support from the Michelin Americas Research & Development Corporation as well as the production of tires for the experiment. Support from the Department of Energy (DOE) is also acknowledged. Additional thanks to Rose McCallen, Fred Browand, Jim Ross and ECI for the organization of The Aerodynamics of Heavy Vehicles II conference.

References

- [1] Marmottant P., Villermaux E., On Spray Formation, *J. Fluid Mech.*, 2004, Vol. 498, pp. 73-111.
- [2] Eastwood C.D., Armi L. and Lasheras J.C., The Breakup of Immiscible Fluids in Turbulent Flows, *J. Fluid Mech.*, 2004, Vol. 502, pp. 309-333.
- [3] Lefebvre A., *Atomization and Sprays (Combustion: An International Series)*, CRC, 1988.

This document highlights work sponsored by agencies of the U.S. Government. Neither the U.S. Government nor any agency thereof, nor any of their employees, makes any warranty, express or implied, or assumes any legal liability or responsibility for the accuracy, completeness, or usefulness of any information, apparatus, product, or process disclosed, or represents that its use would not infringe privately owned rights. Reference herein to any specific commercial product, process, or service by trade name, trademark, manufacturer, or otherwise does not necessarily constitute or imply its endorsement, recommendation, or favoring by the U.S. Government or any agency thereof. The views and opinions of authors expressed herein do not necessarily state or reflect those of the U.S. Government or any agency thereof.



A Strong Energy Portfolio for a Strong America

Energy efficiency and clean, renewable energy will mean a stronger economy, a cleaner environment, and greater energy independence for America. Working with a wide array of state, community, industry, and university partners, the U.S. Department of Energy's Office of Energy Efficiency and Renewable Energy invests in a diverse portfolio of energy technologies.

For more information contact:
EERE Information Center
1-877-EERE-INF (1-877-337-3463)
www.eere.energy.gov